COMMUNICATIONS

https://doi.org/10.26552/com.C.2017.3.3-8

Matej Goraus - Lubos Suslik - Dusan Pudis - Jana Durisova - Daniel Jandura
Jaroslav Kovac - Marek Tlaczala - Wojciech Dawidowski - Beata Sciana*

PHOTONIC DEVICES WITH SILOXANE MEMBRANES

Expansion of polymer nanotechnologies accelerated the polymer photonics. This technology brings novel interesting results with simple and cheap solutions. Promising candidates are siloxane materials as polydimethyl siloxane (PDMS) and polydimethyldiphenyl siloxane (PDMDPS) with unique mechanical and optical properties. In this paper we present laser lithography technologies in a combination with siloxane embossing for fabrication of different grating structures with periodical and quasiperiodical symmetry. We present the concept of siloxane based thin membranes with patterned surface as an effective diffraction element for modification of radiation pattern diagram of light emitting diodes (LEDs) and enhancement of angular detection properties of photodiodes. Also the combination of PDMDPS and PDMS was used for fabrication of a waveguide structure with surface relief Bragg grating. Optical properties of fabricated LEDs are investigated by near- and far-field measurements. Transmission properties of fabricated waveguide are investigated by optical spectrum analyzer.

Keywords: *Photonic crystal, photonic quasicrystal, light emitting diode, waveguide, light extraction efficiency*

1. Introduction

Polymer based photonics bring us novel interesting results with simple and cheap solutions. Creating devices with flexible features was a challenge for polymer photonics where polymer materials are used instead of semiconductor. The siloxanes are flexible silicon based elastomers with unique properties which make it attractive for optical applications. In the waveguide optics, we can use polymer siloxanes for fabrication of the optical waveguides [1], optical fibres [2], optical sensors [3] and optical waveguides with surface relief Bragg gratings (SRBG). Major research was focused on improvement of light extraction efficiency (LEE) and radiation pattern modification of light emitting diodes (LED). Many groups used implementation of photonic crystal (PhC) in the LED surface to change these optical properties [4, 5]. Generally, the current technologies try to pattern the surface of the LED by combination of lithography and surface etching or with colloidal crystals [6]. Another interesting way is using the thin siloxane membranes with the PhC structures which can be applied directly on the LED surface [7]. This technique offers a new solution how to easily modify the LED properties as LEE and radiation pattern diagram.

Good candidates are siloxane materials such as polydimethyl siloxane (PDMS) and polydimethyldiphenyl siloxane (PDMDPS) with unique mechanical and optical properties. These polymers are elastic (elongation 120 %), transparent for visible and near infrared light, thermal stabile and biocompatible [8, 9]. In this paper, we present the results achieved by siloxane based technologies in a combination with laser lithography and siloxane embossing with resolution achieving hundreds of nanometers. Laser interference lithography in Mach-Zehnder configuration is able to create periodical or quasiperiodical PhC (PQC) structures in two dimensions. In the combination with embossing technique, we achieved novel polymer PhC structures. We proposed the concept of thin polymer membranes with patterned PhC structure for improving LEE and modification of radiation pattern diagram of LEDs. Also the combination of polymers PDMDPS and PDMS was used for fabrication of complicated planar waveguides with SR-BG, which can be used as a tunable filter or sensor.

2. Fabrication process of siloxane membranes

There are many techniques favorable for the planar PhC fabrication such as electron and ion beam lithography and nanoimprint. The fabrication technologies based on optical principles as interference lithography, direct laser writing (DLW) laser lithography and near-field scanning optical microscope

---

* **[1]Matej Goraus, [1]Lubos Suslik, [1]Dusan Pudis, [1]Jana Durisova, [1]Daniel Jandura, [2]Jaroslav Kovac, [3]Marek Tlaczala**
[3]Wojciech Dawidowski, [3]Beata Sciana
[1]Department of Physics, Faculty of Electrical Engineering, University of Zilina, Slovakia
[2]Institute of Electronics and Photonics, Slovak University of Technology, Bratislava, Slovakia
[3]Faculty of Microsystem Electronics and Photonics, Wrocław University of Science and Technology, Wroclaw, Poland
E-mail: matej.goraus@fel.uniza.sk

lithography are very useful for PhC structure preparation in two dimensions (2D) in photoresist and different semiconductor surfaces. We demonstrate basic principles of the laser interference lithography as effective tools for PhC structure fabrication in photoresist materials and in a combination with embossing technique of the liquid PDMS also for PDMS patterning. In our experiments, we used positive photoresists of AZ 5214E and S1828 G2.

2.1 Laser interference lithography

Laser interference lithography is promising technique for fabrication of PhC in a large scale area. 1D and 2D interference patterns can be produced by this technique. The design of 1D optical field pattern can be obtained by the interference process of two optical plane waves (Fig. 1a). The 2D interference pattern can be achieved by the multiple exposure process in a combination with the sample rotation between individual exposures (Fig. 1b, 1c). This multiple exposure technique can be used for fabrication of different 2D periodic structures in photoresist materials as well as in different III-V compounds. We can produce different symmetry of PhC and PQC structures depending on the angle of rotation of the sample in the exposure process. For square symmetry of PhC we used sample rotation at 90°. Also PQC structure with 12-fold symmetry was prepared by multiexposure process with the angle of rotation 0 - 360° with 30° step. The design of the structure can be proposed by the simple theoretical approach according to [10].

In our experimental arrangement we used Mach-Zehnder configuration (Fig. 2) to create interference optical field. As a source, we used Toptica Blue Mode laser emitted at 403 nm. For fabrication of PhC structures we used the photoresist layer of AZ 5214E with thickness app. 2 μm. Photoresist layer was prepared by spin coating process on glass substrate using SPIN 150 coater with post-baking at 65 °C for 2 minutes and at 100 °C for 3 minutes to remove the solvent. After exposure, the exposed photoresist sample was developed in AZ 400K developer for 10 s and rinsed in deionized water. For the PQC fabrication, we used S1828 G2 photoresist with thickness app. 3 μm with post-baking at 100 °C for 2 minutes and developing in AZ 400K for 10 s.

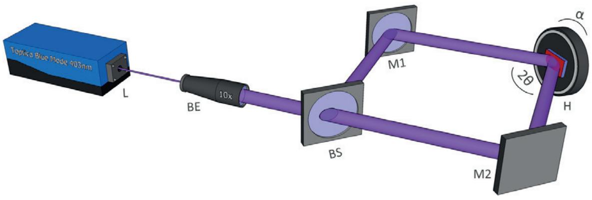

Fig. 2 Experimental arrangement of laser interference lithography in Mach-Zehnder configuration, were L is the laser source, BE - beam expander, BS - 50:50 beam splitter (for wavelengths range 400-700 nm), M1, M2 - mirrors. H - sample holder where 2θ is the angle between two incident beams and α is the angle of sample rotation

2.2 PDMS embossing

For the fabrication of patterned PDMS membranes, the liquid PDMS was prepared from two components of Sylgard 184 elastomer with curing agent ratio 10:1. For uniform surface, the 30 μm thin PDMS layer was spin coated at 4000 rpm on patterned photoresist samples. Subsequently, the sample was cured for 45 min at 75 °C. In order to obtain PDMS membrane we used two methods. First, due to unique elastic properties of PDMS the membrane was mechanically removed from photoresist layer (Fig. 3). Reusability is the best advantage of this method. The other way was based on dissolving photoresist in solvent and lifting off the PDMS membrane. By using both of these ways, we obtained nearly identical PhC PDMS membranes.

3. Fabricated photonic devices

These technologies of fabrication of patterned siloxane membranes can be used in different optical and optoelectronical

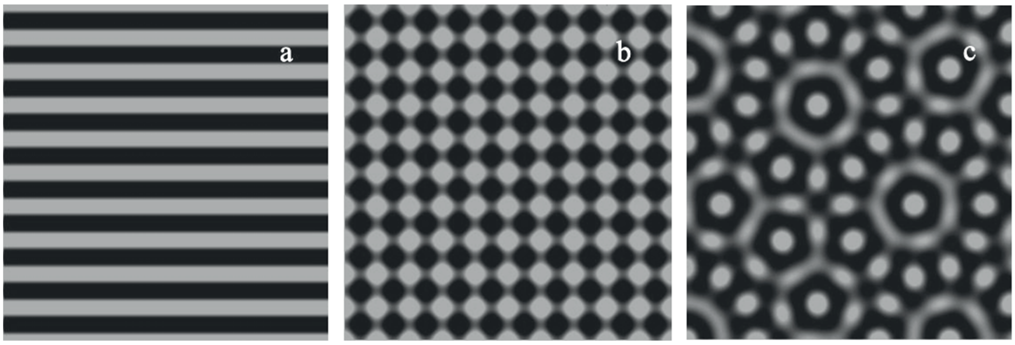

Fig. 1 Simulation of theoretical distribution of interference optical field where a) represents 1D interference pattern b) 2D pattern with square symmetry and c) interference pattern of PQC structure with the 12-fold symmetry

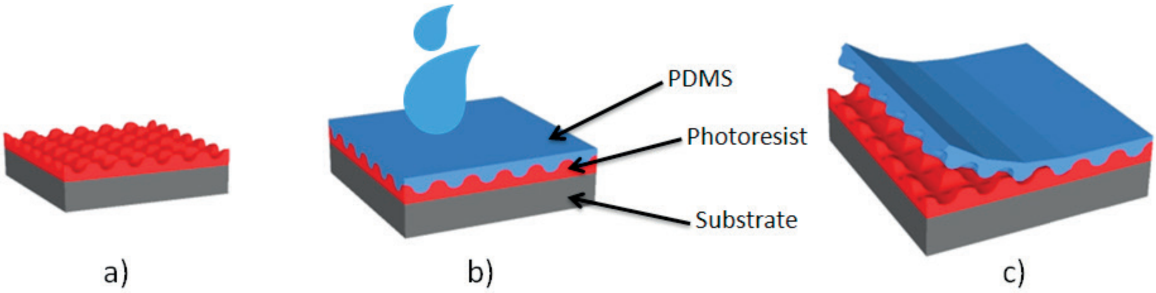

Fig. 3 Embossing and removing process of embossed PDMS membranes a) substrate with photoresist master b) application of liquid PDMS and c) mechanical separation of cured membrane

applications. We focus on optical characterization of LEDs and photodiodes with patterned PDMS membranes and the PDMS waveguide with SR-BG.

3.1 LEDs and photodiodes with PDMS membrane PhC and PQC

Two-dimensional PhC of square symmetry and PQC structures were prepared by the embossing technique in the surface of thin PDMS membranes described above.

It was published, that PhC on the surface can lead to the light extraction efficiency improvement of LEDs and also should modify the radiation pattern diagram [11, 12]. In our experiments we patterned different PDMS membranes for direct application in LED chips. For the PDMS patterning we used the combination of photoresist patterning by interference lithography and PDMS embossing described above. After mechanical selection, the prepared PDMS membrane was directly placed on the LED chip with patterned surface oriented on the top. For the characterization we used commercial Cree LEDs with central emission at wavelength of 635 nm. Quality of prepared embossed PDMS membranes (of thickness app. 30 µm) was analyzed by atomic force microscope (AFM) and is shown in Fig. 4. The period of the embossed structure in PDMS preserves the photoresist pattern with the period of 1600 nm and depth of 420 nm. In our experiments the structures with two different symmetries were prepared to show the effect of PhC on radiation properties using 2D PhC structure with square symmetry (Fig. 4a) and PQC structure with 12-fold symmetry (Fig. 4b).

After the application of patterned PDMS membranes on the LED surface the radiation properties in the near field were measured by using the near-field scanning optical microscope (NSOM) with aperture-less optical fiber tips. As is shown in Fig. 5, the local surface enhancement in the near field reflects the pattern symmetry and corresponds well with AFM structure. The NSOM analysis shows the near-field of the 2D PhC structure with square symmetry and also PQC structures. Radiation properties of both structures were compared by investigation in the far field by goniophotometer measurements. Top view of the radiation pattern clearly shows the effect of higher symmetry of PQC in comparison with double symmetry of square PhC (Fig. 6a). Also an effective angular widening was documented for the PQC structure. The measured optical properties in the near and far field document the effective function of PDMS membranes on modification of radiation pattern of LEDs.

For the implementation of PDMS membranes with patterned surface PhC structure the GaAs-based photodiode with InGaAsN active region was also prepared. We used the epitaxial structure of GaAs-based photodiode grown by atmospheric pressure metal

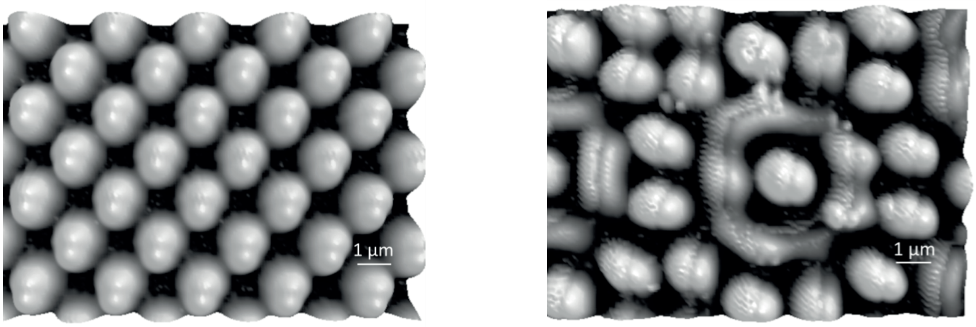

a) *b)*

Fig. 4 AFM image of a) 2D PhC structure of square symmetry and b) PQC structure with 12 fold symmetry embossed in PDMS surface

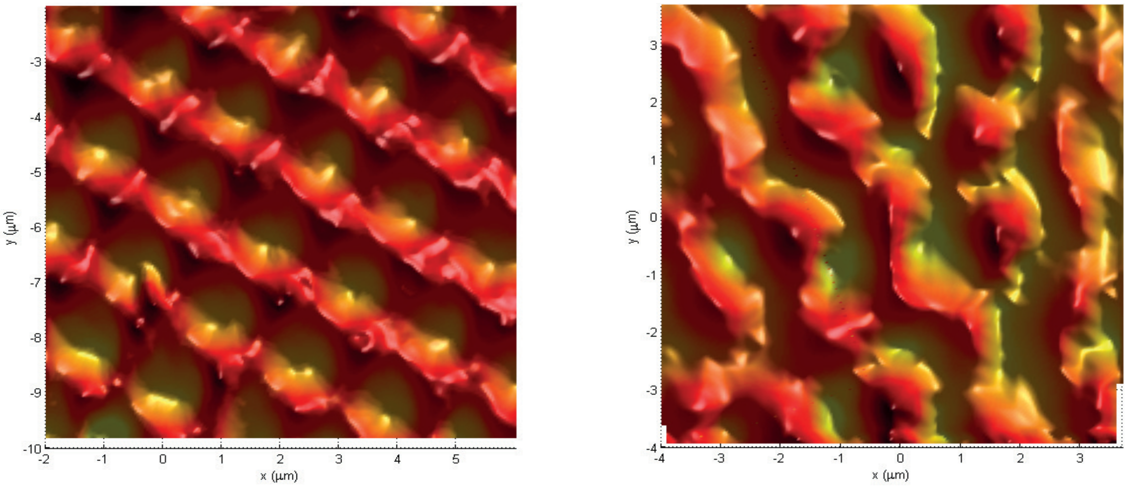

a) b)

Fig. 5 Near-field pattern of LED with a) PhC PDMS membrane with square symmetry and b) PQC structure with 12-fold symmetry

organic vapor phase epitaxy (AP-MOVPE). Detailed information about the growth process conditions, contact preparation and precursors were published in [13]. The active region of p-i-n GaAsbased device consist of undoped InGaAsN active layer sandwiched between silicon doped ntype GaAs buffer and Zn doped p-type InGaAsN layer, capped by heavily Zn doped p-type GaAs contact layer. On the top surface of the photodiode the patterned membrane with PhC structure of square symmetry and period of 800 nm was applied. The angular detection properties were measured by illumination of the photodiode with orange LED source with central emission at the wavelength of 625 nm (Fig. 6b). Evident square symmetry can be found in the angular photoresponse as an effect of 2D square PhC structure on the top of the photodiode. It documents the effectiveness of patterned PDMS membranes also on detection properties.

3.2 Polymer waveguide with surface relief Bragg grating

For polymer waveguide structures with SR-BG preparation, laser interference lithography and embossing technique was used in our experiments. Patterning of thin photoresist layer was carried out by laser interference lithography in MachZehnder arrangement using Toptica Blue Mode 403 nm laser (Fig. 2).

To achieve appropriate refractive index contrast, two types of polymers were used. For the waveguide core formation we used PDMDPS and PDMS was used for the cladding formation. Onedimensional (1D) PhC pattern with period of 21 µm was created in the first step. Next, the sample was developed in AZ400 K developer and 1D PhC pattern with period of 1.61 µm was exposed perpendicularly to the first pattern in the second step. By this technological process, we created a D-shaped array of app. 10 µm wide and app. 2.5 µm high waveguides with SRBG

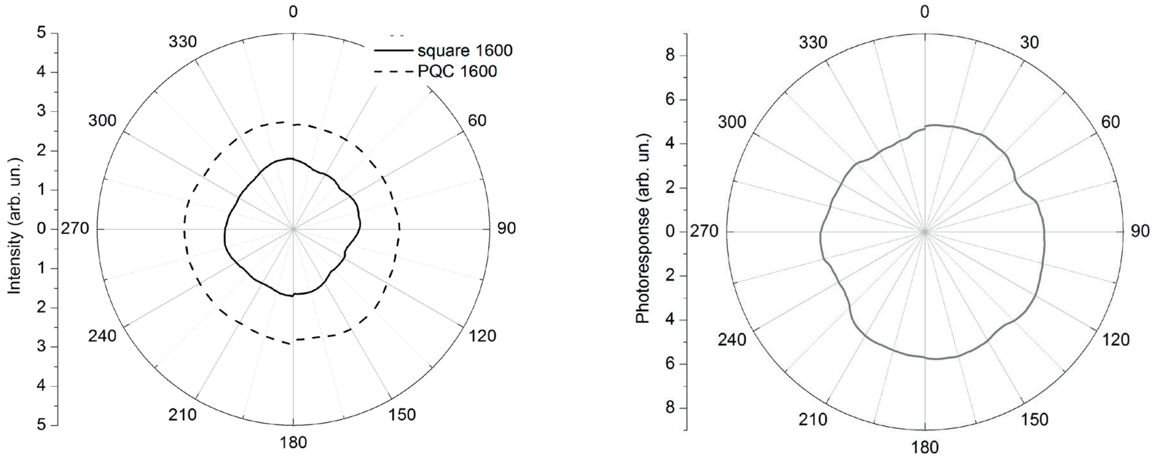

a) b)

Fig. 6 a) Radiation pattern of orange LED chip with applied patterned PDMS membrane with PhC and PQC structures and b) angular photoresponse measured for illumination by orange LED source

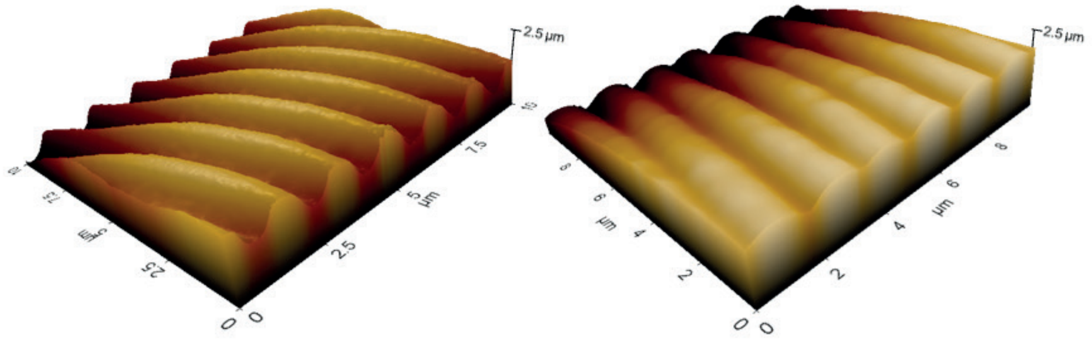

a) b)

Fig. 7 AFM images a) patterned photoresist master with surface Bragg grating and b) embossed PDMDPS polymer membrane with SR-BG before cladding application

in photoresist master as was documented from AFM (Fig. 7a). Array of the polymer SRBG waveguides was formed by filling the valleys with liquid PDMDPS, spin coating and heat curing. Next, the membrane was mechanically separated from the photoresist master (Fig. 7b). Cladding liquid PDMS was deposited on the patterned side of PDMDPS membrane and heat curing. By this process, we created the array of the polymer SR-BG waveguides.

The transmission properties of waveguides with SRBG were measured by light transmission characteristics using the broadband LED with central emission wavelength at λ = 1550 nm. The proposed spectral dip according to equation $\lambda_B = 2n_{eff}\,\Lambda/k$ was at the wavelength λ_B = 1539 nm, where λ_B is the reflected wavelength, n_{eff} is the effective refractive index of the waveguide, Λ is the period of the grating and k is the order of the reflection. The transmission spectral characteristic shows evident dip at the wavelength of 1540 nm, what is in a good coincidence with the proposed dip (Fig. 8).

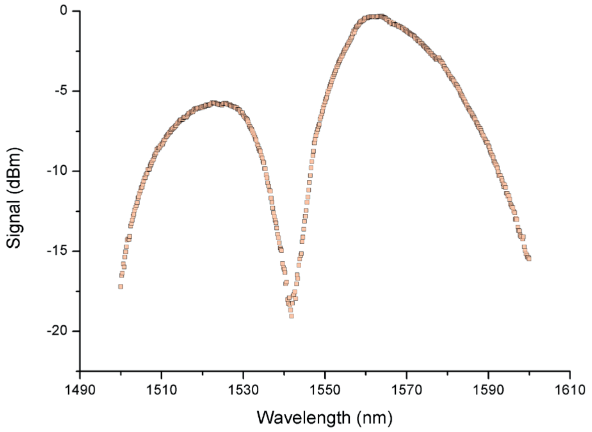

Fig. 8 Transmission spectrum of the SR-BG waveguide with 15 dBm dip and minimum at wavelength 1540 nm

4. Conclusion

In this paper we presented the results achieved using siloxane based technologies. Using the laser interference lithography in Mach-Zehnder configuration we prepared different 2D grating structures in periodical and quasiperiodical. By combining PDMS and PDMDPS embossing techniques we achieved 2D structures for the on-chip applications in optics and optoelectronics. We designed thin polymer membranes with patterned surface using PhC and PQC structures as an effective diffraction element for improving light extraction efficiency and modification of radiation pattern diagram of LEDs. The effect of structures was investigated by the near field measurement from orange emitting LED. Also, the thin PDMS membrane was used for the enhancement of angular detection properties of GaAs –based photodiodes. The combination of PDMDPS and PDMS was used as an alternative material for fabrication of planar photonic devices using waveguide with surface relief Bragg grating. We showed the transmission spectrum of this waveguide with proposed spectral dip. All these results favor the siloxane membranes and the used technologies for using in polymer photonics.

Acknowledgement

This work was supported by the Slovak National Grant Agency under the projects No. VEGA 1/0491/14 and 1/0278/15 and the Slovak Research and Development Agency under the project No. APVV 0395-12.

References

[1] CAI, Z., QIU, W., SHAO, G., WANG, W.: A New Fabrication Method for All-PDMS Waveguides. *Sensors and Actuators A*., 204, 44-47, 2013.

[2] MARTINCEK, I., PUDIS, D., CHALUPOVA, M.: Technology for the Preparation of PDMS Optical Fibers and Some Fiber Structures. *IEEE Photonisc Technology Letters*, 26*,* 1446-1449, 2014.

[3] PAEK, J., KIM, J.: Microsphere-Assisted Fabrication of High Aspect-Ratio Elastomeric Micropillars and Waveguides. *Nature Communications*, 5, 3324, 2014.

[4] JIANG, S., et al: Study on Light Extraction from GaN-Based Green Light-Emitting Diodes Using Anodic Aluminum Oxide Pattern and Nanoimprint Lithography. *Scientificreports*, 6, 21573, 2016.

[5] CHANG, Y., LIOU, J., LIU, W.: Improved Light Extraction Efficiency of a High-Power GaN-Based Light-Emitting Diode with a Three-Dimensional-Photonic Crystal (3-D-PhC) Backside Reflector. *IEEE Electron Device Letters*, 34, 777-779, 2013.

[6] LAI, CH., HSIEH, CH., WU, CH.: Light-Spectrum Modification of Warm White-Light-Emitting Diodeswith 3D Colloidal Photonic Crystals to Approximate Candle Light. *Optics Letters*, 38, 3612-3615, 2013.

[7] PUDIS, D., et al: PDMS-Based Nanoimprint Lithography for Photonics. *Communications-Scientific Letters of University of Zilina,* 16(1), 15-19, 2014.

[8] Sylgard 184 Silicone Elastomer [online]. Date: 17/03/2017. Available at: http://www.dowcorning.com/DataFiles/090276fe80190b08.pdf.

[9] LS-6943 optical thermoset [online]. Date: 17/03/2017. Available at: https://nusil.com/services/downloadfile.ashx?productcode=LS-6943&originalname=LS-6943P.pdf.

[10] SKRINIAROVA, J., et al.: Periodic Structures Prepared by Two-Beam Interference Method. *Microelectronics Journal,* 38, 746-749, 2007.

[11] PUDIS, D., et al: Effect of 2D Photonic Structure Patterned in the LED Surface on Emission Properties. *Applied Surface Science,* 269, 161-165, 2013.

[12] PUDIS, D., et al: *Siloxane Based Photonic Structures and Their Application in Optic and Optoelectronic Devices.* Proc. of SPIE: Wave and Qquantum Aspects of Contemporary Optics, Slovakia, 10142, 2016.

[13] PUDIS, D., et al: *GaAs-Based Photodetector with Applied PDMS Membrane with Photonic Crystal in the Surface.* Conference on Advanced semiconductor devices and microsystems (ASDAM) 2016, Slovakia, 33-36, 2016.

https://doi.org/10.26552/com.C.2017.3.9-15

Jarmila Mullerova - Pavol Sutta*

ON SOME AMBIGUITIES OF THE ABSORPTION EDGE AND OPTICAL BAND GAPS OF AMORPHOUS AND POLYCRYSTALLINE SEMICONDUCTORS

This paper reports on somewhat puzzling character of the determination of the optical band gap energies of amorphous and polycrystalline semiconductors, where probably the mixed-phase composition and structural and compositional disorder are main reasons for the ambiguities. The analysis is performed using spectra of absorption coefficients of the featured samples of Si:H and Zn-Ti-O extracted by numerical analysis of transmittance measurements. The differences originating from using several procedures to process spectra of absorption coefficients are discussed.

Keywords: *Absorption coefficient, thin film, microstructure, optical band gap, Tauc, Cody, Sokolov.*

1. Introduction

For optoelectronic applications, fundamental optical absorption is a relevant issue. The absorption edge or the band edge is an optical property defined as the photon energy of the transition between the strong short- and the weak long-wavelength absorption in the spectrum of a semiconductor. The spectral position of this transition is determined by the energy separation between the valence and conduction bands of a material and corresponds to the threshold of a charge transition between the highest nearly filled band and the lowest nearly empty band. The optical bad gap is in general understood as the photon energy required for this transition.

Optical properties of amorphous and polycrystalline semiconductors have become objective of numerous studies, among all mainly for purposes of the photovoltaic conversion or other photonics applications. In general, amorphous semiconductors are materials with no long-range translational order of atomic sites [1 - 3]. However they often exhibit considerable short-range order of nanometer-sized crystallites. Polycrystalline (sometimes referred as microcrystalline) materials contain crystalline grains of random orientation separated by grain boundaries. Although the crystalline fraction commonly prevails, they may retain amorphous phase and inter- or intra-grain voids [4]. For this reason amorphous/polycrystalline semiconductors can possess the optical band gap which makes them similar to crystalline semiconductors. However an apparent widening of band tails of valence and conduction bands in amorphous and polycrystalline semiconductors leads to some controversies in characterizing the absorption edge and the optical band gap [5 - 7].

In this paper we describe several concepts of determining the optical band gap. Thin films of multi-phase hydrogenated silicon (Si:H) and Zn-Ti-O ternary oxides are featured examples for comparing several attempts. From transmittance spectra the wavelength-dependent absorption coefficients are determined. The puzzle concerning optical band gaps estimated by various approaches is discussed.

2. Band extrapolation methods

It is well-known that a periodic potential typical for long-range ordered solids results in energy bands of sharp edges due to finite overlap integrals. Amorphous semiconductors are solids that do not possess the log-range order of atomic sites. Polycrystalline semiconductors consist of crystalline grains with different orientation and therefore the network is also ordered only in small regions. Additionally polycrystalline semiconductors may also contain amorphous phase and voids. Disorder typical for amorphous/polycrystalline semiconductors is followed by statistically varying widths and/or depths of potentials which result in broadening the edges into exponential tails. Other agents

---

* [1]**Jarmila Mullerova,** [2]**Pavol Sutta**
[1]Institute of Aurel Stodola, Faculty of Electrical Engineering, University of Zilina Liptovsky Mikulas, Slovakia
[2]New Technologies - Research Centre, University of West Bohemia, Plzen, Czech Republic
E-mail: mullerova@lm.uniza.sk

to broaden the edges into tails may be material differences, microstructure development or quantum confinement effects.

Thus, new types of energy states, the so-called localized states appear in inorganic or organic amorphous and polycrystalline semiconductors (Fig. 1). The localized states are considered to be defect states due to disorder leading to the existence of over- and under-coordinated atoms and weak bonds. Besides the localized states in band tails, also deep states in the band gap exist due to dangling bonds, all of them responsible for many unique properties of amorphous/polycrystalline semiconductors [8]. The existence of band tail states has an important impact on their optical properties, especially on the band-to-band absorption crucial for many optoelectronic applications.

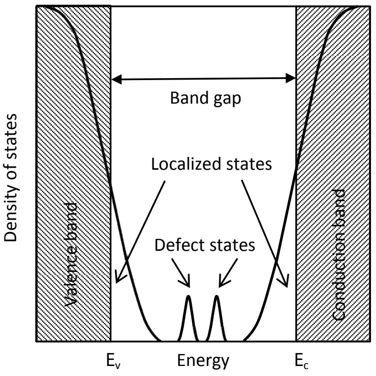

Fig. 1 Density of energy states in the vicinity of the edges of the conduction (E_c) and valence band (E_v) and in the band gap (localized states and deep states; the patterned rectangles represent the extended states

Then the optical band gap in amorphous/polycrystalline semiconductors characterizing the optical transitions between the extended states is a rather vague parameter owing to the localized states between valence and conduction bands. It is ambiguous to deduce the interval between extended states corresponding to the gap. A meaningful procedure to achieve knowledge on the band gap modifications is the inspection of the absorption spectrum of the material, i.e. the dependence of the absorption coefficient α on the wavelength λ or on the photon energy E related to λ as $E = hc/\lambda$, (h is the Planck's constant, c is the speed of light).

Typical optical absorption spectrum α(λ) of amorphous/polycrystalline semiconductors with three apparent regions is in Fig. 2. The Urbach energy characterizes the tailing of the band edges that have an exponential energy distribution. It determines the slope of the exponential manner of the absorption coefficient described as $\alpha(E) = \alpha_0 \exp[(E - E_v)/E_0]$, where and E_v are constants and the Urbach energy E_0 is inversely proportional to the width of the exponential tail. It represents the tailing of the valence band density of states that is larger than the conduction band tailing. As the tail states are the direct figure of merit of the temperature-induced, structural or compositional disorder, the Urbach energy is of considerable interest in a number of studies [5, 6]. Due to the band tailing no sharp absorption threshold is obtained and the absorption edge cannot be clearly determined [2].

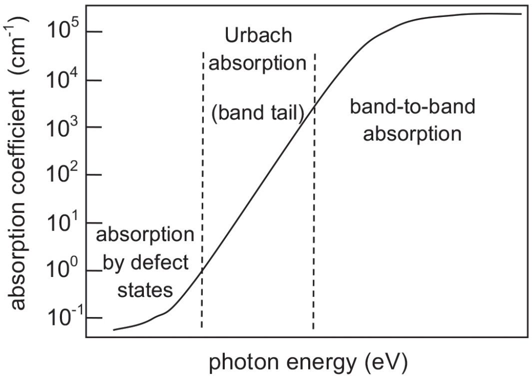

Fig. 2 The typical absorption coefficient of amorphous/polycrystalline semiconductors

Several representative methods have been reported to interpret the absorption region related to the optical transitions between extended states [7, 9]. Assuming parabolic bands and constant matrix elements squared Jan Tauc derived the formula to describe the dependence of the absorption coefficient α on the photon energy E [10]

$$(\alpha E)^{1/2} = B_{Tauc}\left(E - E_g^{Tauc}\right) \tag{1}$$

where E_g^{Tauc} is the so-called Tauc optical band gap energy. Hence the plot of $(\alpha E)^{1/2}$ versus the photon energy E leads to a straight line whose intersection with the E-axis gives E_g^{Tauc}. The Tauc extrapolation has been widely adopted [11 - 13]. The scale factor B_{Tauc} of the plot is often attributed to various aspects of semiconductor network. It includes information on the disorder-induced correlation of optical transitions between the valence and conduction bands and is often accepted to characterize the temperature and compositional disorder in amorphous and polycrystalline materials [5, 14].

Cody assumed the photon-energy dependent transition matrix element and the expression [15]

$$(\alpha/E)^{1/2} = B_{Cody}\left(E - E_g^{Cody}\right) \tag{2}$$

The Cody plot $(\alpha/E)^{1/2}$ versus the photon energy usually obtains better linearity than the Tauc plot $(\alpha E)^{1/2}$. For this reason the Cody optical gap E_g^{Cody} can be determined with less ambiguity than that from $(\alpha E)^{1/2}$ plot.

Sokolov studied optical gap fluctuations in amorphous Si and proposed the cubic root dependence

$$(\alpha E)^{1/3} = B_{Sokolov}\left(E - E_g^{Sokolov}\right) \tag{3}$$

The Sokolov model for the determination of the Sokolov band gap $E_g^{Sokolov}$ is similar to the model of the linear density of states suggested by Mott and Davis supposing a constant transition matrix element [15, 16]. Similarly to the scale factor of the Tauc plot, B_{Cody} and $B_{Sokolov}$ are the scale factors. Thus Cody, Tauc and Sokolov optical band gaps can be determined from extrapolation of the linear part of the plot to the energy axis. Linear parts of Cody plots are obviously more extended than Tauc plots. Hence the optical band gap determination could be more exact.

An alternative way to characterize the optical band gap is the iso-absorption gap E_{03} (E_{04}) defining the photon energy at which the absorption coefficient achieves the value of 10^3 (10^4) cm^{-1}. Although none of them is reflecting particular differences in optical absorption, they are tolerable when the linear part of $(\alpha E)^{1/2}$ plot versus E is reduced, especially in the presence of continuous distribution of localized states between the valence and conduction bands.

3. Experimental determination of the absorption coefficient

Absorption coefficients of transparent solids can be determined from transmittance/reflectance measurements. Transmittance $T(\lambda)$ of a homogeneous thin film of the thickness d with parallel interfaces deposited on a thick substrate at nearly normal incidence of light is the following nonlinear function of λ, the refractive index n_1 and the extinction coefficient k_1 of the film and the refractive index n_2 of the non-absorbing substrate [17]

$$T(\lambda) = \frac{Ax}{B - Cx + Dx^2} \tag{4}$$

where the absorbance $x = \exp(-\alpha d)$. Equation (4) is obtained by summing the multiply-transmitted waves. Here

$$\begin{aligned}
A &= 16n_2(n_1^2 + k_1^2) \\
B &= [(1+n_1)^2 + k_1^2][(n_1 + n_2^2)(n_1 + 1) + k_1^2] \\
C &= 2\cos\varphi[(n_1^2 + k_1^2 - 1)(n_1^2 + k_1^2 - n_2^2) - \\
&\quad - 2k_1^2(n_1^2 + 1)] - 2\sin\varphi[(n_1^2 + k_1^2 - 1) \\
&\quad (n_2^2 + 1) + 2(n_1^2 + k_1^2 - n_2^2)] \\
D &= [(n_1 - 1)^2 + k_1^2][(n_1 - 1)(n_1 - n_2^2) + k_1^2]
\end{aligned}$$

The phase factor is defined as $\varphi = 4\pi n_1 d/\lambda$. The absorption coefficient α (Fig. 2) of the film corresponding to band-to-band transitions is related to k_1 and λ through the relation

$$\alpha = 4\pi k_1/\lambda \tag{5}$$

Theoretical transmittance $T(\lambda)$ to be compared with the experiment can be calculated by Equation (4) using the proper dispersion relations of $n_1(\lambda)$, $k_1(\lambda)$. Currently employed $n_1(\lambda)$, $k_1(\lambda)$ of amorphous/polycrystalline semiconductors are featured by the Tauc-Lorentz or the Cody-Lorentz models [18 - 21]. Refractive indices n_1 and extinction coefficients k_1 of the films as real and imaginary parts of the complex refractive index $\tilde{n}_1 = n_1 + ik_1$ can be extracted from the numerical comparison $T(\lambda)$ and measured transmittance $T_{exp}(\lambda)$. The fitting procedure minimizes deviations between experimental $T_{exp}(\lambda)$ and theoretical $T(\lambda)$ in the broad spectral region including the vicinity of the absorption edge. To calculate $n_1(\lambda)$, $k_1(\lambda)$ by applying an optimization procedure based on genetic algorithm is a proper tool [22]. The absorption coefficient will be known from Equation (5).

Reflectance of the film can be expressed similarly by summing the multiply-reflected waved and can be used for the determination of $n_1(\lambda)$, $k_1(\lambda)$ when the film is deposited on an absorbing substrate [23].

4. Featured examples

Two unalike semiconductors of different compositional order and structure and both of extensive applications in optoelectronics and photovoltaics were used to illustrate the means of the determination of optical band gaps. The series of Si:H and ternary oxides of Zn-Ti-O were deposited on clean Corning Eagle 2000 glass substrates (details here [24, 25]). Si:H is recognized for extensive applications in solar cells, thin film transistors, LEDs, display and imaging technologies etc. In addition to these applications Zn-Ti-O is also known as a semiconducting photocatalyst.

1. A series of Si:H (the thickness of approx. 400 nm) was deposited by parallel plate PECVD. The depositions differ by the amount of additional hydrogen (H_2) added to silane (SiH_4) plasma. The H_2 to SiH_4 flows ratio is the so-called dilution R ranging from $R = 10$ to $R = 70$. In our previous paper [24] multi-phase composition was detected. The samples deposited at $R < 30$ were identified as amorphous Si:H with a certain volume fraction of voids, samples at $R \geq 30$ converted to polycrystalline with certain fractions of voids and amorphous phase.
2. A series of zinc titanium oxide Zn-Ti-O was prepared by reactive magnetron co-sputtering in reactive mode. Seven samples of the thickness of 200 – 300 nm were deposited with increasing atomic percentage Ti content [25]. With increasing Ti content not only compositional changes but also the evolution of a complicated polycrystalline structure of the decreasing crystallite size and the preferred orientation of crystallites in a certain direction against the surface occurred. The sample of the highest Ti content (12.5 %) was identified as amorphous.

Structural properties (Table 1) were analysed by X-ray diffraction using an automatic powder diffractometer X´Pert Pro with CuKα radiation supplemented by several microstructure-devoted methods (Raman and FTIR spectroscopy, HR-TEM, Microstructure details of the featured samples and B_{Tauc} factors. p_c/ p_a [%] - the ratio of the crystalline to amorphous volume fraction in Si:H determined by XRD, pc- polycrystalline structure, prevailing phase of Zn-Ti-O indicated Table 1

Si:H			**Zn-Ti-O**		
R	p_c/p_a [%]	B_{Tauc} [$eV^{-1/2}$ $cm^{-1/2}$]	Ti (at. %)	Structure, composition and prevailing orientation of crystallites	B_{Tauc} [$eV^{-1/2}$ $cm^{-1/2}$]
10	0	670	0	*pc*, (002) ZnO	1860
20	0	580	1.1	*pc*, (002) ZnO	1500
30	0	630	2.4	*pc*, (002), (101) ZnO, bimodal distribution of crystallites	1200
40	54	370	5.2	*pc*, (104) $ZnTiO_3$, (004) TiO_2 atanas, bimodal distribution of crystallites	1140
50	63	370	6.7	*pc*, (104) $ZnTiO_3$, (004) TiO_2 atanas, bimodal distribution of crystallites	1050
60	75	320	8.7	*pc*, (104) $ZnTiO_3$, (004) TiO_2 atanas, bimodal distribution of crystallites	950
70	77	330	12.5	amorphous	1000

EEDS). Optical transmittances recorded by Specord 210 spectrophotometer [24, 25] were used to calculate α (Figs. 3 and 4).

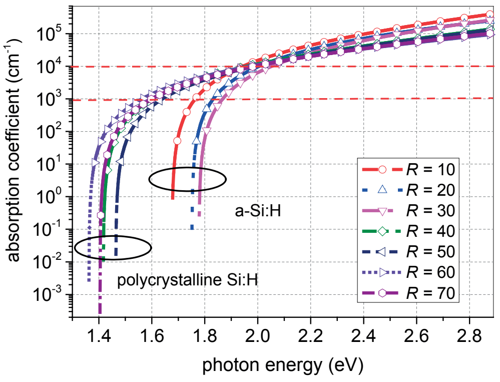

Fig. 3 Absorption coefficients of Si:H (red dash lines: iso-absorption levels of 10^3 cm^{-1}, 10^4 cm^{-1})

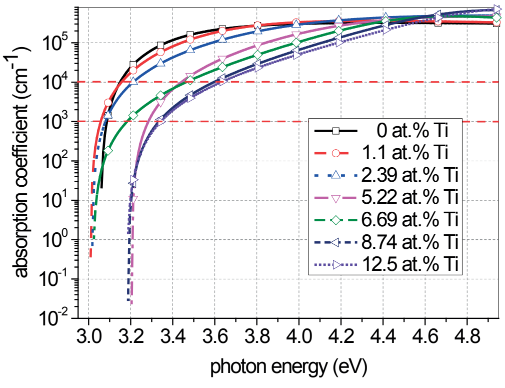

Fig. 4 Absorption coefficients of Zn-Ti-O (red dash lines: iso-absorption level of 10^3 cm^{-1}, 10^4 cm^{-1})

From Fig. 3 the iso-absorption gaps E_{03}, E_{04} of Si:H were directly deduced. The iso-absorption gap E_{03} cannot be considered from Fig. 4 for Zn-Ti-O because it is too close to the Urbach absorption. E_g^{Tauc}, E_g^{Cody} and $E_g^{Sokolov}$ gaps were determined using plots corresponding to Equations (1), (2) and (3). Representative Tauc and Cody plots of Si:H and Zn-Ti-O are in Figs. 5 - 8. Some of linear extrapolations are indicated by dash lines. Sokolov plots return the least linear parts for the optical band gap determination.

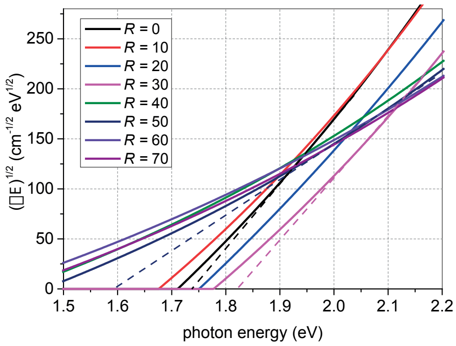

Fig. 5 Tauc plots of Si:H

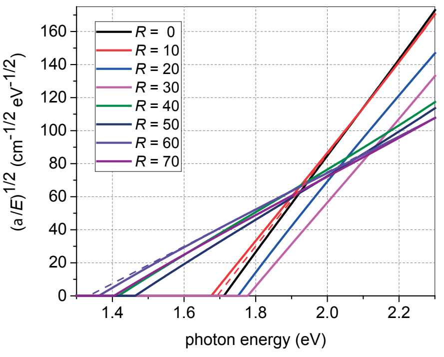

Fig. 6 Cody plots of Si:H

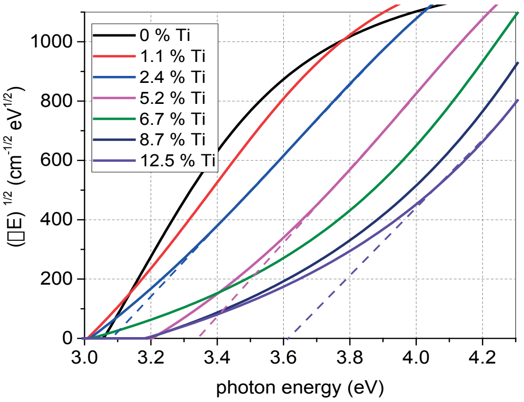

Fig. 7 Tauc plots of Zn-Ti-O

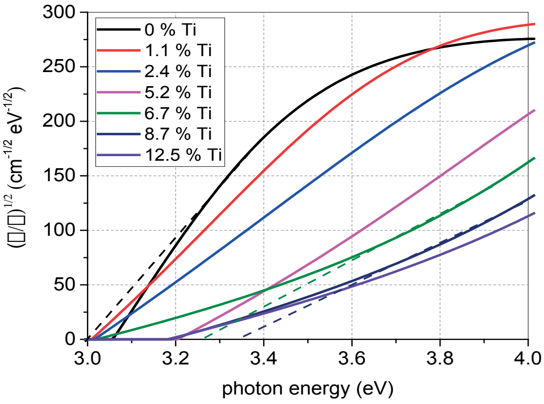

Fig. 8 Cody plots of Zn-Ti-O

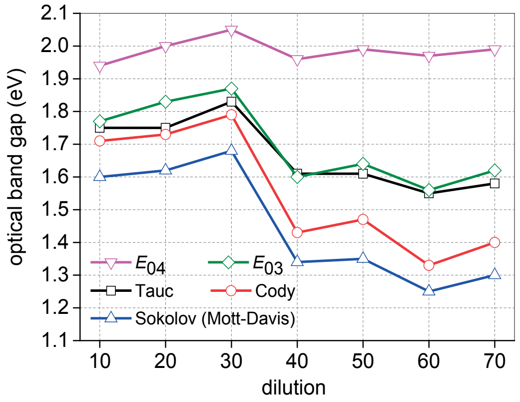

Fig. 9 Optical band gaps of Si:H deposited
at different hydrogen dilution

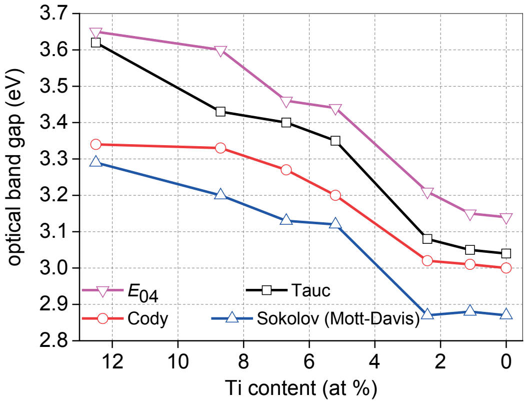

Fig. 10 Optical band gaps of Zn-Ti-O
versus decreasing Ti content

The following conclusions can be made from using several approaches. Zn-Ti-O is apparently a wider-gap semiconductor than Si:H. It is obvious that Cody plots of Si:H have more extended linear parts than Tauc. Therefore the Cody band gaps can be determined in less ambiguity than Tauc. In case of Zn-Ti-O neither Tauc nor Cody extrapolations seem to be more linear. We see that for both materials $E_g^{Sokolov} < E_g^{Cody} < E_g^{Tauc}$ is valid (Figs. 9 and 10). $E_g^{Sokolov}$, E_g^{Cody}, E_g^{Tauc} are decreasing functions of growing dilution in Si:H and dropping Ti content in Zn-Ti-O. It is not difficult to disclose that E_{04} is always larger than E_g^{Tauc}. E_{03} coexists well with E_g^{Tauc} for Si:H.

B_{Tauc} compares well with the structural disorder in Si:H and compositional disorder in Zn-Ti-O (Table 1). Larger values of B_{Tauc} were found in amorphous Si:H in contrast to the polycrystalline Si:H with randomly oriented polycrystalline grains separated by grain boundaries. Surprisingly this is not the case of Zn-Ti-O in which both the increasing compositional disorder and more complex polycrystalline structure with growing Ti content may be the origin of decreasing B_{Tauc}. Moreover Zn-Ti-O samples with increasing Ti content manifest decreasing crystallite size that could indicate the quantum size effect and be followed by the decrease of B_{Tauc}.

5. Conclusions

Knowledge of optical absorption is a relevant issue for all light-based applications of amorphous/polycrystalline semiconductors. However due to the considerable widening of band tails of the valence and conduction bands the optical band gap is not an unambiguous property. Several approaches of the band gap determination are described. As we demonstrate in case of thin films of Si:H and Zn-Ti-O with different structural and compositional disorder no general rule exists to select the proper band extrapolation. For a specific material we recommend using the model resulting in a linear trend in a larger energy range and thus in less uncertainty in determining optical band gaps. Accordingly as Tauc, Cody and Sokolov optical band gaps are considerably dissimilar it should be always obligatory to comment on the applied extrapolation.

Acknowledgements

This work was partly supported by the Slovak Grant Agency under the project VEGA 2/0076/15 and by the Slovak Research and Development Agency under the projects APVV-15-0152, APVV-0888-12. The results were partly developed within the CENTEM project, reg. no. CZ.1.05/2.1.00/03.0088 co-funded by the ERDF within the OP RDI programme, and in the follow-up sustainability stage, supported through CENTEM+ (LO1402) by financial means from the Ministry of Education, Youth and Sports of the Czech Republic under the National Sustainability Programme I.

References

[1] SHIMAKAWA, K., SINGH, J., O'LEARY, S. K.: *Optical Properties of Condensed Matter and Applications.* Singh, J. (Ed.), John Wiley and Sons, Chichester 2007.

[2] CHOPRA, K. L., PAULSON, P. D., DUTTA, V.: Thin Film Solar Cells: An Overview. *Progress in Photovoltaics: Research and Applications*, 12, 69-92, 2004.

[3] SHAH, A.: *Thin-Film Silicon Solar Cells.* EPFL Press, Lausanne, 2010.

[4] MULLEROVA, J., SUTTA, P., VAN ELZAKKER, G., ZEMAN, M., MIKULA, M.: Microstructure of Hydrogenated Silicon Thin Films Prepared from Silane Diluted with Hydrogen. *Applied Surface Science*, 254, 3690-3695, 2008.

[5] LIU, P., LONGO, P., ZASLAVSKY, A., PACIFICI, D.: Optical Band Gap of Single-Nd Multi-Layered Amorphous Germanium Ultra-Thin Films. *Journal of Applied Physics*, 119, 014304, 2016.

[6] ORAPUNT, F., O'LEARY, S.: A Quantitative Characterization of the Optical Absorption Spectrum Associated with Hydrogenated Amorphous Silicon. *Journal of Materials Science: Materials in Electronics*, 20, 1033 – 1038, 2009.

[7] BERSCH, M. D., DIEBOLD, A. C., COSIGLIO, S., CLARK, R. D., LEUSINK, G. J., KAACK, T.: Comparison of Methods to Determine Bandgaps of Ultrathin HfO$_2$ Films Using Spectroscopic Ellipsometry. *Journal of Vacuum Science & Technology A*, A29(4), 041001, 2011.

[8] JURECKA, S., JAMNICKY, I.: Study of the Density Of States Distribution in the SiO$_2$/Si Structure. *Communications - Scienfitic Letters of the Universtiy of Zilina*, 12(2), 58-61, 2010.

[9] MOK, T. M., O'LEARY, S. K.: The Dependence of the Tauc and Cody Optical Gaps Associated with Hydrogenated Amorphous Silicon on the Film Thickness: αl Experimental Limitations and the Impact of Curvature in the Tauc and Cody Plots. *Journal of Applied Physics*, 102, 113525, 2007.

[10] TAUC, J. (Ed.): *Amorphous and Liquid Semiconductors*. Plenum, New York, 1976.

[11] VIEZBICKE, B. D., PATEL, S., DAVIS, B. E., BIRNIE III, D. P.: Evaluation of the Tauc Method for Optical Absorption Edge Determination: ZnO thin Films as a Model System. *Physica Status Solidi B*, B252(8), 1700-1710, 2015.

[12] KODOLBAS, A. O.: Empirical Calibration of the Optical Gap in a-Si$_{1-x}$C$_x$:H (x<0.20) Alloys. *Materials Science and Engineering: B*, B98, 161-166, 2003.

[13] GUERRA, J. A., MONTANEZ, L. M., TUCTO, K., ANGULO, J.: Bandgap Engineering of Amorphous Hydrogenated Silicon Carbide. *MRS Advances*, 1(43), 2929-2934, 2016.

[14] COSENTINO, S., MIRITELLO, M., CRUPI, I., NICOTRA, G., SIMONE, F., SPINELLA, C., TERRASI, A., MIRABELLA, S.: Room-Temperature Efficient Light Detection by Amorphous Ge Quantum Wells. *Nanoscale Research Letters*, 8, 128, 2013.

[15] SINGH, J., SHIMAKAWA, K., KOTLIAR, G., TOKURA, Y.: *Advances in Condensed Matter Science.* Taylor&Francis, London, New York, 2003.

[16] SRIVASTAVA, S., MEHTA, N., TIWARI, R. S., SHUKLA, R. K., KUMAR, A. J.: Chemical Bond Approach to Optical Band Gap in Se100-xSb x Chalcogenide Glasses. Journal of *Optoelectronics & Advanced Materials*, 13(1), 13-18, 2011.

[17] SWANEPOEL, R.: Determination of the Thickness and Optical Constants of Amorphous Silicon. *Journal of Physics E: Scientifics Instruments*, 16, 1214-1222, 1983.

[18] JELLISON Jr., G. E., MODINE, F. A.: Parametrization of the Optical Functions of Amorphous Materials in the Interband Region. *Applied Physics Letters*, 69(3), 371-373, 1996 and erratum *Applied Physics Letters*, 69(14), 2137, 1996.

[19] PRICE, J., HUNG, P. Y., RHOAD, T., FORAN, B., DIEBOLD, A. C.: Spectroscopic Ellipsometry Characterization of HfxSiyOz Films Using the Cody–Lorentz Parameterized Model. *Applied Physics Letters*, 85(10), 1701 – 1703, 2004.

[20] FERLAUTO, A. S., FERREIRA, G. M., PEARCE, J. M., WRONSKI, C. R., COLLINS, R. W., DENG, X., GANGULY, G.: Analytical Model for the Optical Functions of Amorphous Semiconductors from the Near-Infrared to Ultraviolet: Applications in Thin Film Photovoltaics. *Journal of Applied Physics*, 92(5), 2424-2436, 2002.

[21] LIKHACHEV, D. V., MALKOVA, N., POSLAVSKY, L.: Modified Tauc-Lorentz Dispersion Model Leading to a More Accurate Representation of Absorption Features Below the Bandgap. *Thin Solid Films*, 589, 844-851, 2015.

[22] MULLEROVA, J., PRUSAKOVA, L., NETRVALOVA, M., VAVRUNKOVA, V., SUTTA, P.: A Study of Optical Absorption in Amorphous Hydrogenated Silicon Thin Films of Varied Thickness. *Applied Surface Science*, 256, 5667 – 5671, 2010.

[23] JAFAR ABDUL-GADER, M.M.: Comprehensive formulations for the total normal-incidence optical reflectance and transmittance of thin films laid on thick substrates. *European International Journal of Science and Technology*, 2, 214 – 274, 2013.

[24] MULLEROVA, J., SUTTA, P., PRUSAKOVA, L., NETRVALOVA, M.: *Dispersive and BEMA Investigation on Optical Properties of Photovoltaic Thin Filas*. Proceeding of SPIE, 9441, 94411J, 2014.

[25] MULLEROVA, J., SUTTA, P., PRUSAKOVA, L., NETRVALOVA, M.: Optical Properties of Zinc Titanate Perovskite Prepared by Reactive rf Sputtering. Submitted to *Journal Electrical Engineering*, 2017.

https://doi.org/10.26552/com.C.2017.3.16-20

COMMUNICATIONS

Daniel Jandura - Peter Gaso - Dusan Pudis*

POLYMER BASED DEVICES FOR PHOTONICS ON THE CHIP

In this paper we present promising technology for preparation of photonic devices based on polymer materials on the chip. We designed 2D and 3D structures in CAD (computer-aided design) software and we used two-photon polymerization mechanism for direct writing of these structures to IP-Dip photoresist material. This paper also deals with experimental procedures for preparation of polymer photonic devices on the chip and a new way of light coupling to devices on the chip. Morphological properties of prepared devices were investigated by scanning electron microscope (SEM). As a result, transmission spectrum characteristic was measured.

Keywords: *Waveguide, resonator, polymer, laser lithography.*

1. Introduction

Integrated optical structures are the fundamental building blocks for application in optical communications and optical sensing. They also offer interesting perspectives for integrated quantum optics on a chip. At present, however, they are mostly fabricated using essentially planar fabrication approaches like electron-beam lithography [1], UV lithography [2] or focused Ion beam (FIB) etching [3]. All stated processes are used to prepared 2D resp. 2.5D structures. Nowadays, 3D optical devices are very perspective for on-chip applications [4]. Preparation of 3D devices in nanoscale requires technological equipment with femtosecond laser for two-photon polymerization of photoresist master.

While the silicon photonics is a very widespread field, nowadays, polymer materials have become very attractive in photonics and micro optics because of very good material and optical properties. Various optical devices based on polymer materials were presented [5 - 8]. We focused on preparation of polymer devices using modern three-dimensional (3D) laser lithography system. Design, preparation and morphological inspection of photonic devices was performed in this paper.

2. Experimental

For fabrication of photonic devices based on polymer material, Photonic Professional GT system was used in our experiments (Fig. 1a). Principle of this DLW (direct laser writing)

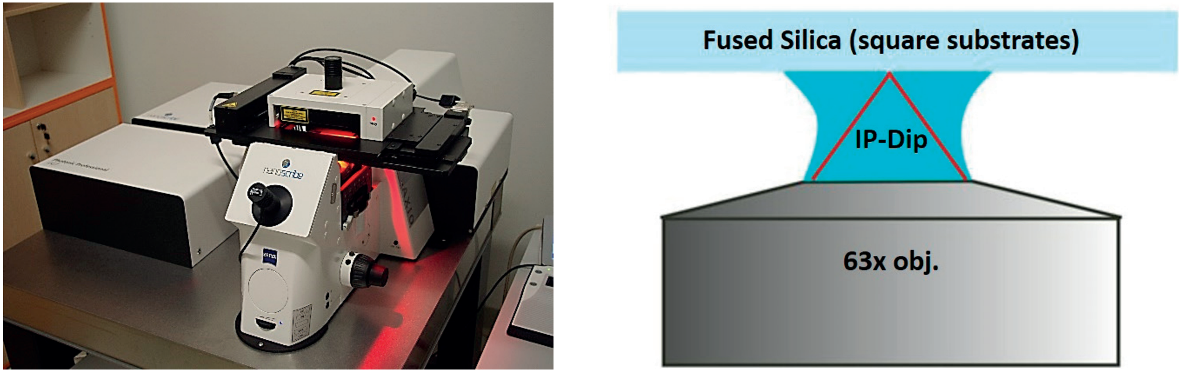

a)

b)

Fig. 1 a) Photonic Professional GT lithography system and b) arrangement of laser lithography system in DiLL (Dip-in Laser Lithography) configuration [10]

---

* **Daniel Jandura, Peter Gaso, Dusan Pudis**
Department of Physics, Faculty of Electrical Engineering, University of Zilina, Slovakia
E-mail: jandura@fyzika.uniza.sk

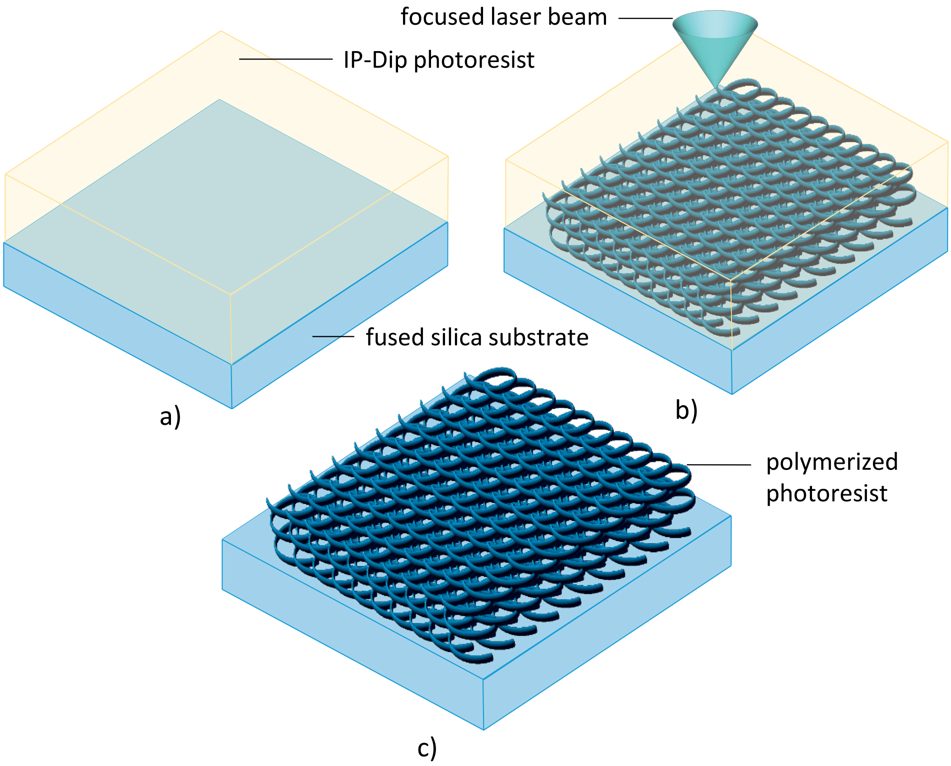

Fig. 2 Illustration of a) IP-Dip photoresist layer deposition on fused silica glass substrate, b) exposition process using two-photon polymerization mechanism and c) final 3D photonic structure after developing process

system is based on 3D scanning of focused laser beam in sample volume [9]. The system uses Er-doped femtosecond frequency-doubled fiber laser emitting pulses at 780 nm wavelength with approximately 100 MHz repetition rate and 150 fs pulse width [10, 11]. Laser beam is scanned in x and y plane by high resolution galvanometer mirror system. The movement in z-axis using motorized micro stage [11] allows preparation of complex micro 3D structures layer by layer directly inside the photosensitive medium. In our experiments, we used laser lithography system in configuration with 63 x immersion objective (Fig. 1b). IP-Dip serves as immersion and photosensitive material at the same time by dipping the microscope objective into this liquid photoresist. Due to its refractive index matched to the focusing optics IP-Dip guarantees ideal focusing and hence the highest resolution for DiLL (Dip-in Laser Lithography) [11, 12].

Technology of 3D structures preparation consists of several steps. First, we deposited IP-Dip photoresist drop on clean fused silica glass substrate (Fig. 2a) and the sample was turned upside down. In this position it remained during the whole DLW process. For photoresist exposure, we used ultrafast laser pulses which caused two-photon polymerization in photoresist volume (Fig. 2b). The writing process has to start on substrate surface in order to achieve the bond of the structure to the substrate. Otherwise, polymerized parts can be washed away from the substrate. Finally, the sample was developed in PGMA (Propylene glycol monomethyl ether acetate) developer for 20 min, rinsed in isopropyl alcohol and polymerized parts were bonded to the substrate (Fig. 2c).

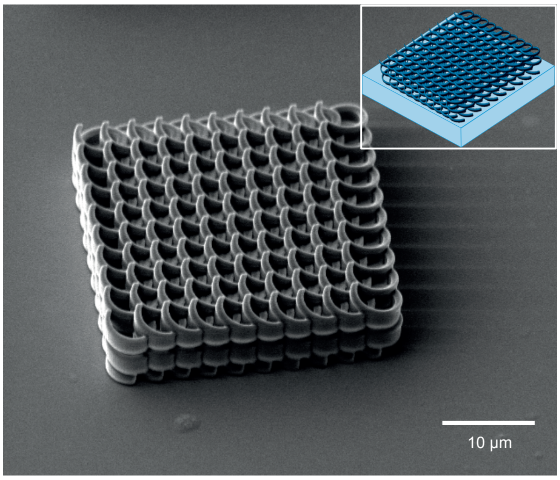

Fig. 3 SEM image of prepared structure in IP-Dip photoresist with 3D CAD model of photonic crystal in helical design (inset)

Precise piezo positioning stage can be used for moving the sample in a vertical dimension. This enabled us to prepare 3D structures using two-photon polymerization in the vertical dimension. As a demonstration, we designed helical photonic crystals with period of 3 μm and height of 8 μm. Final prepared helical photonic crystal with width of 700 nm with corresponding CAD model is shown in Fig. 3.

3. Results and discussion

DiLL configuration used in our experiment enables us to prepare structures in a large area in orders of several cm^2 with 200 nm resolution if the 63 x objective is used. For the preparation of structures in micrometric scale we used higher laser power and coarse hatching distance.

We designed a ring resonator structure in racetrack configuration with the radius of the curved (ring-like) portions of the racetrack resonator R of 100 μm and the racetrack length ΔL of 750 μm. The length of the resonator has a great influence on transmission properties. From the light propagated in the waveguide only part whose wavelength is a divisor of ΔL is coupled into the ring. This coupled light forms a standing wave pattern in the ring resonator part where

$$\lambda_{resonant}^{(m)} = \frac{\Delta L n_{eff}}{m} \tag{1}$$

where m is an integer and n_{eff} is effective refractive index of the waveguide. Frequency separation between two successive resonances is expressed by free spectral range (FSR)

$$FSR \approx \frac{\lambda^2}{n_{eff}\left(2\pi R + L_C\right)} \tag{2}$$

where λ is the wavelength of transmitted signal, L_C is the coupling length between the resonator and the waveguide bus (which is zero for a point coupled ring). This coupling region between the waveguide bus and the ring resonator has a great influence on quality factor of ring resonator. The gap between the waveguides in coupling region was designed 200 nm.

The ring resonator consists of waveguides with an asymmetrical refractive index alignment. The refractive index of IP-Dip core is 1.54 and the bottom glass cladding has refractive index of 1.44. The waveguide is surrounded by air from above. Assuming these parameters and the transmission wavelength of 1550 nm we calculated a value of FSR = 2 nm.

CAD software was used to design our waveguide structures with following parameters. The waveguide height was designed to 3 μm, the width to 3.5 μm and 90° slope angle of the sidewalls. SEM (scanning electron microscope) image of prepared ring resonator in racetrack configuration in IP-Dip polymer with designed parameters is shown in Fig. 4. Very well stitching properties were achieved what is documented in this figure.

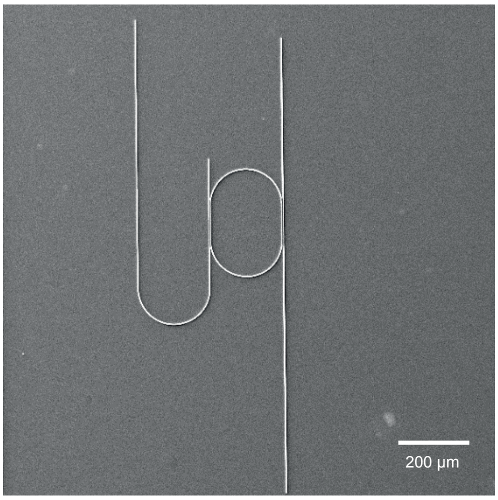

Fig. 4 SEM image of ring resonator in racetrack configuration prepared in IP-Dip photoresist

3D lithography allows us to use a non-conventional way how to couple light into the waveguide and out of the waveguide. The ends of the waveguide are not perpendicular walls but they were modified into 45° slope (Fig. 5). The light can be coupled from optical fiber into optical structure and vice-versa, from structure to detection fiber, due to total internal reflection on the interface between the waveguide and the air.

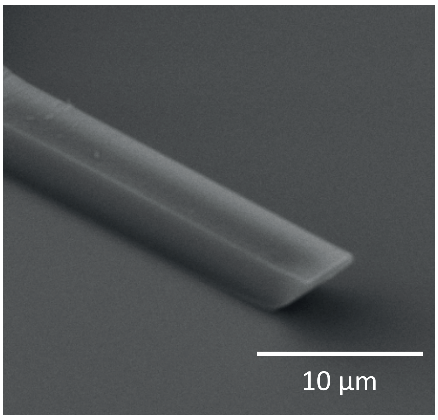

Fig. 5 SEM image of modified end of the waveguide to 45° slope

Finally, we investigated optical transmission properties of prepared racetrack resonator. We coupled light from LED source with central emitting wavelength of 1550 nm to single-mode fiber to the waveguide and we observed the output light using Optical Spectrum Analyzer (Fig. 6). Transmission spectral characteristic was measured from the same channel and is shown in Fig. 7. In this characteristic typical resonance dips were observed. The transmission spectrum corresponds to our calculations where 2 nm free spectral range was measured.

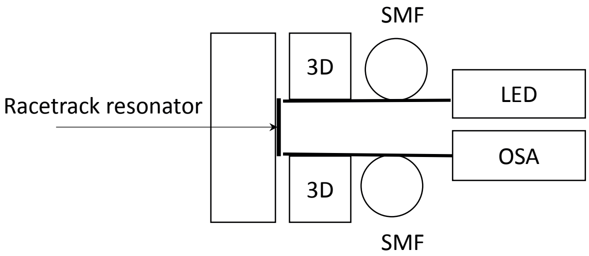

Fig. 6 Experimental setup for the spectral characterization of waveguide structures, LED - light emitting diode, SMF - single-mode optical fiber, 3D - nanopositioning mechanical stage

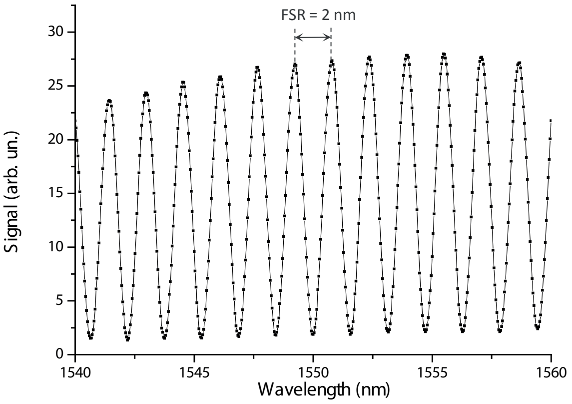

Fig. 7 Measured transmission spectral characteristic of racetrack resonator within the wavelength range 1540-1560 nm

4. Conclusion

In this paper, we highlighted promising technology for preparation of photonic devices based on polymer materials. We presented non-conventional way of light coupling to waveguide devices prepared on fused silica substrates what enables us to measure optical spectral characteristics of prepared devices. This also gives the possibility to integrate more devices on a chip with vertical inputs and outputs. For photoresist master preparation we used 3D laser lithography. We demonstrated the possibilities of this preparation technology on several 2D and 3D devices. The morphological inspection of our structures showed 90° slope angle of the sidewalls. The optical spectrum measurement of racetrack resonator showed typical resonance dips. Final devices are promising for lab on a chip and sensing applications due to unique optical, elastic and chemical properties.

Acknowledgement

This work was supported by the Slovak National Grant Agency under the projects No. VEGA 1/0491/14 and 1/0278/15 and the Slovak Research and Development Agency under the project No. APVV 0395-12. This work was co-funded from EU sources and European regional development by project ITMS 26210120021.

References

[1] ALTISSIMO, M.: E-Beam Lithography for Micro-Nanofabrication. *Biomicrofluidics*, 4(2), 026503, 2010.

[2] DUMON, P., BOGAERTS, W., WIAUX, V., WOUTERS, J., BECKX, S., VAN CAMPENHOUT, D., TAILLAERT, B., LUYSSAERT, P., BIENSTMAN, D., VAN THOURHOUT, J., BAETS, R.: Low-Loss SOI Photonic Wires and Ring Resonators Fabricated with Deep UV Lithography. *IEEE Photonics Technology Letters*, 16(5), 1328-1330, 2004.

[3] SAMANTA, S., BANERJI, P., GANGULY, P.: Focused Ion Beam Fabrication of SU-8 Waveguide Structures on Oxidized Silicon. *MRS Advances*, 2(18), 1-6, 2017.

[4] SCHUMANN, M., BUCKMANN, T., GRUHLER, N., WEGENER, M., PERNICE, W.: Hybrid 2D–3D Optical Devices for Integrated Optics by Direct Laser Writing. *Light: Science & applications*, 3, 1-9, 2014.

[5] MARTINCEK, I., PUDIS, D.: D-Shaped Core Polysiloxane Waveguide with Surface Relief Bragg Grating. *Optik*, 127(20), 10031-10035, 2016.

[6] UDALAGAMA, C. N. B., CHAN, S. F., HOMHUAN, S., BETTIOL, A. A., WOHLAND, T., WATT, F.: *Fabrication of Integrated Channel Waveguides in Polydimethylsiloxane (PDMS) Using Proton Beam Writing (PBW): Applications for Fluorescence Detection in Microfluidic Channels.* Proc. of SPIE 6882, 68820D, 2008.

[7] ELDADA, L., SHACKLETTE, L. W.: Advances in Polymer Integrated Optics. *IEEE Journal of Selected Topics in Quantum Electronics*, 6(1), 54-68, 2000.

[8] PUDIS, D., JANDURA, D., GASO, P., SUSLIK, L., HRONEC, P., MARTINCEK, I., KOVAC, J., BEREZINA, S.: PDMS-Based Nanoimprint Lithography for Photonics. *Communications – Scientific Letters of the University of Zilina,* 16(1), 15-20, 2014.

[9] GISSIBL, T., THIELE, S., HERKOMMER, A., GIESSEN, H.: Two-Photon Direct Laser Writing of Ultracompact Multi-Lens Objectives. *Nature Photonics*, 10, 554-560, 2016.

[10] LINDENMANN, N., BALTHASAR, N. G., HILLERKUSS, D., SCHMOGROW, R., JORDAN, M., LEUTHOLD, J. W., FREUDE, W., KOOS, C.: Photonic Wire Bonding: A Novel Concept for Chip-Scale Interconnects. *Optics Express*, 20(16), 17667-17677, 2012.

[11] Nanoscribe [online]. Date: 06/02/2017. Available: http://www.nanoscribe.de/en.

[12] FREYMANN, G., LEDERMANN, A., THIEL, M., STAUDE, I., ESSIG, S., BUSCH, K., WEGENER, M.: Three-Dimensional Nanostructures for Photonics. *Advanced Functional Materials*, 20(7), 1038-1052, 2010.

https://doi.org/10.26552/com.C.2017.3.21-25

Stanislav Jurecka - Kentaro Imamura - Taketoshi Matsumoto - Hikaru Kobayashi*

ANALYSIS OF PHOTOLUMINISCENCE IN THE ncSi-DMA SYSTEM

Silicon nanocrystalline particles (ncSi) were fabricated from the Si swarf using the beads milling method. Observed photoluminiscence spectra (PL) of the ncSi in hexane with the dimethylanthracene molecules (DMA) show photoluminescence peaks at energies of 2.55, 2.75, 2.92, and 3.09 eV. The shape of PL spectra corresponds to the vibronic structure of adsorbed DMA molecules. The PL intensity of the ncSi-DMA system increases by ~3000 times by adsorption of DMA on Si nanoparticles. The PL enhancement results from an increase in absorption probability of incident light by DMA caused by adsorption on the surface of ncSi. Theoretical model of the PL experiment was constructed and resulting model parameters were used in analysis of possible PL transitions and charge transfer processes.

Keywords: *Semiconductor, silicon nanocrystal, DMA, photoluminiscence.*

1. Introduction

The properties of many materials change when formed from nanoparticles. Nanoparticles have one dimension reaching 100 nanometers or less. Nanoparticles may exhibit size-related properties that differ significantly from those observed in fine particles or bulk materials. Greater surface area of nanoparticle causes higher reactivity to some other molecules as well as increased ability to adsorb and carry other compounds. The reactivity of the surface originates from quantum phenomena. Immediately after the creation, nanoparticles may have their surface modified due to the presence of reactants and adsorbing compounds. Due to the unique properties nanocrystals and other nanoparticles (quantum dots, nanobars, dendrimers, nanoshells and similar) have been receiving important attention for potential applications in various areas – from optical and electronic to biology and medicine [1 - 4].

In the present study, silicon nanoparticles have been fabricated from swarf (industrial waste produced during slicing Si ingots) by the use of the beads milling method [5, 6]. Si nanoparticles can be also formed by various different methods - laser ablation [7, 8], plasma-enhanced chemical vapor deposition (CVD) [9], hot wire CVD [10], sputtering [11], Si implantation [12], intense pulsed ion beam evaporation [13], and other methods. These methods require vacuum conditions and are time- and cost-consuming in comparison to the beads milling method. The size of Si nanoparticles is modified by oxidation and produced nanoparticle system shows increased photoluminiscence. Produced Si nanoparticles show PL spectra with structure which is attributable to the vibronic structure of 9,10-dimethylanthracene molecule, C16H14, adsorbed on the nanoparticle Si surface from the hexane environment. Due to the increased probability of excitation of adsorbed DMA molecule the PL intensity of formed system is increased by ~3000 times. We analysed possible excitation processes leading to modification of experimental PL spectra of ncSi-DMA system. We created theoretical PL model based on modelling of proposed photon emission transitions in the ncSi-DMA system. Theoretical model was optimized in comparison to the experimental PL spectra in order to extract reliable information about the optical excitation and charge transport processes in studied ncSi-DMA system.

2. Experimental

Si nanoparticles were produced by using the beads milling method. Milling with 0.5-mm zirconia beads followed by 0.3-mm zirconia beads was performed in 2-propanol. Fabricated ncSi particles were filtered by the use of a teflon membrane filter, and immersed in hexane with DMA molecules. The PL spectra measurements were carried out with a JASCO FP-8500 spectrometer after removal of aggregated and precipitated Si nanoparticles. Several excitation energies were used in the PL experiments.

---

* **[1]Stanislav Jurecka, [2]Kentaro Imamura, [2]Taketoshi Matsumoto, [2]Hikaru Kobayashi**
[1]Institute of Aurel Stodola, University of Zilina, Liptovsky Mikulas, Slovakia
[2]Institute of Scientific and Industrial Research, Osaka University and CREST, Japan Science and Technology Agency, Ibaraki, Japan
E-mail: jurecka@lm.uniza.sk

3. Results and discussion

Experimental PL spectra of the ncSi-DMA system are shown in Fig. 1. The shape of PL spectra is strongly influenced by the excitation energy. For excitation energies under 4 eV the PL peaks are determined mainly by the the vibronic structure corresponding to transitions between excited states in the DMA molecules with peak positions near 2.55, 2.75, 2.92, and 3.09 eV [14]. Similar PL experiments were also performed by using ncSi in clean 2, 2, 4-trimethyl pentane (without DMA molecules), resulting in PL spectra without the DMA contribution. The vibronic structure arises therefore from the DMA molecules adsorbed on Si nanoparticles, and the PL intensity is enhanced due to the excitation processes in the ncSi-DMA system. For PL excitation energies above 4 eV the shape of PL spectra drastically changes. It is caused by additional photon and charge interactions in studied system. Peak structure corresponding to the DMA excited states is also observed in this case.

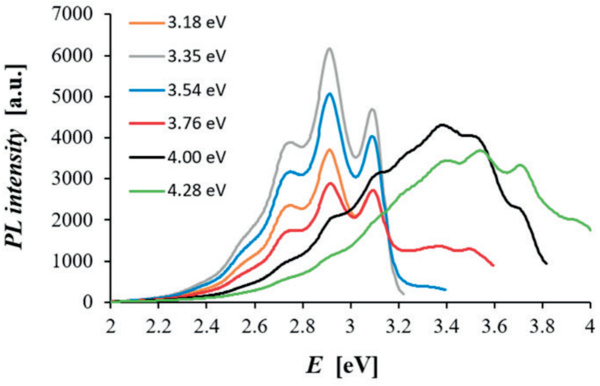

Fig. 1 Experimental PL spectra of the ncSi-DMA system for a set of excitation energies 3.18, 3.35, 3.54, 3.76, 4.00 and 4.28 eV

For description of the structure of energy states in the ncSi-DMA system contributing to the PL transitions we expect excitation of following subsystems: a) ncSi excitons, b) DMA optical excitation, c) dipole-dipole optical excitation of DMA molecules from excitons confined in ncSi (energy transfer), d) energy and charge transfer between excitons in ncSi and DMA molecules (diffuse contact of subsystems). DMA is a molecule with a singlet ground state S_0 and triplet first excited state T_1 . Dipole interaction based on optically allowed transitions in donor (ncSi) – acceptor (DMA) system is forbidden due to the spin-flip rules for $T_1 - S_0$ transitions. Singlet-triplet splitting energy for the DMA molecule is 1.73 eV and therefore the DMA subsystem cannot be efficiently optically excited by $E_{ex} > 1.73$ eV. The direct charge exchange in the ncSi-DMA system is enabled excitation process, triplet exciton annihilation in DMA accompanied by spin-flip is allowed (for ncSi spin restrictions are lifted). For modelling of the PL spectra we constructed theoretical model considering all the excitations mentioned above. It is based on the superposition of Lorentz functions for description of direct charge exchange processes in donor-acceptor system (from 4 to 8 Lorentz functions). Contribution of confined ncSi excitons is modelled in our approach by using a Gaussian function. We suppose excitation of ncSi nanocrystals with certain size distribution, determined by the milling procedure. Motivation for using Gaussian model for this PL process is based on superposition of a large number of independent contributions from individually excited Si nanocrystals according to the central limit theorem. PL quenching of optical excitation in donor-acceptor system is also supposed. Lorentz function I_L is defined by the equation

$$I_L(x) = \frac{I_{0L} w^2}{(x - x_0)^2 + w^2}, \tag{1}$$

where x_0 is the central position of the peak function, I_{0L} is the peak intensity, and w is the width parameter. Gauss function is defined by the equation

$$I_G(x) = \frac{I_{0G}}{\sqrt{2\pi}\,\sigma} \exp\{-(x - x_0)^2/\sigma^2\}, \tag{2}$$

where I_{0G} is the peak intensity and σ is the width parameter. Experimental PL spectrum is modelled by the theoretical model

$$I_{PL}(x) = I_G(x) + \sum_{i=1}^{n} I_{L,i}(x), \tag{3}$$

where x is photon energy in eV, and $n = 4, 8$ for construction of theoretical PL model with 4 or 8 Lorentz functions. The proposed theoretical model is optimized in a comparison with the experimental data by using two step procedure. In the first step, the initial estimation of model parameters is performed by visual modelling, consisting in a modification of model parameters in graphical user interface in order to achieve relatively good agreement between theoretical and experimental PL spectrum. In the next step, this initial estimation is refined by using genetic algorithm combined with Marquardt-Levenberg optimization step [15, 16]. Coefficient of determination r^2 [17], describing the quality of optimized theoretical model, typically reaches values at 0.9999 level. Finally, optimal values of model parameters describing positions and shape characteristics for used peak functions are extracted and used for an interpretation of PL excitation processes.

In Fig. 2 optimized theoretical models based on one Gaussian function and four Lorentz functions for excitation energies a) $E_{ex} = 3.54$ eV and b) $E_{ex} = 3.76$ eV are shown.

Modelling of PL transmission processes based on selected excitation mechanisms provides theoretical model of the PL experiments in good agreement with experimental data. Without accounting for the contribution of the ncSi distribution to the PL spectra acceptable quality of theoretical model cannot be achieved. This is illustrated in Fig. 3, where the PL model is

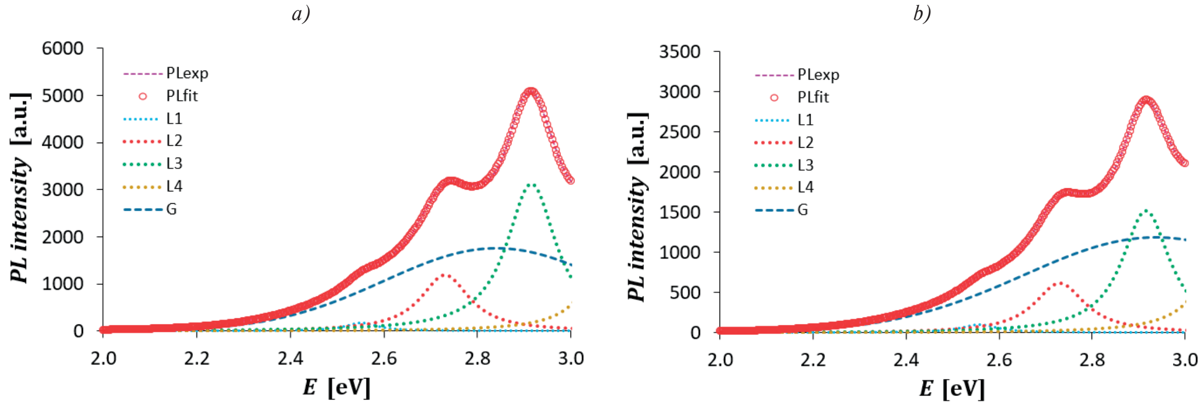

Fig. 2 Theoretical models of the PL spectra: a) 3.54 eV, b) 3.76 eV

constructed without the contribution of excited ncSi distribution. Disagreement between experimental spectrum (dashed line) and theoretical model (circles) can be clearly observed.

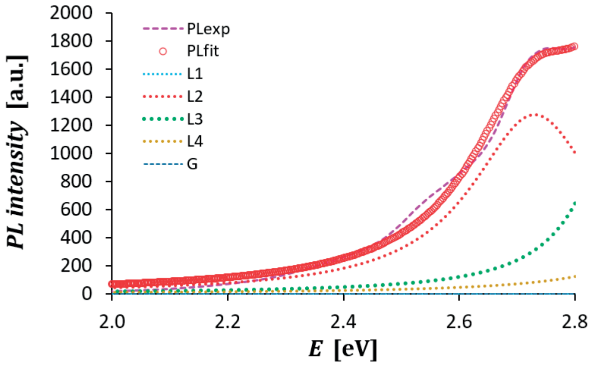

Fig. 3 Theoretical model of the ncSi-DMA PL experiment without contribution of the optical excitation of the ncSi subsystem

In Fig. 4 two optimized theoretical models based on one Gaussian function and eight Lorentz functions for excitation energies a) $E_{ex} = 4.00$ eV and b) $E_{ex} = 4.28$ eV are shown.

For these excitation energies the dominant contribution process to the PL spectrum is connected with the optical excitation of the ncSi distribution. The selected system of discrete energy levels contributing to the PL active transitions (8 Lorentz functions) and modelled contribution of the size distribution of ncSi nanocrystals (Gauss function) suitable describes observed PL spectrum.

Possible sizes of ncSi particles in nanocrystal subsystem are connected with the distribution of energy gaps due to the quantum shape effects. We estimated energy gap E_g dependence of Si nanocrystal on its radius R by using the equation [18]

$$E_g = \frac{h^2\pi^2}{2R^2}\left(\frac{1}{m_e^*}+\frac{1}{m_h^*}\right)-\frac{1.8e^2}{\varepsilon R}, \tag{4}$$

where R is the radius of Si nanocrystal, m_e^* and m_h^* are effective masses of electron and holes, e is electron charge, ε is vacuum permittivity. Values of excitation energies used in PL experiments influence the fraction of ncSi size distribution potentially excited by these photons. This fraction is connected with the distribution of ncSi energy gaps E_g determined by the quantum size effect according Equation 4. In Fig. 5 the energy gap E_g in energy area covering excitation energies in our PL experiments is shown. From this estimation possible ncSi size distribution observed

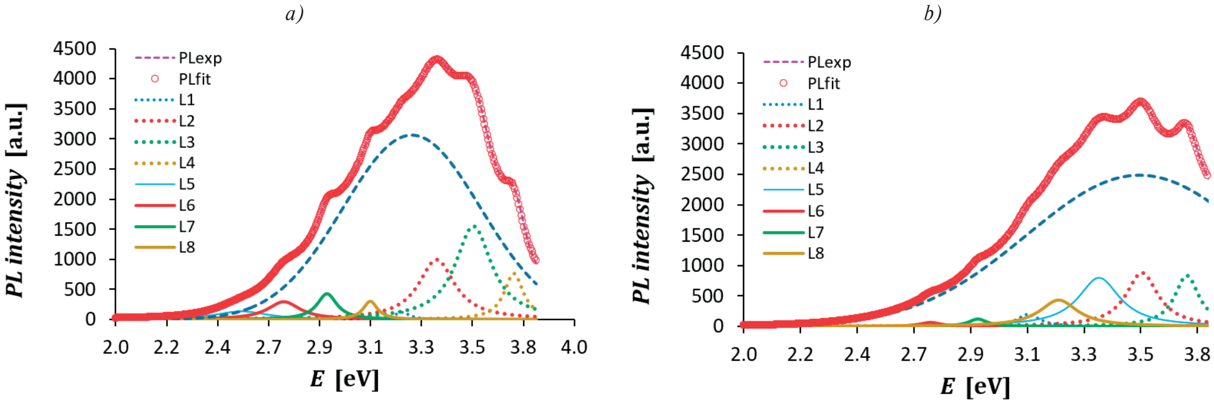

Fig. 4 Theoretical models of the PL spectra: a) 4.00 eV, b) 4.28 eV

in the ncSi-DMA system can be determined. Dominant fraction of the ncSi subsystem formed by the beads milling method has radius in interval 5-6 nm in agreement with the x-ray and TEM methods.

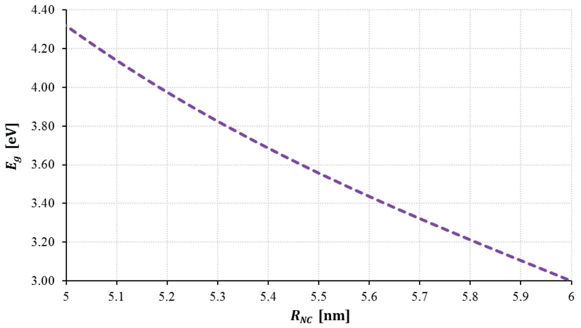

Fig. 5 Energy gap of ncSi

Optimized parameters of Gaussian component of the ncSi-DMA PL theoretical model are shown in Table 1 and development of selected parameters is shown graphically in Fig. 6.

With increasing excitation energy the position of Gaussian distribution centre shifts towards higher energies. It is connected with fraction of Si nanocrystals with suitable sizes in a given distribution, which can be excited by used photon energy in the PL experiment. The width of this component in Fig. 6b increases systematically with significant changes observed in the experiment with excitation energies above 4 eV. Larger amount of ncSi sizes in given distribution can be excited in agreement to available excitation photon energy.

Lorentzian components in the theoretical model of PL experiment demonstrated in Fig. 2 and Fig. 4 show stable values of theoretical peak positions. This is connected with the structure of energy levels of adsorbed DMA molecules and can be used for the study of possible excitation and transition processes from higher energy states as well as for study of DMA excitation caused by the charge transfer processes in the ncSi-DMA system.

4. Conclusions

Silicon nanocrystals were fabricated by the beads milling method from the Si swarf. Experimental PL spectra of the ncSi-DMA system were analysed by modelling of possible excitation and charge transport processes. Properties of observed PL transitions were determined by using theoretical models optimized with the experimental PL spectra. From resulting theoretical model characteristics of PL transitions were determined: a) energy (eV), intensity, and width of transitions between energy states in the ncSi-DMA donor-acceptor system based on Lorentz functions for modelling DMA photoluminiscence, and b) energy (eV), intensity, and width of the Gaussian component modelling the contribution of the excitons confined in a size distribution of ncSi. Experimental PL spectra of the ncSi-DMA system cannot be explained by using only PL transitions in a DMA molecule. Energy and charge transport processes in the ncSi-DMA system substantially influence the shape of the observed PL spectra. PL contribution of the ncSi subsystem strongly depends on particle size distribution (due to presence of the E_g distribution) and

Parameters of Gaussian function in optimized theoretical PL model Table 1

E_{exc} [eV]	**3.02**	**3.18**	**3.54**	**3.76**	**4**	**4.28**
x_0	2.77103	2.87553	2.79019	2.95512	3.11901	3.62252
σ	0.3642	0.25653	0.21812	0.28925	0.27125	0.47642
I_{0G}	56.3661	1390.76	1547.41	1231.27	1670.84	2164.67

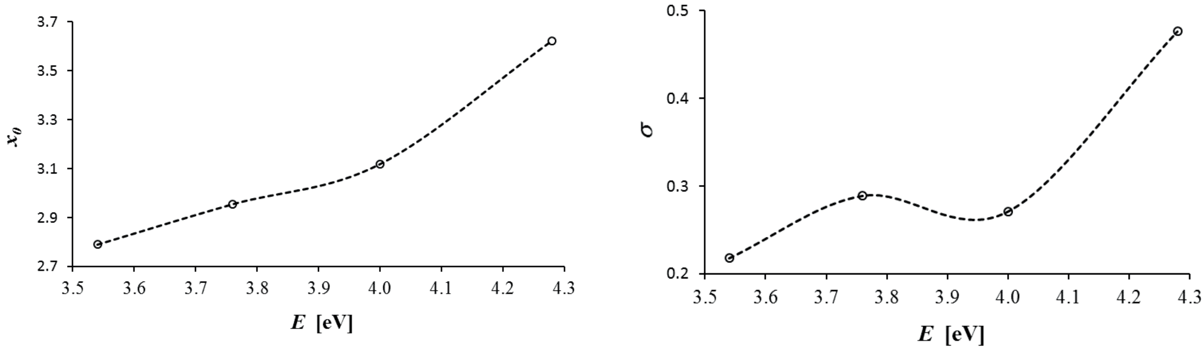
a) *b)*

Fig. 6 Development of a) central position x_0 and b) width parameter σ of Gaussian component of the PL theoretical model is shifted with increasing PL excitation energy. This shift also influences the PL transitions in the structure of energy levels of DMA molecule due to energy and charge transport mechanism in the ncSi-DMA system. The charge transfer process is based on substantial overlay of wavefunctions of two systems – DMA molecule and ncSi particle. It exponentially depends on the distance between these subsystems. This distance is modified during oxidation of ncSi particles and etching processes. This causes drastic quenching of PL transitions caused by the charge transfer mechanism.

Acknowledgements

This work was supported by grant of Science and Technology Assistance Agency APVV-15-0152, Scientific Grant Agency VEGA 1/0676/17 and 1/0076/15, Centre of Excellence of Power Electronics Systems and Materials ITMS 26220120003 and ITMS 26220120046, project ITMS 26210120021 and Japan Society for the Promotion of Science.

References

[1] EPUR, R., MINARDI, L. K., DATTA, M., CHUNG, S. J., KUMTA, P. N.: A Simple Facile Approach to Large Scale Synthesis of High Specific Surface Area Silicon Nanoparticles. *Journal of Solid State Chemistry*, 208, 93-98, 2013.

[2] BULUTAY, C., OSSICINI, S.: *Electronic and Optical Properties of Silicon Nanocrystals*. Pavesi, L., Turan, R. (Eds), Silicon Nanocrytals, Wiley-VCH Verlag GmbH & Co, KGaA, Weinheim, 2010.

[3] EROGBOGBO, F., LIN, T., TUCCIARONE, P. M., LAJOIE, K. M., LAI , L., LATKI, G. D., PRASAD, P. N., SWIHART, M. T.: On-Demand Hydrogen Generation Using Nanosilicon: Splitting Water without Light, Heat, or Electricity. *Nano Letters*, 13, 451-456, 2013.

[4] O'FARRELL, N., HOULTON, A., HORROCKS, B. R.: Silicon Nanoparticles: Applications in Cell Biology and Medicine. *International Journal of Nanomedicine*, 1, 451-472, 2006.

[5] MATSUMOTO, T., MAEDA, M., FURUKAWA, J., KIM, W-B., KOBAYASHI, H.: Si Nanoparticles Fabricated from Si Swarf by Photochemical Method. *Journal of Nanoparticle Research,* 16, 2240-1-7, 2014.

[6] MAEDA, M., IMAMURA, K., MATSUMOTO, T., KOBAYASHI, H.: Fabrication of Si Nanoparticles from Si Swarf and Application to Solar Cells. *Applied Surface Science*, 312, 39-42, 2014.

[7] MAKIMURA, T., KUNII, Y., ONO, N., MURAKAMI, K.: Silicon Nanoparticles Embedded in SiO_2 Films with Visible Photoluminescence. *Applied Surface Science*, 127-129, 388-92, 1988.

[8] WATANABE, K., SAWADA, K., KOSHIBA, M., FUJII, M., HAYASHI, S.: Photo-luminescence Decay Dynamics of Si Nanoparticles Prepared by Pulsed Laser Ablation. *Applied Surface Science,* 197-198, 635–638, 2002.

[9] LACONA, F., BONGIORNO, C., SPINELLA, C., BONINELLI, S., PRIOLO, F.: Formation and Evolution of Luminescent Si Nanoclusters Produced by Thermal Annealing of SiO_x Films. *Journal of Applied Physics,* 95, 3723-3732, 2004.

[10] SALIVATI, N., AN, Y. Q., DOWNER, M. C., EKERDT, J. G.: Hot-Wire Chemical Vapor Deposition of Silicon Nanoparticles on Fused Silica. *Thin Solid Films,* 517, 3481-3483, 2009.

[11] FAUCHET, P. M., RUAN, J., CHEN, H., PAVESI, L., NEGRO, L. D., CAZZANELI, M., ELLIMAN, R. G., SMITH, N., SAMOC, M., LUTHER-DAVIES, B.: Optical Gain in Different Silicon Nanocrystal Systems. *Optical Materials*, 27, 745-749, 2005.

[12] MORALES-SANCHEZ, A., LEYVA, K. M., ACEVES, M., BARRETO, J., DOMINGUEZ, C., LUNA-LOPEZ, J. A., CARRILO, J., PEDRAZA, J.: Photoluminescence Enhancement through Silicon Implantation on SRO-LPCVD Films. *Materials Science and Engineering: B*, 174, 119-122, 2010.

[13] CHOI, B. J., LEE, J. H., YATSUI, K., YANG, S. C.: Preparation of Silicon Nanoparticles for Device of Photoluminescence. *Surface and Coatings Technology*, 201, 50036, 2007.

[14] OHNO, K.: Simple Calculations of Franck-Condon Factors for Electronic Transition Bands of Polyacenes. *Chemical Physics Letters*, 53, 571-577, 1978.

[15] JURECKA, S.: *Theoretical Model of the Physical System: Optimization by the Genetic Algorithm*. Dritsas, I. (Ed.), Stochastic Optimization - Seeing the Optimal for the Uncertain, InTech, Vienna, 2011.

[16] MULLEROVA, J., SUTTA, P., JURECKA, S.: Thin Film Silicon in Photovoltaics: The Role of Structure and Microstructure. *Communications - Scientific Letters of the University of Zilina,* 8(1), 5-9, 2006.

[17] DEVORE, J. L.: *Probability and Statistics for Engineering and the Sciences,* 8th ed. Cengage Learning, Boston, 2011.

[18] HUMMEL, R. E., WISSMANN, P.: *Handbook of Optical Properties: Optics of Small Particles, Interfaces and Surfaces.* CRC Press LLC, Boca Raton, 1997.

https://doi.org/10.26552/com.C.2017.3.26-29

Daniel Kacik - Ivan Martincek - Norbert Tarjanyi*

OPTICAL PDMS MICROFIBRE SENSOR FOR DISPLACEMENT DETERMINATION

We prepared and demonstrated the usage of an optical polydimethylsiloxane (PDMS) microfibre sensor for displacement measurement. The sensor consists of PDMS microfibre placed between two conventional single-mode optical fibres. For proper bend of the microfibre the structure forms Mach-Zehnder interferometer. In that case, one arm of the interferometer consists of the microfibre and second one of the air. In addition, it is possible to resize the air arm in a range of several tens of micrometres with sufficient ratio of intensities between lights transmitted through the interferometer arms. For optical paths difference smaller than optical coherence of light source one can observe the interference of light. Determination of the displacement was done based on the spectral shift of interference pattern for particular lengths of air arm. The sensitivity of the sensor was 2.5 nm/μm.

Keywords: *Microfiber, PDMS, displacement determination, optical sensor, Mach-Zehnder interferometer.*

1. Introduction

Optical devices based on optical microfibres can be used in a wide range of applications for their unique properties such as large evanescent field and strong confinement of the propagated light [1]. Moreover, the optical microfibres can be arranged in different configurations such as taper [2], knot resonator [3], part of interferometers [2, 4, 5] and made from different materials such as silica [6, 7], polysiloxanes [5]. This diversity predisposes them to sensing various physical quantities, for example temperature [7, 8], strain [7, 8], refractive index [9], volatile organic compounds [1, 10], current [4] and displacement [2, 11].

In the paper, we deal with the process of microfibre fabrication from polydimethylsiloxane (PDMS) and its usage for displacement determination. By proper bending of optical microfibre the Mach-Zehnder interferometer is formed, one arm consists of microfibre and the second one of air. Since the optical path difference is smaller than coherence length of optical source the interference of beams is observed. We are focused on the displacement determination by means of determining wavelength shifts of interference minima in frequency domain.

2. Optical microfibre fabrication

For preparation of optical microfibre integrated between two conventional single-mode optical fibres (SMFs) we used liquid silicone Sylgard 184 (Dow Corning) supplied as two-part liquid component kits. The silicone is highly light-transparent material, chemically inert, thermally stable, permeable to gasses, simple to handle, elastically deformable to a large extent and has a great potential for photonics [12]. After mixing the pre-polymer and curing agent at ratio of 10:1, the prepared elastomer was applied on the cleaved ends of conventional optical fibres (Fig. 1a). Thereafter, we connected optical fibre ends covered by PDMS (Fig. 1b). Then PDMS was cured at room temperature for about 10 hours. After that time the PDMS elastomer achieved suitable consistency for microfibre drawing. Axial alignment of SMFs with PDMS joint was mechanically adjusted by 3D microstages

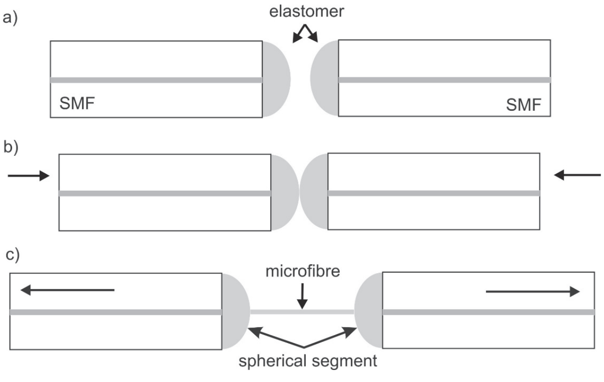

Fig. 1 Illustration of optical microfibre fabrication: a) PDMS deposition on single-mode fibre (SMF) ends, b) connection of fibre ends. c) coaxial drawing

---

* **Daniel Kacik, Ivan Martincek, Norbert Tarjanyi**
Department of Physics, Faculty of Electrical Engineering, University of Zilina, Slovakia
E-mail: daniel.kacik@fel.uniza.sk

to obtain maximal transmitted signal through the PDMS joint at wavelength 1550 nm. PDMS microfibre was created by gradual distancing of single-mode fibres ends (Fig. 1c) together with in-situ controlling the axial position by signal level. When the length and the diameter of microfibre was sufficient the PDMS microfiber was cured at the room temperature for another 40 hours. The prepared optical microfibre had a diameter of 7 micrometres and 270 micrometres in length. This microfiber was formed on the PDMS spherical segments with height of about 50 micrometres placed at the end faces of SMFs.

3. Mach-Zehnder interferometer

The light transmitted through the optical fibre is coupled to the PDMS spherical segment and then to the optical microfibre. After passing the PDMS microfibre the light is recoupled to the output optical fibre and propagates there. But for suitable bend of optical microfibre (the bend of microfibre was done by decreasing the distance between ends of SMFs) it is possible to obtain the state when the light transmitted through the SMF is split at the spherical segment placed on the end of optical fibre: the part of light is still transmitted through the microfibre and another part is propagated in coaxial direction to core of input fibre (so the light propagates in the air path). By proper adjusting of output fibre position it is possible to recouple the light transmitted through the air path to the output fibre (enlargement in Fig. 2).

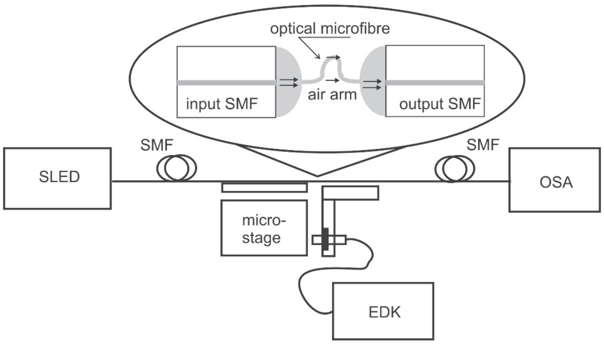

Fig. 2 Experimental setup with detail of sensor: SLED - optical source, EDK - commercial displacement meter with inductance probe, OSA - optical spectrum analyser

If the optical path difference (between light transmitted through the microfibre and air path) is smaller than coherence length of an optical source one can observe the interference of light.

In this case, the interference pattern is formed by two beams, one guided through the microfibre and second one through the air path. The output intensity can be expressed as

$$I(\lambda)=I_1+I_2+2\sqrt{I_1 I_2}\cos\left(\beta(\lambda)z_1-\frac{2\pi n}{\lambda}z_2\right) \qquad (1)$$

where I_1 and I_2 are intensities of light coupled to the core of the output SMF from the microfibre and from the air path, respectively, β is phase constant of the beam (mode) guided through the microfibre, z_1 is the length of the microfibre, z_2 is length of air path, n is refractive index of air and λ is the wavelength of the propagating light in vacuum.

4. Displacement sensing

For investigation of spectral dependence of interference pattern of the prepared PDMS microfibre sensor for the displacement the broadband light source coupled to the optical fibre (SLED Safibra OFLS-6) with central wavelength at 1550 nm and FWHM of 62 nm was used. The output SMF was connected to and the spectrum recorded by an optical spectrum analyser (Anritsu MS9710B), with a resolution of 0.07 nm. The sensor consisting from SMFs ends covered by PDMS and optical microfibre was placed on differential micrometre stages to adjust the relative positions of SMFs and resizing the length of the air arm. The length of air arm was measured by commercial displacement meter with inductance probe, which allows one to distinguish variations of the length with resolution of hundredth of a micrometre. Schematic of experimental setup is shown in Fig. 2.

The transmission spectra of prepared PDMS microfibre sensor in the wavelength range from 1545 nm to 1565 nm (it was measured in wavelength range 1500 nm to 1600 nm but for better illustration was chosen only narrow interval) at constant room temperature and atmospheric pressure for resizing length of the air arm in the interval 0 μm to 4 μm with step 1 μm are shown in Fig. 3. As it can be seen from dependencies shown in Fig. 3 for particular length of the air arm the power level is very slightly changed. It could be caused by the change of the intensity of light recoupled to the output fibre due to the change of the microfibre bend or misalignment of the output fibre. Nevertheless for the evaluation of the measurement this can be neglected.

In paper [11] we investigated the effect of the air arm length on the period of interference pattern. The change in the period of interference pattern of the structure was determined to 0.027 nm per micrometre. For a small displacement (and for resolution of optical spectrum analyser) we could not use this approach. So for determination of such a small displacement we investigated the wavelength shifts of the interference pattern. We choose the minima of the interference pattern and determined its wavelength (reference). For the particular displacement determined by displacement meter, the wavelength shift of reference minima of the interference pattern was observed (see Fig. 3).

The dependence of measured wavelength shift $\Delta\lambda_i$ on the displacement and its linear fit are shown in Fig. 4. The sensitivity of sensor 2.5 nm per micrometre can be determined from the linear fit. According to [11], it has almost 100 times higher

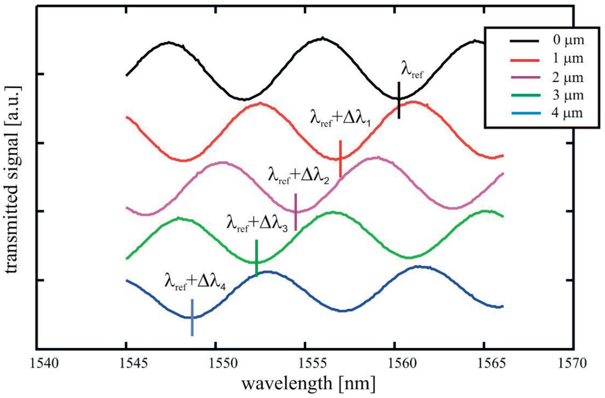

Fig. 3 Vertical shifted transmission spectra of interferometer for different measured air arm lengths; there are also indicated wavelength of reference minima λ_{ref} and its particular shift $\Delta\lambda$ for particular displacement

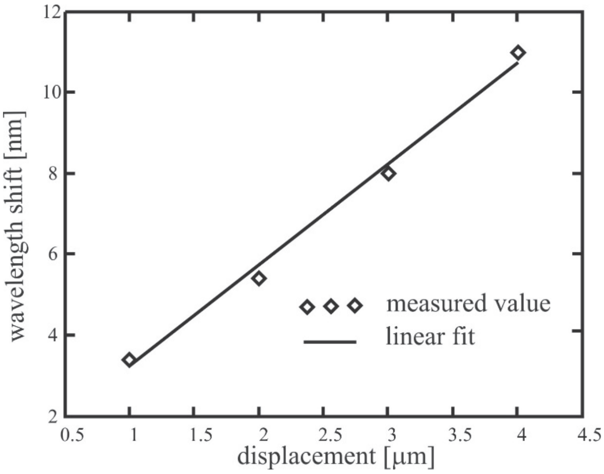

Fig. 4 The dependence of wavelength shift on displacement

sensitivity. But disadvantage of the evaluation is that after crossing phase change by 2π without observation of position of the interference minima it is not possible to determine the value of displacement. So it is possible to determine it only when the displacement is up to 3.14 µm (corresponds to 8.6 nm wavelength shift).

5. Conclusion

We have demonstrated the preparation of an optical PDMS microfibre which is directly integrated between single-mode optical fibres, the transmission properties of the prepared sensor and its application in the displacement determination by the measurement of spectral shifts of minima of interference pattern. The prepared microfibre sensor is a two-arm interferometer in which one arm consists of a bend PDMS microfibre and the second is formed by an air line. We measured the displacement experimentally to the value of 4 micrometres, with an accuracy better than ±0.01 µm. The sensitivity in this range was determined to 2.5 nm/µm. For the optical PDMS microfibre the way of displacement determination can be used to the value of 3.14 µm due to phase of interference pattern is changed over 2π.

Acknowledgements

This work was supported by Slovak National Grant Agency No. VEGA 1/0491/14, 1/0278/15 and Slovak Research and Development Agency under the project No. APVV-15-0441.

References

[1] LUO, J., WANG, Y., TONG, L.: Microfiber Optical Sensors: A Review. *Sensors* 14(4), 5823-5844, 2014.

[2] LUO, H., LI, X., ZOU, W., LI, X., HONG, Z., CHEN, J.: Temperature-Insensitive Microdisplacement Sensor Based on Locally Bent Microfiber Taper Modal Interferometer. *IEEE Photonics Journal,* 4(3), 772-778, 2012.

[3] GOMES, A. D., FRAZAO, O.: *Microfiber Knot Resonator as Sensor - A Review.,* Proc. of 5th intern. Conference on Photonics, Optics and Laser Technology (PHOTOPTICS 2017), Portugal, 356-364, 2017.

[4] JASIM, A. A., HARUN, S. W., MUHAMMAD, M. Z., AROF, H., AHMAD, H.: Current Sensor Based on Inline Microfiber Mach-Zehnder Interferometer. *Sensors and Actuators A,* 192, 9-12, 2013.

[5] MARTINCEK, I.: Fabrication and Characterisation of Polysiloxane Optical Fiber Microloop Interferometers. *Microwave and Optical Technology Letters,* 58(12), 2876-2879, 2016.

[6] LOU, J., TONG, L., YE, Z.: Modeling of Silica Nanowires for Optical Sensing. *Optics Express,* 13(6), 2135-2140, 2005.

[7] MUHAMMAD, M. Z., JASIM, A. A., AHMAD, H., AROF, H., HARUN, S. W.: Non-Adiabatic Silica Microfiber for Strain and Temperature Sensors. *Sensors and Actuators A,* 192, 130-132, 2013.

[8] TIAN, J., LIU, S., YU, W., DENG, P.: Microfiber Bragg Grating for Temperature and Strain Sensing Applications. *Photonic Sensors,* 7(1), 44-47, 2017.

[9] LUO, H., SUN, Q., XU, Z., JIA, W., LIU, D., ZHANG, L.: Microfiber-Based Inline Mach Zehnder Interferometer for Dual-Parameter Measurement. *IEEE Photonics Journal,* **7**(2), 7100908, 2015.

[10] KACIK, D., MARTINCEK, I.: Toluene Optical Fibre Sensor Based on Air Microcavity in PDMS. *Optical Fiber Technology,* 34, 70-73, 2017.

[11] KACIK, D., MARTINCEK, I.: *Optical Structure with PDMS Microfibre for Displacement Measurement*. Proc. of 5th intern. Conference on Photonics, Optics and Laser Technology (PHOTOPTICS 2017), Portugal, 365-368, 2017.

[12] PUDIS, D., JANDURA, D., GASO, P., SUSLIK, L., HRONEC, P., MARTINCEK, I., KOVAC, J., BEREZINA, S.: PDMS-based Nanoimprint Lithography for Photonics. *Communications - Scientific Letters of the University of Zilina,* 16(1), 15-20, 2014.

https://doi.org/10.26552/com.C.2017.3.30-33

Maria Figurova - Peter Gaso - Dusan Pudis*

MICRO-OPTICS FOR LAB-ON-A-CHIP

Lab-on-a-chip (LOC) is nowadays one of the most interesting topics at the field of biomedicine and biosensing applications. Mainly devices that integrate a detection system right into a chip with microfluidic network are highly desirable. In this article we will present Mach-Zehnder interferometer created in IP-Dip photoresist by direct laser lithography system for laboratory on chip applications. Interferometer will be later used for biosensing application as integrated micro-optical device inside a microfluidic chip. Measurements of transmission characteristics of water solution with different sugar concentration show promising ability of the Mach-Zehnder interferometer to detect different liquids on principle of refractive index change.

Keywords: *Mach-Zehnder interferometer, PDMS, DLW lithography, refractive index.*

1. Introduction

In the field of biomedicine and health care is sustained effort to create compact and cheap device for a quick detection of a biologic sample. Lab-on-a-chip is a kind of device that can provide multiple operations on a small chip, similar to conventional laboratory working with biological samples. LOC works on various principles of detection, where optical detection is becoming more and more popular. Implementation of photonic sensing devices such as resonator based sensors [1], crystal-based sensors [2] or interferometers [3] enable us to detect a change in a concentration of biological samples. The detection principle of most of such photonic LOC is based on evanescent field where the biological sample is placed on the one top of resonator arms [4] based on interference change [5].

Unfortunately many sensing devices for LOC have been demonstrated as proof-of-concept experiments, only few work as biosensing applications so far. Usually LOC biosensors working on optical principles are using micro-optical components like silicon-based resonators. In this paper we present functionality of various Mach-Zehnder interferometers (MZI) made in IP-Dip photoresist, which is a polymer material. In general, for LOC biosensors are polymer materials advantageous solution because of their thermal and chemical stability and affordability. One of the most popular materials - polydimethylsiloxane (PDMS) is even biocompatible and appropriate for optical measurements because of its optical properties. A wide range of applications for this material is mainly focused on the process of replica molding for microfluidic parts of chip [6].

In this paper we present fabrication of specially designed MZI created in IP-Dip photoresist by direct laser writing (DLW) lithography system. IP negative photoresists designed for commercial platform of 3D laser lithography provide high resolution and mechanical stability of structures in the micrometer and submicrometer scale [7].

Specially designed MZI's (Figs. 2a, 3a, 4a) were created in IP-Dip photoresist for liquids with different concentrations and refractive indices.

2. Microstructure fabrication

For the structure fabrications, commercial direct laser writing system Nanoscribe was used. This kind of laser lithography enables us to create 3D structures on a principle of two-photon absorption and polymerization in a volume of photoresist. By this method microfluidic and micro-optic component for LOC can be created in high resolution quality (down to 500 nm). Platform of Nanoscribe DLW system allows 3D structures patterning in negative IP-Dip photoresist. For creating our structures we used mode of Dill configuration [8].

We designed various kinds of MZI and the whole process of creating micro-optic structures involves few simple steps. Firstly IP-Dip photoresist was drop-cast on the top of cleaned glass substrate and then of MZI started. For the developing of printed structures, PGMA (polymer glycol monomethyl ether acetate) was used to dissolve unexposed parts. Finally, the substrate was rinsed in isopropyl and deionized water and dried by air. Structure morphology (in case of size parameter larger than 250 μm) and

---

* **Maria Figurova, Peter Gaso, Dusan Pudis**
Department of Physics, Faculty of Electrical Engineering, University of Zilina, Slovakia
E-mail: figurova@fyzika.uniza.sk

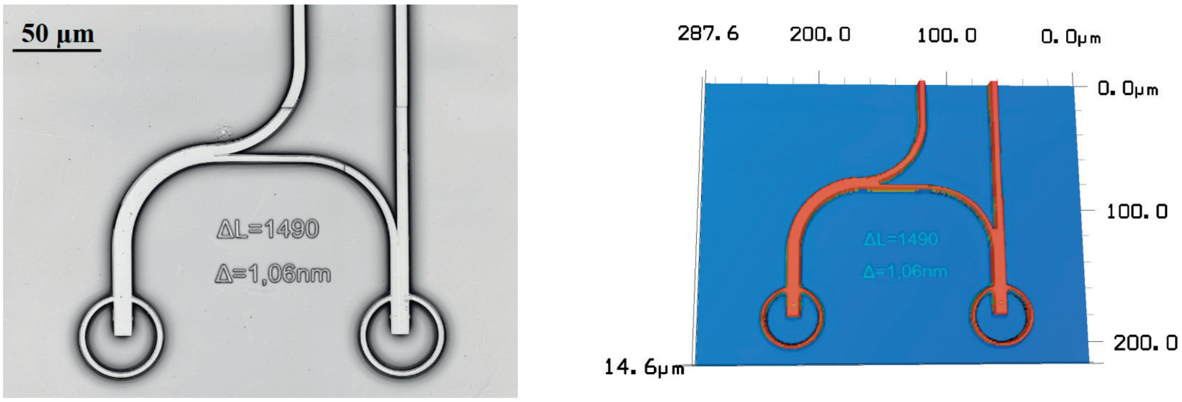

a) b)

Fig. 1 a) Detail picture of MZI from laser mode of confocal microscope and b) 3D image for structure adhesion checking

proper adhesion of glass was checked by confocal microscope (Fig. 1). Optical properties were analysed by spectral transmission measurements using different surrounding cladding liquids.

3. Experiment and results

Optical properties of prepared MZI's were analysed by spectral transmission measurements. Experimental setup for spectral transmission measurements consists of optical spectral analyzer (OSA) Anritsu MS9710B with resolution of 0.1 nm coupled to the output of the MZI using single mode optical fiber (SMF). For light coupling the input and outputs of MZI were specially designed and created by inclined planes as 45° micro-mirrors. Guiding of the lights in these micro-mirrors works on the contrast of refractive indices of used photosensitive IP-Dip resist and surrounding air or liquids. The MZI structure has squared cross section with dimension of 8 µm. The refractive index of applied liquid changes the transmission characteristics of MZI. As the power source for transmission measurements, the light emission diode with central emission wavelength at 1550 nm was used.

The measured properties were compared with simple calculation of free spectral range λ_{FSR}, taking into account the parameters of prepared MZI. Interference spectral dips are distributed according to

$$\lambda_{FSR} = \frac{\lambda^2}{n\Delta L} \tag{1}$$

where ΔL represents arm difference of MZI and $n = 1.52$ is refractive index of IP-Dip photoresist (for $\lambda = 1550$ nm).

Theoretical value of λ_{FSR} for measured MZI is 1 nm and 1.06 nm. By implementation of such MZI in LOC device, we expect good detection properties of fluids based on refractive index change of cladding. Prepared MZI devices will be implemented in

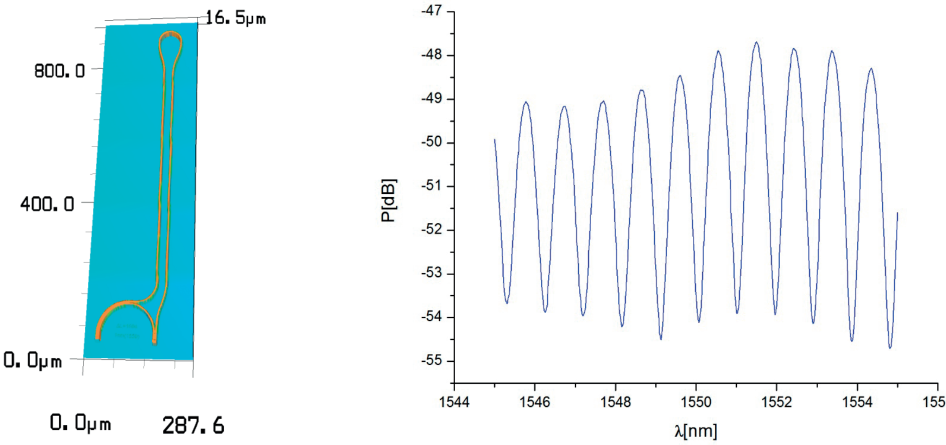

a) b)

Fig. 2 a) Confocal microscope image of MZI 1 structure. b) Transmission characteristics of special MZI in IP - Dip photoresist for air as surrounding cladding, where ΔL = 1604 µm.

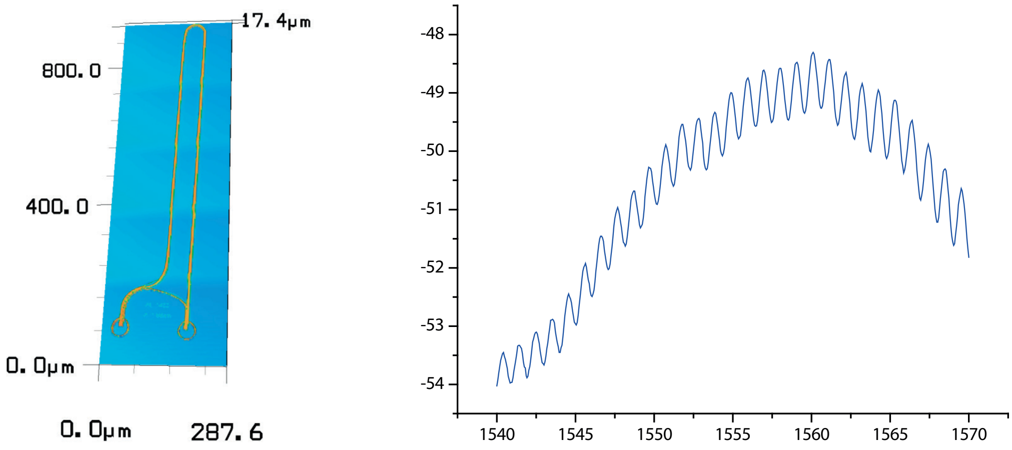

a)

b)

Fig. 3 a) Confocal microscope image of MZI 2 structure. b) Transmission characteristics of special MZI in IP-Dip photoresist for air as cladding surrounding, where ΔL = 1690 μm

next microfluidic systems with the aim of optical characterization of assays in LOC.

We were focusing on the testing of three various designs of MZI's (MZI1, MZI2 and MZI3), where the surroundings are air, water and different concentrations of sugar dissolved in water. MZI1 with long detection arm was created for better contact of MZI with liquids during measurement (Fig. 2a). Transmission characteristic (Fig. 2b) of MZI1 in air surrounding shows 5 dB dips. During experiments we found applicability problems connected with hydrophilic surface of IP-Dip photoresist. Coupling mirrors cannot be sealed with water during application of liquids because of the lowering reflectance what leads to lost signal. Another design brings improvement by ring protection (Fig. 3a).

MZI2 with mirror ring protection showed to be better solution for liquid measurements. Drop-casting in this case was much easier. This structure shows smaller dips, less than 1 dB (Fig. 3b) caused probably by structure discontinuities in the long arm.

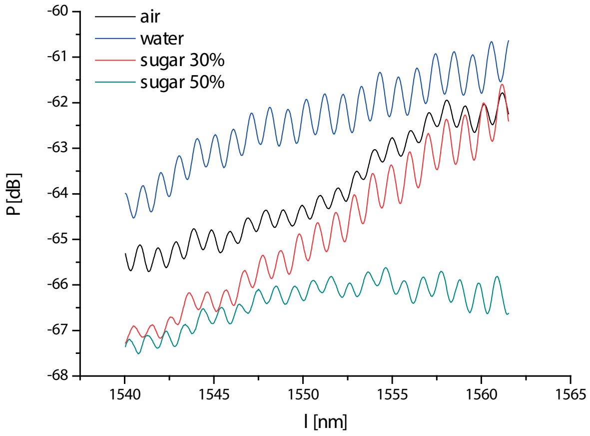

Fig. 4 Transmission characteristics of MZI2 for air, water and water solutions with different sugar concentrations

On the prepared MZI2, we were testing different water solutions of sugar with concentrations 0 %, 30 % and 50 % and air (Fig. 4). With increase of sugar concentration the refractive index of water/sugar solution increases together with free spectral range λ_{FSR} dips in the measured signal. λ_{FSR} from the measured transmission characteristics (Fig. 4) was estimated λ_{FSR} = 1.016 nm for air surrounding.

From the measured spectral transmission characteristics, we estimated the λ_{FSR} for the measured water/sugar solutions. The dependence of λ_{FSR} on sugar concentration is shown in the Fig. 5.

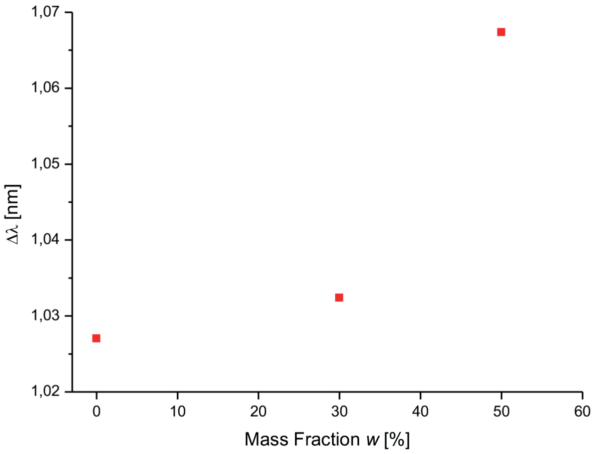

Fig. 5 Dependence of FSR of transmission peaks on mass fraction of aqueous mixture of sugar

The last tested design for MZI3 (Fig. 6a) keeps the mirror protection and has smoother curves mainly for the reference arm and shorter sensing arm. It was proved by transmission characteristic (Fig. 6b), that the dips for surrounding air are better, almost 15 dB. From the transmission characteristics we estimated λ_{FSR} = 1.105 nm.

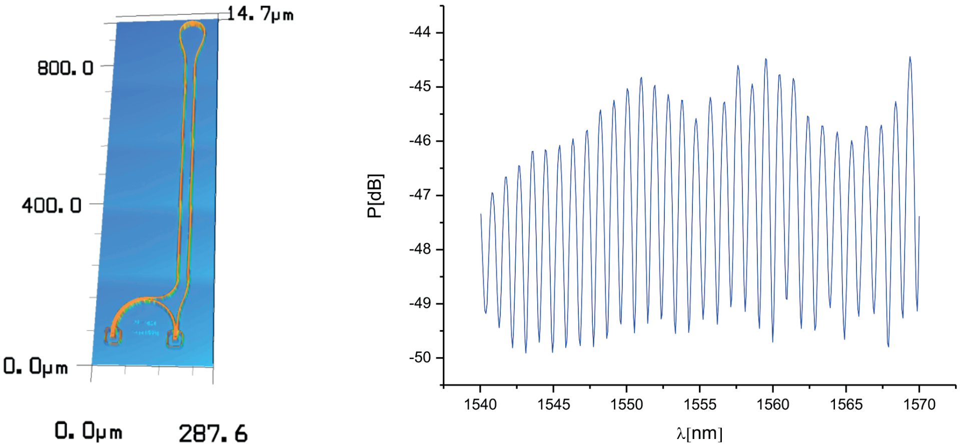

a) *b)*

Fig. 6 a) Confocal microscope image of MZI3 structure. b) Transmission characteristics of special MZI3 in IP-Dip photoresist for air as cladding surrounding, where ΔL = 1604 μm

According to the obtained results, we suppose the improvement of resolution of this sensing method for precise measurements of water solutions of different chemicals. However, it needs optimisation process of MZI design, especially the core dimensions.

4. Conclusions

In this paper we presented new concept of MZI prepared by laser lithography in IP-Dip photoresist. Designed and prepared MZI's show effective interference with significant dips in spectral transmission characteristics. For different designs we achieved 15 dB dips. Effect of different water/sugar solutions was tested for sensing properties of the prepared MZI's. In the present state, only high concentrations of sugar resolved the increase of free spectral range in measured transmission spectral characteristics. More precise measurements need to also optimize the core dimensions of MZI's.

Acknowledgement

This work was supported by the Slovak National Grant Agency under the projects No. VEGA 1/0491/14 and 1/0278/15 and the Slovak Research and Development Agency under the project No. APVV-16-0129.

References

[1] WANG, J., YAO, J., LEI, T., POON, A. W.: Silicon Coupled-Resonator Optical-Waveguide-Based Biosensors Using Light-Scattering Pattern Recognition With Pixelized Mode-Field-Intensity Distributions. *Scientific Reports*, 4, 1-9, 2014.

[2] YAN, H., ZOU, Y., CHAKRAVARTY, S., YANG, CH.-Y., WANG, Z., TANG, N., FAN, D., CHEN, R. T.: Silicon On-Chip Bandpass Filters for the Multiplexing of High Sensitivity Photonic Crystal Microcavity Biosensors. *Optic Express*, 20, 7195-7205, 2012.

[3] DANTE, S., DUVAL, D., SEPULVEDA, Y., GONZALEZ-GUERRERO, A. B., SENDRA, J. R., LECHUGA, L. M.: Integrated Optical Devices for Lab-On-A-Chip Biosensing Applications. *Applied Physics Letters*, 106, 1-5, 2015.

[4] ESTEVEZ, M. C., ALVAREZ, M., LECHUGA, L. M.: Integrated Optical Devices for Lab-On-A-Chip Biosensing Applications. *Laser Photonics Reviews*, 6, 463-487, 2011.

[5] MARTINCEK, I., PUDIS, D.: A Theoretical Study of the Temperature Sensor Based on the LP_{01}- LP_{02} Intermodal Interference in Optical Fiber with a Liquid Core. *Communications - Scientific Letters of the University of Zilina*, 10(2), 10-13, 2010.

[6] Sylgard® 184 Silicone Elastomer [online]. Date: 20/09/2016. Available: http://www.dowcorning.com/DataFiles/090276fe80190b08.pdf.

[7] IP Photoresists, Nanoscribe [online]. Date: 29/09/2016. Available: http://www.nanoscribe.de/files/1814/0662/4393/IP-Resist_IP-Dip_web.pdf.

[8] GASO, P., JANDURA, D., PUDIS, D.: *Fabrication of 2D and 3D Photonic Structures Using Laser Lithography*. Proc. of SPIE, 1-5, 2016.

https://doi.org/10.26552/com.C.2017.3.34-45

COMMUNICATIONS

Jan Latal - Miroslav Kralik - Zdenek Wilcek - Jakub Kolar - Josef Vojtech*

DEPLOYMENT AND MEASUREMENT OF QUALITY OF SERVICE PARAMETERS FOR TRIPLE PLAY SERVICES IN OPTICAL ACCESS NETWORKS

Broadband telecommunication networks are the future of communication and distribution of multimedia services. Thanks to the high transmission potential and capacity of optical fibres, the optical networks are predestined to be more widely used in telecommunications considering the higher data rates through Triple Play services. This paper describes the impact of selected quality parameters on multimedia services defined as Triple Play within an optical network based on the EPON standard. The Triple Play services are then evaluated with measuring instruments and software applications according to QoS requirements and using evaluation methods based on generally defined standards. These are mainly subjective (listening and conversational) and objective (MSE, PSNR, SSIM) methods, or parameters (MOS) and factors (bitrate, delay, packet loss rate, jitter, BER) that are defined for the respective service. The values measured during the experimental tests were related to the limiting parameters of optical topology based on EPON networks for individual services according to their QoS requirements and objective user evaluation.

Keywords: *Triple play, QoS, EPON, MSE, PSNR, SSIM, MOS, MPEG.*

1. Introduction

By using the broadband optical networks, telecom operators were allowed to distribute new types of multimedia services. To make it happen, however, it was necessary to find a suitable type of telecommunication system that would provide high transfer rates and allow reconfiguration. Nowadays, the role of this system is primarily played by optical networks. It was necessary to define the termination of the optical connection at the end customer according to FTTx (Fiber To The x), where x defines the termination of the optical line. FTTx networks are interconnected with PON (Passive Optical Network) optical access networks, which can be classified by their type into several kinds of EPON (Ethernet PON), GPON (Gigabit PON) or 10 GEPON (10 Gigabit EPON). They are going to gradually replace other technologies of access networks (e.g. xDSL-x Digital Subscriber Line, WiFi, etc.) and will probably very soon become the dominant access technology for access networks of the next generation – NGA (Next Generation Access). However, instead of using TDM (Time Division Multiplex) communication, the development of optical networks seems to head towards WDM (Wavelength Division Multiplexing), which brings new possibilities for increasing transmission capabilities and sharing multiple wavelengths between several end customers. There has also been a change of access to the media, as in passive optical networks, the TDMA (Time Division Multiple Access) time sharing approach is now being used more often, and new hybrid optical networks known as WDM-TDMA PON (Wavelength Division Multiplexing-Time Division Multiple Access Passive Optical Network) emerge with data rates of tens of Gbps. Moreover, the termination by FTTx enables to connect either directly to the home (FTTH, Fiber To The Home option) or to the office for corporate or office spaces (FTTO, Fiber To The Office option), but there is also the possibility of combined optical-copper connections using the current copper wiring in buildings, objects or larger blocks. These are the most often the FTTB (Fiber To The Building), FTTC (Fiber To The Curb) or FTTN (Fiber To The Node) variants. However, the main idea of the proposed solution of terminating all FTTx optical connections is the same. It is based on our intention to provide sufficient data rates for network endpoints and thus enable the end subscribers to access modern multimedia services. The one thing that the

---

* **^{1}Jan Latal, ^{1}Miroslav Kralik, ^{1}Zdenek Wilcek, ^{1}Jakub Kolar, ^{2}Josef Vojtech**
^{1}VSB-Technical University of Ostrava, Faculty of Electrical Engineering and Computer Science, Department of Telecommunications,
17. listopadu 15, Ostrava-Poruba, 70800, Czech Republic
^{2}CESNET, a. l. e., Zikova 1903/4, 160 00 Prague 6 Czech Republic
E-mail: jan.latal@vsb.cz

aforementioned possibilities of using up-to-date services have in common is that we need a very careful and comprehensive design and planning of such network topology or infrastructure. It is necessary to pay attention to the fact that the given topology will be assembled not only from optical, but also metallic or wireless systems that must cooperate with each other. As a result, this can lead to lowered costs of both OPEX (Operating Expense) and CAPEX (Capital Expenditures) [1, 2].

By cooperation we mean the mutual synergy and adjustment, the management and reconfiguration options, and last but not least the available effective bandwidth for data transmission. Taking into account the different demands of the stated essential services within the "Triple Play" offer, it is also necessary to guarantee their QoS (Quality of Service) by establishing the necessary mechanisms for reserving sufficient transmission resources. For multimedia and voice services it will be necessary to solve the issues of delays in signal propagation, its fluctuations, etc. in a satisfactory manner [3 - 5].

The object of the following paper is to focus on Triple Play services and their requirements with regard to the parameters that have the largest impact on them, such as packet loss rate, delay, jitter and bandwidth, and also to demonstrate how these services behave in an experimental optical network [2, 3, 5]. All of these parameters are then related to the limiting values of the ODN (Optical Distribution Network), which is modified using fibres according to the ITU-T G.652 D standard and has a digital variable attenuator that can simulate longer and lossy transmission lines.

2. State of the art

Nowadays, the ever-growing demand for multimedia services and their development will, beside other things, require a thorough analysis to enable their smooth deployment and transmission, either within the existing or newly built networks. Optical networks serve as an example of a stable and high-quality system that represents the future for distribution of data communication. However, the deployment of multimedia services lies not only in using EPON, WDM-PON (Wavelength Division Multiplexing Passive Optical Network) or NGA/NGN (Next Generation Access/Next Generation Network) technologies, but also in GPON networks. GPON is a standard in compliance with ITU-T G.984 and is based on the use of GEM (GPON Encapsulation metod) protocol with ATM (Asynchronous Transfer Mode) cell support, while EPON (IEEE 802.3 ah) is based on the IP protocol. The GPON technology is very often deployed in Asian and American countries, where it is used for broadband access networks. GPON allows adjusting SBA (Static Bandwidth Allocation) or DBA (Dynamic Bandwidth Allocation), which is also used in EPON networks. However, neither of these networks defines the maximum possible parameters when achieving QoS for end units/users through Triple Play services [1, 2, 4, 6].

The research team of authors [7] has pursued the idea of improving the dynamic bandwidth allocation among differentiated services while maintaining QoS parameters defined for Triple Play in EPON networks through FIPACT (Frame-Oriented Interleaved Polling with Adaptive Cycle Time) algorithm [8]. To optimize the use of FQ-DBA (Frame-based QoS provisioning Dynamic Bandwidth Allocation) for allocating multimedia streams, a combination of EPON and WDM-PON is used while maintaining QoS parameters. Data streams for terminal units are preferentially defined using FQ-DBA in order to achieve sufficient bandwidth for a given service with respect to QoS.

In another paper, the team of authors discussed the possibilities of faster channel switching in EPON networks for IPTV (Internet Protocol Television) service using a new algorithm [9].

The IPTV and the use of IGMP (Internet Group Management Protocol) protocol in NGN will gain more importance. However, there are also associated problems with QoS and multicast distribution guarantees. The EPON networks meet the stringent demands on higher bandwidth and QoS, but they do not have satisfactory algorithms for allocating channels or streams among individual terminal units. For IPTV, the multicast mode needs a unique LLID (Logical Link Identificator) per channel for each ONU (Optical Network Unit) terminal unit. To prevent congestions of the network and OLT (Optical Line Termination) unit, a new type of algorithm for assigning LLID for individual IPTV channels has been designed [10].

Video quality analysis was researched in the study, comparing video codecs with relation to packet losses in the network. The results of them were artefacts in the video [11]. In other publications, however, the authors have focused on the impact of multiplying variable bitrate HD (High Definition) video streams with variable QoS settings. They have produced numerical simulations for various settings of packet loss, delay, jitter, bandwidth, etc. SwissQual VQuadHD and Telchemy VQMon applications were used for the evaluation [12].

Several research teams have also decided to simulate the behaviour of an EPON network with the Triple Play services implemented. They created an EPON network topology with a variable number of ONU terminal units and ODN network length of 0–65 km in a simulation environment. The results of the simulations confirm that the error rate changes with increasing number of terminal units, which affects the overall error rate of the given topology [13]. Apart from studying the ODN network range, other teams have also focused on the Q-factor, differential settings of system transfer rates from 2.5 to 10 Gbps with a variable number of terminal units connected in a network of 60–130. Based on simulations, it has been found that the EPON network can distribute sufficient transmission capacities even at 10 Gbps at a distance of up to 40 km [14].

3. Triple play

The term Triple Play service is well known nowadays, primarily when referring to multimedia services provided to ordinary customers. Triple Play is a term for a package of three services: high-speed data, internet television (IPTV) and internet telephony (VoIP, Voice over Internet Protocol) provided to the end user over a single connection. All of these services are distributed using the IP protocol (ISO/OSI model layer 3) in Ethernet network (ISO/OSI layer 2). The services are differentiated by the transport layer (ISO/OSI model layer 4). For transferring the data service, the TCP (Transmission Control Protocol) is used, which provides a reliable connection-oriented data transfer. In case of a data loss, a request to retransmit the lost data is sent. VoIP and IPTV multimedia services use the UDP (User Datagram Protocol), which provides connectionless and unreliable type of data distribution. In case of a data loss, there is no retransmission of the lost data. This approach eliminates delays, but degrades the service. Apart from the delay, other important parameters that affect the quality of multimedia services are also the bandwidth, packet loss rate and jitter (delay fluctuations) [15]. Another parameter that also has an impact on the distribution of Triple Play services is OoS (Out of Sequence), which indicates wrong order of data reception, i.e. when the data is received in an order that is different from the order in which it was originally sent. This phenomenon can occur when the data travels through different paths in the network. The QoS (Quality of Service) term is defined with the multimedia services and describes the technical part that must be maintained for the right functionality of the individual services. Based on the requirements, the services can be classified with regard to the transmission type [2]. Therefore, the distribution of Triple Play services has much higher demands on the quality of the distribution infrastructure when compared to the conventional data transfers. The applied technology must provide enough capacity to support the QoS mechanisms (CoS/DiffServ, etc.) that will allow the distribution of services with different requirements for bandwidth, sufficient level of QoE (Quality of Experience), security and reliability.

3.1 Factors affecting the quality of audio and video services

There are numerous of factors that affect multimedia services and have a negative effect, causing gradual deterioration in the quality of the individual audio and video services. Applications used for voice, video and data transmission need more bandwidth for the transfer and they are sensitive to delay and packet loss. As soon as these parameters are exceeded, the service becomes unusable. During the transmission of data, there can be several possible causes of problems on the way from the sender to the recipient. We talk about latency, packet order, delay, bitrate, delay fluctuation (jitter) and packet loss [2].

3.2 Methods for determining the quality of VoIP service

The methods for evaluating speech quality can be classified into two basic groups: the subjective and the objective evaluation methods. During our measurements we were focused on subjective as well as on objective methods for evaluating the quality of VoIP. They will be mentioned and described in the following chapters.

3.2.1 Subjective VoIP service quality evaluation

The conversational methods (CQ – Conversational Quality) are laboratory simulations where two subjects communicate via a phone call and evaluate the transmission quality of the call signal. A third person measures the test conditions. The evaluation uses the MOS (Mean Opinion Score) rating scale. The listening methods (LQ – Listening Quality) do not reflect reality as much as the previous type, but they are easier. They consist of playing speech signals to the subject who evaluates them using multiple possible methods (ACR - Absolute Category Rating, QRDM - QR-decomposition with M-algorithm, DCR - Degradation Category Rating, CCR - Comparison Category Rating). The MOS rating parameter was created based on the ITU P.800 recommendation. It is a part of ACR family – the Absolute Category Rating, based on the comparison of a received signal with the reference signal. The result is obtained by averaging the subjective user opinions about the perceived voice [2].

3.2.2 Objective VoIP service quality evaluation

Here, the statistical evaluation of mathematical models that simulate the human auditory system is used. Among the best algorithms are PAQM (Perceptual Audio Quality Measure), PSQM (Perceptual Speech Quality Measure), NMR (Noise-to-Masked-Ration, PERCEVAL (Perceptual Evaluation), DIX (Distrubance Index), OASE (Objective Audio Signal Evaluation) and POM (Perceptual Objective Measure). We can also mention a metric one which, apart from factors affecting quality, also takes user perception into account. This metric is called R-factor and is used in a calculation model known as the E-model. This model is described in detail in the recommendation G.107. The basic formula for calculating the value of R-factor is [16]:

$$R = R_0 - I_s - I_d - I_e + A \tag{1}$$

where R_0 is the basic signal-to-noise ratio, I_S is the simultaneous interference factor defined as the sum of all deterioration effects (noise from the surroundings, etc.) which can occur simultaneously with voice transmission, I_d represents all deteriorations caused by the delay of voice propagation, I_e (also labelled as $I_{E\text{-}EFF}$ in the literature) is a factor representing the degradation of quality caused by the packet loss, and A is an advantage factor that depends on the concentration of the listener (from 0 to 20 depending on the codec) [2]. The above mentioned calculation also includes a set of recommended values which allows to simplify the calculations to suit the packet networks. Among the important parameters with regard to QoS in packet-based networks are the network delay, jitter and packet loss. These parameters are included in two of the parameters mentioned in the R-factors calculations, namely in I_d and I_e (or $I_{E\text{-}EFF}$) [3, 5].

$$I_d = I_{DTE} + I_{DD} \tag{2}$$

The I_{DTE} parameter represents the factor of impairment caused by echo (echo cancellation has been solved in ITU-T G.168 recommendation). The I_{DD} factor represents the factor of interference caused by a too long transmission delay. By keeping all the default values in R-factor calculation we obtain the final value of 93.35. The value of 93.35 can be achieved only in ideal environment without any disturbance. In order to meet the user expectations, it is necessary to get a value of 70 or more. A simplified R-factor calculation uses this final form:

$$R = 93.35 - I_d - I_e \tag{3}$$

The resulting R-factor is a numerical value that usually lies between 15–94, while the value above 70 is considered to be acceptable.

3.3 Methods for determining the quality of IPTV

There are recommendations for evaluating image and video signal quality available, e.g. ITU-T P.910. Subjective measurements of image and video signal quality are based on the human perception. The advantage of this measurement is that people can describe the image according to what they really see and therefore suppress information that is imperceptible to the human eye. The subjective measurements are influenced by a number of factors which makes the repeatability of these subjective measurements difficult. There are several approaches to IPTV quality measurements, for instance MSE, PSNR, SSIM, MDI (Media Delivery Index) or MPQM (Moving Pictures Quality Metric) to name some of the objective methods. The group of subjective methods for evaluation of IPTV quality include MOS, DSCQS (Double Stimulus Continuous Quality Scale), DSIS (Double Stimulus Impairment Scale), and ACR (Absolute Category Rating). Within experimental measurements we were primarily focused on the objective methods of IPTV quality evaluation, namely on the MSE, PSNR and SSIM described in more detail below, and supplemented them with real measured values in later chapters [2, 17, 18].

3.3.1 MSE (Mean Square Error)

MSE represents the mean square error between the received and original video signals. The following formula is used for the calculation:

$$MSE = \frac{1}{M \times N} \Sigma_{j=0}^{M-1} \Sigma_{j=0}^{N-1} \left(x_{ij} - y_{ij}\right)^2 \; [-] \tag{4}$$

where x is the original image, y is the received image, elements i and j are the elements of the image matrix, M is the image height in pixels and N is the image width in pixels [2].

3.3.2 PSNR (Peak Signal to Noise Ratio)

PSNR is the ratio between the highest values relative to the MSE and is expressed by the following formula:

$$\begin{aligned} PSNR = 10 \times \log \frac{m^2}{MSE} = \\ 20 \times \log_{10}(m) - 10 \times \log_{10}(MSE) \; [dB] \end{aligned} \tag{5}$$

where m is the maximum value a pixel can get [2].

3.3.3 SSIM (Structural Similarity Index)

The SSIM parameter takes the human visual system into account. It measures the similarity between two images. The SSIM has been developed to improve conventional metrics such as MSE and PSNR that were proven to be inconsistent with human perception. The reference values lie within the interval of <0,1>, where 0 represents no relationship to the original image and the value of 1 is reached when two identical pictures are compared.

$$SSIM(x,y) = [l(x,y)]^{\alpha}[c(x,y)]^{\beta}[s(x,y)]^{\gamma} \tag{6}$$

The term $l(x, y)$ is used to compare the signal luminance, the term $c(x, y)$ compares the signal contrast and the term $s(x,y)$ is used to measure the structural correlation, which is calculated from the following relations:

$$l(x,y) = \frac{2\mu_x \mu_y + c_1}{\mu_x^2 + \mu_y^2 + c_1} \tag{7}$$

$$l(x,y)=\frac{2\sigma_x\sigma_y+c_2}{\sigma_x^2+\sigma_y^2+c_2} \tag{8}$$

$$l(x,y)=\frac{\sigma_{xy}+c_3}{\sigma_x\sigma_y+c_3} \tag{9}$$

where μ_x and μ_y represent the average of x and y samples, C_1, C_2 are constant and σ_x and σ_y represent the dispersion of x and y samples [2].

4. Carrying out experimental measurements of triple play services in EPON network

Here we come to the real results that were obtained in the course of measuring the effects of ODN limiting parameters on the built optical topology for different types of Triple Play services. However, the main motive is to demonstrate and verify the practical impact of the main network parameters on the behaviour of multimedia as well as traditional data services. This chapter gives an overview of the impact of QoS parameters on Triple Play services within the EPON network (EPON type 2). The introduction provides a description of the used experimental topology and devices designed to simulate Triple Play services in a network, and then a set of tests and their results. The processed measured values are a subject to evaluation through objective tests based on mathematical foundations described above.

4.1 Measurement of triple play services in EPON network

The basis for the measurement was the topology shown in Figure 1, using a core of OLT EPON type 2 unit with the following basic parameters: the range of about 20 km, the maximum defined split ratio of 1:32 at the used wavelengths 1310 nm (upstream), 1490 nm (downstream) and a transmission rate of 1 Gbps or 1.25 Gbps, where 250 Mbps is used for overhead needed for data transmission and administration [1]. Among other parts was an optical line with the length of 5.773 km made of an ITU-T G.652 D fibre and six ONT/ONU terminal units connected through a symmetric optical splitter (1:7 ratio) having an insertion loss of 8 dB. Additionally, the tested topology was supplemented by EXFO FVA-60B device that was supposed to simulate the ODN network range by increasing insertion loss into the line. The topology was also supplemented by a Simena NE1000 network element for impairment creation, Abacus server used as an IPTV server, a PC (Acer laptop) with MSU Video Quality Measurement Tool application, IP phones (Grandstream GXV3140) to create VoIP service and finally a EXFO AXS200/625 measuring instrument to evaluate qualitative parameters of the multimedia services.

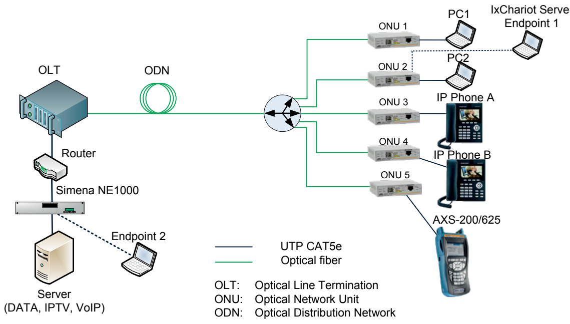

Fig. 1 The topology for Triple Play services deployment and for monitoring the impact of QoS parameters on the services

The Triple Play services were enabled by an Abacus server on which the individual services were implemented, and the user side used laptops or IP phones. The tested topology was also supplemented by a PC with the IxChariot tool (and also serving as an Endpoint 1 for this tool) and by another PC which worked as an Endpoint 2. This topology extension marked with a dashed line in the diagram enabled us to define the quality of VoIP services and to evaluate it. As our goal was to determine the limiting values of the optical distribution network (ODN) and its impact on the Triple Play multimedia services, we have defined the values at which the given topology was still fully functional without communication breakdowns or increased error rates. During the experimental measuring it has been proven that with an additional insertion loss in the line created by a variable digital attenuator, the given topology was able to bridge a gap of 21.95 dB at the wavelength of 1310 nm. It should be noted that the value is related primarily to the ONU unit, as the OLT unit was still able to transmit with 32.2 dB insertion loss at the wavelength of 1490 nm. However, this is caused by the fact that the transmitter located in the OLT unit has more power than the source of radiation used in the ONU unit.

For our purposes, the service for VoIP was distributed via IxChariot. The codecs used were G.711 μ-law, G.723.1 ACELP (Algebraic Code-Excited Linear Prediction), G.729. These types of codecs are often used for VoIP communications and compression of audio data. The most bandwidth/bitrate-demanding codec is G.711 μ-law, which requires 64 kbps. The G.711 standard was designed in 1992 and is intended for PSTN networks. G.723.1 – this standard is intended for multimedia applications and includes two speech coders. One of them uses a transmission rate of 5.3 kbps and the other one a transmission rate of 6.4 kbps. The distinctions between them are in different codebooks with different excitation sequences. The frame size is 30 ms, the delay due to frame overlapping is 7.5 ms, and the total delay of the coder is 67.5 ms. The G.729 standard has been developed primarily for mobile networks applications. A coder based on G.729 has a low bit rate of 8 kbps. The frame size was set to be 10 ms, which allowed reaching a compromise between the quality of the reconstructed speech signal and the computational complexity of the coding algorithm. The delay caused by frame overlapping (lookahead) is 5 ms and the total delay is 25 ms. Nowadays, however, we can find more advanced types of codecs [2, 16].

The distribution of video streams was prepared using VLC Streamer and Abacus server with three main HDTV (High-definition television) and SDTV (Standard-definition television) video samples and different types of MPEG-2 (Moving Picture Experts Group) or MPEG-4 compliant compression codecs. MPEG-2 is the older of the codecs and was developed in 1994. Its predecessor is the MPEG-1 format and its more advanced technological successor is the MPEG-4 format. MPEG-2 is the standard format used for storing and transferring video on DVDs or for the distribution of DVB-T (Digital Video Broadcasting - Terrestrial) digital television signal. Applications that require real-time MPEG-2 video compression and decompression are much more demanding in terms of the computing capacity of a processor than with the MPEG-1 format. The difference between MPEG-1 and MPEG-2 formats is that the latter can work with the so-called VBR (Variable Bit Rate). MPEG-2 was developed for the resolution of 720×576 pixels which corresponds to SDTV. MPEG-4 is a collection of patented methods that define the compression and storage of audio and video data. It was introduced to the world in 1998 and it represented a group of standards for encoding audio, video and related technologies. It was formally issued by ISO/IEC MPEG as an ISO/IEC 14496 standard. Many features of the MPEG-4 standard are defined as optional. MPEG-4 is a standard which is still being developed, especially some of its parts. The new compression method according to H.264 for MPEG-4 version 10 will also come in handy to those who need to effectively archive or download/upload video recordings. The H.264 codecs allow reducing the capacity demands for the transmission of video data streams to one half or one third when compared to MPEG-2, which makes them an ideal type of codec for any kind of broadcast. The following chapters state all measurement methodologies for Triple Play services in EPON networks [2, 17, 18].

4.2 Measuring IPTV using EXFO AXS 200/625

The first step of the experiment with the Triple Play services implemented in the EPON network was measuring the data rates of three different video samples. These samples were distributed via a network established from a server to a terminal unit represented by EXFO AXS 200/625 analyser. The analyser performed detailed measurements of the impact of the loss rate in the selected video samples on the limit value of the experimental topology with EPON. In Table 1 we can see the test samples used for measuring the change of transmission rate and the impact of

Samples used for transmitting in the analysis with AXS 200/650

Table 1

Samples	File type	Size [MB]	Average bitrate [kbps]	Frames per second	Resolution	Codec	Length
MPEG-2 HDTV	MPEG	374	9 843	29.970	1 280×720	MPEG2	5 min 9 s
MPEG-4 HDTV	AVI	420	11 456	29.970	1 920×1 080	MPEG4	5 min 7 s
MPEG-2 SDTV	MPEG	136	1 154	25.000	720×480	MPEG2	14 min 46 s

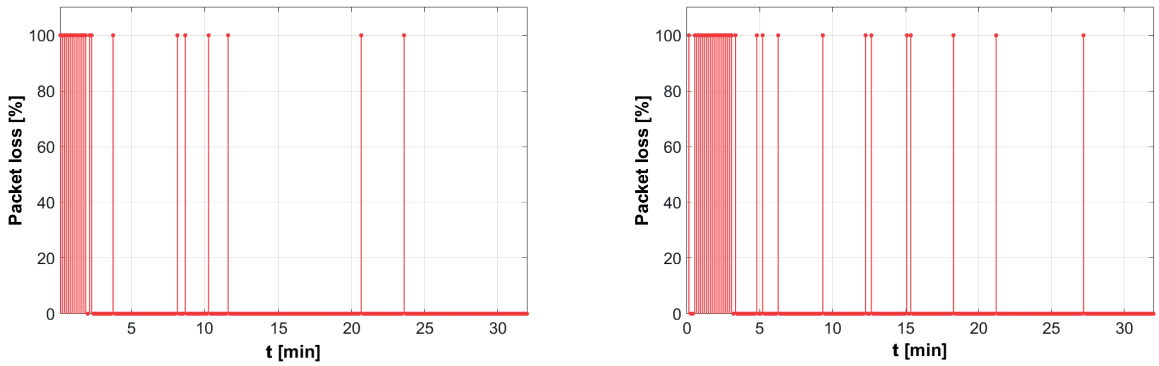

Fig. 2 MPEG-2 HD (left) and MPEG-4 HD (right) video

transmission time on the error rate (packet loss) for the limiting settings of the experimental topology with EPON.

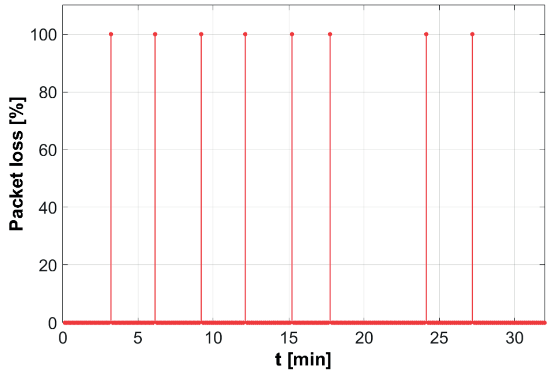

Fig. 3 MPEG-2 SD video

Figures 2 and 3 present the effect of the transfer rate on the error rate, i.e. packet loss. The length of the measurement was 30 minutes (to be more specific, although the test samples are shorter than the test period, they were played in a loop) and the network throughput was changed from 10 Mbps to 100 Mbps in steps of 10 Mbps every 3 minutes. The EXFO AXS 200/625 analyser evaluated the error rate using a 1/0 method, where "1" means there was an error and "0" means there was no error. We can see that the transfer rate influenced the error rate primarily in the HD video samples. The occurrence of errors depended on the video *bitrate* and the large occurrence of errors took place only during the first step (the first 3 minutes) at a speed of 10 Mbps, which confirms the demand for a minimum data rate defined for a particular video format in QoS [2]. In the subsequent steps, the errors in the HD video samples occurred just rarely. For the MPEG-2 SD sample, the errors occurred rarely from the beginning to the end of the experimental measurement.

4.3 MSU video quality measurement tool – IPTV service

For the next step of testing the IPTV services, the MSU VQMT software application was used to evaluate and analyse the objective methods. Using a Simena NE1000 network emulator we modified the critical parameters of the network that in turn affected the IPTV. Three basic types of video samples (see Table 2) were used for experimental measuring, which are the types currently used for distributing IPTV to its customers.

The effect of bitrate on the objective methods MSE, PSNR and SSIM can be seen in Figs. 4-6. Figure 4 shows the plot of the MSE objective method that represents the mean square error between the original signal and the signal received on the other side of the network. Deterioration can be seen in MPEG-2 HD and HD MPEG-4 video samples at speeds lower than 20 Mbps. It comes from their demand for bitrate which for the given video resolution varied up to a maximum of 20 Mbps and did not exceed this value. The MPEG-2 SD sample shows no errors, even when it requires a bitrate lower than 10 Mbps. The PSNR objective method is similar.

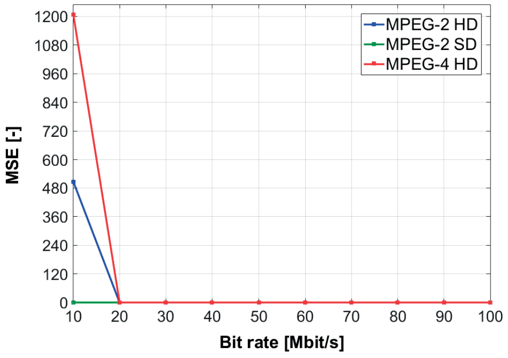

Fig.4 The effect of bitrate on MSE

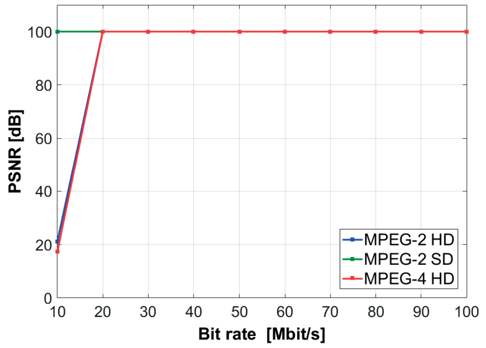

Fig. 5 The effect of bitrate on PSNR

Video samples used for analysis by the objective methods with the VQMT MSU application Table 2

Sample	File type	Size [MB]	Average bitrate [kbps]	Frames per second	Resolution	Codec	Time
MPEG-2 HDTV	AVI	26.7	10 427	29.970	1 280×720	MPEG-2	20 s 19 ms
MPEG-4 HDTV	AVI	24	9 061	29.970	1 920×1 080	MPEG-4	20 s 89 ms
MPEG-2 SDTV	AVI	5.9	2 132	25.000	720×480	MPEG-2	20 s 88 ms

Figure 6 shows plots of the SSIM objective method, which is based on the MSE and PSNR methods. The results of the measurement are very similar. Slightly worse results were obtained for the MPEG-4 HD video sample when the bitrate was 10 Mbps.

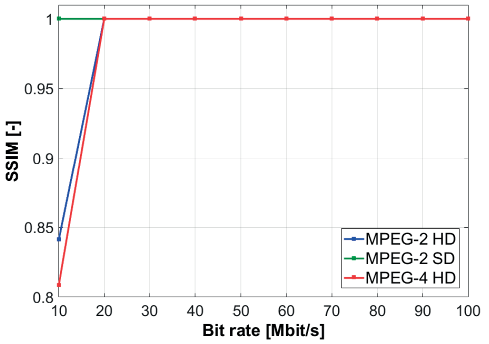

Fig. 6 The effect of bitrate on the SSIM

Figure 7 plots the effect of error rate on the MSE and PSNR objective methods. The worst results were obtained for the MPEG-4 HD sample and the results were very good for the less demanding video represented by MPEG-2 SD. The effect or change of the values for each of the objective method appears for BER = 10^{-8} or lower.

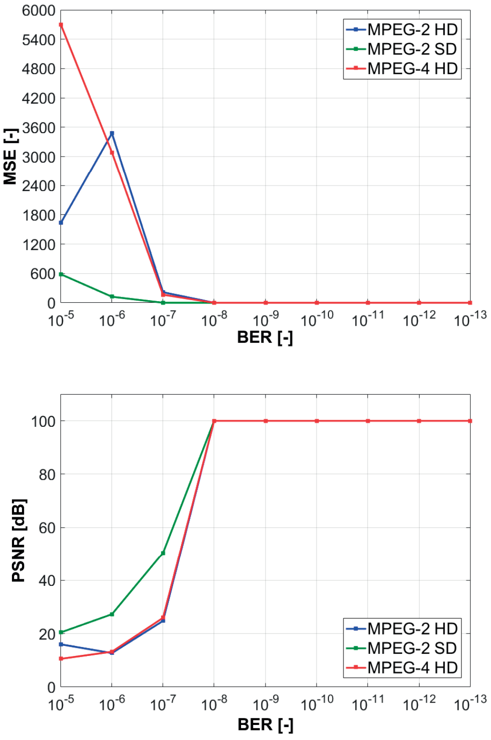

Fig. 7 The effect of BER on MSE (top) and PSNR (bottom)

Figure 8 shows the effect of the error rate on the SSIM objective method. The results are similar as for the previous methods. Here again the MPEG-4 HD sample gives the worst values and the effect can be seen for BER values below 10^{-8}.

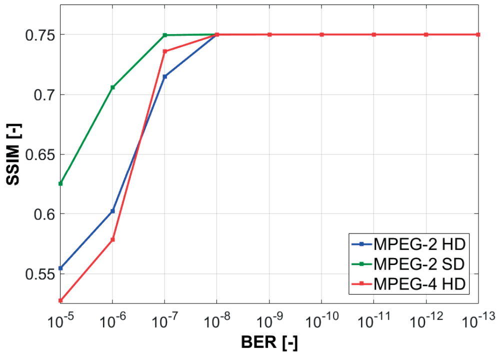

Fig. 8 The effect of BER on SSIM for the tested video samples

Figures 9 and 10 show the impact of packet loss rate on the objective methods MSE, PSNR and SSIM. For these parameters it is possible to see the effect starting from the smallest set values. We can also see relatively large fluctuations of the values, which may be caused by the set dynamic packet loss rates at the individual percentage values. The real measurements show that MPEG-4 HD has the worst results and by contrast, the best results can be seen for the MPEG-2 SD sample.

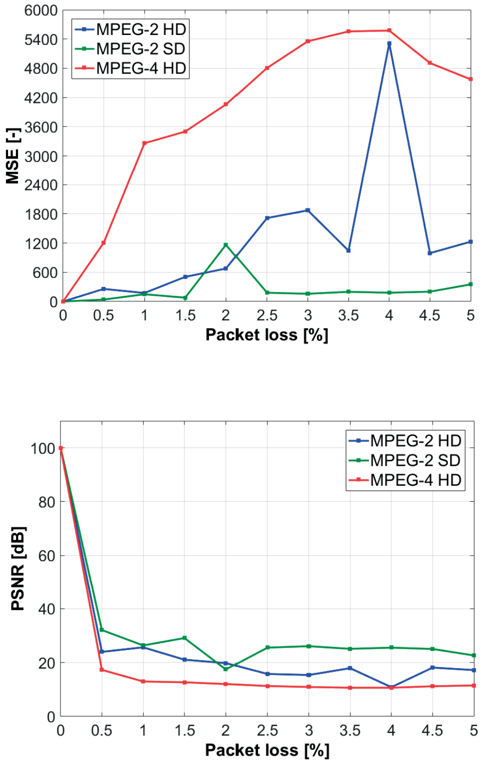

Fig. 9 Impact of packet loss rate on MSE (top) and PSNR (bottom)

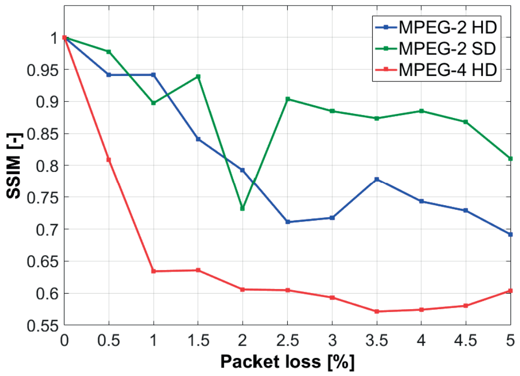

Fig. 10 Impact of packet loss rate on SSIM

By using the quoted results and our observations of the video samples we can evaluate the impact of the individual parameters on the video quality. For the BER (Bit Error Ratio) parameter, the quality is deteriorated for values of 10^{-7}. The packet loss rate parameter affects the video from the lowest set value, but the difference can be seen in MPEG-2 SD and MPEG-2 HD, where MPEG-2 HD with high loss rate (about 3 %) is hard to watch, while MPEG-2 SD image is much better to distinguish and watch. The difference can also be seen for admissibility, which has an impact on the format and resolution of the video. The effects of QoS parameters such as *jitter* and delay was also observed. The requirements state the maximum value of *jitter* to be less than 50 ms and delay under 200 ms. During testing, these parameters were set at much higher values, yet there was no impact on the video quality. However, they did cause a delay of the received audio signal from the original transmitted one.

4.4 IxChariot – VoIP service

The evaluation of VoIP call quality has been carried out mainly on the G.711 μ-law codec, which is supposed to be the most often used codec by voice service providers. A comparison with other codecs (G.723.1 ACELP, G.729) has also been made. The main parameters by which the voice call was evaluated were MOS and R-factor values, which are related and can be compared with each other. To evaluate the VoIP service, we have used the IxChariot program that allows the simulation of calls with various settings. We have evaluated the effects of several critical parameters (bitrate, jitter, BER, delay and packet loss rate) that have the greatest impact on the quality of the service. The values obtained from the experimental measurements are shown in Figs. 11 - 13.

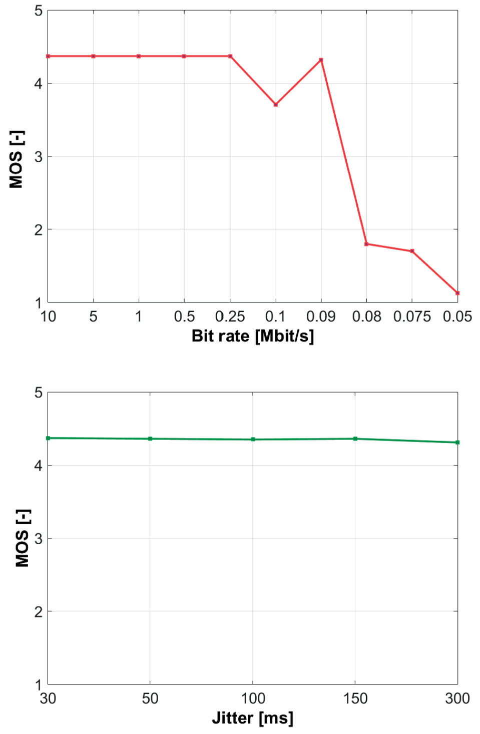

Fig. 11 The impact of the bitrate (top) and jitter-u (bottom) on the call quality (MOS) for VoIP codec G.711

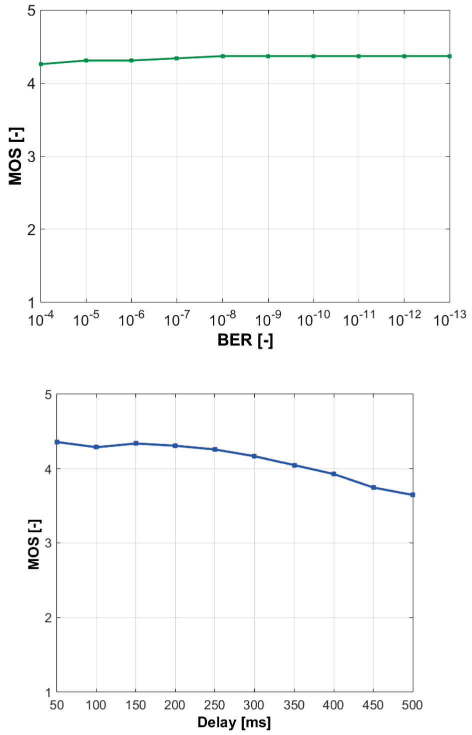

Fig. 12 The impact of the BER (up) and delay (down) on the call quality (MOS) for VoIP codec G.711

Figures 11 and 12 show the impact that the changes of individual parameters have on the call quality for codec G.711 μ-law. Parameters such as delay, jitter and error rate have almost no effect on the call quality, even when they are set above the values defined as maximum for QoS requirements in ITU-T. This was caused by the fact that the network load was low during the measurement as there were no running services for IPTV or data transmissions. The effect on the MOS value is apparent for the bitrate change (see Fig. 11) when the value was set to 0.09 Mbps or less. These are low bitrate values, but the given topology can cover them without major problems. The last parameter also has the largest impact – it is the packet loss rate. That is why this parameter was also tested on other types of codecs. Apart from G.711 μ-law these were G.729 and G.723.1 ACELP.

Figure 13 shows that the highest impact of packet loss rate can be seen with the G.711 μ-law codec, for which the MOS value dropped from 4.2 down to 1.73, which is already a value showing unsatisfactory to poor call quality, while the limiting value of MOS for a satisfactory call is 3 or above. For G.729 and G.723.1 ACELP codecs the MOS value turned out to be just under the limit of 3 (the G.723.1 ACELP codec), where these codecs reach the limits of acceptability for call quality at the packet loss rate of 5 %. The codec that is most resistant against packet loss is G.729.

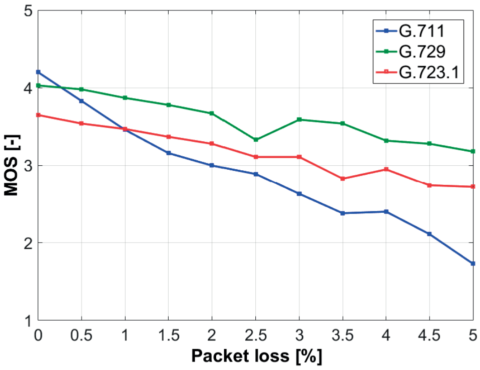

Fig. 13 The impact of packet loss rate on VoIP call quality (MOS) for individual codecs

4.5 The impact of QoS parameters – data service

The impact of QoS on the data transfer was recorded using the BWMeter software application. It allowed us to record the actual transfer rates in both directions in one second intervals. The data was transferred using a created data server from which the data was downloaded and on which it was also uploaded. The data sample used had a size of 18100 Mb. During the measurement we observed the extent of limitations that the error rate and packet loss rate parameters had on the data transfer service.

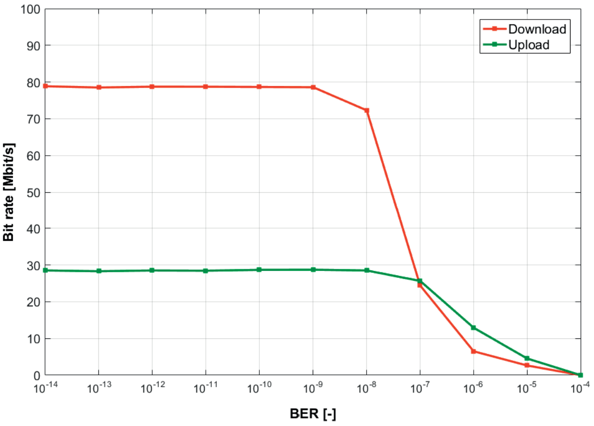

Fig. 14 The effect of BER on the transfer rate – download/upload

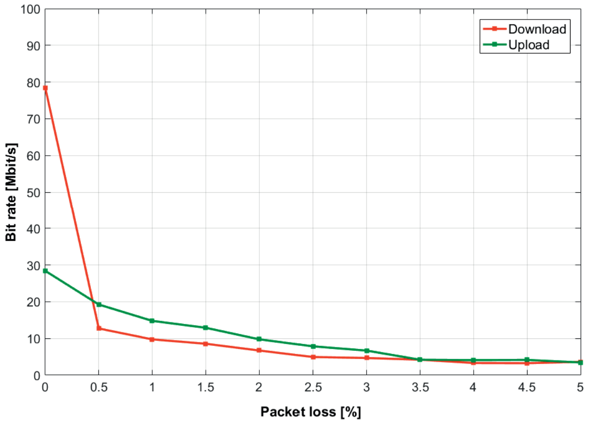

Fig. 15 The effect of packet loss rate on the transfer rate – download/upload

In Fig. 14 we can see the effect that the error rate parameter has on the data transfer. The measurements show that up to BER values of 10^{-9}, the transfer is error-free, but when the values go lower, a drop in transfer rates is apparent in both directions. The complete breakdown occurs at the value of 10^{-4}. Figure 15 describes the effect of the packet loss rate on the data transfer. We can see that the effect of this parameter is more noticeable even at the first step with a packet loss rate of 0.5 %, when there is a significant decrease in transfer rates. Increasing the packet loss rate further only causes moderate constant descent of the transfer rate in both directions. The connection still works until the last step of 5 %, where the value is around 3.6 Mbps.

5. Conclusion and evaluation

The results of the experimental measurements demonstrate the characteristics of the EPON network that shows itself to be a suitable candidate for the implementation into the infrastructure with regard to Triple Play services deployment by internet service providers. The paper introduces various measurement options that demonstrate the impact and limits of the parameters affecting the multimedia services and methods for evaluating the quality of Triple Play services. The results show that the most appropriate format for distribution in IPTV services is MPEG-2 HD, which is a sort of compromise between quality and network requirements. For VoIP voice services, the most often used codec is G.711 μ-law. However, in the last test of packet loss rate, the G.729 codec that requires less bitrate has shown better results.

For data services, the essential parameter for an end user is the bandwidth or bitrate, but the error rate or packet loss rate in the network are also quite important. From a global viewpoint, the EPON standard and its extensions are a great choice, as they have excellent transmission characteristics and offer to set up QoS policies in the network for individual multimedia services. The main contribution of this paper is the way in which it is possible to deploy and subsequently evaluate the behaviour of a network based on the EPON standard and also the deployment of Triple Play services with regard to the evaluation of quality and their demands. The future work will be primarily focused on creating new types of NGA/NGN networks and setting up QoS policies with regard to the parameters critical for the Triple Play services. We will also look at the possibilities of adding new video formats (e.g. UHD, h.265, VP9) [19, 20] or higher transmission rates that will be offered to end users by their providers together with other services (Smart applications, etc.).

Acknowledgement

The research described in this article could be carried out thanks to the active support of the projects No. SP2017/79, SP2017/97, VI20172019071, CZ.1.07/2.3.00/20.0217, CESNET 614R1/2017. The presented research has been supported by project E-infrastructure CESNET – modernization, registration no. CZ.02.1.01/0.0/0.0/16 013/0001797.

References

[1] LAM, C. F.: *Passive Optical Networks: Principles and Practice.* Elsevier,Boston, p. 324, 2007.

[2] HENS, F. J., CABALLERO, J. M.: *Triple Play: Building the Converged Network for IP, VoIP and IPTV.* Wiley, Hoboken, p. 401, 2008.

[3] FRNDA, J., VOZNAK, M., SEVCIK, L.: Impact of Packet Loss and Delay Variation on the Quality of Real-Time Video Streaming. *Telecommunication Systems,* 62(2), 265-275, 2016.

[4] IFTIKHAR, R., KALEEM, I. M., ABDULLAH, S. M.: *Triple Play Services over EPON Triple Play Services over Ethernet-Passive Optical Networks.* IEEEP Symposium, EIR-16(5), Pakistan, 2010.

[5] FRNDA, J., VOZNAK, M., FAZIO, P., ROZHON, J.: *Network Performance QoS Estimation.* Intern. Conference on Telecommunications and Signal Processing (TSP 2015), Czech Republic, 2015.

[6] SULTAN, D. M. S., TASLIM, MD. A.: GPON, The Ultimate Pertinent of Next Generation Triple-Play Bandwidth Resolution. *Journal of Telecommunications and Information Technology*, 2, 53-60, 2011.

[7] LIN, H. –T., LAI, CH.-L., WANG, T.-SH, HUANG, Y.-CH.: *Supporting Triple-Play Services with Private Networking over WDM EPONs.* Intern. Symposium on Communications and Information Technologies (ISCIT 2014), South Korea, 2014.

[8] LIN, H.-T., LAI, CH.-L., LIU, CH.-L.: Design and Analysis of a Frame-Oriented Dynamic Bandwidth Allocation Scheme for Triple-Play Services over EPONs. *Computer Networks*, 64, 339-352, 2014.

[9] NIE, Y., YOSHIUCHI. H.: *A Fast Channel Switching Method in EPON System for IPTV Service*.Springer, Berlin Heidelberg, p. 280, 2009.

[10] HWANG, I.-SH., NIKOUKAR, A.-A., LIEM,A. T., CHEN, K.-CH.: *A New Architecture for Multicasting Live IPTV Traffic in Ethernet Passive Optical Network.* Intern. Conference on Electronics, Computer and Computation (ICECCO 2013), Turkey, 2013.

[11] YIM, CH., BOVIK, A. C.: Evaluation of Temporal Variation of Video Quality in Packet Loss Networks. *Signal Processing: Image Communication*, 26(1), 24-38, 2011.

[12] MAKOWSKI, P.: Quality of Variable Bitrate HD Video Transmission in New Generation Access Network. *Journal of Telecommunications and Information Technology*, 1, 21-26, 2014.

[13] KOCHER, D., KALER, R. S., RANDHAWA, R.: Simulation of Fiber to the Home Triple Play Services at 2Gbit/s using GE-PON Architecture for 56 ONUs. *Optik*, 124(21), 5007-5010, 2013.

[14] SINGH, S.: Performance Evaluation of Bi-Directional Passive Optical Networks in the Scenario of Triple Play Service. *Optik*, 125(19), 5837-5841, 2014.

[15] VODRAZKA, J., LAFATA, P.: Transmission Delay Modelling of Packet Communication over Digital Subscriber Line. *Advances in Electrical and Electronic Engineering, 11*(4), 260-265, 2013.

[16] KOVAC, A., HALAS, M.: E-Model MOS Estimate Precision Improvement and Modelling of Jitter Effects. *Advances in Electrical and Electronic Engineering*, 10(4), 276-281, 2012.

[17] BIENIK, J., UHRINA, M., VACULIK, M., MIZDOS, T.: Perceived Quality of Full HD Video - Subjective Quality Assessment. *Advances in Electrical and Electronic Engineering*, 14(4), 437-444, 2016.

[18] UHRINA, M., HLUBIK, J., VACULIK, M.: Correlation between Objective and Subjective Methods Used for Video Quality Evaluation. *Advances in Electrical and Electronic Engineering, 11*(2), 135-146, 2013.

[19] UHRINA, M., FRNDA, J., SEVCIK, L., VACULIK, M.: Impact of H.264/AVC and H.265/HEVC Compression Standards on the Video Quality for 4K Resolution. *Advances in Electrical and Electronic Engineering*, 12(4), 545-551, 2014.

[20] UHRINA, M., BIENIK,J., VACULIK, M.: Impact of GoP on the Video Quality of VP9 Compression Standard for Full HD Resolution. *Advances in Electrical and Electronic Engineering*, 14(4), 445-452, 2016.

https://doi.org/10.26552/com.C.2017.3.46-50

Jana Mizerakova - Peter Hockicko - Francisco Munoz*

DIELECTRIC STUDY OF LITHIUM AND SODIUM BOROPHOSPHATE GLASSES

Ionic conductivity and dielectric properties such as dielectric permittivity and loss tangent for the samples of lithium and sodium borophosphate glasses were investigated using the electrical conductivity measurements in the range of frequency from 10 Hz to 2 MHz and various temperatures below T_g. The measured data of ac conductivity were described according Jonscher's power law and experimental values of imaginary part of electric modulus were fitted by KWW function. From the fitted parameters, the activation energies for conduction and relaxation time were found which characterize the hopping processes and transport mechanism in these ion conducting glasses.

Keywords: *Borophosphate glasses, ionic conduction, dielectric properties, electric modulus formalism, relaxation time.*

1. Introduction

Borophosphate glasses may find potential use in different technological applications. They are suitable as host materials in laser applications, solar energy converters or electrode materials in Li secondary batteries [1]. However, the biggest demand of their possible usage is for the developing of solid state electrolytes [2, 3]. Next-generation of battery for electronic devices e.g. electrical vehicle, energy storage systems or smart phones, have to possess high energy density, low cost and stable interface between the interphase of the electrodes and electrolyte [4]. Especially for the intercorpotation of Li metal into secondary batteries, it is important to avoid dendrite formation which may lead to safety problems due to possible shortcircuiting [5]. So, the developing of the stable interface is the biggest issue for the solid state electrolyte materials. These glasses have shown to be promising candidates for improved electrolytes of Li-ion batteries due to their physical properties than high ionic conductivity at room temperature (about 10^{-7} S/cm), chemical stability and compatibility with the electrode materials [4 - 6]. The maitanance of stable interface between electrode and electrolyte requires the precise reproduction of components which is based on the good knowledge of physical properties.

From the review of literature we can see several spectroscopy studies such as Raman spectroscopy, X-ray photoelectron spectroscopy or Nuclear Magnetic Resonance which are focused on the relationship between the structural changes and physical properties in alkali borophosphate glasses [6, 8, 9]. The choise of this system is often used for theoretical interest as a model sample for studies of the mixed glass former effect (MGF). The MGF describes the change in ionic conductivity in glasses which can be revealed as decrease or increase in the ionic conductivity with the change of the glass forming oxides while keeping the modifier oxide content constant [2, 3, 8].

As Jonscher has shown in [10] there are wide-reaching similarities between the electrical and mechanical response of system, also shown in [11], although only partially understood. So, this paper represents the first stage of our investigation aiming to compare the electrical and mechanical response of ionic conducting systems Na-B-PO and Li-B-PO. In this paper we present the conductivity and dielectric measurements of glasses of the systems with composition $50R_2O$-xB_2O_3-$(50\text{-}x)P_2O_5$ (R = Li or Na), which are analyzed by several formalisms.

2. Experimental part

The lithium and sodium borophosphate glasses of the systems of composition $50Li_2O–xB_2O_3–(50\text{-}x)P_2O_5$ and $50Na_2O–xB_2O_3–(50\text{-}x)P_2O_5$ were prepared by the melting and quenching method. Glass batches were obtained through mixing reagent grade raw materials, Li_2CO_3 and Na_2CO_3 (Sharlau, ACS), B_2O_3 (Panreac) and $(NH_4)_2HPO_4$ (Sharlau, ACS), which were calcined in porcelain crucibles up to 450 ^{o}C in an electric furnace and then melted during 2 h at temperatures ranging from 800 ^{o}C to 1000 ^{o}C depending on their composition. The melts were

---

* [1]**Jana Mizerakova,** [1]**Peter Hockicko,** [2]**Francisco Munoz**
[1]Department of Physics, Faculty of Electrical Engineering, University of Zilina, Slovakia
[2]Ceramics and Glass Institute (CSIC), Kelsen, Madrid, Spain
E-mail: hockicko@fyzika.uniza.sk

poured onto brass molds and annealed above their corresponding glass transition temperature. The samples were prepared at the Ceramics and Glass Institute of the Spanish Research Council (CSIC) in Madrid, Spain.

The prepared samples were polished to be flat and plane-parallel. The both sides of samples were sputtered with gold electrodes of thickness ~ 1 μm.

The dielectric spectroscopy is widely used tool for the investigation of materials [12]. Spectroscopy measurements were done using LCR Meter OT 7600 Plus at frequencies in the range from 10 Hz to 2 MHz (200 measurements for each of the range of temperature in steady state) for increasing temperature in the range below T_g - transition point. We performed measurements of chosen temperatures (with time per measurements: 5 min and time per stabilization of measured system: 20 min).

The evaluation of measurements were carried out by different electrical and dielectric quantities $Z^*(f)$, $\sigma^*(f)$, $\varepsilon^*(f)$ and $M^*(f)$ which are plotted in the both real and imaginary representation. Also, they are related through their reciprocal representation, then we can write $\sigma^*(f) = \sigma'(f) + \sigma''(f) = 1/Z^*(f)$, $\varepsilon^*(f) = \varepsilon'(f) + \varepsilon''(f) = 1/M^*(f)$ and $\sigma^*(f)$ is described by the following equation $\sigma^*(f) = j\omega\varepsilon_0\varepsilon^*(f)$, where ω is the angular frequency and ε_0 is the permittivity of free space. According to the symbolic-complex method of circuit analysis we can designate the complex permittivity of the investigated material using the equation:

$$\varepsilon' = \left(\frac{C}{\varepsilon_0}\frac{h}{A}\right) \text{ and } \varepsilon'' = \left(\frac{h}{\omega\varepsilon_0 RA}\right) \qquad (1)$$

where C is measured capacitance, R is the value of measured resistance, A denotes the area of the plates and h is thickness of the sample.

3. Results and discussion

3.1 Ionic conductivity

Figure 1 shows the results of the ac conductivity measurements provided at the investigated samples which have been studied over wide ranges of frequencies and temperatures for sample $50Li_2O$-xB_2O_3-$(50-x)P_2O_5$ ($x = 5$ mol%). Typically, the ionic conduction follows the Jonscher's power law function:

$$\sigma(\omega) = \sigma_{DC} + A\omega^s \qquad (2)$$

where A is constant related to strength polarizability, s is power law exponent and σ_{DC} is dc conductivity and corresponds to the independent frequency part at low frequency. The conductivity dependence exhibits the significant increase according with power law trend in the high frequency region. The motion of charge carried in dc region is related to the long-range diffusion of ions which are moving via activated hopping. The rate of hopping is given by Arrhenius equation:

$$\sigma_{DC} = \sigma_0 \exp\left(-\frac{E^{DC}}{k_B T}\right) \qquad (3)$$

where σ_0 is pre-exponencial factor, E^{DC} is activation energy for ionic conduction, T is temperature in K and k_B is Boltzmann's constant. The values of σ_{DC} were determined from the Equation 2 and used for the evaluation of the activation energy. The calculated values of activation energies for conduction are shown in Table 1.

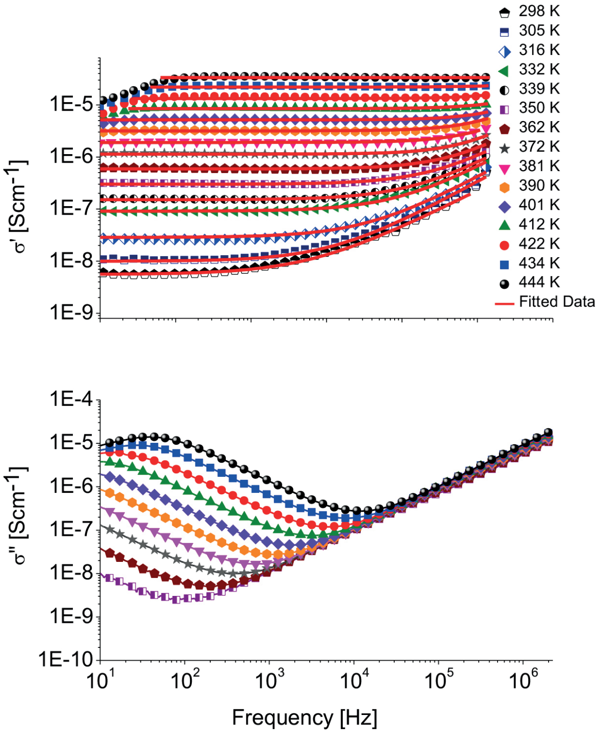

Fig. 1 Frequency dependence of real and imaginary parts of ac conductivity for glass $50Li_2O$-xB_2O_3-$(50-x)P_2O_5$ ($x = 5$ mol%). Red lines represent theoretical fit accordance with Equation 2

Figure 2 depicts the real and imaginary parts of complex impedance where characteristic peak of Z'' is shifted to higher frequency with the increase of temperature. The graphical inset in the Fig. 2 represents the Nyquist diagram which is plotted as the dependence of real and imaginary part of complex impedance and the intersection of the bulk response semicircle with zero value of Z" at low frequencies give us the value of bulk resistance. For the determination of the dc conductivity the following expression is used: $\sigma_{DC} = d/(RxA)$, where d is diameter of sample, A is area of electrodes surface and R is bulk resistivity as determined from the intercept with the x-axis in the Nyquist diagram. The calculated values of dc conductivity from Nyquist diagram were in the good agreement with evaluated values from fitted data according Jonscher's function.

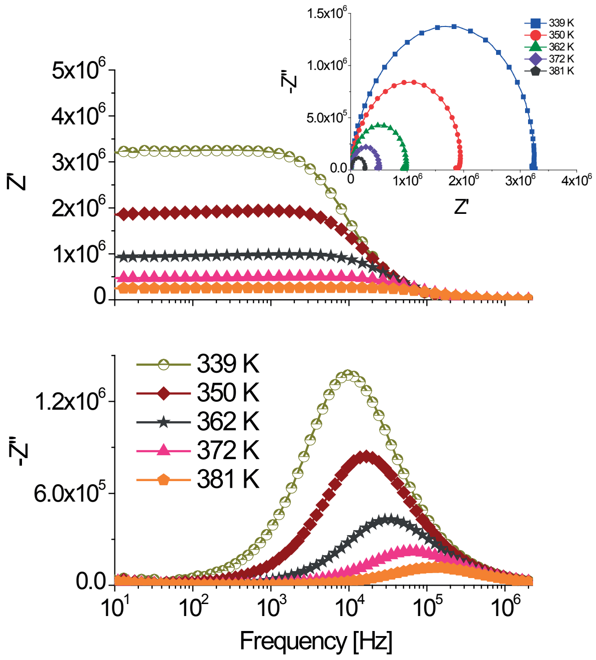

Fig. 2 Frequency dependence of real and imaginary parts the complex impedance measured at different temperatures for sample $50Li_2O$-xB_2O_3-$(50$-$x)P_2O_5$ (x = 5 mol%). Nyquist diagram is shown in the graphical inset for $50Li_2O$-xB_2O_3-$(50$-$x)P_2O_5$ (x = 5 mol%) at different steady state value of temperature

3.2 Dielectric behaviour

For the investigation of the dielectric properties, we used two different formalisms, complex permittivity and the reciprocal approach electrical modulus. Figure 3 shows the frequency dependence of complex permittivity in log-log scale for the temperature below T_g, for one sample with composition $50Li_2O$-xB_2O_3-$(50$-$x)P_2O_5$ (x = 5 mol%). In the plot of frequency dependent ε', we can observe two characteristic values $\varepsilon_\infty'(\omega)$ and $\varepsilon_s'(\omega)$ for a material with ionic conduction. The value $\varepsilon_\infty'(\omega)$ is observed in the higher range of frequencies where ε' reaches a constant value that is the result of a much rapid polarization process in material. The static value $\varepsilon_s'(\omega)$ is observed in the low-frequency plateu before the appearance of electrode polarization. What is more, we can notice that plateau region shifts to higher frequency with the increase of temperature.

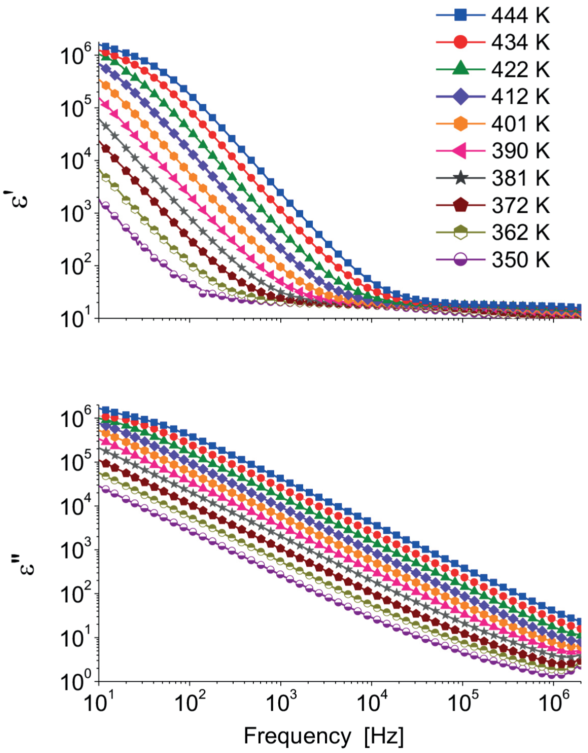

Fig. 3 Real and imaginary parts of the dielectric permittivity as a function of frequency at selected temperatures for sample $50Li_2O$-xB_2O_3-$(50$-$x)P_2O_5$ (x = 5 mol%)

The electric modulus is related to dielectric permittivity through the expression $M^*=1/\varepsilon^*$, and is commonly used in the investigation of relaxation phenomena for ionic conducting glasses. Figure 4 depicts the variation of imaginary and real parts of complex modulus as a function of frequency. In the imaginary part of modulus typical asymmetric peaks can be observed, which shift to higher frequencies with increasing temperature. The quantity f_{MAX} is the frequency corresponding to the maximum of the modulus peak and divides the transition of mobile ions from the short range transition occurring at higher frequency part of peak to a long range in the lower frequency part of imaginary modulus peak. From the value of frequency f_{MAX}, we can get the conductivity relaxation time by condition $2\pi f_{MAX}=1$. The parameters of f_{MAX} are determined by fitting process with the modified KWW function suggested by Bergman [13]. According to this, the imaginary part of electric modulus may be represented as

$$M'' = \frac{M''_{MAX}}{(1-\beta)+\frac{\beta}{1+\beta}\left[\beta\left(\frac{f_{MAX}}{f}\right)+\left(\frac{f}{f_{MAX}}\right)^{\beta}\right]} \qquad (4)$$

where M''_{MAX} is the peak value and β is the stretching exponent in the range $0 \le \beta \le 1$ and indicates the deviation from Debye type relaxation.

The activation energies E^{τ}, for each glass were determined from the slope of log vs. 1000/T using the equation $\tau = \tau_0 \exp\left(E^{\tau}/k_B T\right)$. This Arrhenius type dependence of the relaxation time from which the activation energy was determined is plotted in Fig. 5b. The calculated activation energies are listed in Table 1. The inset in Fig. 4 represents the normalized value of M''_{MAX} and frequency is scaled by f_{MAX}, the collapse of data to a master curve is indicative of a common transport mechanism.

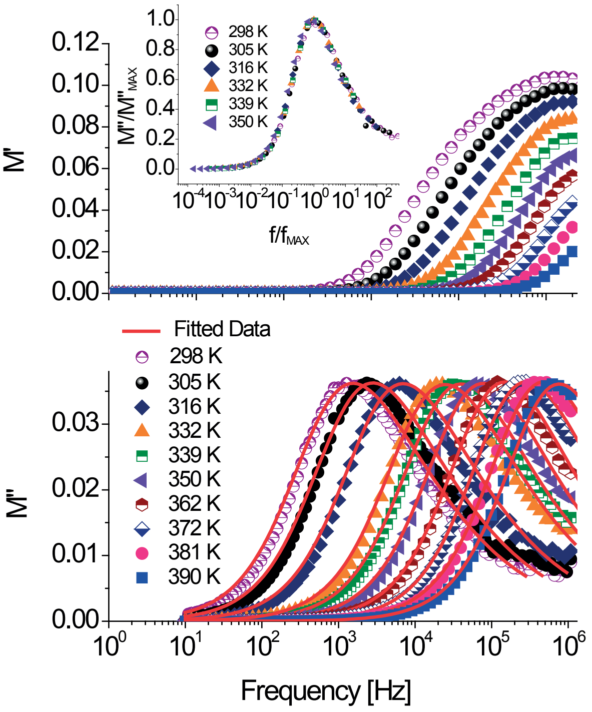

Fig. 4 Imaginary and real representation of frequency dependent modulus; red lines represent the fitted data with KWW function

For the investigated systems Na-B-PO and Li-B-PO, dc conductivities (listed in Table 1) increase with the decrease of the alkali cation radius, i.e. conductivity increases from Na to Li containing glasses.

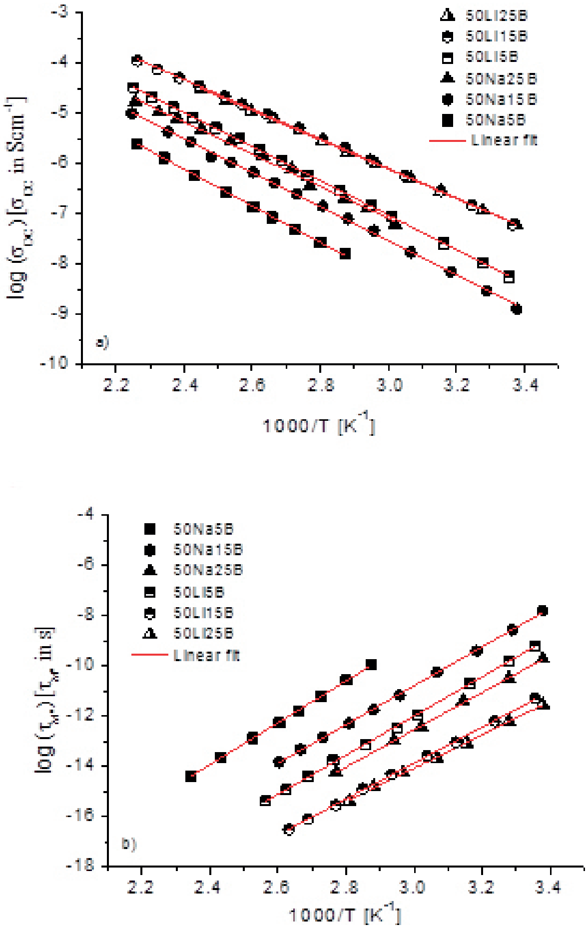

Fig. 5 Arrhenius dependence of dc conductivity a), and relaxation time for conduction b), depicted for all investigated samples

4. Conclusions

The choice of samples $50Li_2O\text{-}xB_2O_3\text{-}(50\text{-}x)P_2O_5$ (x = 5–25 mol%) and $50Na_2O\text{-}xB_2O_3\text{-}(50\text{-}x)P_2O_5$ (x = 5–25 mol%) is due to investigating of the change in ionic conductivity which can be revealed as decrease or increase in the ionic conductivity with

The selected properties of investigated samples $50R_2O\text{-}xB_2O_3\text{-}(50\text{-}x)P_2O_5$ (x= 5-25 mol %), R=Li, Na Table 1

Sample	**E^{DC}** [±0.01eV]	**σ_{dc}^{*}** [S/cm]	**E^{τ}** [±0.01eV]	**τ^{*}** [s]	**s^{*}**	**β^{Δ}**
50Li5B*	0.71	2.99×10^{-7}	0.68	1.28×10^{-5}	0.82	0.51-0.59
50Li15B*	0.62	2.09×10^{-6}	0.62	2.95×10^{-6}	0.9	0.52-0.6
50Li25B*	0.61	1.73×10^{-6}	0.61	2.31×10^{-6}	0.91	0.53-0.57
50Na5B*	0.76	1.63×10^{-8}	0.72	2.96×10^{-4}	0.87	0.58-0.65
50Na15B*	0.7	8.16×10^{-8}	0.67	5.98×10^{-5}	0.73	0.52-0.59
50Na25B*	0.67	1.31×10^{-7}	0.64	1.45×10^{-5}	0.5	0.53-0.57

* measured at 348 K, Δ evaluated for all measured temperatures

the change of glass former substance while keeping the modifier composition constant. The concentration of glass former was in the range from 5 to 25 mol% with two types of modifier ions (Li and Na) that allows us the study of the influence of the structure from the ionic radius point of view. For these two sets, electrical measurements were performed for various temperatures below T_g and frequency range form 10 Hz to 2 MHz. From conductivity investigation, the value of dc conductivities and activation energies for conduction were calculated for all samples. Dc conductivities vary from 2.99×10^{-7} S/cm to 1.73×10^{-6} S/cm for lithium borophosphate glasses and from 1.63×10^{-8} S/cm to 1.31×10^{-7} S/cm for sodium borophosphate glasses at 348 K. Furthermore, we can see the increasing character of conductivity with increasing concentration of B_2O_3. The activation energy decreases with increasing concentration of B_2O_3 in both series of composition, which is in accordance with previous structural studies in alkali borophosphate glasses [7]. The activation energies associated to dielectric loss were estimated from the imaginary part of electric modulus, and the both activation energies are supposed to be activated with similar activation energy.

Acknowledgment

The authors would like to thank to F. Cernobila for technical assistance. This study was supported by projects VEGA No. 1/0510/17. F. Muñoz thanks funding from project MAT2013-48246-C2-1-P from Ministerio de Economía y Competitividad (MINECO) of Spain.

References

[1] YUSUB, S., et al.: Ionic Conductivity, Dielectric and Optical Properties of Lithium Lead Borophosphate Glasses Combined with Manganese Ions. *Journal of Alloys and Compounds,* 663, 708-717, 2016.

[2] CHRISTENSEN, R., et al.: Ionic Conductivity of Mixed Glass Former $0.35Na_2O + 0.65[xB_2O_3 + (1 - x)P_2O_5]$ Glasses. *Journal of Physical Chemistry B,* 117, 16577-16586, 2013.

[3] THO, T. D., et al.: Structure Property Correlation in Lithium Borophosphate Glasses. *European Physical Journal E,* 35(8), 2012.

[4] YOON, Y., et al.: Characterization of Lithium Borophosphate Glass thin Film Electrolytes Deposited by FR-magnetron Sputtering for Mico-batteries. *Solid State Ionics,* 225, 636-640, 2012.

[5] NISHIKAWA, K., et al. Lidendrite Growth and Li^+ Ionic Mass Transfer Phenomenom. *Journal of Electroanalytical Chemistry,* 661, 84-89, 2011.

[6] KUMAR, S., et al.: Investigations of Structure and Transport in Lithium and Silver Borophosphate Glasses. *Journal of Solid State Chemistry,* 177, 1723-1737, 2004.

[7] MUNOZ, F., et al.: Composition and Structure Dependence of the Properties of Lithium Borophosphate Glasses Showing Boron Anomaly. *Journal of Non-Crystalline Solids,* 355, 2571-2577, 2009.

[8] MOGUS-MILANKOVIC, A., et al.: Lithium-Ion Mobility in Quaternary Boro-Germano-Phosphate Glasses. *Journal of Physical Chemistry,* 120, 3978-3987, 2016.

[9] MAGISTRIS, A., et al.: Lithium Borophosphate Vitreous Electrolytes. *Journal of Power Sources,* 14, 87-91, 1985.

[10] JONSCHER, A. K.: The Universal Dielectric Response. Annual Conference on Electrical Insulation and Dielectric Phenomena, USA, 23-40, 1990.

[11] HOCKICKO, P., et al.: Investigation of Acoustic and Electrical Properties of a $LiPO_3$ Metaphosphate Glass. *Communications-Scientific Letters of the University of Zilina*, 16(1), 45-49, 2014.

[12] KUDELCIK, J., et al.: The Dielectric Breakdown of Magnetic Fluids. *Communications- Scientific Letters of the University of Zilina,* 12(2), 34-37, 2010.

[13] MEENAKSHI, D., et al.: Temperature and frequency dependent conductivity and electric modulus formulation of manganese modified bismuth silicate glasses. *Journal of NonCrystalline Solids*, 423-424, 1-8, 2015.

https://doi.org/10.26552/com.C.2017.3.51-56

Jozef Kudelcik - Peter Bury - Stefan Hardon - Michal Sedlacik - Tomas Plachy*

ACOUSTIC INVESTIGATION OF THE STRUCTURE OF MAGNETO-RHEOLOGICAL FLUID

The acoustic spectroscopy is used to study properties and changes in structural arrangement in silicone oil based magneto-rheological fluids with carbonyl iron particles upon the effect of an external magnetic field. Attenuation spectra at three temperatures for various concentrations of magnetic particles are presented. The attenuation of acoustic waves was measured for a jump change of the magnetic field to 200 mT as a function of the temperature. The relaxation effects for the acoustic attenuation after switching off the magnetic field and its decrease to the similar value as for clean silicone oil were observed. The change of acoustic attenuation in magneto-rheological fluid versus angle between the wave vector of acoustic waves and direction of the applied magnetic field was measured, too. For the anisotropy measurement are characteristic two local maxima from which results chain orientation in direction of the magnetic field.

Keywords: *Particle structure, magneto-rheological fluid, acoustic spectroscopy, anisotropy.*

1. Introduction

Magneto-rheological (MR) fluids are defined as suspensions of magnetic particles in a carrier liquid with some additives to stabilize this smart system. The particles are of sizes between 1 to 10 microns. In the absence of an external magnetic field, MR fluids are reasonably well approximated as Newtonian liquids. A problem of these systems is the sedimentation due to the density difference between microparticles and carrier liquid. Surfactants are often added to delay the sedimentation process and re-disperse the particles easily [1, 2]. Their rheological properties (e.g. viscosity) are rapidly varied by applying the external magnetic field. Changes in their properties are caused by efficiency of magnetic microparticles polarization, affected further by shear conditions, magnetic field expressed herein in terms of magnetic flux density, ***B***, and its direction, structural and physicochemical characteristics of dispersed phase, volume concentration of magnetic particles, carrier liquid properties, stabilization components, as it was founded for the similar electrorheological fluids [3, 4]. When the external magnetic field is applied, a magnetic dipole moment is induced in the particles parallel to the magnetic field and as the result; particles tend to align forming ordered structures, giving rise to significant variations not only in viscosity but also in its inner order (particle rearrangement). In most engineering applications a simple Bingham plastic model is effective for describing the field-dependent fluid characteristics. So they can be applied in various fields of civil engineering, safety engineering, transportation and life science, in the design of brakes, dampers, clutches and shock absorbing systems [5 - 7].

The corrosion, oxidation, and abrasive properties of iron and iron alloys frequently used as optimal magnetic agents in MR fluids are, however, obstacles for their wider commercial usage. The modification of particle surface by chemical process has proven to be efficient to overcome this problem [6, 8]. The improvement of properties of MR fluids by plasma-enhanced chemical vapour deposition of octafluorocyclobutane onto carbonyl iron (CI) particles using rotary plasma reactor was used in work [8]. The results revealed successful fluorination of CI particles with a maximum of fluorine content of 2.9 %. The fluoropolymer film fabricated onto particles improved their corrosion protection and friction properties by 40 %. Amorphous alloy particles can be used instead of the traditional CI particles as the dispersed phase to prepare amorphous based MR fluid [Dong6]. The amorphous particles have larger magnetization intensity and permeability at lower field intensities as well as lower density. MR performance and sedimentation stability are better in the MR fluid based on amorphous particles than that based on conventionally used CI particles. Magneto-rheological fluids exhibit some advantages over typical electrorheological (ER) materials. In contrast to ER materials, MR fluids are more useful because the change in their rheological properties is more pronounced compared to ER fluids,

---

* **[1]Jozef Kudelcik, [1]Peter Bury, [1]Stefan Hardon, [2]Michal Sedlacik, [2]Tomas Plachy**
[1]Department of Physics, University of Zilina, Slovakia
[2]Centre of Polymer Systems, University Institute, Tomas Bata University in Zlin, Czech Republic
E-mail: kudelcik@fyzika.uniza.sk

i.e. an increase of yield stress is 20-55 times higher [5]. There are also electro-magneto-rheological fluids, which consist of particles responsive to both electric and magnetic fields. The results from the molecular dynamic simulation studies have shown that under these fields various types of structural formation and transition between them can exist [9].

The fluids with microstructure and particle aggregation are studied using optical measurements [1, 10], the dielectric spectroscopy [11 - 14] and also there are a few works using ultrasonic techniques [15, 16]. These ultrasonic techniques are appearing advantageous when the number of particles is high and optical observation becomes difficult. Some aspects of the acoustic behavior between magnetic fluids (MF) and MR fluids were compared and in other work properties such as the anisotropic effect and hysteresis when a uniform magnetic field is applied were studied. It should be noted that the theories describing action of magnetic field on mechanism of acoustic wave interaction with structure in colloidal fluids are not well developed and there are not experimental data reliable enough on this problem. The former theories were created only for diluted dispersive mediums and did not take into account very important processes of the internal ordered structures from magnetic particles formation in the fluid, volume and interaction of particles and its aggregates at the boundary. Currently, there are only few papers involved in the acoustic properties of MR fluids as studied in this work. One of them is work by Baev, et all. [3], who made similar acoustic measurement for higher concentration of magnetic particles, but with different type of MR fluid. Data analysis confirmed dependence of the sound velocity and the acoustic attenuation on the magnitude and direction of magnetic field in MR fluid. Their measurement also showed that interparticle interactions also depend on the processes in the interface boundary.

Many other works are focused on the structural changes in MF with magnetic nanoparticles by the influence of the magnetic field using the acoustic spectroscopy [3, 7, 17 - 20]. The diameters and magnetic moments of magnetic nanoparticles in stable colloidal solutions are much lower than in MR fluids. Under the effect of the magnetic field, the nanoparticles within MF become arranged into oligomers, chains or clusters. The propagation of the acoustic wave in MF and change of acoustic attenuation by magnetic field was studied by several authors both theoretically and experimentally [20 - 22].

2. Experiment

Carbonyl iron particles (HQ grade, BASF, Germany) were used for preparation of MR fluid, which was investigated by acoustic methods. The main material characteristics of CI particles with HQ grade according to the manufacturer are following: spherical shape of particles with the average size of about 1 μm, non-modified surface, and content of α-iron >97%. Carbonyl iron particles are soft magnetic particles since their increasing and decreasing branches of the hysteresis cycles are hardly distinguishable, the magnetization saturation in the field of 777 $kA \cdot m^{-1}$ is 174 $emu \cdot g^{-1}$. The MR fluids with the particle concentration of 1 and 2 wt.% in silicone oil - Lukosiol M50 [23] were prepared. Figure 1 shows the size and surface morphology of CI particles employed as a dispersed phase in MR fluid under investigation. All the particles are evidently of a spherical shape with the average size of about 1 μm confirming the manufacturer data.

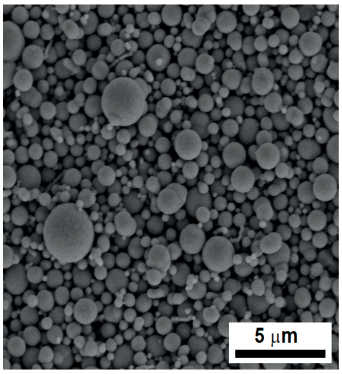

Fig. 1 SEM image of CI particles under investigation

The ultrasound spectrometer DT-100, as the first acoustic method, was used for the characterization of MR fluids (Fig. 2). In addition to the acoustic sensor, probes to measure the temperature and pH are incorporated. The controller box sent a high frequency signal, which was transferred from the deep-seated sender into an ultrasound wave by means of a piezo transducer. The frequency range of the DT-100 is 1-100 MHz and the gap between sound-sender and - detector is variable from 0.1 to 21 mm. The wave was attenuated in the MR fluid and the signal was detected by the receiver at the opposite ultrasound transducer and used for the particle size analysis. The principle of measurement is the so called „tone-burst“-method: short wave packets with a very narrow frequency distribution and a few numbers of oscillation cycles are sent through the dispersion chamber (Fig. 2) filled with the MR fluid. Sound attenuation and - speed are measured by detecting signal attenuation and - delay: The program using experimental data and integrated modern theories allows the determination of particle sizes in the range of 5 nm to 1000 μm at a concentration range of 1 to 50 vol.% [24].

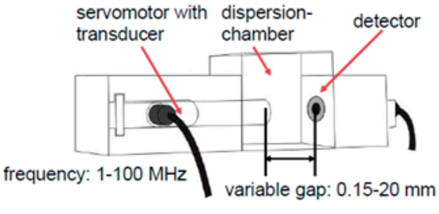

Fig. 2 The principal scheme of ultrasound spectrometer DT 100 [25]

An ultrasound wave, which is transmitting through a liquid dispersion, is attenuated with the increasing path length. Basically, there are three effects responsible for this: intrinsic absorption, dissipative absorption (visco-inertial, thermal and structural effects) and sound scattering. After measuring the acoustic attenuation spectrum, the theoretical fit-spectrum is automatically adapted to the measured spectrum. The particle size distribution is based on the calculated best fit-parameters. The used model for the calculation or the combination of the models depends on the type of the dispersed phase(s). In our case for fine particles (< 5 μm) just the dissipative mechanism is important. In case of rigid particles (e.g. ceramics, metals), only the visco-inertial effect will be considered [25].

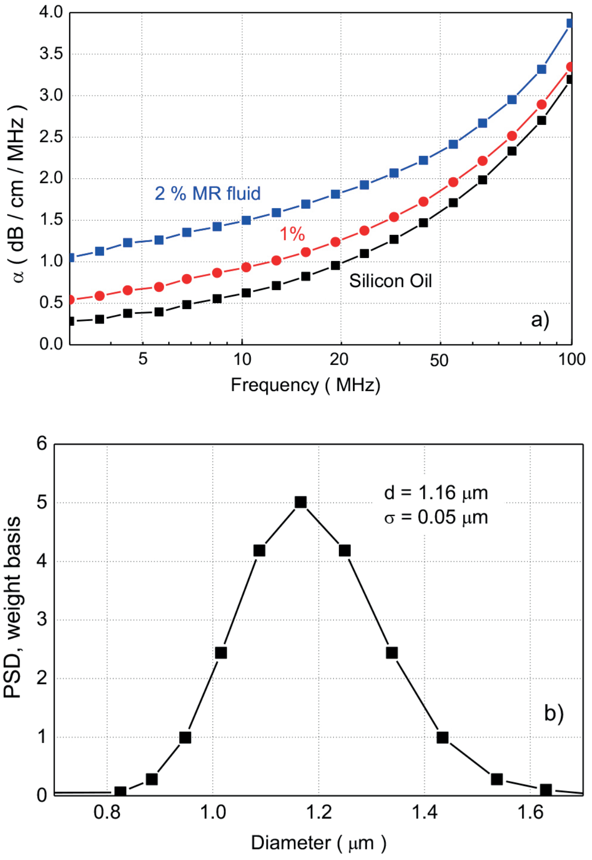

Fig. 3 a) Attenuation spectra measured for MR fluids and silicone oil; b) Size distribution of 2 % wt. MR fluid at 20 °C (d- mean diameter of magnetic nanoparticles, σ - standard deviation)

Two different concentrations (1 and 2 wt.%) of MR fluid based on silicone oil LUKOSIOL M50 with microscale particles carbonyl iron of HQ grade were measured. The samples were analysed regarding their attenuation spectra with stirring with external motor. All measurements were repeated twice in order to test the stability of the sample in the limits of the measurement period. The measured attenuation spectra are given in Fig. 3a). Beyond the intrinsic attenuation spectrum of pure silicon oil is shown. All dispersions are stable in the limits of the measurement period. The measurements were also made for various temperatures. Attenuation of all samples slightly decreased with increasing temperature. The main attenuation effect, which plays a role here due to the small size of the particles, is the viscous effect. The attenuation for MR fluid is higher because micro-particles cause additional dissipative attenuation by structural effect. The particle size distribution (PSD) for 2 wt.% MR fluid is presented in Fig. 3b). The diameter of carbonyl iron particles calculated from measured distribution agrees with the manufacturer data.

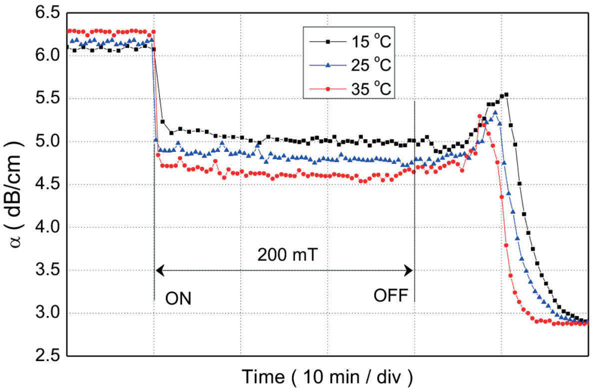

Fig. 4 Experimental data of the changes of acoustic attenuation for a jump change of the magnetic field to 200 mT at various temperatures for 2 wt.% MR fluid

The second acoustic method was used for the study of structural changes occurring during the application of external magnetic field. The experimental equipment used for this type of measurement was the same as in our previous works [26, 27]. The frequency of the ultrasonic wave was 4.9 MHz with pulse length 0.6 μs. The changes in the ultrasonic wave attenuation were measured by the pulse method based on measurement of intensity of the ultrasonic pulse passed through or reflected by the medium studied. The MR fluid was placed in the thermostated closed measuring cell (1.5 x 0.9 x 1 cm^3, temperature stabilization with an accuracy ±0.1 °C by JULABO Refrigerated & Heating Circulators F25-HE) and the distance between two piezoelectric transducers was 9 mm.

Figure 4 presents the changes of acoustic attenuation for a jump change of the magnetic field to 200 mT for 2 wt.% MR fluid at 15 °C, 25 °C, and 35 °C, respectively. The given value of magnetic field was kept constant during next 30 min. As can be seen from the measured development, the change of acoustic attenuation follows immediately the step change of the magnetic field and after a few minutes the acoustic attenuation was stable. The developments are almost the same, only with the increase of the temperature smaller stabilized values can be observed. After the magnetic field was switched off, the value of acoustic attenuation did not change during next 5 min. After this time the acoustic attenuation increased and then it exponentially decreased with time constant of about 500 s. The value of acoustic attenuation decreased during next minutes to the value as was measured for clean silicone oil.

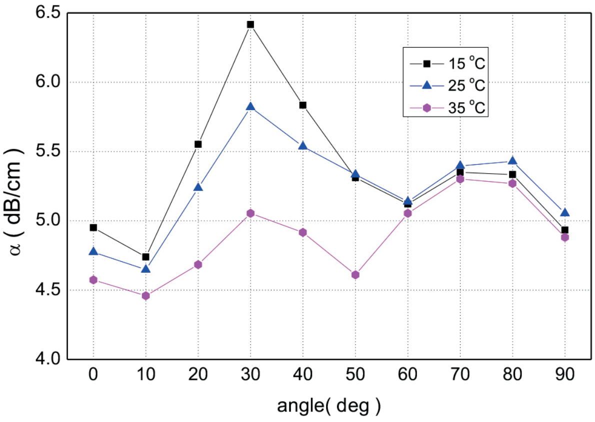

Fig. 5 Anisotropy measurement of the acoustic attenuation at constant magnetic field of 200 mT for 2 wt.% MR fluid at various temperatures

Figure 5 illustrates the anisotropy of acoustic attenuation within the 2 wt.% MR fluid at constant value of magnetic field applied (200 mT) studied in the dependence on the angle ϕ between wave vector $\boldsymbol{k}$ and the magnetic field $\boldsymbol{B}$ measured for three different temperatures. The results indicate an effect of the angle on the acoustic attenuation within the MR fluid. The development of the anisotropy depends on the temperature, but for all cases it has similar characteristics. The acoustic attenuation firstly slowly decreases and then it increases to the angle 30°, where is the first local maximum. With the next increase of the angle attenuation decreases and it again increases to the second local maxima at the angle around 75°. The value of this local maximum is independent of the temperature. Finally, in perpendicular orientation of the magnetic field and the wave vector of acoustic wave, the acoustic attenuation decreases to the value which is slightly higher than for parallel orientation.

Interesting phenomena was observed when the magnetic field was switched off after anisotropy measurement. The time of the application of magnetic field during this type of measurement was more than 150 min. In this case for each temperature the immediate decrease of acoustic attenuation to value as for clean silicone oil was observed. There was no relaxation time as is observed for the results present in Fig. 4 when the magnetic field was applied only 30 min.

3. Discussion

The study of MR fluids by the acoustic spectroscopy provides important information about their properties and structures. The mean diameter determined by acoustic spectrometer DT-100 agrees with manufacture data quite well. The acoustic attenuation at frequency 4.9 MHz is the same as from the second method used for study of structural changes of MR fluid in the presence of magnetic field. Thus, the acoustic spectroscopy is a very useful method for studying the structure changes occurring in MR fluids, which are the result of the interaction between the magnetic field applied and the magnetic moment of the microparticles generated by this field. These structures enlarge with the magnetic field and this process has the influence on the value of the acoustic attenuation. Similar results were observed also in works [17, 20 - 22] for MF with nanoparticles.

Magneto-rheological fluids contain microparticles which have chaotic distribution in fluid as depicted in Fig. 6a. In the presence of an external magnetic field, the particles acquire a dipole moment aligned with the field causing the particles can form linear chains aligned in direction with the external magnetic field. (Fig. 6b). This arrangement is confirmed by other measurements [5, 7, 16] where the degree of change is related to the magnitude of the applied magnetic field, and can occur in a time scale of a few milliseconds. The similar quick effect on the acoustic attenuation after the application of magnetic field was observed (Fig. 4). After the immediate change of the acoustic attenuation, the next development depends on the magnitude of applied field and concentration. In the case of 2 wt.% MR fluid for 100 mT and higher values the stable state or the constant value of acoustic attenuation during the whole time of application of magnetic field was observed [27]. This stable arrangement of microparticles is the result of higher numbers of particles, thus produce stable chains. From the realized experiment it can be seen that for all temperatures stable value of acoustic attenuation was observed.

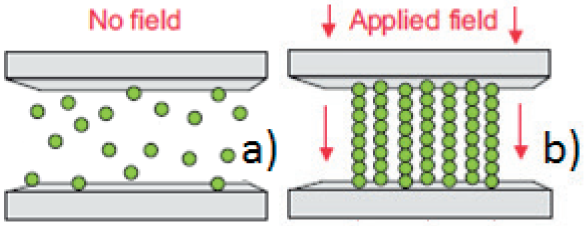

Fig. 6 MR fluid model without (a) and under (b) the magnetic field applied

After switching off the magnetic field, a few interesting effects were observed. The first of them is that no significant changes in the relative long time lasting acoustic attenuation were noted during 5 min. This effect could be described by a long lifetime, times of chains and an interaction of dispersive phase on the boundary fluid-transducer. The second effect is suddenly increased of the acoustic attenuation after switching the magnetic field off. This can be the result of slowly chaotic rotation of chains during the process of sedimentation, what causes the increase of acoustic attenuation. The last one is the decrease of acoustic attenuation to the value as for clean silicone oil. It can be supposed that this effect is caused by the sedimentation of particles. The process of sedimentation for MF has not been observed since the mass of nanoparticles or created structures is much smaller than the mass of microparticles used in MR fluids. Very interesting phenomena was the immediate decrease of acoustic attenuation after anisotropy measurements, when the magnetic field was switched off. This means that long time application of the magnetic field to static MR fluids created stable big chains which sediment considerably without the magnetic field.

The anisotropy of acoustic attenuation was measured for three temperatures (15 °C, 25 °C and 35 °C) in constant magnetic field of 200 mT (Fig. 5). As it can be seen from the results, there is the significant effect of the angle between the magnetic field and the wave vector on the acoustic attenuation what is coupled with the process of chains orientation along the direction of magnetic field. Evidently, there are two local maxima at angles 30° and 75°, as can be observed from the anisotropy measurements result. The first local maximum is dependent on the temperature, while the other is not. It should be noted that the anisotropy measurements of MR fluid of the acoustical properties on B and φ are similar to the dependencies obtained when MF has instable structure or subjected before to the magnetic field during some days [3, 26]. In MF case, sizes of the formed aggregates of particles are relatively close to particles or aggregates which are in MR fluid. Dynamic effects caused by complicated interaction of magnetic field with such structure – large chains or big clusters may initiate a new non-local mechanism of relaxation processes, like the peculiarities of dipole–dipole interaction, magnetostriction and some other effects. These effects explain why two local maxima were observed. The first one is mainly connected with more complex structures (the influence of translational vibrations and rotational degrees of freedom of structures [20, 22]) which further decreases with temperature. Number of microparticles involved into structures decrease with the increasing temperature, so the attenuation is smaller. The second maxima could be connected with the above relaxation processes. The acoustic attenuation is also slightly higher for perpendicular orientation as for parallel orientation. This could be caused by higher possibility of oscillation of the individual particles or clusters in perpendicular orientation to the chain, as in the direction of the chain.

4. Conclusions

The methods of acoustic spectroscopy to determine parameters of MR fluid and its structural change in the magnetic field were used. The acoustic attenuation in a frequency range from 3 to 100 MHz and particle size distribution of MR fluids by the ultrasound spectrometer DT-100 were measured. Magnetorheological fluids immediately create stabilized structures – chains after the application of an external magnetic field, which are mainly the result of the interaction of microparticles magnetic moments with the field. This phenomenon was confirmed by the jump change of the magnetic field to 200 mT at various temperatures. The slow change on decrease of acoustic attenuation to the similar value as for clean silicone oil after switching the magnetic field off was caused by sedimentation. The study of the anisotropy of acoustic attenuation showed also the importance of the orientation of magnetic field in the MR fluids structure. For better describing dependencies between acoustical and structural parameters of MR fluid, it is necessary to know not only the peculiarities of interaction between microparticles and chains and internal field but also to determine the mechanism of interaction of dispersive phase on the boundary fluid–solid and relaxation processes.

Acknowledgment

This work was supported by project VEGA 1/0510/17 and ITMS: 26210120021, co-funded from EU sources and European Regional Development Fund. This work was supported by the Ministry of Education, Youth and Sports of the Czech Republic – Program NPU I (LO1504).

References

[1] RODRIGUEZ-LOPEZ, J., SEGURA, L. E., ESPINOSA-FREIJO, F. M.: Ultrasonic Velocity and Amplitude Characterization of Magnetorheological Fluids under Magnetic Fields. *Journal of Magnetism and Magnetic Materials,* 324, 222-230, 2012.

[2] BOSSIS, G., LACIS, S., MEUNIER, A., VOLKOV, O.: Magnetorheological Fluids. *Journal of Magnetism and Magnetic Materials*, 252, 224-228, 2002.

[3] BAEV, A. R., KOROBKO, E. V., NOVIKAVA, Z. A.: Acoustical Properties of Magnetorheological Fluids under Applied Magnetic Field. *Journal of Intelligent Material Systems and Structures*, 26(14), 1913-1919, 2015.

[4] KOROBKO, E. V., NOVIKOVA, Z. A., SERMYAZHKO, E. S., MURASHKEVICH, A. N., ESHENKO, L. S.: Time Stability Studies of Electrorheological Response of Dispersions with Different Types of Charge Carriers. *Journal of Intelligent Material Systems and Structures,* 26(14), 1782-1788, 2015.

[5] BARANWAL, D., DESHMUKH, T. S.: MR-Fluid Technology and Its Application - A Review. *International Journal of Emerging Technology and Advanced Engineering*, 2(12), 563–569, 2012.

[6] DONG, X., MA, N., QI, M., LI, J., GUAN, X., OU, J.: Properties of Magneto-Rheological Fluids Based on Amorphous Micro-Particles. *Transactions of Nonferrous Metal Society of China*, 22, 2979-2983, 2012.

[7] KCIUK, M., TURCZYN, R.: Properties and Application of Magnetorheological Fluids, *Journal of Achievements in Materials and Manufacturing Engineering*, 18(1-2), 127-130, 2006.

[8] SEDLACIK, M., PAVLINEK, V., LEHOCKY, M., JUNKAR, I., VESEL, A.: Plasma-Enhanced Chemical Vapour Deposition of Octaflourocyclobutane onto Carbonyl Iron Particles. *Materiali in Tehnologije*, 46(1), 43-46**,** 2012**.**

[9] WANG, Z., FANG, H., LIN, Z., ZHOU, L.: Dynamic Simulation Studies of Structural Formation and Transition in Electro-Magneto-Rheological Fluids. *International Journal of Modern Physics B*, 15(6, 7), 842-850, 2001.

[10] MELLE, S., CALDERON, O. G., RUBIO, M. A., FULLER, G. G.: Microstructure Evolution in Magnetorheological Suspensions Governed by Mason Number. *Physical Review E*, 68(4), 041501–041511, 2003.

[11] HOCKICKO, P., BURY, P., MUNOZ, F., MUNOZ-SENOVILLA, L.: Investigation of Acoustic and Electrical Properties of a $LiPO_3$ Metaphosphate Glass. *Communications - Scientific Letters of the University of Zilina*, 16(1), 45-49, 2014.

[12] MUNOZ-SENOVILLA, L., BIRESOVA, J., HOCKICKO, P., MUNOZ, F.: Investigation of the Relationships between Acoustic Attenuation and Ionic Conduction of Metaphosphate Glasses. *Journal of Non-crystalline Solids,* 440, 26-30, 2016.

[13] KOLTUNOWICZ, T. N., et al.: Study of Dielectric Function of (FeCoZr)(x)(CaF2)((100-x)) Nanocomposites Produced with a Beam of Argon Ions. *Journal of Alloys and Compounds*, 650, 262-267, 2015.

[14] RAJNAK, M., TIMKO, M., KOPCANSKY, P., PAULOVICOVA, K., TOTHOVA, J., KURIMSKY, J., DOLNIK, B., CIMBALA, R., AVDEEV, M.V., PETRENKO, V.I., FEOKTYSTOV, A.: Structure and Viscosity of a Transformer Oil-Based Ferrofluid under an External Electric Field. *Journal of Magnetism and Magnetic Materials*, 431, 99-102, 2017.

[15] BRAMANTY, M. A., MOTOZAWA, M., TAKUMA, H., FAIZ, M., SAWADA, T.: Experimental Analysis of Clustering Structures in Magnetic and MR Fluids using Ultrasound. *Journal of Physics: Conference Series,* 149, 012040, 2009.

[16] BRAMANTY, M. A., MOTOZAWA, M., SAWADA, T.: Ultrasonic Propagation Velocity in Magnetic and Magnetorheological Fluids Due to an External Magnetic Field. *Journal of Physics: Condensed Matter*, 22, 324102, 2010.

[17] PATEL, J. K., PAREKH, K.: Effect of Carrier and Particle Concentration on Ultrasound Properties of Magnetic Nanofluids. *ULTRASONICS*, 55, 26-32, 2015.

[18] ODENBACH, S.: Ferrofluids-Magnetically Controlled Suspensions. *Colloids and Surfaces A: Physicochemical and Engineering Aspects,* 217, 171-178, 2003.

[19] ROZYNEK, Z., et al.: Structuring from Nanoparticles in Oil-Based Ferrofluids. *European Physics Journal E*, 34(3), 2011.

[20] HORNOWSKI, T., JOZEFCZAK, J., KOLODZIEJCZYK, B., TIMKO, M., SKUMIEL, A., RAJNAK, M.: The Effect of Particle Aggregate Shape on Ultrasonic Anisotropy in Concentrated Magnetic Fluids. *Journal of Physics D: Applied Physics*, 48(17), 175303, 2015.

[21] KUDELCIK, J., BURY, P., KOPCANSKY, P., TIMKO, M.: Temperature Effect on Anisotropy of Acoustic Attenuation in Magnetic Fluids Based on Transformer Oil. *Communications – Scientific Letters of the University of Zilina*, 16(1), 33-38, 2014.

[22] SKUMIEL, A.: The Effect of Temperature on the Anisotropy of Ultrasound Attenuation in a Ferrofluid. *Journal of Physics D: Applied Physics*, 37(22), 3073, 2004.

[23] [Online]. Available: https://www.stavochemie.cz/tl/LZK_TL_Lukosiol.pdf.

[24] Technical Papers of QUANTACHROME: PARTICLE WORD*,* Edition 3, 2009 [online]. Available: internet: http://www.quantachrome.de/4129-bD1lbg-/de/Home/home.html.

[25] DUKHIN, A. S., GOETZ, P. J.: *Characterization of Liquids, Nano- and Microparticulates, and Porous Bodies using Ultrasound*. ELSEVIER, New York, p. 503, 2002.

[26] KUDELCIK, J., BURY, P., DRGA, J., KOPCANSKY, P., ZAVISOVA, V., TIMKO, M.: Comparison of Theories of Anisotropy in Transformer Oil-Based Magnetic Fluids. *Advances in Electrical and Electronic Engineering*, 11(2), 147-155, 2013.

[27] KUDELCIK, J., BURY, P., HARDON, S., SEDLACIK, M., MRLIK, M.: *Study of Structural Changes in Magneto-Rheological Fluids by Acoustic Spectroscopy*. *ELEKTRO* 2016, Slovakia, 624-627, 2016.

https://doi.org/10.26552/com.C.2017.3.57-61

Stanislav Jurecka - Maria Jureckova*

STATISTICAL AND FRACTAL ANALYSIS OF RANDOM HEIGHT FUNCTION

Nanostructured semiconductor surfaces are commonly used for suppression of the light reflection. We prepared several kinds of surface structures on silicon substrate and analyzed the properties of the random height function used for the description of observed surface morphology. Statistical and fractal methods used in this analysis provide useful information for the optimization of the surface forming procedure. Multifractal analysis provides additional information about the surface morphology, not contained in the results of standard statistical methods. Numerical procedures used in the multifractal analysis were tested by using theoretical random height function created from large sets of Cantor numbers.

Keywords: *Multifractal analysis, statistical methods, semiconductor structures.*

1. Introduction

The properties of microstructure play an important role in fabrication of electronic and photonic devices, especially in solar cells [1]. In order to decrease the reflection losses and increase the absorption probability by light trapping in the solar cell structure random pyramidal textures are usually prepared at the semiconductor surface [2 - 8]. Pyramidal texture is formed by etching of the silicon surface and contains a large variety of surface shapes depending on the technological treatment. For characterization of the pyramidal surface morphology, the random height function $h(x,y)$ describing the height of atom above the reference plane at position (x,y) can be used. The characteristics of the random height function are visually apparent but not sufficiently described by conventional measures like mean value or standard deviation. The values of the random height function $h(x,y)$ can be experimentally obtained by the electron microscopy or by the scanning probe methods with atomic resolution [9, 10]. Experimental values of $h(x,y)$ posses a scale invariant structure. The particular kind of scale invariant structure in the experimental data $s(x)$ is defined by the power exponent H in an equation for scaling of observed data $s(cx) = c^H s(x)$. The complex shape of the random height function can be described by the fractal methods in this case [11 - 14]. The variations in scale invariant structure can be often observed in the experimental surface images. This indicates a multifractal structure of scanned surface image that is defined by a multifractal spectrum of power law exponents rather than a single power law exponent for monofractal.

In this paper we describe results of statistical and multifractal analysis of theoretical surface generated by using Cantor numbers [15] as well as the random height function of real semiconductor structures, observed with atomic resolution.

2. Multifractal analysis

For the description of the random height function properties the multifractal singularity spectrum $f(\alpha)$ and generalized fractal dimension D_q can be used. The box-counting method is often used for the multifractal analysis studied structure. The observed surface is divided into square areas with the size of side ε. In a selected area the probability measure is defined by

$$P_i(\varepsilon) \sim \varepsilon^{\alpha_i} \tag{1}$$

where α_i is singularity exponent. If $N(\alpha)$ is the number of surface areas in which P_i has singularity α_i in an interval $\alpha_i \in (\alpha, \alpha + d\alpha)$, then multifractal singularity spectrum $f(\alpha)$ is defined by equation

$$N(\alpha) \sim \varepsilon^{-f(\alpha)} \tag{2}$$

---

* [1]**Stanislav Jurecka,** [2,3]**Maria Jureckova**
[1]Institute of Aurel Stodola, University of Zilina, Liptovsky Mikulas, Slovakia
[2]Mathematical Institute, Slovak Academy of Sciences, Bratislava Slovakia
[3]Catholic University in Ruzomberok, Slovak Republic
E-mail: jurecka@lm.uniza.sk

Function $f(\alpha)$ can be interpreted as the fractal dimension of surface areas with singularity α. This definition is connected with the multifractal measure described by the multifractal singularity spectrum.

For the characterization of multifractal properties of the studied surface generalized fractal dimension D_q can be alternatively used. The *q-th* moment of the P_i measure is defined by the equation

$$D_q = \frac{1}{q-1} \lim_{q \to 0} \frac{\log \sum_i P_i(\varepsilon)^q}{\log \varepsilon} \tag{3}$$

In case when D_q does not depend on q then the studied surface $h(x,y)$ is monofractal. By using the Legendre transformation we obtain relation of $f(\alpha)$ and D_q in form

$$f(\alpha) = \alpha q - (q-1) D_q \tag{4}$$

For $q = 0$ we obtain Hausdorff fractal dimension

$$D_0 = -\lim_{q \to 0} \frac{\log N}{\log \varepsilon} = \lim_{q \to 0} \frac{\log N}{\log 1/\varepsilon} \tag{5}$$

By using L'Hospital's rule we obtain for $q = 1$

$$\begin{aligned} D_1 &= \lim_{q \to 1} \frac{1}{q-1} \lim_{\varepsilon \to 0} \frac{\log \sum_i P_i^q}{\log \varepsilon} = \\ &= \lim_{\varepsilon \to 0} \lim_{q \to 1} \frac{\sum_i P_i^q \log P_i}{\log \varepsilon \sum_i P_i^q} = \lim_{\varepsilon \to 0} \frac{\sum_i P_i \log P_i}{\log \varepsilon} \end{aligned} \tag{6}$$

Dimension D_1 corresponds to the entropy or information dimension. Lower value of D_1 indicate higher disorder of observed random height function $h(x,y)$.

For $q = 2$ we obtain correlation dimension

$$D_2 = \lim_{\varepsilon \to 0} \frac{\log P_i(\varepsilon)^2}{\log \varepsilon} \tag{7}$$

suitable for an identification of the surface homogeneity. The higher degree of the surface homogeneity, the higher value of D_2 is observed [12, 13, 16, 17].

3. Results and discussion

For analysis of multifractal properties of the $h(x,y)$ function, we generated theoretical surface by using Cantor numbers. We determined values of the $h(x,y)$ function by random selections from large Cantor sets $C(n)$. Cantor sets were constructed by dividing of unit interval into three subintervals ($C(3)$), five ($C(5)$), seven ($C(7)$) and nine subintervals ($C(9)$). By the random selection (with uniform distribution) from these Cantor sets the different $h(x,y)$ functions representing surface areas of various size were constructed. Random surface generated by this way is shown in Fig. 1.

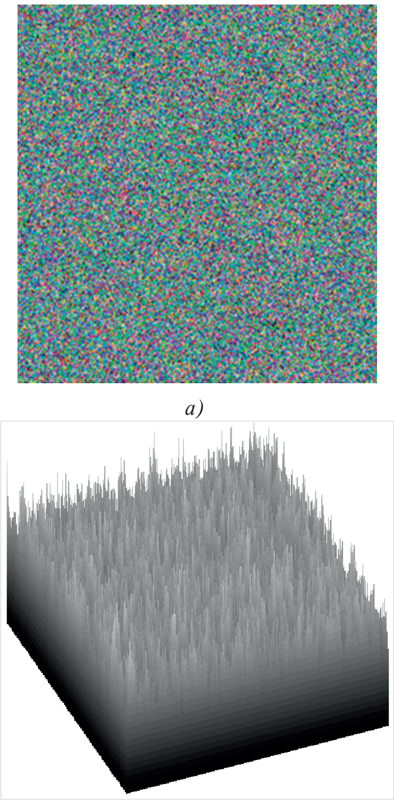

a)

b)

Fig. 1 Random height function generated from Cantor set numbers C(3); a) 2D plot, b) 3D plot

For computation of the P_i in (Equation 1) we used the box-counting method

$$P_{ij} = \frac{h_{ij}}{\sum h_{ij}} \tag{8}$$

where h_{ij} is the mean value of the $h(i,j)$ function in the box $box(i,j)$. By using this probability we computed generalized fractal dimension D_q (Equation 3) and multifractal spectrum $f(\alpha)$ (Equation 4). The results of developed numerical procedures show expected behaviour for multifractal structures of theoretical Cantor test surfaces and were used for analysis of real semiconductor surfaces. In Fig. 2 two distributions of pyramidal textures formed on flat silicon surface are shown. In pyramidal structure d1 a quasi homogeneous distribution of pyramidal shapes was formed whereas in structure d2 dominant fraction of small pyramids with random occurrence of very high pyramids was created.

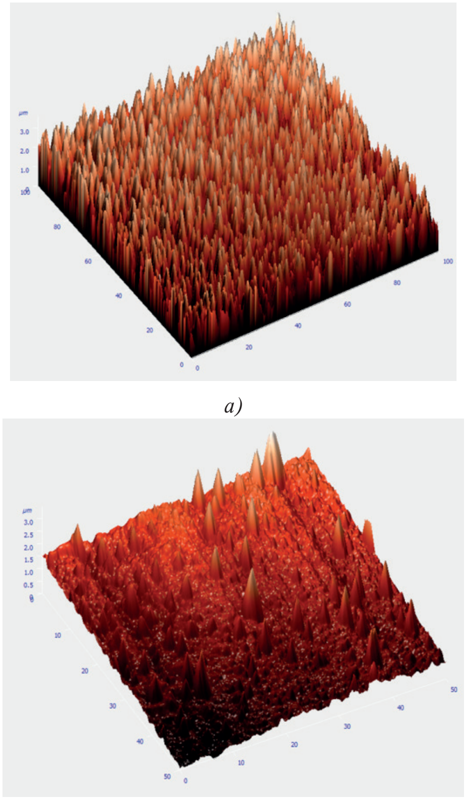

a)

b)

Fig. 2 Pyramidal structures prepared on Si surface:
a) distribution d1, b) distribution d2

Statistical characteristics of the random height function $h(i,j)$ values obtained by the atomic force microscopy experiment for these pyramidal structures are shown in Table 1.

Statistical characteristics of the experimental random height function Table 1

Distribution		d1	d2
Max	nm	2946.51	2206.76
Peek-to-peek S_y	nm	2946.51	2206.76
10-point height S_z	nm	1483.12	1069.98
Average roughness S_α	nm	1417.75	664.146
Mean square roughness S_q	nm	461.827	146.431
Coefficient of variation S_q/S_α		0.326	0.22
Skewness S_{sk}		0.154	2.467
Kurtosis S_{ku}		-0.389	11.761

The values of these statistical characteristics can be used in study of the surface roughness properties. Coefficient of variation is a relative measure of variability between structures with different averages. For distribution d1 this indicates higher surface roughness. Higher value of the skewness for distribution d2 is influenced by higher inhomogeneity of the pyramidal shapes in this distribution (dominant fraction of small pyramids). Negative value of kurtosis for distribution d1 shows low influence of different pyramidal shapes onto the statistical properties of d1 distribution and high value of kurtosis for distribution d2 indicates the presence of abnormally high pyramidal shapes at observed surface.

Statistical analysis provides useful information about the random height function properties. Supplementary information can be obtained by using multifractal methods. In Fig. 3 results of multifractal analysis of four pyramidally textured surfaces are shown.

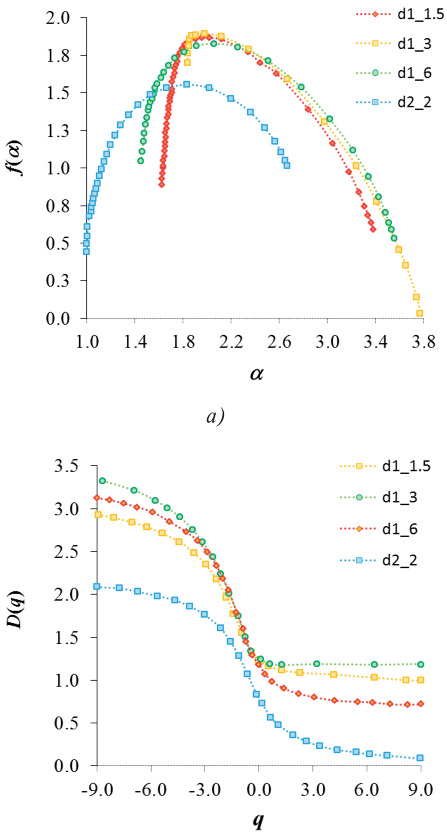

a)

b)

Fig. 3 Results of multifractal analysis of pyramidal texture with maximal heights of pyramids 1.5, 1.3, 1.6, and 2.2 μm:
a) multifractal singularity spectrum f(α),
b) generalized fractal dimension D(q)

We analyzed distributions d1 and d2 where maximal height of the pyramid equals 3 μm and we studied also distribution d1 with maximal height of pyramidal shapes 6 μm and 1.5 μm. Generalized fractal dimension D_q curves show decreasing trend significant for multifractal surface morphology. In plot of the D_q curves we observe important difference between characteristics for d1 and d2 distribution. Surface structure d2 has significantly lower D_q values in comparison to homogeneous distribution d1 for all q values. Value of dimension D_0 connected with traditional fractal dimension is very similar for all pyramidal distributions (with different heights of pyramids). On the other side significant differences can be seen in comparison of distributions d1 and d2. Lower value of dimension D_1 for distribution d2 indicates higher disorder in this pyramidal distribution (higher randomness) in comparison to d1 distribution. Maximal value of the correlation dimension D_2 indicates the highest homogeneity of the observed surface.

Multifractal characteristics are therefore very sensitive to small changes in the surface height function and in the distribution of pyramidal shapes. Different shapes of the D_q curves enable us to distinguish reliably between the properties of different distributions d1 and d2 as well as between small changes in the same distribution of pyramidal shapes (for example, for distributions type d1 with different heights of pyramids). The obtained results can be therefore used for the optimization of technological steps of surface texture forming procedure.

Multifractal singularity spectrum $f(\alpha)$ has concave shape typical for multifractal morphology. The maximal height of the $f(\alpha)$ spectrum is given by the D_0 value and the width of $f(\alpha)$ spectrum corresponds to the variability of shapes of the morphological objects. Symmetry of the $f(\alpha)$ curve is different for distribution d2, which indicates higher non-uniformity of distribution d2 in comparison to distribution d1.

In Fig. 4 multifractal spectrum $f(\alpha)$ curves for thin nanocrystalline layers formed by etching of silicon surface in the HF acid in contact with the Pt electrode are shown.

The analyzed structures were etched for 10, 20, and 30 seconds and values of the random height function were obtained by the scanning electron microscope with magnification 2000. From the shape of $f(\alpha)$ curves we can see, that the surface morphology develops primarily in the first stages of etching procedure (during the first 20 seconds). With the prolongation of etching time the development of surface morphology stabilizes.

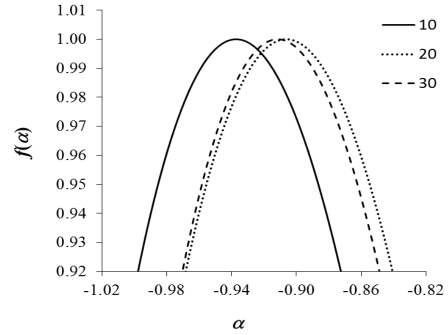

Fig. 4 Multifractal spectrum f(α) curves of the nanocrystalline Si layers

4. Conclusions

Statistical and multifractal analysis provides information about the shape of morphological objects development as well as about the intensity of modification of treated surface morphology. Multifractal analysis is a suitable tool for study of the random height function properties, providing additional information about the surface morphology, not contained in the results of standard statistical methods.

Acknowledgements

This work was supported by grant of Science and Technology Assistance Agency APVV-15-0152, Scientific Grant Agency VEGA 2/0031/15 and VEGA 1/0076/15, Centre of Excellence of Power Electronics Systems and Materials II - ITMS 26220120046, project ITMS 26210120021, and Japan Society for the Promotion of Science.

References

[1] MULLEROVA, J., SUTTA, P., JURECKA, S.: Thin Film Silicon in Photovoltaics: The Role of Structure and Microstructure. *Communications - Scientific Letters of the University of Zilina,* 8(1), 5-9, 2006.

[2] ANGERMANN, H., RAPPICH, J., KORTE, L., SIEBER, I., CONRAD, E., SCHMIDT, M., HUBENER, K., POLTE, J., HAUSCHILD, J.: Wet-Chemical Passivation of Atomically Flat and Structured Silicon Substrates for Solar Cell Application. *Applied Surface Science*, 254, 3615-3625,2008.

[3] ANGERMANN, H., CONRAD, E., KORTE, L., RAPPICH, J., SCHULZE, T. F., SCHMIDT, M.: Passivation of Textured Substrates for a-Si:H/c-Si Hetero-junction Solar Cells: Effect of Wet-Cchemical Smoothing and Intrinsic a-Si:H Interlayer. *Materials Science and Engineering: B*, 159-160, 219-223, 2009.

[4] STEGEMANN, B., KEGEL, J., MEWS, M., CONRAD, E., KORTE, L., STURZE-BECHER, U., ANGERMANN, H.: Passivation of Textured Silicon Wafers: Influence of Pyramid Size Distribution, a-Si:H Deposition Temperature, and Post-treatment. *Energy Procedia*, 38, 881-889, 2013.

[5] TAKAHASHI, M., FUKUSHIMA, T., SEINO, Y., KIM, W.-B., IMAMURA, K., KOBAYASHI, H.: Surface Structure Chemical Transfer Method for Formation of Ultralow Reflectivity Si Surfaces. *Journal of Electrochemical Society*, 160, H443-H445, 2013.

[6] IMAMURA, K., FRANCO JR., F. C., MATSUMOTO, T., KOBAYASHI, H.: Ultra-Low Reflectivity Polycrystalline Silicon Surfaces Formed by Surface Structure Chemical Transfer Method. *Applied Physics Letters*, 103, 3110-1-3110-4, 2013.

[7] FUKUSHIMA, T., OHNAKA, A., TAKAHASHI, M., KOBAYASHI, H.: Fabrication of Low Reflectivity Poly-Crystalline Si Surfaces by Structure Transfer Method, Electrochem. *Solid-State Letters*, 14, B13-B15, 2011.

[8] JURECKA, S., ANGERMANN, H., KOBAYASHI, H., TAKAHASHI, M., PINCIK, E.: Multifractal Analysis of Textured Silicon Surfaces. *Applied Surface Science*, 301, 46-50, 2014.

[9] JURECKA, S., JURECKOVA, M., KOBAYASHI, H., TAKAHASHI, M., MADANI, M., PINCIK, E.: Statistical and Fractal Properties of Semiconductor Surface Roughness. *Advances in Electrical and Electronic Engineering,* 7(1-2), 377-381, 2008.

[10] JURECKA, S., KOBAYASHI, H., TAKAHASHI, M., MATSUMOTO, T., JURECKOVA, M., CHOVANEC, F., PINCIK, E.: On the Influence of the Surface Roughness onto the Ultrathin SiO_2/Si Structure Properties. *Applied Surface Science*, 256, 5623-5628, 2010.

[11] GOLLION, P., GREENE, G.: Determination of Fractured Steel Surface Roughness by Atomic Force Microscopy Using Fractal-based Approaches, *Surface and Interface Analysis*, 24, 282, 1996.

[12] HOSSEINABADI, S., MORTEZAALI, A., MASOUDI, A. A.: Investigating Aluminum Thin Films Properties by Stochastic Analysis. *Surface and Interface Analysis*, 40, 71, 2008.

[13] TENG, H. T., EWE, H. T., TAN, S. L.: Multifractal Dimension and Its Geometrical Terrain Properties for Classification of Multi-Band Multi-Polarized Sar Image. *Progress in Electromagnetics Research*, 104, 221-237, 2010.

[14] ANNADHASON, A.: Methods of Fractal Dimension. *International Journal of Computer Science and Information Technology & Security*, 2(1), 166-169, 2012.

[15] CHOVANEC, F.: Cantor Sets. *Science & Military*, 5(1), 5-10, 2010.

[16] HARTE, D.: *Multifractals: Theory and Applications*. Chapman and Hall/CRC, Boca Raton, 2001.

[17] CHHABRA, A. B., MENEVEAU, C., JENSEN R. V., SREENIVASAN K. R.: Direct Determination of the $f(\alpha)$ Singularity Spectrum and its Application to Fully Developed Turbulence. *Physical Review*, 40(9), 5284-5294, 1989.

https://doi.org/10.26552/com.C.2017.3.62-65

Marian Janek - Vladimir P. Ladygin - Semen M. Piyadin - Yuri V. Gurchin - Alexander Yu. Isupov
Julia-Tatiana Karachuk - Anatoly N. Khrenov - Pavel K. Kurilkin - Alexei N. Livanov - Sergei G. Reznikov
Yaroslav T. Skhomenko - Gabriela Tarjanyiova - Arkady A. Terekhin*

ANALYZING POWERS iT_{11} AND T_{20} OF dp → ppn REACTION AT 400 MeV INVESTIGATED AT NUCLOTRON

One of the tools to study spin structure of short range correlations (SRCs) and three nucleon forces is the measurement of the polarization observables. Deuteron induced reactions at intermediate energies are investigated at Internal Target Station (ITS) of Nuclotron through the dp elastic and dp → ppn reactions. Analyzing powers iT11 and T20 analyzing powers of dp → ppn reaction at 400 MeV are presented.

Keywords: *iT11 and T20 analyzing powers, dp → ppn reaction, few nucleon correlations.*

1. Introduction

Reactions with few nucleons have a rich phase space. Polarization observables can be measured under various kinematic conditions. Intermediate energy region is of a special interest. In the region of few hundreds MeV QCD cannot be applied. Many experimental and theoretic studies are aimed in the region below the pion threshold where the exact calculations can be done. The most used contribution in theoretical models which include three nucleon forces (3NFs) is two pion exchange, e.g. Urbana IX [1] and Tucson-Melbourne [2]. These models properly describe binding energies of three and four nucleon systems. Generally, cross section of reactions with few nucleons in which the nucleon is unpolarized is better described than for the polarized case. Much worst situation is when the beam or target is polarized, especially in the case of polarization observables measurement. The simplest reactions in which three nucleon forces can be investigated are dp elastic scattering and dp → ppn reactions. Spin structure of the np SRCs has been investigated at JINR via the measurements of the tensor analyzing power A_{yy} in deuteron inclusive breakup at different energies in the wide regions of the x_F and transverse proton momentum p_T [3]. The A_{yy} data demonstrate the dependence on two internal variables, x_F and p_T or their combinations. However, none of used approaches [4, 5] describe the data. In the vicinity of the Sagara discrepancy the currently known 3NF contribute by up to 30 % to the dp elastic scattering cross section at intermediate energies [6]. The investigation of dp → ppn reaction at deuteron energy of 270 MeV at RIKEN [7] and IUCF [8] reveals that vector analyzing power A_y can be described using only NN forces. But other polarization observables need 3NFs to describe the data. The investigation of dp → ppn reaction at energy of 130 MeV measured at KVI [9] shows similar behavior. Inclusion of 3NF improves the description of a part of the data but breaks the other.

Reactions dp elastic and dp → ppn are studied in intermediate energy region from 300 - 2000 MeV and 300 - 500 MeV with unpolarized and polarized beam at Nuclotron with the aim of the study of a few nucleon correlations.

2. Experiment and results

The goal of the Deuteron Spin Structure (DSS) experimental program is to obtain the information about two and three nucleon forces including their spin dependent parts from dp elastic scattering at the energies between 300 – 2000 MeV and dp → ppn reactions with registration of two protons at deuteron energies of 300 – 500 MeV [10]. Deuteron beam is accelerated up to the required energy with Nuclotron. Polarization of deuteron beam is provided by new polarization ion source (PIS). The new PIS can provide unique opportunity for the studies of the spin effects and polarization phenomena in a few body systems at internal target

---

* [1]**Marian Janek**, [2]**Vladimir P. Ladygin**, [2]**Semen M. Piyadin**, [2]**Yuri V. Gurchin**, [2]**Alexander Yu. Isupov**, [2,3]**Julia-Tatiana Karachuk**, [2]**Anatoly N. Khrenov**, [2]**Pavel K. Kurilkin**, [2]**Alexei N. Livanov**, [2]**Sergei G. Reznikov**, [2,4]**Yaroslav T. Skhomenko**, [1]**Gabriela Tarjanyiova**, [2]**Arkady A. Terekhin**
[1]Physics Department, University of Zilina, Slovakia
[2]Joint Institute for Nuclear Research, Joliot-Curie 6, Dubna, Russia
[3]Advanced Research Institute for Electrical Engineering, Bucharest, Romania
[4]Belgorod State University, Belgorod, Russia
E-mail: janek@fyzika.uniza.sk

station (ITS) and also on extracted beam with the BM@N setup. Commissioning of the upgraded DSS setup has been performed at 270 MeV using unpolarized and polarized deuteron beam in June-July 2016. Good values of vector and tensor polarizations [11] were obtained at low energy polarimeter.

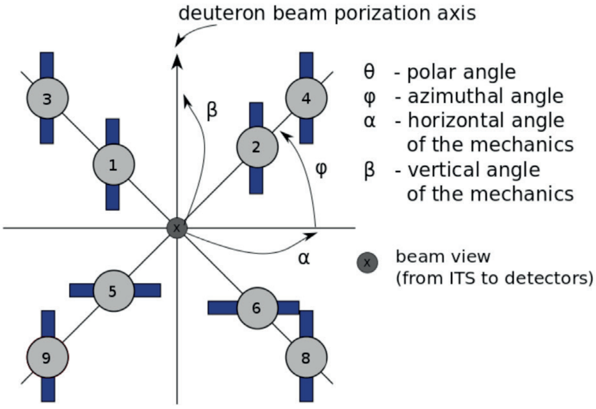

Fig. 1 Placement of ΔE-E detectors in case of dp → ppn reaction measurement at 400 MeV; detectors are placed in the vicinity of the ITS; position of each detector is defined by physical angles θ (not shown) and φ; angles of mechanics are used to adjust detector position related to beam direction

The transversely polarized deuteron beam interacting with the polyethylene and carbon targets. The effect on hydrogen is obtained by subtracting of carbon spectra from spectra on polyethylene. The polarization was flipped each spill between "spin-up" and "spin-down" (perpendicular to the plane of the accelerator) and no polarization. Ideal values of polarization were (*pz, pzz*) = (-1/3, 1) and (-1/3, -1), respectively. The polarization of deuteron beam was monitored continuously during the whole experiment. Vector and tensor polarizations are obtained from the asymmetries and known values of analyzing powers of dp elastic reaction at energy of 270 MeV. These values were used in determination of analyzing powers of dp → ppn reaction at 400 MeV. The measured values of polarization for "mode +" when tensor component is positive are: *pz* = -0.190 ± 0.009, *pzz* = 0.533 ± 0.017 and for "mode -": *pz* = -0.230 ± 0.007, *pzz* = - 0.705 ± 0.013. Statistical and systematical errors are taken into account. Statistical error comes from the ratio of dp elastic to pp quasi elastic events. Eight Δ*E* - *E* detectors are used in dp → ppn experiment to obtain the asymmetries. The details of the Δ*E* − *E* detector construction can be found in [12]. Each detector lays on the plane which is rotated by the angle of 45° or -45° related to the beam orbit one, see Fig. 1. The detector placement is determined by polar θ and azimuthal φ angles, see Table 1. Azimuthal angle φ have anticlockwise direction and is related to the detector closest to beam direction.

Detectors layout - polar (θ) and azimuthal (φ) angles; α and β - angles of mechanics Table 1

Detector No.	θ [°]	φ [°]	α[°]	β[°]
1	34.8	45.0	24.1	24.1
2	36.8	315.0	-25.0	25.0
3	50.4	45.0	38.6	38.6
4	52.5	315.0	-39.6	39.6
5	34.8	135.0	24.1	-24.1
6	36.8	225.0	-25.0	-25.0
8	52.5	225.0	-39.6	-39.6
9	50.4	135.0	38.6	-38.6

Monte Carlo simulation has been performed to confirm the suitability of the experiment and to find the criteria for selection of the useful events [13]. The cross section σ of the investigated reaction can be expressed through the cross section of unpolarized one $\sigma_{0,}$ deuteron beam polarizations p_Z and p_{ZZ}, angles θ, φ, β and analyzing powers in spherical representation iT_{11}, T_{20}, T_{21} and T_{22} by following:

$$\sigma = \sigma_0 \Big(1 + \sqrt{3}\, iT_{11}(\theta) p_z \sin\beta \cos\phi + \frac{T_{20}(\theta)}{\sqrt{8}} p_{zz} \\ (3\cos^2\beta - 1) + \sqrt{3}\, T_{21}(\theta) p_{zz} \cos\beta \sin\phi - \frac{\sqrt{3}}{2} T_{22}(\theta) p_{zz} \\ \sin^2\beta \cos 2\phi \Big) \tag{1}$$

The last two terms vanish because of the polarization of deuteron beam is perpendicular to the accelerator orbit and slope of detectors plane is 45° or -45°, respectively. The obtained counts for two polarized modes and one unpolarized have been normalized on the beam luminosity. Tensor analyzing powers are vanishing in a case of registration of two protons under pp quasi condition. Therefore only vector analyzing powers A_y have non zero value. Vector analyzing power A_y is related to iT_{11} through the following equation:

$$A_y = \frac{\sqrt{3}}{2} iT_{11} \tag{2}$$

The obtained vector analyzing powers A_y for two angles at 72.3° and 76.5° in the pp centre of mass system (CMS) are shown In Fig. 2 along with the world data at 200 MeV/N [14, 15]. One can see agreement between data at the obtained experimental level of accuracy. The measured values of iT_{11} and T_{20} analyzing powers for four detector configurations are shown in Table 2. The configurations which contain detectors 8 and 9 were not taken into account due to some interference between them and accelerator device support mainly rails. Each detector configuration is determined by polar (θ_1, θ_2) and azimuthal φ angles. The azimuthal angle φ is related to the angle of detector closest to the beam direction, see Fig. 1. Analyzing power T_{20} is equal to zero in case of pp quasi elastic scattering at 90°. Values of iT_{11} and T_{20} analyzing powers should be equal for the detector configuration 1, 6 and 5, 2 in case that angles θ_1, θ_2 and ϕ and vector and tensor polarization are the same for both cases. One can see agreement between the obtained data at the experimental level of accuracy. In the last column, iT_{11} and T_{20} analyzing powers for 1, 6 and 5, 2 configurations are combined. A low yield has been observed in other detector configurations.

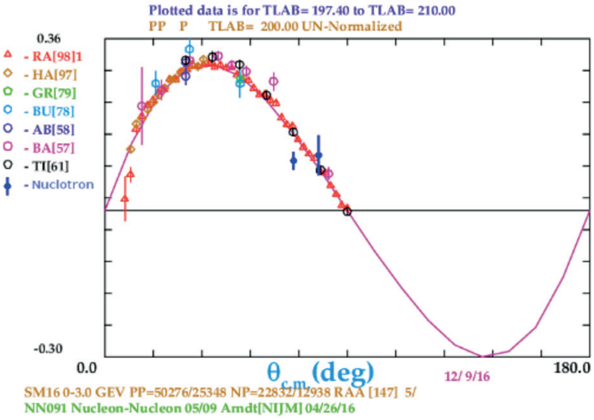

Fig. 2 Angular dependence of the vector analyzing power at energy of 200 MeV/N; data obtained at Nuclotron JINR are represented by full blue symbols (72.3° and 76.5° in CMS); other symbols represent world data [14, 15] and references therein

3. Conclusion

Values of the vector analyzing powers iT_{11} at 72.3° and 76.5° in CMS are 0.10 ± 0.02 and 0.11 ± 0.06, respectively. They are in agreement with world pp- elastic scattering data within experimental errors. Values of the vector iT_{11} and tensor T_{20} analyzing powers are 0.47 ± 0.10 and 0.02 ± 0.20.To substantially decrease the errors of analyzing powers the beam luminosity needs to be increased at about factor of 10. The future plans are connected with the measurements of tensor and vector analyzing powers in interesting regions of phase space where the contributions of three nucleon forces is expected to be large enough to observe. The sufficient statistics will allow obtaining kinematic (S curve) dependence of analyzing powers.

Acknowledgments

The authors thank the staff of the Nuclotron for providing of the good conditions of the experiment. We are grateful to A.V. Averianov, E.V. Chernykh, D.O. Krivenkov and A.V. Tishevsky for their assistance during the experiment. This work has been supported partly by the scientific cooperation program JINR-Slovak Republic in 2016 and 2017 years and by the Russian Foundation for Basic Research under grant no. 16-02-00203a.

Spherical analyzing powers iT_{11} and T_{20} for different detector configuration - polar (θ_1, θ_2) and azimuthal φ angles Table 2

Conf.	θ_1 [°]	θ_2 [°]	ϕ [°]	iT_{11}	T_{20}	iT_{11} combined	T_{20} combined
detectors – 5, 4	34.8	52.5	135	0.10 ± 0.02	0	-	-
detectors – 6, 3	36.8	50.4	45	0.11 ± 0.06	0	-	-
detectors – 1, 6	34.8	36.8	135	0.55 ± 0.15	0.13 ± 0.30	0.47 ± 0.10	0.02 ± 0.20
detectors – 5, 2	34.8	36.8	135	0.39 ± 0.13	-0.09 ± 0.27		

References

[1] RAUPRICH G., et al.: Study of the Kinematically Complete Breakup Reaction 2H($\bar{p}$, pp)n at Ep=3 Mev with Polarized Protons. *Nuclear Physics A,* 535, 313-330, 1991.

[2] PATBERG H., et al.: Deuteron Breakup Reaction 2H(p$^{\rightarrow}$, pp)n Induced by Polarized Protons at Ep=9.0 MeV. *Physical Review C*, 53, 1497-1505, 1996.

[3] AZHGIREY L. S., et al.: Measurement of the Tensor analyzing Power T(20) in Inclusive Deuteron Breakup at 9-GeV/c on Hydrogen and Carbon. *Physics Letters B*, 387, 37-42, 1996.

[4] MACHLEIDT R.: High-Precision, Charge-Dependent Bonn Nucleon-Nucleon Potential. *Physical Review C*, 63, 024001, 2001.

[5] KARMANOV V. A., SMIRNOV A. V.: Electromagnetic Form Factors in the Light-Front Dynamics. *Nuclear Physics A*, 546, 691-717, 1992.

[6] SAKAMOTO N., et al.: Measurement of the Vector and Tensor Analyzing Powers for the d-p Elastic Scattering at Ed=270 MeV. *Physics Letters B*, 367, 60-64, 1996.

[7] SEKIGUCHI K., et al.: Three-Nucleon Force Effects in the ^{1}H($^{\rightarrow}$d, $^{\rightarrow}$pp)n Reaction at 135 MeV/nucleon. *Physical Review C*, 79, 054008, 2009.

[8] MEYER H. O., et al.: Axial Observables in $^{\rightarrow}$d$^{\rightarrow}$p Breakup and the Three-Nucleon Force. *Physical Review Letters*, 93, 112502, 2004.

[9] KISTRYN S., et al.: Systematic Study of Three-Nucleon Force Effects in the Cross Section of the Deuteron-Proton Breakup at 130-MeV. *Physical Review C*, 72, 044006, 2005.

[10] LADYGIN V. P., et al.: Recent Results with Polarized Deuterons and Polarimetry at Nuclotron-NICA. *Journal of Physics: Conference Series*, 295, 012131, 2011.

[11] JANEK M., et al.: Investigation of the dp Breakup and dp Elastic Reactions at Intermediate Energies at Nuclotron. *Few-Body Systems*, 58(2), 40, 2017.

[12] PIYADIN S. M., et al.: ΔE-E Detector for Proton Registration in Nonmesonic Deuteron Breakup at the Nuclotron Internal Target. *Physics of Particles and Nuclei Letters*, 8(2), 107-113, 2011.

[13] JANEK M., TRPISOVA B., LADYGIN V. P., PIYADIN S. M.: *Communications - Scientific Letters of the University of Zilina*, 16(1), 59-63, 2014.

[14] RAHM S., et al.: np Scattering Measurements at 162 MeV and the π NN Coupling Constant. *Physical Review C,* 57, 1077-1096, 1998.

[15] HAEBERLI W., et al.: Proton-Proton Spin Correlation Measurements at 200 MeV with an Internal Target in a Storage Ring. *Physical Review C,* 55, 597, 1997.

https://doi.org/10.26552/com.C.2017.3.66-70

COMMUNICATIONS

Boris Tomasik - Ivan Melo - Jakub Cimerman*

GENERATION OF RANDOM DEVIATES FOR RELATIVISTIC QUANTUM-STATISTICAL DISTRIBUTIONS

We provide an algorithm for generation of momenta (or energies) of relativistic particles according to the relativistic Bose-Einstein or Fermi-Dirac distributions. The algorithm uses rejection method with effectively selected comparison function so that the acceptance rate of the generated values is always better than 0.9. It might find its use in Monte-Carlo generators of particles from reactions in high-energy physics.

Keywords: *Bose-Einstein distribution, Fermi-Dirac distribution, random number generator.*

1. Introduction

In projects related to multiparticle production in hadronic or nuclear collisions it is often demanded to generate a large number of particles with momenta distributed according to relativistic Bose-Einstein or Fermi-Dirac distribution. Here one has to take into account the total energy (i.e. including the mass) when evaluating the exponent of the distributions

$$f(\vec{p}) = \frac{1}{(2\pi\hbar)^3}\left[\exp\left(\frac{c\sqrt{m^2c^2+p^2}-\mu}{k_BT}\right)+q\right]^{-1} \tag{1.1}$$

where m is the mass of the particles, $p = |\vec{p}|$, μ is the chemical potential and T is temperature. Parameter q assumes the value of 1 for fermions and −1 for bosons. For the generation of invariant momentum distributions one also needs this distribution multiplied with the energy

$$S(\vec{p}) = \frac{c\sqrt{m^2c^2+p^2}}{(2\pi\hbar)^3}\left[\exp\left(\frac{c\sqrt{m^2c^2+p^2}-\mu}{k_BT}\right)+q\right]^{-1} \tag{1.2}$$

As the distribution is spherically symmetric, the angles are trivially integrated and we are left with the distributions for the size of the momentum vector. In order to make it suitable for a general procedure, it is expressed with the help of dimensionless variable

$$x = \frac{p}{mc} \tag{1.3}$$

Thus we get

$$f(x) = x^2\left[\exp\left(A\sqrt{1+x^2}-M\right)+q\right]^{-1} \tag{1.4}$$

or for the other distribution

$$S(x) = \sqrt{1+x^2}\,x^2\left[\exp\left(A\sqrt{1+x^2}-M\right)+q\right]^{-1} \tag{1.5}$$

where

$$A = \frac{mc^2}{k_BT}, \quad M = \frac{\mu}{mc^2} \tag{1.6}$$

In these functions we have suppressed the constant pre-factors which also contain dimensions.

For the Monte Carlo generation we shall proceed with the dimensionless distributions without the dimensionfull pre-factors.

A similar algorithm for the generation of relativistic Maxwellian distribution has been reported in [1, 2]. In our work we properly account for quantum statistics and allow for non-zero chemical potential, which can influence the momentum distribution. We describe the procedure for the distribution (1.5) with the energy factor. The procedure for the distribution (1.4) can easily be derived along the same steps as we shall proceed.

---

* **^{1,2}Boris Tomasik, ^{3}Ivan Melo, ^{4}Jakub Cimerman**
^{1}Univerzita Mateja Bela, Banska Bystrica, Slovakia
^{2}FNSPE, Czech Technical University in Prague, Czech Republic
^{3}University of Zilina, Slovakia
^{4}FMFI, Comenius University, Bratislava, Slovakia
E-mail: melo@fyzika.uniza.sk

2. The algorithm

We demonstrate in the Appendix that the distribution (1.5) is log-concave for large enough x, i.e. its logarithm is a concave function. For such a distribution there always exists an exponential that is everywhere above the demanded distribution. One can generate random deviates according to the exponential and use the rejection method [2].

In order to achieve the smallest possible rejection rate we use piecewise analytic comparison function, as indicated in Fig. 1. The three pieces are determined so that

- for $x \leq x_-$ the comparison function is linear;
- for $x_- < x \leq x_+$ the comparison function is constant and equal to the value of the distribution at the mode;
- for $x > x_+$ the comparison function is exponential.

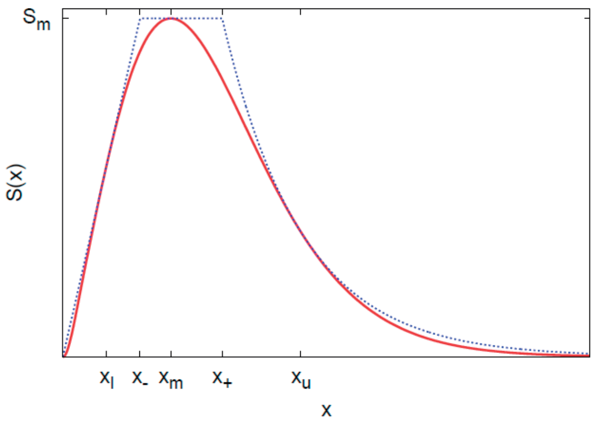

Fig. 1 Dimensionless Bose-Einstein distribution with energy pre-factor according to Eq. (1.5); the shape corresponds to A=2/3 and M=3/4 but we have suppressed the values on the axes in order to demonstrate the comparison function and locate the important points for the determination of the comparison function

The joint points x_- and x_+ are chosen so that the comparison function is always continuous.

For the determination of the comparison function we thus need to determine the five points indicated on the horizontal axis.

x_m The mode of $S(x)$. This is easily obtained by differentiating and we get

$$2 + 3x_m^2 - \frac{Ax_m^2\sqrt{1+x_m^2}}{1+q\exp\left(-A\left(\sqrt{1+x_m^2}-M\right)\right)} = 0 \qquad (2.1)$$

Unfortunately this expression cannot be solved analytically and numerical methods must be invoked.

Subsequently, the value of $S(x)$ at the mode can be determined

$$S_m = S(x_m) = \sqrt{1+x_m^2}\,x_m^2\left[A\left(\sqrt{1+x_m^2}-M\right)+q\right]^{-1} \qquad (2.2)$$

x_l The point left from the mode in which the linear comparison function touches the distribution. It is found from the condition for the derivative of the distribution

$$\left.\frac{dS(x)}{dx}\right|_{x=x_l} = \frac{S(x_l)}{x_l}$$

which leads to

$$1 + 2x_l^2 - \frac{Ax_l^2\sqrt{1+x_l^2}}{1+q\exp\left(-A\left(\sqrt{1+x_l^2}-M\right)\right)} = 0 \qquad (2.3)$$

The slope of the linear comparison function is then

$$K = \frac{S(x_l)}{x_l} = \frac{x_l\sqrt{1+x_l^2}}{\exp\left(A\left(\sqrt{1+x_l^2}-M\right)\right)+q} \qquad (2.4)$$

x_- The point in which the linear part of the comparison function and its constant part meet. It can be determined as

$$x_- = \frac{S_m}{x_l\sqrt{1+x_l^2}}\left[\exp\left(A\left(\sqrt{1+x_l^2}-M\right)\right)+q\right] \qquad (2.5)$$

The knowledge of x_- also allows to express

$$K = \frac{S_m}{x_-} \qquad (2.6)$$

x_u The point in which the exponential part of the comparison function touches the distribution.

Above the mode the distribution is log-concave. Therefore, x_u can be chosen anywhere above x_m. However, we checked that the acceptance rate is optimised with x_u chosen so that the distribution there drops to $1/e$ of its maximum value. We get the value by solving the equation for the logarithms of the distribution

$$\ln S(x_u) = \ln S_m - 1,$$

which leads to

$$\begin{aligned} &1 - \ln S_m + \frac{1}{2}\ln\left(1+x_u^2\right) + 2\ln x_u - \\ &-\ln\left[\exp\left(A\left(\sqrt{1+x_u^2}-M\right)\right)+q\right] = 0 \end{aligned} \qquad (2.7)$$

Again, this equation must be solved numerically.

Once x_u is determined, we can determine the slope parameter of the exponential comparison function. It is given by the logarithm of the distribution. Thus

$$\begin{aligned} &\lambda = -\left.\frac{d\ln S(x)}{dx}\right|_{x=x_u} = \frac{x_u}{\sqrt{1+x_u^2}} \\ &\left[1 - A\frac{\exp\left(A\left(\sqrt{1+x_u^2}-M\right)\right)}{\exp\left(A\left(\sqrt{1+x_u^2}-M\right)\right)+q}\right] - \frac{2}{x_u} \end{aligned} \qquad (2.8)$$

x_+ Finally, this is the point in which the constant part of the comparison function and its exponential part join. It is determined from a simple equation

$$x_+ = x_u - \frac{1}{\lambda} \qquad (2.9)$$

Once we have x_+, we also know the exponential part of the comparison function which reads

$$S'(x) = S_m e^{-\lambda(x-x_+)} \tag{2.10}$$

Thus we can formulate the comparison function

$$S'(x) = \begin{cases} \frac{S_m}{x_-}x & : \quad x \le x_- \\ S_m & : \quad x_- < x \le x_+ \\ S_m e^{-\lambda(x-x_+)} & : \quad x > x_+ \end{cases} \tag{2.11}$$

In order to use this comparison function as probability density (after normalisation) for random variate generation we need the values

$$y_- = \int_0^{x_-} S'(x)dx = \frac{1}{2}S_m x_- \tag{2.12a}$$

$$y_+ = \int_0^{x_+} S'(x)dx = S_m\left(x_+ - \frac{1}{2}x_-\right) \tag{2.12b}$$

$$y_\infty = \int_0^{\infty} S'(x)dx = S_m\left(x_+ - \frac{1}{2}x_- + \frac{1}{\lambda}\right) \tag{2.12c}$$

For the rejection step we need the probabilities to accept the generated value of x.

They are given as $P(x)=S(x)/S'(x)$. In the three intervals they read

$$P(x) = \frac{x_- x\sqrt{1+x^2}}{S_m\left[\exp\left(A\left(\sqrt{1+x^2}-M\right)\right)+q\right]} : x \le x_- \tag{2.14a}$$

$$P(x) = \frac{x^2\sqrt{1+x^2}}{S_m\left[\exp\left(A\left(\sqrt{1+x^2}-M\right)\right)+q\right]} : x_- < x \le x_+ \tag{2.14b}$$

$$P(x) = \frac{x^2\sqrt{1+x^2}\exp\left(\lambda(x-x_+)\right)}{S_m\left[\exp\left(A\left(\sqrt{1+x^2}-M\right)\right)+q\right]} : x_+ < x \tag{2.14c}$$

Now we have collected all expressions needed to build up the algorithm. Because of the need to numerically solve a few equations the procedure may be lengthy if one needs to generate just one random value. However, if many values must be generated for the same temperature, chemical potential and particle mass, then all parameters can be calculated first and then used repeatedly. Thus the first part of the algorithm is the calculation of the parameters:

The inverse of the integral of $S'(x)$ is

$$x(y) = \begin{cases} \sqrt{\frac{2x_- y}{S_m}} & : \quad y \le y_- \quad \text{gives} \quad x \le x_- \\ \frac{1}{2}x_- + \frac{y}{S_m} & : \quad y_- < y \le y_+ \quad \text{gives} \quad x_- < x \le x_- \\ x_+ - \frac{1}{\lambda}\ln\left[1+\left(x_+ - \frac{1}{2}x_-\right)\lambda - \frac{\lambda}{S_m}y\right] & : \quad y_+ < y \le y_\infty \quad \text{gives} \quad x > x_+ \end{cases} \tag{2.13}$$

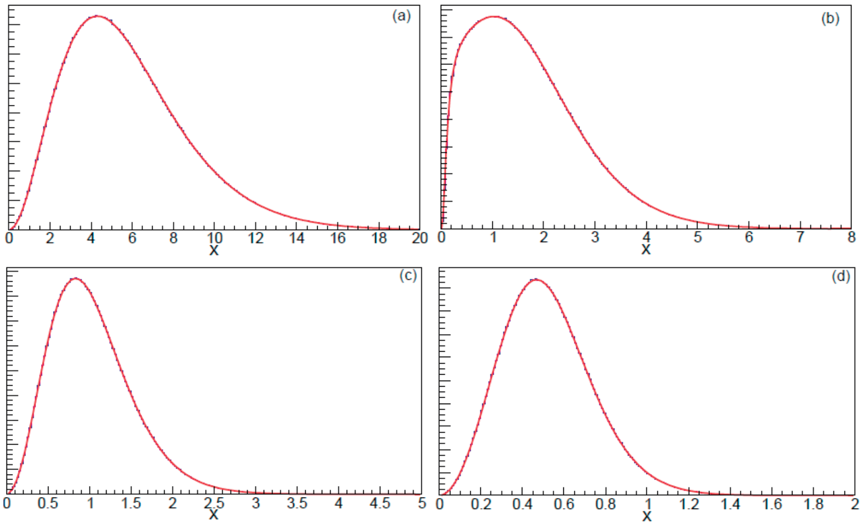

Fig. 2 Histograms of 10^7 random deviates fitted by function S(x) with only the absolute normalisation as a fit parameter; values of A and M are fixed in the fit function in order to be the same as in the Monte Carlo generation; the values are: (a) A=2/3, M=0, bosons (e.g. pions with μ=0 at temperature k_BT=207 MeV); (b) A=2, M=0.993, bosons (e.g. pions with μ=137 MeV/c^2 at temperature k_BT=69 MeV, close to condensation); (c) A=4.536, M=0, fermions (e.g. protons with μ=0 at temperature k_BT =(3/2)$m_\pi c^2$ =207 MeV); (d) A=13.609, M=0.9989, fermions (e.g. protons with μ=938 MeV at temperature $k_BT=m_\pi c^2/2$=69 MeV)

1. Determine x_m by solving Equation (2.1).
2. Calculate S_m from Equation (2.2).
3. Determine x_l by solving Equation (2.3).
4. Calculate x_- from Equation (2.5).
5. Determine x_u by solving Equation (2.7).
6. Calculate λ from Equation (2.8).
7. Calculate x_+ from Equation. (2.9).
8. For later convenience calculate also the values of y_-, y_+, and y_∞ from Equations (2.12).

This is the common part of the preparation. Then, in order to generate a value, follow these steps:

9. Generate uniform random deviate y from the interval $[0,y_\infty]$.
10. Calculate $x=x(y)$ from Equation (2.13).
11. Accept the value of x with the probability given by Equations (2.14). If the value is not accepted, return to the step 9.

3. Illustration of results

We have tested this algorithm in a wide range of parameters A and M. Particle masses were chosen both smaller than temperature so that large momenta are available and also much larger than temperature so that the momenta are practically non-relativistic. Chemical potentials up to the value of particle mass for bosons, i.e. the point of condensation, were tested, as well (Fig. 2). In all cases the acceptance rate was around 90 %. This shows that the comparison function is very well adapted to the present problem.

4. Conclusions

The presented algorithm has been successfully implemented in an upgrade of the Monte Carlo event generator DRAGON [3], which serves for the generation of hadrons produced in high energy nuclear collisions. It is, however, general and can serve in any other application where relativistic momenta must be generated from quantum-statistical distributions.

Acknowledgments

We gratefully acknowledge financial support by grants APVV-0050-11, VEGA 1/0469/15 (Slovakia) and MSMT grant LG15001 (Czech Republic). The reported algorithm has been used in our software which run in the High Performance Computing Center of the Matej Bel University in Banska Bystrica using the HPC infrastructure acquired in project ITMS 26230120002 and 26210120002 (Slovak infrastructure for high-performance computing) supported by the Research & Development Operational Programme funded by the ERDF.

A Log-concave distribution

In this Appendix we demonstrate that the distribution $S(x)$ according to Eq. (1.5) is indeed log-concave on the interval above the mode. Therefore, an exponential function which touches $S(x)$ from above in one point will never be smaller than $S(x)$.

The calculation is straightforward. We take the second derivative of $\ln S(x)$. For fermions (q=1), this leads to

$$\begin{aligned}\frac{d^2 \ln S(x)}{dx^2} &= -\frac{1}{1+x^2}\left\{\frac{2}{x^2}+1+\frac{2x^2}{1+x^2}+\right.\\ &\left.+\frac{A}{\sqrt{1+x^2}}(1-s_f(x))+A^2x^2 s_f(x)(1-s_f(x))\right\}\end{aligned} \qquad \text{(A.1)}$$

where

$$s_f(x)=\frac{1}{\exp[A(\sqrt{1+x^2}-M)]+1}.$$

Note that $s_f(x) \le 1$ for any x. Therefore, $(1- s_f(x)) \ge 0$ and all terms in the bracket in Equation (A.1) are non-negative. In summary, we see that for fermions

$$\frac{d^2 \ln S(x)}{dx^2} < 0 \qquad \text{(A.2)}$$

and thus the distribution is log-concave everywhere.

The case of bosons is slightly more involved. Again, we take the second derivative

$$\begin{aligned}\frac{d^2 \ln S(x)}{dx^2} &= -\frac{1}{1+x^2}\left\{\frac{2}{x^2}+1+\frac{2x^2}{1+x^2}+\right.\\ &\left.+\frac{A}{\sqrt{1+x^2}}(1+s_b(x))+A^2x^2 s_b(x)(1+s_b(x))\right\}\end{aligned} \qquad \text{(A.3)}$$

where

$$s_b(x)=\frac{1}{\exp[A(\sqrt{1+x^2}-M)]-1}.$$

Note the change of the sign in $(1+s_b(x))$ and in front of the last term. Due to this, for bosons the second derivative may become positive in some cases. We want to demonstrate that such pathological intervals are always below the mode of $S(x)$.

For $x \to \infty$ the terms $s_b(x)$ go to 0 exponentially (we chose the letter s for "small"), and one can inspect that

$$\lim_{x\to\infty}\frac{d^2 \ln S(x)}{dx^2} = 0$$

and the value of the limit is being approached from below. Thus the second derivative is either negative everywhere or there is a point $x = x_c$ where it crosses the horizontal axis and stays negative for $x > x_c$. It is enough to show that $x_c < x_m$.

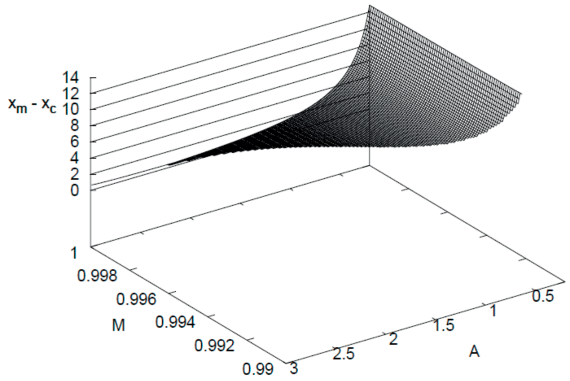

Fig. 3 The difference in positions $x_m - x_c$ *as function of A and M. Values are not plotted if the secondderivative* $d^2 \ln S(x)/dx^2$ *for bosons stays negative everywhere; One sees that always* $x_c < x_m$

It turns out that the second derivative becomes positive only if the particles are light with $A \leq 3$ and M is close to 1, which is quite an extreme case. (Recall that for bosons M must be smaller than 1 and $M = 1$ corresponds to the condensation point where the distribution does not longer apply.) In such a case, for small values of x one obtains $s_b >> 1$ and the last term in Equation (A.3) prevails. We have scanned the whole relevant parameter region of A and M and checked that always $x_c < x_m$ (Fig. 3). In all other cases the function $S(x)$ is log-concave everywhere.

We conclude that it is safe to use the exponential comparison function in the interval (x_m,∞).

References

[1] SWISDAK, M.: The Generation of Random Variates from a Relativistic Maxwellian Distribution. *Physics of Plasmas*, 20, 062110, 2013.

[2] DEVROYE, L.: *Non-Uniform Random Variete Generation,* Chapter 7 [online]. Springer Verlag, New York, p. 286-357, 1986. Available: http://luc.devroye.org/rnbookindex.html.

[3] TOMASIK, B.: DRAGON: Monte Carlo Generator of Particle Production from a Fragmented Fireball in Ultrarelativistic Nuclear Collisions. *Computer Physics Communications*, 180, 1642-1653, 2009, ibid. 207, 545, 2016.

https://doi.org/10.26552/com.C.2017.3.71-76

Mikulas Gintner - Josef Juran*

THE CURRENT LHC LIMITS FOR THE tBESS LAGRANGIAN

We investigate how the recent LHC measurements limit the parameters of the hypothetical vector resonance triplet. The vector resonances are assumed to represent bound states of hypothetical strongly-interacting new physics, a candidate of the extension of the Standard model.

Keywords: *New vector resonances, LHC limits, tBESS effective Lagrangian.*

1. Introduction

Even though the LHC experiments ATLAS and CMS achieved a spectacular success by discovering the 125 GeV Higgs boson [1] it was more the beginning rather than the end of the struggle to uncover the character of physics beyond the Standard Model (SM). To this moment, it has not been settled down whether new physics takes the form of weakly coupled supersymmetry or strongly coupled composites; this can be translated into question whether the observed Higgs boson is a fundamental field or a bound state of hypothetical new strong interactions.

The search for answers to these questions requires the close interplay between theory and experiment. On the theory side, the formulation of possible extensions of the SM along with their predictions for suitable observables is needed. In this context, we have formulated the effective Lagrangian (called the tBESS model) [2, 3] that could provide the framework for the description and analysis of phenomena that could be observed at the LHC if new strong physics is what lies behind the SM extension. Our effective description includes an explicit presence of a new vector resonance triplet.

In our previous papers [2 - 4], the tBESS model was a subject of a thorough investigation in an attempt to find how its parameters are restricted by the existing measurements. In our most recent work [3], our model faced the confrontation with the latest LHC measurements performed by the ATLAS and CMS Collaborations. Among other things we calculated the model's predictions for the LHC cross sections of the vector resonance production processes considering various final states to which the produced resonance can decay. We found that in the case of no direct coupling of the vector resonance with fermions the LHC data provide only weak or no restrictions for the parameters of our model through this observable. In particular, considering ten decay channels of the resonance, namely *WW, ZW, WH. ZH*, $jj_{neutral}$, $jj_{charged}$, $\ell\ell$, $\ell\nu$, tt and *tb*, the 1 TeV – 1.5 TeV resonances get excluded in the *WW* and *ZW* channels for certain values of the vector resonance gauge coupling g''. However, even this restriction can get weakened once the direct interactions of the vector resonance with the fermion sector are introduced. None of the other reviewed decay channels excludes our model within the considered range of the values of g''.

We would like to extend the analysis of the resonance production cross section limits to the case when the direct interactions of the vector resonance with fermions are turned on. We believe that the presence of the direct interaction of the resonance to heavy fermions represents a more realistic case of new strong physics. It also offers a richer phenomenology to be investigated. The goal of this paper is to prepare and test the means necessary for performing such an analysis. It includes an upgrade of the means that were used in [3]. We will replace the parton distribution function set CTEQ6L1 used in [3] for the set CT10 which is more suitable for the LHC processes. In [3], we have used the vector boson luminosity functions calculated for the 14 TeV collision energy. These will be replaced with the 13 TeV functions so that they correspond to the actual collision energy at which the data were taken.

In the next section we will briefly introduce the tBESS model. In Section 3 the procedure for the calculation of the production cross section will be presented. Section 4 shows the results obtained for the $e^+e^- + \mu^+\mu^-$ final state. The comparison of the results of the upgraded calculations with the results of [3] is performed. Finally, Section 5 presents conclusions of the paper.

---

* [1,2]**Mikulas Gintner,** [2,3]**Josef Juran**
[1]Physics Department, University of Zilina, Slovakia
[2]Institute of Experimental and Applied Physics, Czech Technical University in Prague, Czech Republic
[3]Institute of Physics, Silesian University in Opava, Czech Republic
E-mail: gintner@fyzika.uniza.sk

2. The effective tBESS Lagrangian

The effective tBESS Lagrangian [2, 3] serves as the effective description of a hypothetical strongly interacting extension of the SM where the principal manifestation of this scenario at the LHC energies would be the existence of a vector resonance triplet as a bound state of new strong interactions. The Lagrangian is built to respect the global $SU(2)_L \times SU(2)_R \times U(1)_{B-L} \times SU(2)_{HLS}$ symmetry of which the $SU(2)_L \times U(1)_Y \times SU(2)_{HLS}$ subgroup is also a local symmetry. The $SU(2)_{HLS}$ symmetry is an auxiliary gauge symmetry invoked to accommodate the $SU(2)$ triplet of new vector resonances. Each of the gauge groups is accompanied by its gauge coupling: g, g', g'' respectively. Beside the scalar singlet representing the 125 GeV Higgs boson and the hypothetical vector triplet, the effective Lagrangian is built out of the SM fields only.

The way the description of the vector resonance is introduced implies the mixing between the resonance and electroweak gauge boson fields. The mixing induces the (indirect) couplings between the vector resonance and fermions that are proportional to $1/g''$. The considered symmetry also admits the introduction of the direct interactions of the vector resonance with fermions. The existing experimental limits inspired the tBESS specific assumption that only the third quark doublet couples directly to the vector resonance. This chiral coupling is parameterized by the $b_{L,R}$ parameters. In addition, the vector resonance coupling to the right bottom quark can be made weaker than the right top coupling. The ratio is parameterized by $p \in \langle 0;1 \rangle$. Finally, the symmetry admits a further modifications of the electroweak gauge boson couplings to fermions parameterized by $\lambda_{L,R}$.

The deviations from the SM interactions of the $SU(2)_L \times U(1)_Y$ gauge boson with the Higgs boson is parametrized by a_V. The analogical coupling of the vector resonance to the Higgs is parametrized by a_ρ.

The masses of the charged and neutral vector resonances in the model are virtually degenerated. The leading order formula for the mass reads

$$M_\rho = \frac{v}{2}\sqrt{\alpha}\, g'' \tag{1}$$

where α is a dimensionless free parameter in the tBESS Lagrangian and *v* is the electroweak symmetry breaking scale. Usually, α is traded off for M_ρ so that the latter can serve as one of the free parameters of the model. Our previous studies of the low-energy [2], Higgs-related [3] and unitarity limits [2, 3] suggest that we should consider $10 \leq g'' \leq 20$ and $1\,\text{TeV} \leq M_\rho \leq 3\,\text{TeV}$. Furthemore, $a_V = 1$ and $a_\rho = 0$ are quite close to one of the experimentally preferred point of the parameter space. Therefore these will be the values we use throughout this paper. Note though that the dependence of the results presented below on a_V and a_ρ will be negligible. These parameters influence significantly only decay channels of the vector resonance with very small branching ratios.

In this paper, we will consider no direct interactions of the vector resonance with fermions $(b_{L,R} = p = \lambda_{L,R} = 0)$. Then, the total decay width of the resonance can be approximated by

$$\Gamma_\rho = \frac{1}{48\pi v^4}\frac{M_\rho^5}{g''^2}. \tag{2}$$

In Fig. 1 we depict how the vector resonance width in this approximation depends on the resonance mass and g''.

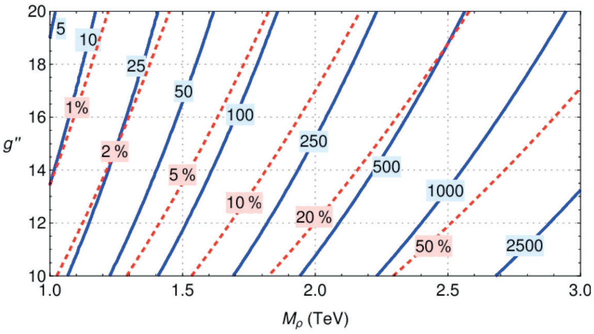

Fig. 1 The solid lines represent the contours of the total decay width of the vector resonance (labeled in GeV) in the $g'' - M\rho$ parameter space; the dashed lines represent the width-to-mass ratio of the vector resonance (labeled in percents); no direct interactions of the resonance to fermions is assumed

3. The cross section calculations

We are interested in the LHC cross sections of the two-particle final state processes that would proceed via the vector resonance production. We calculate the cross sections $\sigma(pp \to a + b + X)$ in the Narrow Width Approximation (NWA), i.e. we approximate the cross sections by the product of the on-shell production cross section of the resonance, σ_{prod}, and the branching ratio for the vector resonance decay channel under consideration

$$\sigma(pp \to ab + X) \approx \sigma^{NWA} = \sigma_{prod}(pp \to \rho + X) \times \\ \times BR(\rho \to ab) \tag{3}$$

As the name suggests the NWA works when $\Gamma_\rho \ll M_\rho$. It also ignores the signal-background interference effects. The influence of these effects on the precision of the approximation has been investigated in [5].

In general, the production cross section of a resonance can be expressed as

$$\sigma_{prod}(pp \to \rho + X) = \sum_{i \leq j \in p} 16\pi^2 K_{ij} \frac{\Gamma_{\rho \to ij}}{M_\rho}\frac{dL_{ij}}{d\hat{s}}\bigg|_{\hat{s}=M_\rho^2} \tag{4}$$

where *i, j* run through all partons of the colliding protons and $\Gamma_{\rho \to ij}$ is the partial decay width of the resonance to the partons.

Furthermore, $dL_{ij}/d\hat{s}$ is a parton-parton luminosity of the colliding partons, and

$$K_{ij} = \frac{2J+1}{(2S_i+1)(2S_j+1)}\frac{C}{C_iC_j} \tag{5}$$

where J is a spin of the resonance, C is its color factor, and S_i, S_j and C_i, C_j are the spins and colors of the initial partons, respectively. Note that a model dependence enters the production cross section (4) virtually[1] only via the partial decay width $\Gamma_{\rho\to ij}$.

Two dominant production mechanisms for the triplet of our vector resonances are the Drell-Yan (DY) and the vector boson fusion (VBF) processes. We will consider them both in our analysis. The VBF production will be calculated in the Effective *W* Approximation (EWA) [6]. For the sake of simplicity, in our calculations of the production cross sections the proton contents is reduced down to the up and down quarks[2]. Thus, the DY partons include $\{u, \bar{u}, d, \bar{d}\}$ and the VBF partons are $\{W^+, W^-, Z\}$. When the vector resonance (J = 1, C = 1) is produced, the factor K_{ij} in the formula (4) assumes the value $K^{DY} = 1/12$ in the case of the DY production; $K^{VBF} = 1/3$ for the VBF process. Any of the three charged states of the vector resonance ρ can be produced: $\rho^\pm$ can be created in the $u\bar{d}/\bar{u}d\,(\mathrm{DY})$ and $W^\pm Z\,(\mathrm{VBF})$ collisions, while the neutral resonance ρ^0 can be produced in $u\bar{u}, d\bar{d}\,(\mathrm{DY})$ and $W^+W^-\,(\mathrm{VBF})$ collisions. If the b-quark contents of the proton is ignored the production cross section is not sensitive to the parameters $b_{L,R}, p, \lambda_{L,R}$.

The parton-parton luminosity appearing in (4) is defined as

$$\frac{dL_{ij}}{d\hat{s}} = \frac{1}{s}\int_\tau^1 \frac{dx}{x}\frac{1}{1+\delta_{ij}}\left[f_i(x,\hat{s})f_j(\tau/x,\hat{s}) + i \leftrightarrow j\right] \tag{6}$$

where s and $\hat{s}$ are the squared center of mass energies of the colliding protons and partons, respectively, $\tau \equiv \hat{s}/s$, and f_i is a parton distribution function of the i^{th} parton with the momentum fraction x of its proton's momentum. In the DY case, f_i's are the parton distribution functions (PDF) of quarks and gluons in the proton. When the EWA is applied to the VBF case, the *W* and *Z* bosons are also treated as partons in the proton. In this approximation, their PDF's are calculated as the convolutions of the quark PDF's with the probability that a given quark would emit *W* or *Z* boson. Then the VBF luminosity can be expressed as

$$\begin{aligned}\frac{dL_{V_mV_n[pp]}}{d\tau} = \sum_{i\leq j}\frac{1}{1+\delta_{ij}}\int_\tau^1 \frac{dx_1}{x_1}\int_{\tau/x_1}^1 \frac{dx_2}{x_2}\Big[f_i(x_1,q^2)f_j(x_2,q^2)\times \\ \frac{dL_{V_mV_n[q_iq_j]}}{d\hat{\tau}} + i \leftrightarrow j\Big]\end{aligned} \tag{7}$$

where $\hat{\tau} = \tau/(x_1x_2)$, and $dL_{V_mV_n[q_1q_2]}/d\hat{\tau}$ is the luminosity for two vector bosons V_m and V_n emitted from i^{th} and j^{th} quarks, respectively,

$$\frac{dL_{V_mV_n[q_1q_2]}}{d\hat{\tau}} = \int_{\hat{\tau}}^1 \frac{dx}{x} f_{V_m[q_i]}(x) f_{V_n[q_j]}(\hat{\tau}/x) \tag{8}$$

where $f_{V_m[q_i]}$'s represent the gauge boson contents of quarks in the same way the PDF's represent the quark/gluon contents of protons. Contrary to the PDF's case though, we know how to calculate $f_{V_m[q_i]}$'s from the first principles. Finally, the scale q^2 in (7) will be set to M_W^2.

The EWA's PDF's are derived under the assumptions that the gauge bosons are emitted on-shell and in small angles to their parental quarks. Also, if the gauge bosons fuse to a heavy resonance their masses should be negligibly small compare to the resonance mass. Moreover, in this approximation, the transverse and longitudinal polarizations of the emitted gauge bosons are considered as separate modes and, in some cases, one of them becomes negligible to the other. For example, in the SM the VBF production is dominated by the transverse mode due to the exact mutual cancellation of the ill-behaved longitudinal gauge boson and Higgs amplitudes. On the other hand, new physics contributions are expected to tip this balance and let dominate the longitudinal mode as the collision energy grows. Since we deal with new physics in our analysis, we restrict our calculations to the use of the longitudinal mode only.

The luminosity for two longitudinal vector bosons V_m and V_n emitted from i^{th} and j^{th} quarks reads

$$\begin{aligned}\frac{dL_{V_m^LV_n^L[q_iq_j]}}{d\hat{\tau}} = \frac{v_{m[i]}^2 + a_{m[i]}^2}{4\pi^2}\frac{v_{n[i]}^2 + a_{n[i]}^2}{4\pi^2}\frac{1}{\hat{\tau}}\times \\ \left[(1+\hat{\tau})\log(1/\tau) - 2(1-\hat{\tau})\right]\end{aligned} \tag{9}$$

where $v_{m[i]}$ and $a_{m[i]}$ are the vector and axial couplings of the gauge boson V_m to the quark current q_i. In particular,

$$v_{W[q_i]} = -a_{W[q_i]} = \frac{g}{2\sqrt{2}} \tag{10}$$

for any q_i, and

$$v_{Z[u]} = \frac{g}{4c_W}\left(1 - \frac{8}{3}s_W^2\right),\ a_{Z[u]} = \frac{g}{4c_W} \tag{11}$$

$$v_{Z[d]} = -\frac{g}{4c_W}\left(1 - \frac{4}{3}s_W^2\right),\ a_{Z[d]} = -\frac{g}{4c_W} \tag{12}$$

where $s_W = \sin\theta_W$ and $c_W = \cos\theta_W$.

For the numerical evaluation of the parton-parton luminosity $dL_{ij}/d\hat{s}$ we used the Mathematica [8] package Mane Parse [9] with the PDF set CT10 from the LHAPDF 6 library at HepForge repository [7]. The obtained parton-parton luminosities for both production mechanisms of the new vector resonance at the LHC ($\sqrt{s}$ = 13 TeV) are depicted in Fig. 2.

---

[1] In principle, the parton-parton luminosity is also sensitive to new physics via modifications of the SM couplings and the parton distribution functions. Nevertheless, we expect these effects to be negligible and ignore them in our analysis.

[2] We do not expect that this approximation would significantly influence conclusions of this study since we assume no direct interactions of the vector resonance to fermions. The investigation of the more general case with the direct interactions present is in progress.

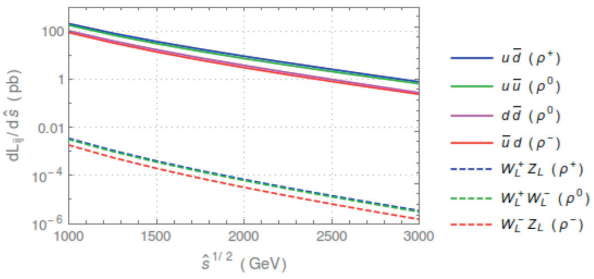

Fig. 2 The parton-parton luminosities for the DY (solid lines) and longitudinal VBF (dashed lines) production in the proton-proton collisions at $\sqrt{s} = 13$ TeV*; the CT10 set [7] of parton distribution functions was used*

As we can see the DY luminosities dominate over VBF ones by about 4 – 5 orders of magnitude. However, since the partial decay widths $\Gamma_{\rho \to WZ}$ and $\Gamma_{\rho \to WW}$ grow with the fifth power of the resonance mass their contributions can significantly increase the VBF production cross sections when heavier resonances are considered. This can be observed in the graph of the production cross sections shown in Fig. 3 for $g'' = 15$. Note that in the mass region above 2 TeV the Γ_ρ / M_ρ ratio exceeds 10 % which increases tension between reality and the assumptions for the NWA.

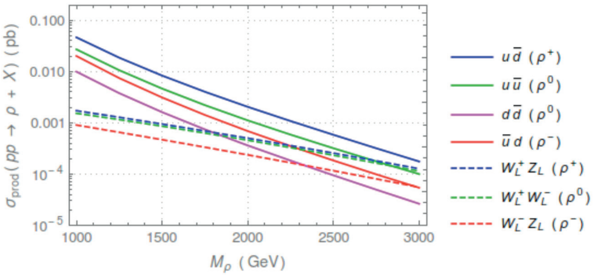

Fig. 3 The production cross sections of the new vector resonance via various initial states (see the legend) in proton-proton collisions at $\sqrt{s} = 13$ TeV *as a functions of* M_ρ*. The solid lines represent the DY processes, the dashed lines are for VBF processes. The shown curves were calculated at* $g'' = 15$

4. Results for the dilepton channel

Once the production cross sections have been evaluated, we are a single step from finalizing the predictions of the LHC cross sections of the processes under investigation. As we can see in (3) the final step involves the multiplication of the production cross section with the appropriate branching ratio. The branching ratios of the various decay channels of the resonance are those principal quantities through which the final cross section receives its sensitivity to the model under consideration. Thus, in this stage, we are in the position of investigating the cross section dependence on various model parameters. In addition, these predictions can be confronted with the experimental measurements provided by the LHC experiments. Consequently, various experimental restrictions on the model parameters can be derived.

The thorough analysis suggested at the end of the previous paragraph is not within the scope of this paper. Here, we will demonstrate only how much the results obtained by the upgraded computational approach influences the results obtained in our previous paper [3]. For that sake, we have calculated the cross section of the process with dileptons in the final state: $pp \to \ell\bar{\ell} + X$, where $\ell = e, \mu$. While this is not the dominant decay channel it is not very sensitive to the fermion couplings of the vector resonance and thus the obtained prediction is quite universal in this sense. The low sensitivity and the low cross section infers from the fact that light fermions do not couple directly to the vector resonances in our model. The interaction occurs only via the vector-boson mixing and is proportional to $1/g''$. From the experimental point of view, the dielectron and dimuon final states have the advantage of a relatively clean signal. The branching ratios of the combined dielectron and dimuon final states for various combinations of the values of g'' and M_ρ are shown in Table 1.

Using the dilepton branching ratios we calculate the cross section $\sigma(pp \to e^+e^- + \mu^+\mu^- + X)$ at $\sqrt{s} = 13$ TeV. The result as a function of M_ρ and for three different values of g'' is shown in Fig. 4. In addition, the graph of predicted cross section is superimposed with the ATLAS Collaboration curve showing the expected upper 95 % C.L. limit on the cross section times branching ratio [10]. The current experimental data do not contradict the ATLAS expectation curve [10] so we take it as the boundary of the sensitivity of the existing measurements in this channel. We can see that the predictions of our model lie well below this boundary. Thus none of the considered resonance masses are ruled out by the LHC measurement in this channel. This confirms our findings in [3].

The branching ratios of the combined dielectron and dimuon final states for various combinations of the values of g'' and M_ρ Table 1

	$BR(\rho^0 \to e^+e^- + \mu^+\mu^-) \times 10^3$				
M_ρ (GeV)	1000	1500	2000	2500	3000
g'' = 10	1.224	0.2529	0.08127	0.03353	0.01623
g'' = 15	1.223	0.2528	0.08125	0.03352	0.01623
g'' = 20	1.223	0.2528	0.08124	0.03352	0.01623

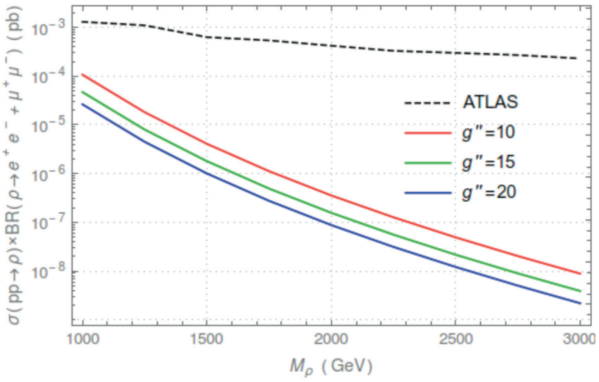

Fig. 4 The LHC production cross section times the branching ratio as a function of M_ρ *for the* $e^+e^- + \mu^+\mu^-$ *final state at* $\sqrt{s} = 13\,\mathrm{TeV}$ *calculated for three different values of the parameter* g'' *(solid lines); the dashed line shows the expected upper 95 % C.L. limit obtained by the ATLAS Collaboration*

The main goal of this work was to develop and test the upgraded version of the cross section calculations so that it can be used in a more complex analysis of the current limits for the tBESS model parameters. When our upgraded prediction of $\sigma(pp \to e^+e^- + \mu^+\mu^- + X)$ is compared with our previous calculations in [3] we find a difference at a level of several percents. The difference grows with the mass of the resonance. In particular, the upgraded calculation exceeds the previous prediction by about 0.5 % when $M_\rho = 1\,\mathrm{TeV}$ and falls below it by about 5 % when $M_\rho = 2\,\mathrm{TeV}$. We believe that our upgrade have had the most significant impact on the calculations of the VBF production. Since the contribution of the VBF production grows with M_ρ (see Fig. 3) this could explain the observed tendency in the discrepancy behaviour.

5. Conclusions

We have calculated the vector resonance production cross section for the $e^+e^- + \mu^+\mu^-$ final state as a function of the vector resonance mass and for various values of g'' within the effective description of new physics provided by the tBESS model. The predicted cross section is significantly below the sensitivity of the latest ATLAS measurements in this channel. Thus, the data provide no restrictions for the model there. This is in the agreement with our previous findings based on more rudimentary calculations in [3]. The upgraded calculations in this paper differ from the results in [3] from 0.5 to 5 % when M_ρ ranges from 1 TeV to 2 TeV. The upgrade of the calculations included the use of the CT10 set for the PDF's of protons and the use of the vector boson luminosity functions calculated precisely at the collision energy at which the used data had been collected.

This calculation was a part of preparing steps for more thorough analysis that would confront the tBESS model with the current LHC data in all measured channels: *WW*, *ZW*, *WH*, *ZH*, $jj_{neutral}$, $jj_{charged}$, $\ell\ell$, $\ell\nu$, *tt*, and *tb*. Beside analyzing all additional channels with a more restrictive potential expected from some, we will also turn on the direct interactions of the vector resonance with heavy fermions. It can provide the explanation why such a new vector resonance avoids its discovery at the LHC.

Acknowledgments

We would like to thank Karol Kovarik for useful discussions. The work of M.G. and J.J. was supported by the Grants LTT17018 and LG15052 of the Ministry of Education, Youth and Sports of the Czech Republic. M.G. was supported by the Slovak CERN Fund. J.J. was supported by the National Scholarship Programme of the Slovak Republic.

References

[1] AAD, G., et al. (ATLAS Collaboration): Observation of a New Boson at a Mass of 125 GeV with the CMS Experiment at the LHC. *Physics Letters B*, 716(1), 30-61, 2012; CHATRCHYAN, S., et al. (CMS Collaboration), ibid. 30, 2012.

[2] GINTNER, M., JURAN, J.: The Vector Resonance Triplet with the Direct Coupling to the Third Quark Generation. *The European Physical Journal C*, 73, 2577, 2013.

[3] GINTNER, M., JURAN, J.: The Limits on the Strong Higgs Sector Parameters in the Presence of New Vector Resonances. *The European Physical Journal C,* 76, 651, 2016; erratum: The European Physical Journal C, 77, 6, 2017.

[4] GINTNER, M., JURAN, J, MELO, I.: Top-BESS Model and its Phenomenology. *Physical Review D*, 84, 035013, 2011.

[5] PAPPADOPULO, D., THAMM, A., TORRE, R., WULZER, A.: Heavy Vector Triplets: Bridging Theory and Data. *Journal of High Energy Physics*, 1409, 060, 2014.

[6] DAWSON, S.: The Effective W Approximation. *Nuclear Physics B*, 249(1), 42-60, 1985.

[7] BUCKLEY, A., et al.: LHAPDF6: Parton Density Access in the LHC Precision Era [online]. *The European Physical Journal C*, 75, 132, 2015. Available: http://lhapdf.hepforge.org/pdfsets.

[8] WOLFRAM RESEARCH, Inc.: *Mathematica*, Version 10.4. Champaign, IL., 2016.

[9] CLARK, D. B., GODAT, E., OLNESS, F. I.: ManeParse: A Mathematica Reader for Parton Distribution Functions [online]. Available: https://ncteq.hepforge.org/mma/index.html.

[10] ATLAS COLLABORATION: Search for New High-Mass Resonances in the Dilepton Final State Using Proton–Proton Collisions at $\sqrt{s}$ = 13 TeV with the ATLAS detector. *ATLAS-CONF-2016-045*, Switzerland, 2016.

https://doi.org/10.26552/com.C.2017.3.77-82

COMMUNICATIONS

Norbert Tarjanyi - Daniel Kacik*

LITHIUM NIOBATE-BASED INTEGRATED PHOTONICS UTILIZING PHOTOREFRACTIVE EFFECT

Lithium niobate ($LiNbO_3$) is an ideal material with many interesting properties for integrated photonics. Despite the rich set of properties the technology of lithium niobate integrated optics has not evolved as much as integrated optics in III-V semiconductors and silicon photonics. Future applications of $LiNbO_3$ as an integrated optical platform require a technology that can materialize ultracompact and efficient optical circuits on the material. To achieve the goal two possible approaches can be considered: developing of tightly-confined lithium niobate photonic devices and circuits on silicon substrates by hybrid technologies and, developing pure lithium niobate photonic devices employing strong photorefractive effect. The latter approach is in more details discussed in the contribution and concrete examples of practically realized photonic structures are presented.

Keywords: *Lithium niobate, integrated optics, photonic integrated circuit, photorefractive effect, waveguide.*

1. Introduction

The development of the laser in the 1960s opened the possibility to transmit and process signals carried by optical beams. Since then the idea has attracted many researchers. The primary problems regarding a proper medium for signal transmission and optical components for signal processing were solved rather soon. As a result, the concept of integrated optics emerged, in which the through-the-air optical paths commonly used in laboratories were replaced by dielectric light-guides and conventional electrical integrated circuits were replaced by optical integrated circuits (OIC's) or photonic integrated circuits (PIC's). A decade later the development of low-loss optical fibers and connectors, creation of semiconductor laser diodes (e.g. GaAlAs and GaInAsP) and huge advances in photolithographic microfabrication techniques as well, helped to bring the integrated optics into real life and solve many practical problems. Moreover, in last two decades the microtechnology naturally evolved into nanotechnology giving birth to nanophotonics the important part of which is the fabrication of photonic crystals [1].

The OIC has a number of advantages compared to conventional electrical integrated circuit [2]: increased bandwidth; expanded frequency (wavelength) division multiplexing; low-loss couplers; expanded multipole switching; smaller size; light weight; low power consumption; batch fabrication economy; improved reliability; improved optical alignment; immunity from electromagnetic interference; immunity to vibration; safety in combustible environment; freedom from electrical short circuits or ground loop, etc. The major disadvantages of OIC's can be considered difficulty to use for electrical power transmission and high cost of developing new fabrication technology.

1.1 Material basis for OIC's and fabrication approach

The choice in which material fabricate an optical integrated circuit depends mostly on the function to be performed by the circuit. The OIC may be required to consist of different optical devices, passive and/or active. However, none of the material is suitable for both kinds of the devices working at once so a compromise must be made. This is reflected also in the OIC's fabrication.

There are two basic approaches to fabricate an OIC. One of these is the monolithic in which a single material is used for all devices. Monolithic circuits requiring a source of light can only be fabricated in active materials, mainly semiconductors such as GaAs, GaAlAs, GaAsP, GaInAs and other III-V and II-VI semiconductors. Passive materials like quartz, lithium niobate or polymers are also useful as substrate materials but generally an external light source, such as a semiconductor laser, must somehow be optically and mechanically coupled to the substrate [2].

The other approach is a hybrid one in which two, but usually more, materials are technologically bonded together

---

* **Norbert Tarjanyi, Daniel Kacik**
Department of Physics, Faculty of Electrical Engineering, University of Zilina, Slovakia
E-mail: tarjanyi@fyzika.uniza.sk

and optimized for performance of different integrated devices. The major advantage of the approach is that the OIC's can be fabricated using existing technology, piecing together devices which have been substantially optimized in a given material. The main disadvantage is that the bonds between the various elements of the circuit are subject to misalignment, or even failure, because of vibration and thermal expansion. Also, the monolithic approach is ultimately cheaper if mass production of the circuit is desired, because of the usage of automated batch processing.

2. Lithium niobate as a basis for integrated photonics

Lithium niobate is an ideal material with many interesting properties for integrated photonics. First, it is transparent from the UV to IR range of the electromagnetic spectrum. Doping the crystal with rare earth elements, such as erbium can lead to optical gain. A unique advantage is the material's strong second-order nonlinear optical properties, which allows the control of the refractive index of the material via the electro-optic effect. The nonlinearity also allows mixing of optical signals at different wavelengths for parametric amplification, second-harmonic generation [3], wavelength conversion, as well as generation of entangled photon pairs [4]. Using the piezo-electric properties of $LiNbO_3$, it is possible to make various acousto-optical devices but nowadays, the most widely used devices based on $LiNbO_3$ are high-speed electro-optical modulators [5, 6].

As optical components continue to replace its electrical counterparts in various signal processing applications there is a growing demand to integrate more photonic devices onto a single chip. In the last few years strong efforts have been made to develop silicon based photonic chips [7]. However, the physical limitations of the material and demanding technology as well, naturally led to an idea combine the advantages of various traditional materials and other technologies also used in photonics. The result is a hybrid technology called "lithium niobate on insulator" (LNOI) which is very promising for preparation of photonic circuits and their components [7 - 11]. The monolithic fabrication technology is still mainly used for preparation of passive PIC's on $LiNbO_3$ substrate. Here, several quite different approaches can be distinguished like [e.g. 12]: local doping followed by thermal diffusion, proton exchange, ion implantation; ferroelectric domain engineering; use of light-induced phenomena including solitons [12]. Nowadays, first three approaches represent a well-established techniques and a number of various kinds of waveguides and wave guiding structures was prepared using them up to date. The last two approaches are rather new and offer new possibilities hardly achievable by traditional techniques. Recently, the last approach mentioned is of a great interest as, in principle, it does not require any complicated supplementary technology, and is chemicals free. As a laser light with the proper wavelength, power and gradient of intensity is used to induce processes within the $LiNbO_3$ crystal leading to required local change of its optical properties the technique is often regarded as direct laser writing (DLW) [13 - 16].

3. DLW technique of fabrication PIC's and their components

In lithium niobate the direct laser writing technique can be performed in visible using a proper continuous wave laser light source as well as in ultraviolet or infrared regions of electromagnetic spectrum, using ultra-short laser pulses. Even if there are numerous analogies such as the setup scheme, the dependence on the crystal orientation and the obtainable structures, the mechanisms responsible mainly for refractive index change are different. In the case the changes are induced due to visible light the effect is called photorefractive. Actually, the photorefractive effect is a combination of several mechanisms including optical ionization of certain impurities, spatial redistribution of released charge carriers which gives rise to internal electric field and finally, linear electro-optic effect [17]. Further, we will limit our discussion to photorefractive effect only as it is still the most common phenomenon used for fabrication of photonic structures. Recently, we have investigated the effect in various $LiNbO_3$ crystals and, besides the investigation, also created some applications useful for the implementation into photonic integrated circuits. An overview that follows documents exceptional technological potential of the photorefractive phenomenon.

3.1 Photorefractive gratings

The most common structure produced in a $LiNbO_3$ crystal is a holographic grating created due to illumination of the crystal by light with harmonic spatial distribution of intensity. The desired distribution of intensity of light can be simply obtained by interference of two laser beams (we usually used the blue line of Ar ion laser) [1]. Since the setup is similar to that used in holography when recording a hologram, the produced grating is often called the holographic one. The existence of the recorded grating can be proved by diffraction of an extra light beam of a different wavelength (e.g. red line of He-Ne laser) as was the wavelength of the recording beams or by putting the crystal into one arm of Mach-Zehnder interferometer, for example, or both [18]. As the grating is represented by a region of spatially modulated refractive index, it behaves like a phase object and can be imaged by means of an interferometer. For illustration, the spatial distribution of the refractive index change representing a grating imaged in this way is shown in Fig. 1a.

In principle, the grating can work in either transmission (Fig. 1b) or reflection (Fig. 1c) regimes depending on desired

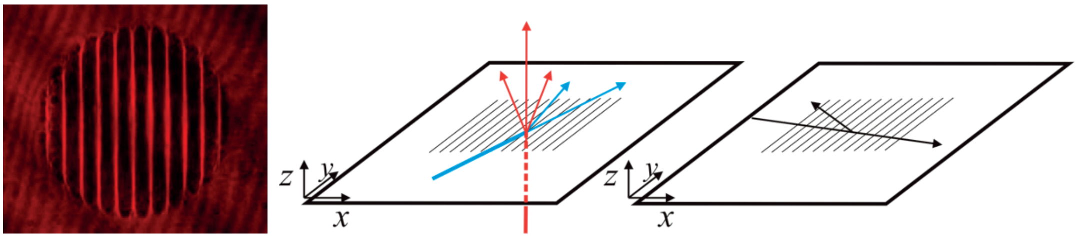

(a) (b) (c)

Fig. 1 The refractive index distribution representing the photorefractive grating with a spatial period Λ *= 200 μm recorded in 1 mm thick sample of LiNbO$_3$ imaged by Mach-Zehnder interferometer (a). Photorefractive grating can be used to work in the transmission regime (b) or the reflection regime (c).*

function of the device. In the transmission regime, the wavelength dependence of diffraction of light on the grating with constant spatial period leads simply to spatial separation of signals with different wavelengths, which can be used for demultiplexing and redirecting of those signals. However, in a real life the situation might become a bit complicated in case the grating is thick (one cannot neglect the thickness of the grating with respect to grating spacing) because of energy coupling between diffraction orders. In the reflection regime the same grating will show the wavelength selectivity, which can be used for signal filtering.

Depending on the wavelength of the recording beams and the mutual angle between beams we can conveniently create gratings with various spatial periods in the range from few micrometers up to few hundreds of micrometers. Another important parameter of a grating is its diffraction efficiency. For reflection grating the diffraction efficiency is function of grating spacing, amplitude of refractive index modulation Δn and wavelength of light. As an example the diffraction efficiencies (the so called reflection spectra) for the reflection grating with grating spacing of 1 mm and length 10 mm are shown in the Fig. 2.

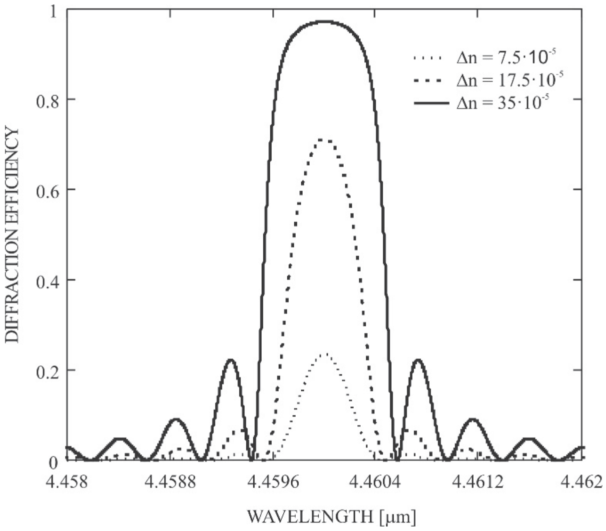

Fig. 2 Diffraction efficiencies of 10 mm long reflection grating with grating period Λ *= 1 μm for various amplitudes of refractive index modulation Δn*

The diffraction efficiencies η were calculated according to coupled mode theory approach [19]

$$\eta = \frac{|\kappa|^2 \cdot \sinh^2(s \cdot L)}{s^2 \cdot \cosh^2(s \cdot L) + \left(\frac{\Delta\beta}{2}\right)^2 \cdot \sinh^2(s \cdot L)}, \tag{1}$$

where parameters κ, $\Delta\beta$ and s are

$$\kappa = \frac{2\pi \cdot \Delta n \cdot n_0 \cdot \Lambda}{\lambda^2}, \tag{2}$$

$$\Delta\beta = \frac{2\pi}{\Lambda} - \frac{4\pi}{\lambda_B} \cdot n_o \cdot \sin\theta_B = 0, \tag{3}$$

$$s^2 = |\kappa|^2 - \left(\frac{\Delta\beta}{2}\right)^2. \tag{4}$$

In Equations (1) - (4) L is the length of the grating, Δn is the refractive index modulation, n_0 is the refractive index of the crystal, Λ is the grating period, λ is the wavelength of light, λ_B and θ_B are the Bragg wavelength and the Bragg angle, respectively.

In photorefractive LiNbO$_3$ crystals the amplitude of the refractive index modulation depends on the exposure (product of intensity of recording light and time) and can reach, in the used samples, the values up to $7.5 \cdot 10^{-4}$. It can be seen from the Fig. 2 that reflection grating with 1 mm spacing and 10 mm length is set to work with high efficiency at wavelength λ = 4.46 μm. Such grating would be suitable for the devices and applications designed for mid-infrared region of electromagnetic spectrum.To get closer to NIR or even VIS region one has to set the grating spacing to the sub-micrometer values. This can be done, for example, by changing the recording geometry.

When we let the two coherent optical waves counter-propagate in the crystal, they will interfere with each other and form a standing optical wave with the spacing between two maxima being half of the wavelength of the original waves in the medium [20]. If the waves are propagating along *c*-direction of the LiNbO$_3$ crystal, the gradient of the interference pattern will be along this direction, too. This is the welcome situation for the standing wave being successfully recorded. The counter-propagating waves can be formed for example, using one beam propagating through the crystal and reflecting on the backside of the crystal due to Fresnel reflection. The efficiency of the reflection can be increased, for example, by metalizing the backside of the crystal and so the modulation of the interference pattern of the standing wave can be increased, too. The calculated diffraction efficiency for such grating written by light with wavelength λ = 488 nm is shown in Fig. 3.

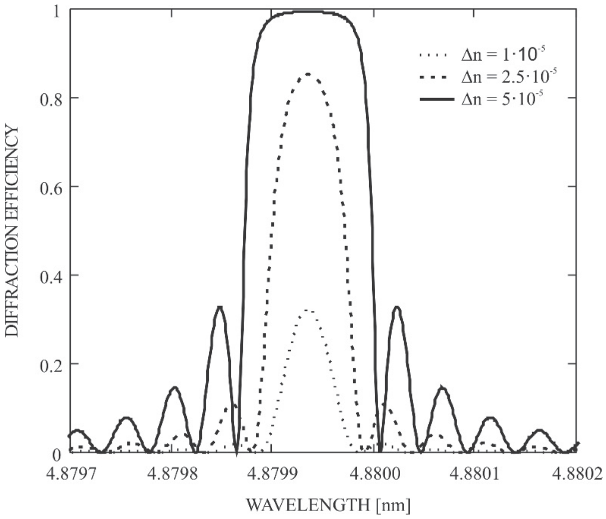

Fig. 3 Diffraction efficiency of the grating formed by standing optical wave calculated for various amplitudes of refractive index modulation Δn. Grating spacing $\Lambda \sim 0.1\mu m$*, interaction length* $L = 10 mm$*.*

The disadvantage of this ‘standing wave’ geometry is evident: only reflection grating for wavelength to which the crystal is photosensitive can be produced. To overcome the disadvantage the gratings with sub-micrometer periods can be fabricated by point-by-point direct laser writing method which combines the stationary, focused laser beam with computer-controlled motion of the crystal or vice versa. The result is a photonic structure with desired parameters.

There is one more feature of the light induced refractive index inhomogeneity within the crystal – it also possesses the dioptric properties [21]. After illumination of the grating shown in Fig. 1a by light the phase of the light-wave behind the structure will be modified resulting in a focusing of rays into lines. The grating thus behaves like an array of cylindrical microlenses [22]. Combining two sets of such arrays oriented perpendicularly to each other will produce a microarray of spherical lenses. The spatial period of the array and the focal length of the lenses can be well controlled by the angle of interfering beams creating the grating and exposure, respectively.

3.2 Photorefractive waveguide

The optical waveguide is the fundamental element for the integrated photonics. Utilizing the photorefractive effect a properly structured optical field can create a waveguide in $LiNbO_3$ crystal. It is practical to use the optical fields with spatial symmetry being somehow related to the symmetry of the waveguide. Thus a Gaussian laser beam expanded by a cylindrical lens or such a beam spatially restricted in order to form a strip or set of strips can be considered the appropriate optical field. For the structure to behave as a waveguide must be assured that the refractive index of the guiding layer is higher than that of the surroundings. As already mentioned the best contrast in the refractive index change is between the illuminated and dark regions and is achieved when the gradient of the illumination is parallel with *c*-axis of the crystal. When the crystal is irradiated by the optical field with the Gaussian spatial distribution of the intensity modified by a cylindrical lens the inhomogeneity of the refractive index of the shape as shown in Fig. 4 is induced in the crystal. The spatial distribution of the refractive index was calculated according to the assumptions that: (i) the refractive index changes are dominantly due to electro-optic effect, (ii) the diffusion of the charge carriers is negligibly small and the photogalvanic current is dominantly contributing to the distribution of the charge density, (iii) the crystal is surrounded by an electrically conductive medium [23].

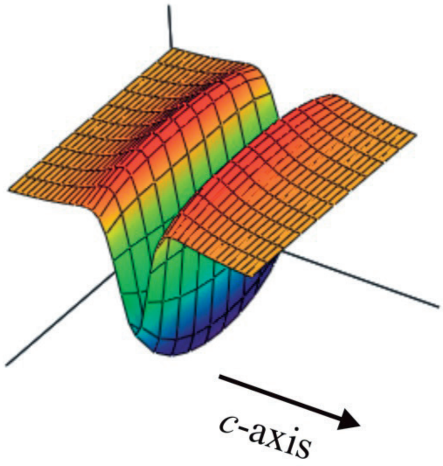

Fig. 4 Calculated refractive index change induced by an expanded Gaussian beam

The pattern shown in Fig. 4 consists in a negative refractive index variation at the core of the beam and in a two-sided lobe structure disposed along the *c*-direction with a positive refractive index change. Thus each one of these lobes with positive refractive index can be used to guide light.

We used a different approach and recorded the waveguide by means of a spatially restricted Gaussian beam modified by a cylindrical lens in two steps. Firstly, we applied the recording optical field with intensity 1.2 $mWmm^{-2}$ onto the crystal and set the proper recording time to achieve the steady-state value of refractive index change (t = 300 s in this case). After that the sample was moved mechanically along *c*-axis of the crystal by about 150 μm and the second exposure at the same conditions finished the process of the waveguide formation (Fig. 5) and the guiding properties were demonstrated [23, 24].

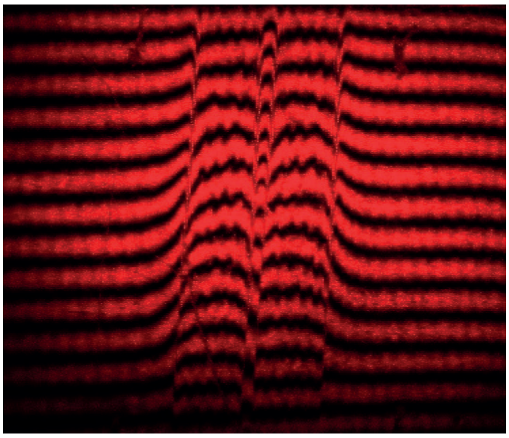

Fig. 5 Spatial distribution of refractive index in the sample with recorded waveguide imaged by means of Mach-Zehnder interferometer. The width of the illumination strip (two wider strips in the figure) is 1 mm. The width of the waveguiding area in between the strips is 150 μm

4. Conclusion

We presented an overview of the issue of integrated optics and photonics in general and with focus on the current state of photonics employing lithium niobate as a basis for various passive and active photonic devices. Our recent work devoted to investigation of photorefractive effect in lithium niobate showed applicability of the effect in the fabrication of passive photonic devices based on waveguides, gratings and microlens arrays. These can be combined and naturally integrated on a single lithium niobate substrate material forming a photonic integrated circuit performing e.g. waveguiding, filtering and/or demultiplexing functions. The direct laser writing method of fabrication of the photonic devices in $LiNbO_3$ has a big potential due to its simplicity, no need of post-processing and 'green' (chemicals free) approach.

Acknowledgements

This work was supported by Slovak National Grant Agency No. VEGA 1/0491/14, 1/0278/15 and Slovak Research and Development Agency under the project No. APVV-15-0441.

References

[1] KACIK, D., et al.: Photonic Crystals: Optical Structures for Advanced Technology. *Communications - Scientific Letters of the University of Zilina*, 10(2), 25-29, 2008.

[2] HUNSPERGER, R. G.: *Integrated Optics: Theory and Technology*, Chapter 1. Springer, New York, p. 1-12, 2009.

[3] GEISS, R., et al.: Fabrication of Nanoscale Lithium Niobate Waveguides for Second-Harmonic Generation. *Optics Letters*, 40(12), 2715-2718, 2015.

[4] JIN, H., et al.: On-Chip Generation and Manipulation of Entangled Photons Based on Reconfigurable Lithium-Niobate Waveguide Circuits. *Physical Review Letters,* 113(10), 103601-1-103601-5, 2014.

[5] WOOTEN, E.L., et al.: A Review of Lithium Niobate Modulators for Fiber-Optic Communications Systems. *IEEE Journal of Selected Topics in Quantum Electronics,* 6(1), 69-81, 2000.

[6] SAKAMOTO, T., et al.: Novel Photonic Devices Based on Electro-Optic Modulation Technologies. *Journal of the National Institute of Information and Communications Technologies*, 53(3), 25-32, 2006.

[7] POBERAJ, G., HU, H., SOHLER, W., GUNTER, P.: Lithium Niobate on Insulator (LNOI) for Micro-Photonic Devices. *Laser Photonics Reviews*, 6(4), 488-503, 2012.

[8] WEIGEL, P.O., et al.: Lightwave Circuits in Lithium Niobatethrough Hybrid Waveguides with Silicon Photonics.*Scientific Reports*, 6, 22301, 2016.

[9] GORBACH, A.V., DING, W.: Microfiber-Lithium Niobateon Insulator Hybrid Waveguides for Efficient and Reconfigurable Second-Order Optical Nonlinearity on a Chip. *Photonics*, 2, 946-956, 2015.

[10] CHEN, L., NAGY, J., REANO, R.M.: Patterned Ion-Sliced Lithium Niobate for Hybrid Photonic Integration on Silicon. *Optical Materials Express*, 6(7), 2460-2467, 2016.

[11] CHEN, L., CHEN, J., NAGY, J., REANO, R. M.: Highly Linear Ring Modulator from Hybrid Silicon and Lithium Niobate. *Optics Express*, 23(10), 13255-13264, 2015.

[12] BAZZAN, M., SADA, C.: Optical Waveguides in Lithium Niobate: Recent Developments and Applications. *Applied Physics Reviews*, 2, 040603-1-040603-25, 2015.

[13] MAILIS, S., et al.: Direct Ultraviolet Writing of Channel Waveguides in Congruent Lithium Niobate Single Crystals. *Optics Letters*, 28(16), 1433-1435, 2003.

[14] MIZEIKIS, V., et al.: Direct Laser Writing: Versatile Tool for Microfabrication of Lithium Niobate. *Journal of Laser Micro/Nanoengineering*, 7(3), 345-350, 2012.

[15] PAIPULAS, D., BUIVIDAS, R., JUODKAZIS, S., MIZEIKIS, V.: Local Photorefractive Modification in Lithium Niobate Using Ultrafast Direct Laser Write Technique. *Journal of Laser Micro/Nanoengineering*, 11(2), 246-252, 2016.

[16] VITTADELLO, L., et al.: Photorefractive Direct Laser Writing, *Journal of Physics D: Applied Physics,* 49, 125103, 2016.

[17] YEH, P.: *Introduction to Photorefractive Nonlinear Optics*, Chapter 3. John Wiley & Sons, Inc., New York, p. 82-117, 1993.

[18] TARJANYI, N.: Real-Time Imaging of Grating Formation in $LiNbO_3$:Fe Using Mach-Zehnder Interferometer. *Optical Engineering*, 49(8), 085602, 2010.

[19] KOGELNIK, H.: Coupled Wave Theory for Thick Hologram Grating. *Bell System Technical Journal*, 48, 2909-2947, 1969.

[20] TARJANYI, N., KACIK, D., TARJANYIOVA, G.: *Light-Induced Microstructures in $LiNbO_3$:Fe Crystal in Photonic Crystal Fibers*. Proceeding of SPIE 6588, 658812, 2007.

[21] TARJANYI, N.: Specially Shaped Negative Lens Produced in Lithium Niobate Crystal. *Optical Engineering*, 53(5), 057104, 2014.

[22] ZILINSKA UNIVERZITA V ZILINE: *System of Dioptric Elements from Photorefractive Material* (in Slovak). Inventors: TUREK, I., TARJANYI, N., DUBRAVKA, M., G02B 17/00.UV 4988, Industrial property office of the Slovak Republic, 2007.

[23] TARJANYI, N., TUREK, I.: Influence of Surroundings on Photorefractive Effect in Lithium Niobate Crystals. *Physica B*, 407, 4347-4353, 2012.

[24] TARJANYI, N., KACIK, D.: *Fabrication and Evaluation of Photorefractive Vaweguide in $LiNbO_3$:Fe, in Integrated Photonics: Materials, Devices and Applications.* Proceeding of SPIE 8069, 80690B, 2011.

https://doi.org/10.26552/com.C.2017.3.83-87

Tomas Nahlik*

COMPARISON OF CONTRASTING METHOD BASED ON LOCAL CONTRAST MEASUREMENT

Some biological experiments and techniques, especially electron microscopy, require special sample treatments. These treatments usually change the samples and biologist cannot apply different techniques on the very same sample. In this case, it is necessary to have some comparison method to compare different treatments. In the electron microscopy, the heavy metals are used as contrasting chemicals. Question is which contrasting method is the best or which is better for imaging of given samples. Standard method is based on visual comparison and it is user dependent. We propose to measure local contrast and some other values like SNR (Signal-to-Noise Ratio), histograms, intensity profiles on the borders of the object and calculate statistical values for pixels' intensities.

Keywords: *TEM images, local contrast measurement, image comparison, biological samples, SNR.*

1. Introduction

Imaging of biological samples using the TEM (Transmission Electron Microscope) working at the accelerating voltage 100 kV requires usually an enhancement of contrast. This is achieved by addition of heavy metals, like Os, U, Pb, etc., into the cell structure during the staining steps of the specimen preparation [1]. The next question is how to compare the resulting contrast of selected organelles in the TEM images.

The contrast or contrast resolution is defined as ability to distinguish between differences in intensity values of the object or area of interest and its surroundings in the image [2]. In our case, we are trying to find methods which will increase the difference between organelles and the rest of the cell and also between organelles themselves. The standard way of comparison is that user looks at the images and says what is better. This is of course very subjective and almost irreproducible measurement (observation). The question is how to measure local contrast in the image. There are several methods using the SNR (Signal-to-Noise Ratio), RMS Contrast or others [3, 4]. But not all of them are useable for the TEM images due to the high level of noise. And many of them are only for evaluation of the whole image.

2. Materials and methods

To determine the difference between contrasting methods we need to define some ratio or some scale. Contrast of the object depends on the intensity of this object and on the intensity of its surroundings. We developed a tool, which provides us with the basic statistical analysis of these values. It is necessary to select the object of interest manually but the rest of the analysis is done automatically. The automatic detection does not work properly due to the high magnification, high level of noise and fuzzy borders of the object.

The decision about which method is better will not be made based on the SNR nor difference between the value of average intensity of the object and its neighbourhood, this can be misleading, but on the contrast value, calculated based on the Michelson contrast:

$$C = \frac{L_{\max} - L_{\min}}{L_{\max} + L_{\min}} \tag{1}$$

where $L_{\max}$ and $L_{\min}$ are the highest and the lowest luminance [5]. We cannot use the maximum and minimum luminance or intensities because of the high level of noise. We decided to change the Michelson formula to use the average (or median) values of intensities:

$$C = \frac{I_O - I_B}{I_O + I_B} \tag{2}$$

---

* **Tomas Nahlik**
The Institute of Technology and Business in Ceske Budejovice, Faculty of Technology,
Department of Informatics and Natural Sciences, Czech Republic
E-mail: nahlik@mail.vstecb.cz

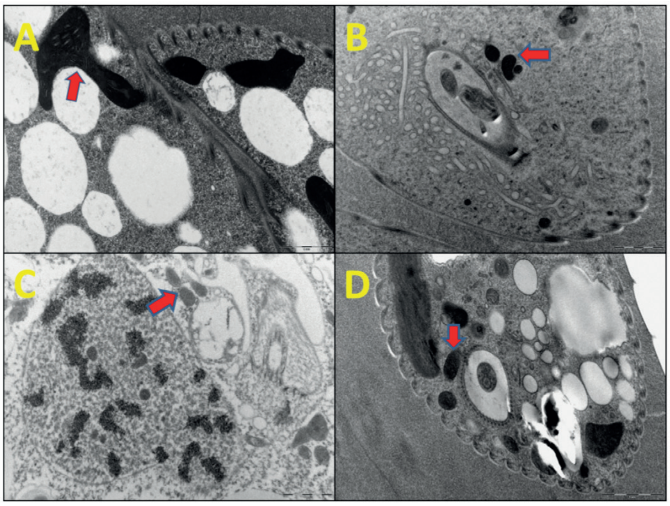

Fig. 1 Images of Euglena gracilis using different contrasting methods: A - 2 % OsO_4 in 100 % acetone; B – OTO (O-osmium, T-thiocarbohydrazide, O-osmium) method (2 % OsO_4, 100 % acetone, thiocarbohydrazide); C – OTO plus 0.1 % UA, $Pb(NO_3)_2$ and methanol; D – Ferrikyanide plus OTO and 0.1 % UA

where I_O and I_B are values of average (or median) intensity of the object and its close surroundings.

We are calculating the SNR value, as well; in our case this value is lower than unity, because the object is darker than the background. In addition, the graphs of the intensity profiles over the borders of the object can be helpful. The steeper and higher the line is, the more contrast the object has. We used this approach to evaluate the contrast of mitochondria in cells of Euglena gracilis prepared under different procedures using various staining agents (see Fig. 1).

The analysis of the figure is semiautomatic as mentioned above. The manual selection of the ROI (Region of Interest) is required. Selected ROI is eroded by the disc structural element of size 2. This is done because even the manual selection of the borders can be inaccurate. Erosion shrinks little bit the selection but it is more probable that the whole eroded area will be inside the object. This eroded area serves as binary mask of the object. Similar step is done for analysis of the surroundings. The original ROI is dilated by the disc structural element of size 2. In this case the area is enlarged. This step gives us some tolerance (±2 px from original selection) of inaccurate selection of the object's borders. This final mask is dilated by a disc of size 25. When we subtract these two masks we obtain the surroundings (close neighbourhood) of the object.

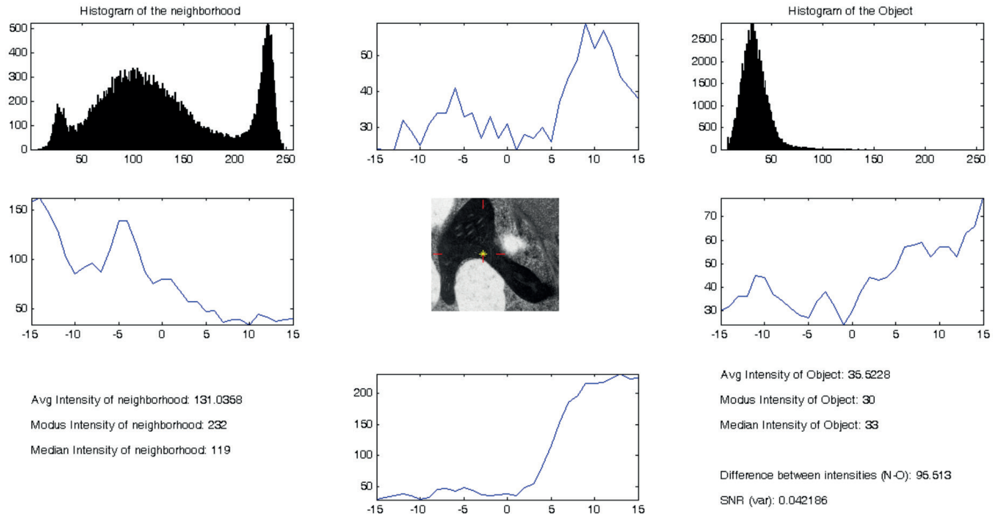

```
Avg Intensity of neighborhood: 131.0358
Modus Intensity of neighborhood: 232
Median Intensity of neighborhood: 119
```

```
Avg Intensity of Object: 35.5228
Modus Intensity of Object: 30
Median Intensity of Object: 33

Difference between intensities (N-O): 95.513
SNR (var): 0.042186
```

Fig. 2 Analysis of the sample A. Upper row: Histogram of neighborhood, top intensity profile, histogram of the object; Middle row: Left intensity profile, image of ROI with marked center (yellow star) and intensity profiles (red lines), right intensity profile; Bottom row: Measured characteristics of the neighborhood, bottom intensity profile, measured characteristics of the object

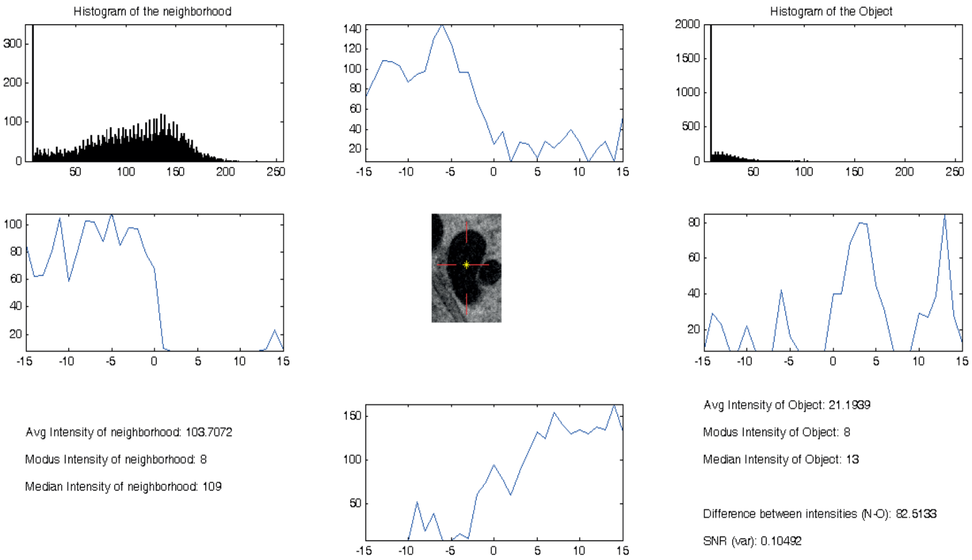

Fig. 3 Analysis of the sample B. Upper row: Histogram of the neighbourhood, top intensity profile, histogram of the object; Middle row: Left intensity profile, image of ROI with marked centre (yellow star) and intensity profiles (red lines), right intensity profile; Bottom row: Measured characteristics of the neighbourhood, bottom intensity profile, measured characteristics of the object

We are plotting the histograms of the neighbourhood and the object to have better impression how the intensities in these areas are represented. There are 4 graphs of the intensity profiles at the borders of the object, as well. We found the centre as a centroid of the object and the profiles are taken horizontally and vertically according to the centre. On these graphs we can see how precisely the object was selected.

3. Results and discussion

Measurement of the sample A (same as in Fig. 1A - contrasting method 2 % OsO_4 and 100 % acetone - is presented in Fig. 2, of the sample B - contrasted with OTO method (2 % OsO_4, 100 % acetone, thiocarbohydrazide) - in Fig. 3, of the sample C - with OTO plus 0.1 % UA, $Pb(NO_3)_2$ and methanol - in Fig. 4, and the last sample D - contrasted with Ferrikyanide plus OTO and 0.1% UA - Fig. 5.

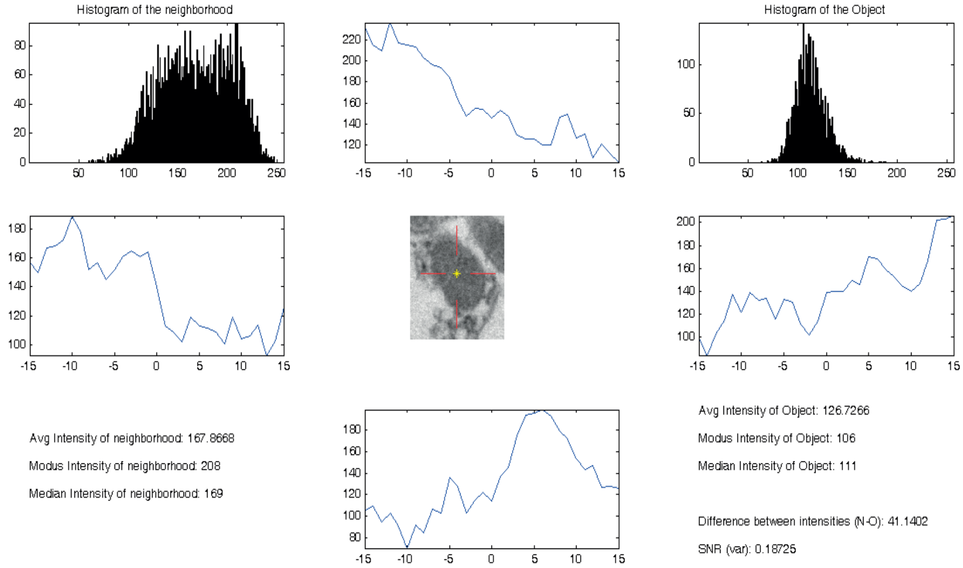

Fig. 4 Analysis of the sample C. Upper row: Histogram of the neighbourhood, top intensity profile, histogram of the object; Middle row: Left intensity profile, image of ROI with marked centre (yellow star) and intensity profiles (red lines), right intensity profile; Bottom row: Measured characteristics of the neighbourhood, bottom intensity profile, measured characteristics of the object

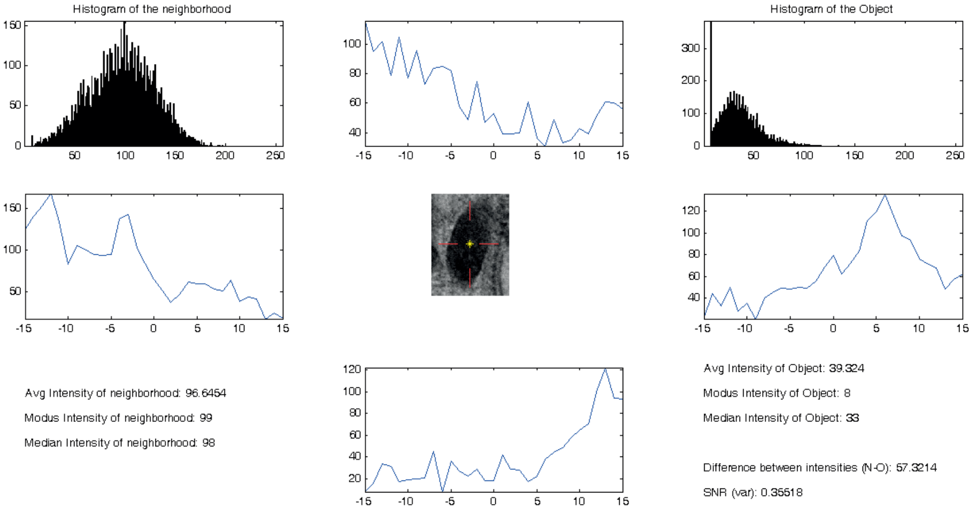

Avg Intensity of neighborhood: 96.6454

Modus Intensity of neighborhood: 99

Median Intensity of neighborhood: 98

Avg Intensity of Object: 39.324

Modus Intensity of Object: 8

Median Intensity of Object: 33

Difference between intensities (N-O): 57.3214

SNR (var): 0.35518

Fig. 5 Analysis of the sample D. Upper row: Histogram of the neighbourhood, top intensity profile, histogram of the object; Middle row: Left intensity profile, image of ROI with marked centre (yellow star) and intensity profiles (red lines), right intensity profile; Bottom row: Measured characteristics of the neighbourhood, bottom intensity profile, measured characteristics of the object

If we looked at images, we can say something about the contrast. The methods (or images) can be sorted by the decreasing contrast by the user probably as B, A, D, C. Maybe someone can swap B and A to A, B, D and C. This evaluation is very individual and subjective. Can we find some objectively defined metric, which can be used universaly?

In Table 1 are shown the measured values and in Table 2 are shown the calculated properties and statistical analysis of measured values.

If we looked at values in these tables, we can estimate the order with the decreasing contrast. The first clue can be the differences in the average intensities. This gives us the sequence A, B, D and C. This corresponds to the visual comparison, but we cannot say that the contrast of the sample B is twice higher than in image C, because the numbers represent only the average intensities.

The standard measure is the signal-to-noise ratio. SNR for images is defined as the ratio of the average intensity of the object and standard deviation of the intensity the background. We can also take the value of the signal divided by the value of the noise (background).If we have a look at numbers in Table 2, corresponding to the SNR, we can claim that in this case the SNR is not useful (maybe the SNR calculated with average values in reverse order).

The next measure is the Michelson contrast. The contrast calculated using average or median values gives us sequence B, A, D and C. This value is lower than zero, because in formula is intensity of the object minus intensity of the background and the

Measured characteristics of the object and its neighbourhood Table 1

Neighborhood and Object characteristics	**A**	**B**	**C**	**D**
Average intensity of the neighbourhood	131.0358	103.7072	167.8668	96.6454
Modus intensity of the neighbourhood	232	8	208	99
Median intensity of the neighbourhood	119	109	169	98
STD of the neighbourhood	62.77	45.55	35.69	31.84
IQR of the neighbourhood	98	66	57	45
Average intesity of the object	35.5228	21.1939	126.7266	39.324
Modus intensity of the object	30	8	106	8
Median intensity of the object	33	13	111	33
STD of the object	14.36	19.75	15.06	18.39
IQR of the object	15	20	19	24

Statistical evaluation of measured characteristics Table 2

Neighbourhood and Object evaluation	A	B	C	D
Difference between avg. intensities (N-O)	95.513	82.5133	41.1402	57.3214
SNR – standard definition	0.56592	0.465289	3.550759	1.23505
SNR – variance	0.042186	0.10492	0.18725	0.35518
SNR – avg.	0.2710923	0.2043629	0.7549235	0.4068895
SNR – median	0.2773109	0.1192661	0.6568047	0.3367347
SNR – modus	0.1293103	1	0.5096154	0.0808081
Contrast – average	-0.57599	-0.60963	-0.14257	-0.41625
Contrast – median	-0.565789	-0.786885	-0.207143	-0.496183
Contrast – modus	-0.770992	0	-0.324841	-0.850467

background is brighter than the object itself. If the object would be brighter than the background the number would be positive.

Of course, the intensity of the sample can be affected by many variables. We expected in our test that images were taken under the same or almost the same conditions and with the focus on the best images. This means that we try to avoid changes of other conditions except the contrasting technique and changes of the sample.

The shape of histogram of the intensities distribution in the object, as well as STD and IQR values, gives us the knowledge about contrast inside the object, whether we can determine the inner structure or not.

Also comparison of STD (IQR) values of the object and STD (IQR) values of the surroundings can tell us something about the intensity distribution of these parts of the image.

Evaluation of contrast, based on measurement, gives us the opportunity to redesign the experiments to get better image and use automatic image processing of obtained results.

Problem with biological samples (experiments) is that they are not fully repeatable. You need to use different part of the cell, different cut through the sample or completely different cells. Some differences in samples and measurements should be considered as differences in the samples and not in contrasting methods because the organelles do not have the same surroundings in every cell.

4. Conclusion

Our analysis brings another view on the local contrast measurement. This analysis can be used, due to manual selection of borders, in cases where the standard algorithms for automatic edge detection fails. As can be seen, objects in the images from the electron microscope can have very fuzzy borders.

Testing of this algorithm was done by using 8 bit images, but it can be used with very small changes for analysis of 12 bit or 16 bit images. The 8 bit images were used because we already had many different images with different contrasting methods which were used for the visual comparison of the contrasting methods.

From comparison of different metrics and different statistics with the visual evaluation of the images, we can claim that for the TEM images and images with similar structure, the changed Michelson contrast (Equation 2) using average or median values, is the appropriate method for local contrast measurement.

Acknowledgement

I would like to thank to Jana Nebesarova and Marie Vancova for the collaboration and for images. The images were taken on the TEM at the Biology Centre of the Czech Academy of Sciences.

References

[1] ELLIS, E. A.: *Staining Sectioned Biological Specimens for Transmission Electron Microscopy: Conventional and En Bloc Stains*. Kuo, J. (Ed.), Electron Microscopy, p. 57-72, Springer, New York, 2014.

[2] ALLISON, D., VON SCHULTHESS, G. K.: *The Encyclopedias of Medical Imaging*, 2nd ed. Isis Medical Media, New York, 1998.

[3] PELI, E.: Contrast in Complex Images. *Journal of the Optical Society of America,* 7(10), 2032-2040, 1990.

[4] GONZALEZ, R.S., WINTZ P.: *Digital Image Processing*. Addison-Wesley Publishing Co., USA, 1977.

[5] MICHELSON, A. A.: *Studies in Optics.* University of Chicago Press, Chicago, 1927.

https://doi.org/10.26552/com.C.2017.3.88-95

Tomas Ivaniga - Petr Ivaniga - Jan Turan - Lubos Ovsenik*

ANALYSIS OF POSSIBILITIES OF INCREASING THE SPANNED DISTANCE USING EDFA AND DRA IN DWDM SYSTEM

The aim of this article is a comparison of the EDFA (Erbium Doped Fibre Amplifier) and the DRA (Distributed Raman Amplifier) in a fully optical communication system, working on a specific wavelength. The amplifiers are compared based on their position in the optical loop and are evaluated according to the Q-factor and bit error rate (BER). In the case of the DRA, the accomplished distance was smaller, while changing the optical power in CW (Continuous Wave) to attain better BER. In the application of the EDFA a similar optical loop was created, as well, while the basic parameter for comparison was a bit speed. For the EDFA the bit speed was changed from 10 to 15 Gbps. For the DRA the change was in the power from 1 to 3 mW with the bit speed kept at 10 Gbps. This publication also focuses on the need for such application of a transfer system in a software environment. It would enable examination and research and consequently a minimising of the influence of non-linear effects impacting the particular WDM (Wavelength Division Multiplex) system.

Keywords: *BER, DRA, EDFA, WDM.*

1. Introduction

Our age cannot be called anything but the age of information and telecommunication technologies. Year by year a heightened demand for information is recorded, enabling new services, especially in the area of telecommunication. The internet connection is a matter of course for every household. With it is also connected a greater demand for services like video on demand (VoD), video or music streaming, VoIP and many others. The growing number of users who need to transfer a still greater amount of data though the current infrastructure leads to many problems which the current data networks find hard to manage [1 - 3]. One of these problems is the bandwidth. Until recently the most widespread type of medium for network transfer was metallic wiring. However they reached their physical limits of capacity and bandwidth. Metallic wiring is becoming more and more insufficient. Because of that there had to be found a new transfer medium. This new type of medium is optical fibre.

One convenient faculty of optical fibre springs from the property of light. It is a large bandwidth limited only by the frequency of the light mode. Optical fibres are preferred mostly due to their ability to ensure a faster transfer and of a greater quality for a large amount of data in a very short time. Nowadays optical fibre enables the transfer of data in amounts up to 10 Gbps - 40 Gbps [4 - 6]. The capacity of optical networks can be additionally enlarged by using the technology of the WDM. The WDM enables several channels to be transferred while using one physical optical fibre. Thanks to the WDM systems it is possible to attain the transfer speed of 1 Tbps. The increasing number of transfer speeds for ever-lengthening distances is also beginning to reach the limits for optical fibre. The main factor influencing the quality and reliability is the attenuation and the dispersion of the optical fibre [7, 8]. In addtion, one cannot omit mentioning such non-linear effects as, for example: SPM (Self Phase Modulation), XPM (Cross Phase Modulation) and FWM (Four Wave Mixing), which significantly influence the signal transfer by the optical fibres [9].

2. Basic theory about the EDFA and the Raman amplifier

At the signal transfer by the optical communication system on long distances (>100 km) there can be an attenuation of the transferred signal. This loss is necessary to compensate somehow. The most sensible way of compensation in this case is using amplifiers. The optical amplifiers are very convenient - mostly when it is necessary to cross great distances between the optical transmitter and the receiver. In the past the electronic

---

* [1]**Tomas Ivaniga,** [2]**Petr Ivaniga,** [1]**Jan Turan,** [1]**Lubos Ovsenik**
[1]Department of Electronics and Multimedia Communications, Faculty of Electrical Engineering and Informatics,
University of Technology Kosice, Slovakia
[2]Department of Information Networks, Faculty of Management Science and Informatics, University of Zilina, Zilina, Slovakia
E-mail: tomas.ivaniga@tuke.sk

regeneration systems were used which performed the opto-electric conversion, to increase the level of signal in the electrical area and finally to perform the electrical-optical conversion [9]. With the entrance of the optical amplifiers these conversions are no longer needed.

Optical amplifiers are used in one-cable and multi-cable optical communication systems. The optical amplifier is a component of the optical network which can markedly influence the quality of the transferred signal. The placement of the optical amplifier within the optical network and its particular amplification greatly influences the occurrence of the nonlinear effects, for example: SPM, XPM and FWM.

2.1 Erbium Doped Fibre Amplifier

The history of the EDFA dates back to the 60's in the 20th century. However the real application of the EDFA started in the 90's. The discovery of this technology is an important milestone in the development of the optical communication systems. Since then the EDFA is used in a wide range of applications – wideband optical amplifiers, optical sources or tuneable lasers, and it can be found also in the optical coherent tomograph. The EDFA is successfully used mostly in the WDM transfer systems. The EDFA enabled the constructors of optical communication systems to use an optical window around 1.55 µm for transfers [9, 10]. It also significantly contributed to the increase of the transfer speed and the transfer distance. Erbium-doped fibre is a type of silicate optical fibre with its nucleus doped by ions of Erbium Er^{3+}. The electrons of the erbium-doped optical fibre can be excited into the higher energy levels by the excitation of light with a shorter wavelength. The EDFA is very effective in bands C (1530 nm–1560 nm) and L (1570 nm–1610 nm) [11 - 13]. The ideal characteristic of gain for the EDFA is reachable within 1530 nm–1560 nm. A typical gain of the erbium-doped optical amplifier was 20–30 dB for a distance of approximately 10 metres. Maximal reachable power on the output of the amplifier is limited by the power of the pumped light source. The value of this power can be between 20–50 mW (13–17 dBm).

The important factor significantly influencing the effectivity of the EDFA is the choice of the pumped light source. In practice are used light sources pumping light of wavelength of 980 nm and 1480 nm. The use of the pumping light source of the wavelength of 980 nm leads to high values of amplification and relatively low values of noise. The usage of wavelength of 1480 nm for the pumping light source produces larger values of amplification than when using the wavelength of 980 nm, but this light source causes a lower effectivity and a higher noise. In practice is common to use also both types of the pumping sources [14, 15]. On the first level the pumping light source of 980 nm ensures the low noise and a sufficient gain. A high output power is attained in the second level by using the pumping light source with wavelength of 1480 nm [16]. With such ways we can reach low noise and high output power of the EDFA. A typical course of gain and saturated output power are on the Fig. 1.

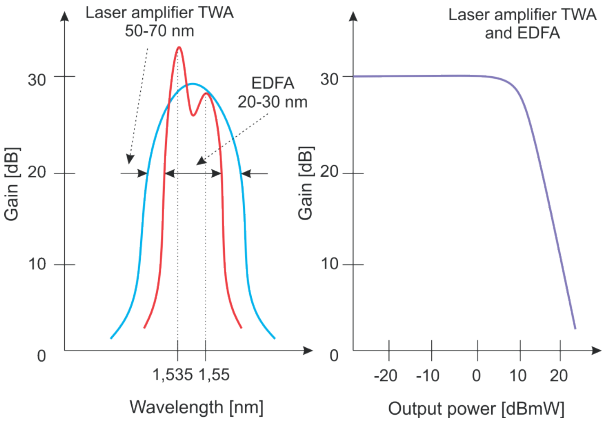

Fig. 1 Characteristics of the EDFA: a) typical gain profile b) typical saturated output power

2.2 Raman amplifier

For the purpose of intensifying the optical signal the Raman amplifier can also be used. Basically it is a laser source of radiation connected to the optical line. Signal strengthening utilises the Raman scatter on particles of the waveguide material. The energy transfer from lower wavelengths (wavelength of the radiation of the Raman pump) to higher (wavelengths of the transferred signal) also happens during the scatter [16]. Based on that the signal gains intensity right in its own fibre of the transferred line. This type of amplifier does not reach the values of the EDFA, the level of signal can be amplified by 15 to 20 dB. Raman amplifier is placed at the end of the transfer optical fibre and the radiation of the laser pump flows against the intensified signal [17]. It can be used to strengthen any wavelength under the condition of a correct choice of the wavelength of the laser source. EDFA and Raman amplifier can be conveniently and mutually combined [18]. However these amplifiers also intensify the distortion and so with long distances there has to be another classic repeater connected due to the signal recovery.

2.2.1 Gain of Raman amplifier

The wavelength of generated optical radiation is shifted up to 30 THz compared to the original wavelength. Maximal gain (30 dB) can be observed at the shift by 13 THz. For the practice it translates as the necessity to use pumping source working on wavelength of 1450 nm for the amplifier working on the wavelength of 1550 nm. The power of the amplifier depends on the power and wavelength of the pump, spectral effectivity, the length of the fibre and on the size of the mode surface. The most convenient medium to generate optical gain are fibres with small effective mode surface of the nucleus of the fibre [17, 18]. The Fig. 2 portrays the profile of the gain of the Raman amplifier. The non-linear fibres seem optimal and the fibres for suppression dispersion. In practice it is used the combination of a single-mode fibre with the step change of the refractive index SMF (Single Mode Fibre), fibres compensating the dispersion DCF (Dispersion Compensating Fibre), or also fibres with the shifted dispersion DSF (Dispersion Shifted Fibre).

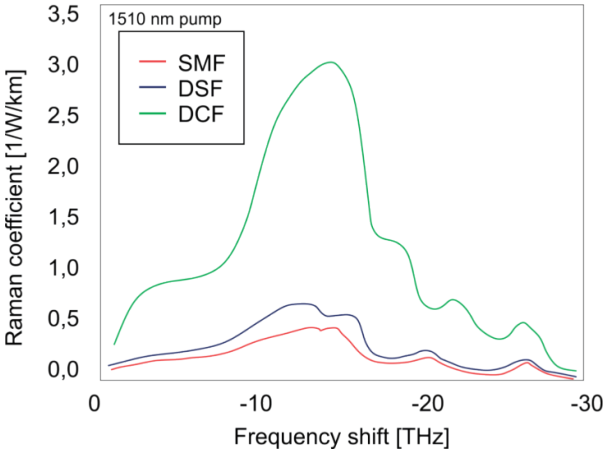

Fig. 2 Gain profile of the Raman amplifier

2.2.2 Pumping sources for the Raman amplifier

The source of the Raman amplifier is optical radiation. The pump radiation has shorter wavelength than the intensified optical signal. The contra-flow pumping is more beneficial because of lower noise and limitation of the gain ripple (the whole line absorbs generated influence of the spontaneous emission ASE) [19 - 21]. In addtion a greater number of pumping sources can be used, for example at the beginning or the end of the line - mostly for the maximal gain of the amplifier functioning as the booster. Regimes of the amplifiers' work depend on the placement of the pump [22]. There are two regimes of work:

- **DRA (Distributed Raman Amplifier)**–with expanded amplifier. This regime requires contra-flow pump. If the optical pumping is placed at the opposite end of the line, the whole line contributes to the gain. These amplifiers are notable for their lower noise, greater gain and lesser non-linear distortion. The disadvantage is the limitation of the maximal number of working wavelengths. In practice it is necessary to connect more amplifiers into the transfer band.
- **LRA (Lumped Raman Amplifier)**–discrete regime. The amplifier creates one block placed at a certain part of the line. It enables the gain generation at certain wavelengths - usually the ones not available for the amplifiers utilising doped mixtures of rare elements. The LRA can work for example in telecommunication band S where it enables to attain twice the transfer capacity than EDFA in C-band.

3. Published results

Ivaniga, et al., 2016 [23], designed a two-channel WDM system to examine the SPM effect. The aim of this article is to point to the non-linear effect SPM present in fully optical communication systems. Based on that article individual powers of CW and also the EDFA placement in the optical communication system were set. Because DWDM was created according to ITU-T G.694.1 it was necessary to prevent FWM. The individual simulations started at 12.5 GHz, 25 GHz and then 50 GHz with gaps between the channels. At 50 GHz FWM did not express in such prominent way as in the UDWDM system [23]. Ivaniga, et al., 2017 [24], formed a four-channel DWDM where they compared the EDFA and the SOA in band C. Individual amplifiers were placed as IN-Line amplifiers and were compared according to BER for two wavelengths. These amplifiers were not compared in order to reach the maximal distance but to compare it in two specific wavelengths. With that contribution it was possible to choose the length of the erbium-doped fibre as 10 m [24]. Bobrovs, et al., 2013 [25], designed DWDM where they compared Raman-SOA and Raman-EDFA in sixteen-channel DWDM system. Their article also summarised the individual comparisons and the advantages of given connections. Based on the stated distances there were created optical loops in our system [25]. Olonkins, et al., 2016 [26], presented the comparison of EDFA and LRA for eight-channel DWDM system at the speed of 10 Gbps with the modulation of type NRZ. In their simulations the placement of the amplifier was as that of the pre-amplifier. Based on those results we have set NRZ modulation in the receiving part [26]. Nain et al., 2016 [27], examined the non-linear effects in the WDM system. Thanks to this article it was possible to set the length of fibre in every loop. The authors focused on the improvement or the decrease of BER, Q-factor at the change of dispersion and the optical fibre [27]. Ivaniga, et al., 2017 [28], designed a single-channel optical line were the necessity of optical amplifiers after certain distance was proven. The length of fibres and the parameter of amplification were conducted based on those values. In addtion it includes basic mathematical process of calculating BER and Q-factor [28]. Because of the attained results and the publicised articles we have designed our own system for the EDFA and the DRA comparison.

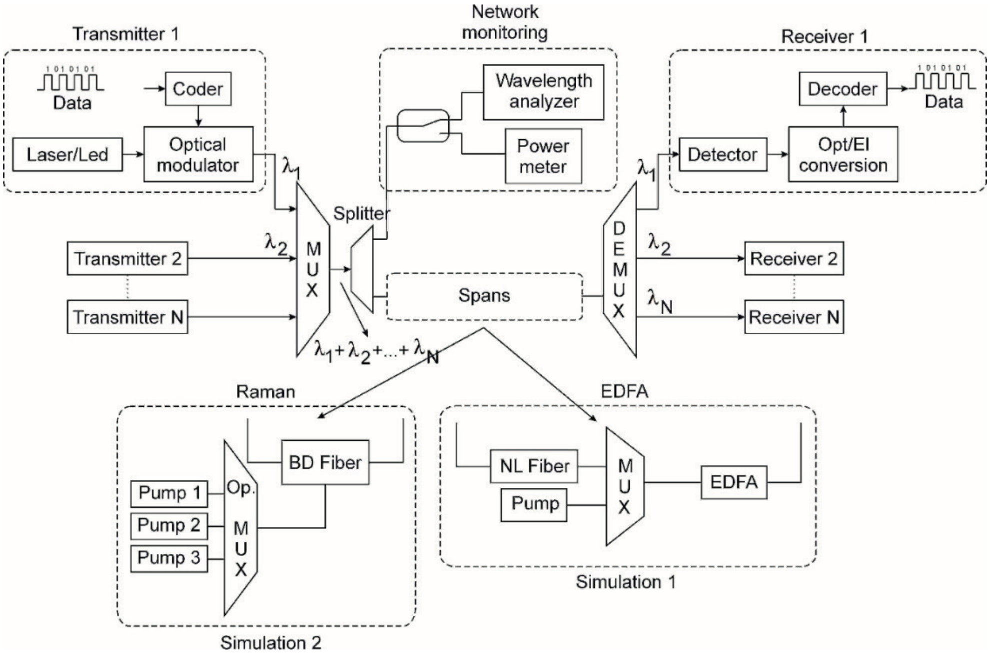

Fig. 3 Topology of the connection for the comparison between EDFA and DRA

4. Simulation and setting the parameters for EDFA and DRA

This section contains comparison of the EDFA and the DRA in optical span. These amplifiers were chosen for purpose of increasing maximal distance of communication path. The whole optical communication system contains three elementary parts: transmitting, receiving and transfer part (Fig. 3). There were two simulations carried out, for each one was used a unique transfer part. This was necessary to do for the comparison of BER for the individual systems.

4.1 Transmitting part

The transmitting part is created by four basic blocks. The first block is the source of data, able to generate various types of binary sequences. In our case it is set as the block PRBS (Pseudo - Random Binary Sequence) for every transfer channel set to produce the maximal length of the pseudo-random binary sequences. PL (Pattern Length) is exactly 7 (the amount of bits generated in the bit sequence). The number of zero bits at the beginning of the sequence equals 2 and at the end of the sequence 3. The bit speed is set to 10 Gbps during all simulations of the DRA and with the EDFA it increases to 15 Gbps. The function of the modulator is to ensure the conversion of the input binary signal into the output electrical signal. The electrical signal is generated by the On - off - ramp (electrical signal is generated by the period of rise and decay periods and jitter's timing). The used modulation is of the type NRZ (Non Return to Zero), the output value is expressed in Volt units with the amount of units per bit in the electrical signal has the value of 5. The maximal value of the output electrical signal V_{max} is 1 and the minimal value of the output signal V_{min} is 0. This block contains two types of ports: the first is logical with the input values from PRBS and the second is electric with the output values from the generator. The next created block is the Laser. Designed by us the CW laser has these defined parameters: power, RIN (Relative Intensive Noise), wavelength, phase and linewidth. The transmitted power in every block is established on the level 1 mW and RIN has the value of -150 dB/Hz. In case of the DRA the power with increment 1 mW the changed to manage a greater distance. The last block is the modulator. We chose the model of an electro-optical modulator using the modulation of the type MZ (Mach Zhender). Given signal then travels into the multiplexor where the optical signals are joined. Our created system has 8 channels with the gap of 50 GHz according to the ITU-T G.694.1, which is basically a standard DWDM. In our simulations we follow only one channel with the wavelength of 1550 nm to span the distance with a sufficient BER.

4.2 Transfer part

The whole transfer part in both topologies is unique. For the EDFA the emphasis is on spanning the distance and it incorporates a different bit speed. For the DRA the distance used was smaller but the change was in the input power of the CW laser.

4.2.1 Optical loop connected to the EDFA

In the Configuration connected to EDFA these following components are in an optical loop: optical fibre, multiplexor, laser pump and EDFA (Fig. 3). In order to span the greatest possible distance the number of iterations changes in the loop. The optical fibre is set to a constant distance of 75 km. This fibre represented the attenuation of 0.33 dB/km during all simulations. The dispersion λ_0 was set to the value of 1,312 μm and the group index n_1 to the value of 1.4786. The chosen non-linear model was constant, representing non-linear refractive index of n_2 $2.6.10^{-20}$, the diameter was 8.2 μm. During the simulations the PMD, SBS or Raman effect were ignored. This constructed model represented the input optical and also the output optical port. After the fibre is the multiplexor. The multiplexor contains two input optical ports and one output optical port. Into the first port the signal enters from the optical fibre and into the second enters the signal from the laser pump. Our designed model has the wavelength set to 980 nm with the power of 4.39 mW. RIN equalled -150 dB/Hz and timestpas was set to 3.125 ps. The key component in this loop is the EDFA. On Fig. 4 is the line of gain/loss with the wavelength for our designed model EDFA. The EDFA has the saturation parameter set to the value of 3.10^{15} $m^{-1}s^{-1}$.

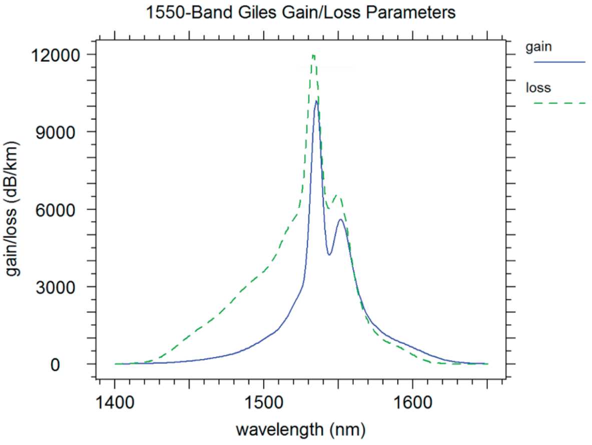

Fig. 4 Band Giles Gain/Loss Parameters

The aim of the simulation was the formation of a loop. One loop represented the trajectory of the optical signal through the fibre of 75 km and its following amplification. This loop increases with the increment 5. This means that the loop with the number of iterations 10 passes through the amplifier 10 times and the distance is 750 km.

4.2.2 Optical loop connected to the DRA

When the DRA was connected to the optical loop, there are three laser pumps used, an optical multiplex and a Bi-directional non-linear optical fibre. The first laser pump had the power set to 118 mW at the wavelength of 1450 nm and RIN for every pump equals -150 dB/Hz. The second laser pump has the value of 82 mW and it worked at the wavelength of 1458 nm. The third laser pump had 81 mW and was using the wavelength of 1447 nm. Signals enter the optical multiplex were they are joined and they proceed into the fibre. On Fig. 5 are the lines for the three laser pumps with the change of power and distance.

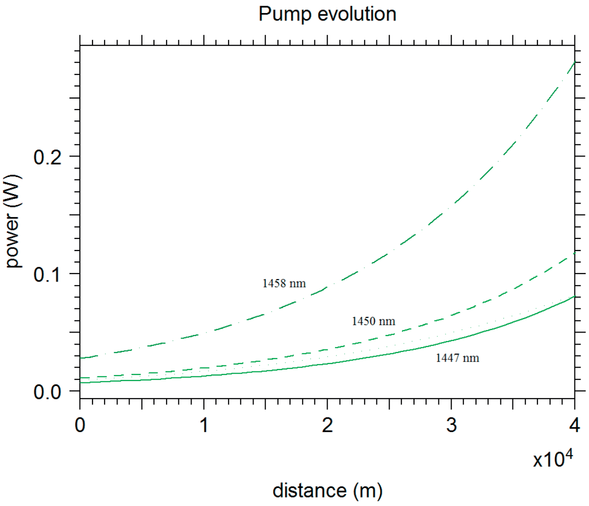

Fig. 5 Pump evolution for 3 laser pumps

The created model of the optical fibre represents a smaller distance, only a 50 km. The total attenuation was 0.3 dB/km. The dispersion λ_0 was set to the value of 1,312 μm and the group index n_1 to the value of 1.4786. The chosen non-linear model was constant which meant the non-linear refractory index n_2 $2.6.10^{-20}$, the diameter was 8.2 μm. In addtion in this case the PMD and SBS were turned off but the Raman effect was turned on here. The Raman gain for the particular wavelength was $9.8.10^{-14}$ m/W and the wavelength was 1 μm. The setting of the Rayleigh scattering coefficients for *k* equals $2.16.10^{-7}$ m^{-1} and *m* equals 2.7 with the set temperature of 298.15 K.

4.3 Receiving part

The receiving part of the fully optical communication system is the same in both topologies. The aim of this part is the evaluation of quality of the optical line based on BER and also the related Q-factor. The representation of the simulated values is according to the MC method (Monte Carlo). The filter in the receiver is the Bessel type and the quantum effectivity is 0.8. The component is designed to receive the input optical signal and at the output the signal is electrical. In Figs. 6 and 7 are the measured values of BER. In Fig. 6 are the acceptable values for EDFA with 2625 km, 10 Gbps and BER equals $6.4325.10^{-11}$.

In Fig. 7 are the acceptable values for DRA 700 km, 10 Gbps and BER equals $7.1877.10^{-7}$ while the power in this case was 3 mW. The measured values after connecting EDFA with the changed bit speed are in Table 1. The measured values for the DRA with changed power are in Table 2.

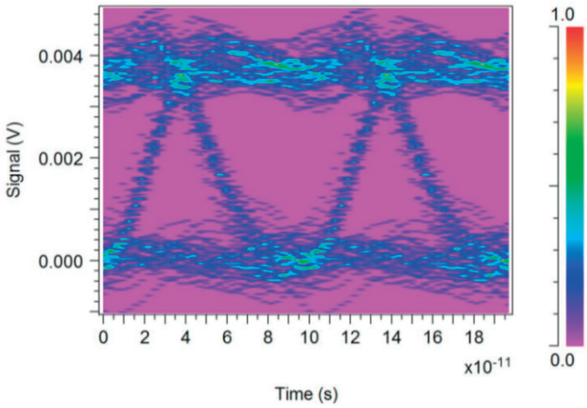

Fig. 6 BER for the EDFA with the distance of 2625 km

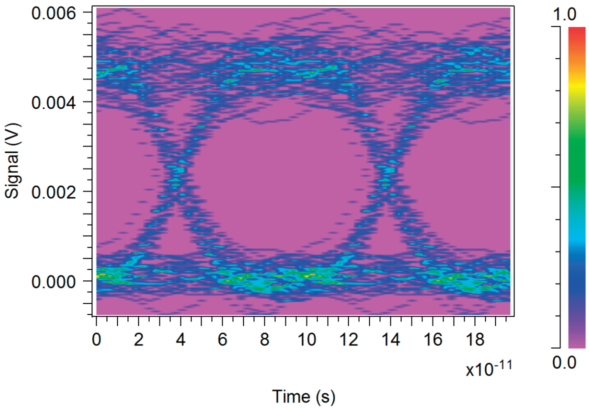

Fig. 7 BER for the DRA at length 700 km and power of 3 mW

Simulated values for the EDFA configuration Table 1

Distance [km]	BER/ 10 Gbps	Q-factor/ 10 Gbps	BER/ 15 Gbps	Q-factor/ 15 Gbps
1500	$6.9258.10^{-28}$	10.883	$3.7513.10^{-13}$	7.1699
1875	$1.6492.10^{-20}$	9.2088	$5.9885.10^{-10}$	6.0806
2250	$1.4174.10^{-14}$	7.6057	$5.8837.10^{-7}$	4.8595
2625	$6.4325.10^{-11}$	6.4288	$7.2964.10^{-5}$	3.7979
3000	$1.5673.10^{-7}$	5.1152	$3.1125.10^{-3}$	2.9987
3150	$2.2292.10^{-6}$	4.5888	0	0

Simulated values with the DRA connected Table 2

Distance [km]	Power[mW]	BER	Q-factor
500	1	$1.9696.10^{-23}$	9.9055
550	1	$2.6630.10^{-13}$	7.2167
600	1	$1.0001.10^{-7}$	5.1993
650	1	$9.8651.10^{-5}$	3.7224
700	1	$4.4423.10^{-3}$	2.6165
700	2	$7.1877.10^{-7}$	4.8197
700	3	$7.0922.10^{-12}$	6.7560
750	2	$2.8737.10^{-4}$	3.4433
750	3	$5.8286.10^{-7}$	4.8614
750	3	$2.5457.10^{-4}$	3.4759

5. Conclusion

The aim of this article was a comparison of two optical fibre amplifiers, namely the EDFA and the DRA. In the configuration with EDFA the distance was 2625 km at the bit speed of 10 Gbps, while BER reached the value of $6.4325.10^{-11}$ (Fig. 6). An optical line is considered as acceptable when the bit error rate is under 10^{-12}. Changing the bit speed to 15 Gbps the distance becomes 1500 km with BER of $3.7513.10^{-13}$. With the configuration with DRA the distance was 700 km with the power of 3 mW which corresponded with BER of $7.0922.10^{-12}$. The designed system was constructed to compare the distance coverage from the placement viewpoint. When choosing the correct setting it is necessary to consider non-linear effects, the distance, price or the number of users. The choice will be influenced by the compromise of whether the provider decides to lower the price (which decreases the bit speed) or increases the bit speed and shorten the distance of the optical line, or whether it decides to use more frequent channels where the FWM can interfere, etc. That is why the analysis of the individual optical networks in simulation programmes is an essential part of the design of all new optical communication networks. After an appropriate number of simulations are provided to address all of the customers' demands it is possible to create the most effective model taking into consideration all undesirable effects influencing the particular optical network.

Acknowledgment

This work was supported by research grant KEGA No. 023TUKE-4/2017.

References

[1] SMIESKO, J., URAMOVA, J.: Access Node Dimensioning for IPTV Traffic Using Effective Bandwidth. *Communications - Scientific Letters of the University of Zilina*, 14(2), 11-16, 2012.

[2] STEINGARTNER, W., NOVITZKA, V.: *A New Approach to Semantics of Procedures in Categorical Terms.* Proc. of IEEE 13th intern. scientific conference on informatics (INFORMATICS 2015), Serbia, 7377842, 252-257, 2015.

[3] RUZBARSKY, J., TURAN, J., OVSENIK, L.: *Stimulated Brillouin Scattering in DWDM All Optical Communication Systems*. 26th intern. conference radioelektronika (RADIOELEKTRONIKA 2016), Slovakia, 7477354, 395-398, 2016.

[4] ABDULLAEV, A., TURAN, J.: Survey of the Problems and Solutions of Arrayed Waveguide Gratings Used in the Optical Network. *Acta Electrotechnica et Informatica,* 14(3), 49-53, 2014.

[5] MIKUS, L.: Evaluations of the Error Rate in Backbone Networks. *Elektrorevue*, 12(2), 1-6, 2010.

[6] UDAYAKUMAR, R., KHANAA, V., SARAVANAN, T.: Chromatic Dispersion Compensation in Optical Fiber Communication System and its Simulation. *Indian Journal of Science and Technology*, 6, 4762-4766, 2013.

[7] SMIESKO, J.: IP Network Management of Sources for IP Traffics (in Slovak). *Scientific Papers of the University of Pardubice*, *Series D: Faculty of Economics and Administration*, 21(32), 109-117, 2014.

[8] IVANIGA, T., OVSENIK, L., TURAN, J.: *The Four-channel WDM System Using Semiconductor Optical Amplifier.* 26th intern. conference radioelektronika (RADIOELEKTRONIKA 2016), Slovakia, 7477350, 354-357, 2016.

[9] SIFTA, R., MUNSTER, P., KRAJSA, O., FILKA, M.: Simulation of Bidirectional Traffic in WDM-PON Networks (in Polish). *Przeglad Elektrotechniczny*, 90(1), 95-100, 2014.

[10] AZAWE, M. I.: Low Noise C-band EDFA/DRA Hybrid Amplifier Using the Same Pump Laser Diodes. *Photonics Letters of Poland*, 3(4), 165-167, 2011.

[11] STEINGARTNER, W., NOVITZKA, V.: Categorical Model of Structural Operational Semantics for Imperative Language. *Journal of Information and Organizational Sciences*, 40(2), 203-219, 2016.

[12] OLONKINS, S., BOBROVS, V., IVANOVS, G.: Investigation of Fiber Optical Parametric Amplifier Performance in DWDM Transmission Systems. *Elektronika ir Elektrotechnika*, 20(1), 88-91, 2014.

[13] ZYSKIND, J.: *Erbium-Doped Fiber: Amplifiers: What Everyone Needs to Know*. Optical Fiber Communications Conference and Exhibition (OFC 2016), USA, 7537552, 2016.

[14] SHARMA, S., MOHAN, S.: *Countering the Gain Behavior of Erbium Doped Fiber Amplifiers: A Cross Layer Aapproach*. IEEE intern. conference on Advanced Networks and Telecommunications Systems (ANTS 2013), India, 6802885, 2013.

[15] LIPTAI, P., MORAVEC, M., LUMNITZER, E., LUKACOVA, K.: Impact Analysis of the Electromagnetic Fields of Transformer Stations Close to Residential Buildings. *SGEM*, 1, 355-360, 2014.

[16] LUCERO, A.: *Advanced Amplifier Schemes in Long-Haul Undersea Systems*. Zyskind, J., Srivastava, A. (Eds.), Optically Amplified WDM Networks, Elsevier, USA, 253-276, 2011.

[17] AGALLIU, R., LUCKI, M.: System Performance and Limits of Optical Modulation Formats in Dense Wavelength Division Multiplexing Systems. *Elektronika ir Elektrotechnika*, 22(2), 123-129, 2016.

[18] OLONKINS, S., STANKUNOVS, I., ALSEVSKA, A., GEGERE, L., BOBROVS, V.: *Investigation of In-Line Distributed Raman Amplifiers with Co and Counter-Propagating Pumping Schemes.* Proc. of Progress in Electromagnetics Research Symposium (PIERS 2016), China, 7735423, 3773-3777, 2016.

[19] FELINSKYI, G. S., DYRIV, M. Y.: Noise Gain Features of Fiber Raman Amplifier. *Advances in OptoElectronics,* 5843636, 2016.

[20] TITHI, F. H., MAJUMDER, S. P.: *Performance Limitations Due to Combined Influence of ASE and Raman Amplifier Induced Crosstalk in a WDM System with Direct Detection Receiver.* 9th intern. conference on Electrical and Computer Engineering (ICECE 2016), Bangladesh, 566-569, 2016.

[21] AL-KHATEEB, M. A. Z., TAN, M., IQBAL, M. A., MCCARTHY, M., HARPER, P., ELLIS, A. D.: *Four Wave Mixing in Distributed Raman Amplified Optical Transmission Systems.* IEEE Photonics Conference (IPC 2016), USA, 7831072, 795-796, 2016.

[22] MASUDA, H., TOMIZAWA, M., MIYAMOTO, Y., HAGIMOTO, K.: Impacts of Distributed Raman Amplification Transmission Technologies on Terrestrial Large-Capacity WDM Systems. *Electronics and Communications in Japan, part I: Communications* (English translation of Denshi Tsushin Gakkai Ronbunshi), 90(6), 20-28, 2007.

[23] IVANIGA, T., OVSENIK, L., TURAN, J.: Investigation of SPM in WDM System with EDFA. *Carpathian Journal of Electronic & Computer Engineering,* 9(2), 7-12, 2016.

[24] IVANIGA, T., IVANIGA, P.: Comparison of the Optical Amplifiers EDFA and SOA Based on the BER and Q-factor in C-band. *Advances in Optical Technologies*, 9053582, 2017.

[25] BOBROVS, V., OLONKINS, S., ALSEVSKA, A., GEGERE, L., IVANOVS, G.: Comparative Performance of Raman-SOA and Raman-EDFA Hybrid Optical Amplifiers in DWDM Transmission Systems. *International Journal of Physical Sciences*, 8(39), 1898-1906, 2013.

[26] OLONKINS, S., BOBROVS, V., PILATS, D., PORINS, J.: *Comparison of EDFA and LRA Preamplifier Performance in WDM Transmission Systems.* Proc. of Progress in Electromagnetics Research Symposium (PIERS 2016), China, 7735424, 3778-3782, 2016.

[27] NAIN, H., JADON. U., MISHRA. V.: *Evaluation and Analysis of Non-Linear Effect in WDM Optical Network.* IEEE intern. conference on Recent Trends in Electronics, Information & Communication Technology (RTEICT 2016), India, 36-39, 2016.

[28] IVANIGA, P., IVANIGA, T.: 10 Gbps Optical Line Using EDFA for Long Distance Lines (in Polish). *Przeglad Elektrotechniczny*, 93(3), 193-196, 2017.

https://doi.org/10.26552/com.C.2017.3.96-101

COMMUNICATIONS

Milan Moravcik - Martin Moravcik*

RESONANCE VIBRATION OF RAILWAY BRIDGES SUBJECTED TO PASSING VEHICLES

This paper discusses some issues related to dynamic effects in railway bridges focussed on the simulation of the resonant vibration for the small and medium span simply supported railway bridges subjected to a series of moving vehicle. Presented parametric study is concerned with the dynamic deflection of the simply supported railway truss bridge of the span $L_b = 38\,m$*, due to the series of the ten moving loads representing a conventional train with the IC-coaches employed in Slovakia, with the impact to the resonance speed* $c_{2res} = 65.03$ *m/s = 234.11 km/h. The deflection amplitude* ${}^{(c_2=33)}w_{(1),(P_1,P_2\ldots P_N)}(L_b/2,t)$ *increase with an increasing number of load forces n = 1, 2, ... N forces moving along the bridge.*

Keywords: *The dynamic response, railway bridge deflections, resonance amplitudes, the modal superposition method.*

1. Introduction

The dynamic response of railway bridges, subjected to moving trains is influenced by a number of factors such as the speed of load, the bridge span, natural frequencies of the bridge and railways vehicles, the inertia and damping of the two interaction systems (vehicles and the bridge), the distance between the vehicles, and arranging axles of vehicles. At present, the actual question for the bridge loading follows from high speed trains, which may consist of a number of identical cars connected together moving with the speed *c*. In those cases, the resonance caused by configuration of the train, consisting of a number of vehicles of similar types (Fig. 1), may occur, especially at high speed ranges.

To solve indicated problems one needs to apply the special dynamic analysis depending on the type of the bridge structure with regards to the static determination of the structure. For statically indeterminate structures, like continuous deck bridges or frame structures, more sophisticated methods of analysis (FEM) must be applied. For the simple bridges, the solution is based on the modal superposition method [1-3].

Railway vehicles travelling along the bridge are modelled as a series of identical moving loads and assuming that the vehicle/bridge mass ratio is small $m_v \ll m_b$ and loads move along the bridge, the close form of solution can be obtained. The dynamic displacement $w(x,t)$ and acceleration $\ddot{w}(x,t)$ of the bridge are governed at different extents by the two sets of frequencies:

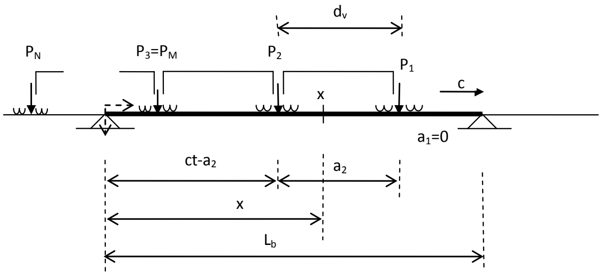

Fig. 1 Loading of the bridge by a series of identical IC-vehicles

- the driving frequency of a vehicle crossing the bridge, $\omega_{(j),dr}$ $j = 1, 2\ldots$,
- the natural frequency of the bridge $\omega_{(j)}$, $j = 1, 2, \ldots$

One of the actual problems is the solution of the dynamic behaviour of the bridge subjected to a series of identical loads $\sum_n p_n$, *n = 1, 2,.. N*, with identical space intervals d_v (the length of the vehicle) passing the bridge with a constant speed *c* [4] as is shown in Fig. 2.

In this paper the dynamic behaviour of the simply supported railway bridge with the span $L_b = 38$ m, subjected to the successive identical moving loads is solved. The close form solution is obtained by means of the modal superposition method [1-2, 5-6]. The presented parametric study is focused on the dynamic deflection of the bridge at the mid-span ${}^{(c)}w(L_2/2,t)$ due to loading of the conventional train with the Slovak IC-coaches for the resonance speed $c_{2res} = 65.03$ m/s = 234.11 km/h, [7].

---

* **Milan Moravcik, Martin Moravcik**
Faculty of Civil Engineering, University of Zilina, Slovakia
E-mail: mimo@fstav.uniza.sk

Using the analytical approach, the key parameters that govern the dynamic displacement response – the vertical beam vibration ${}^{(c)}w_{(P_1,P_2,\ldots P_N)}(x,t)$, for M loads moving on the railway steel girder of the length L_b = 38 m loaded by the ten IC-cars length d_v= 24.5 m with the magnitude P_v= 524 kN, Fig. 1.

2. Formulation of the theory for the bridge response induced by moving load series

Consider a simply supported beam (without damping) subjected to a series of concentrated constant loads *P*, which are moving at a uniform speed *c*, in the meaning of Fig. 2. The motion equation for the beam subjected to periodical loading of moving load series can be writing as

$$EI\frac{\partial^4 w(x,t)}{\partial x^4}+m_1\frac{\partial^2 w(x,t)}{\partial t^4}=\sum_{n=0}^{M-1}P\delta\left(x-c\left(t-\frac{nd_v}{c}\right)\right), \qquad (1)$$
$$n=1,2,\ldots M,$$

where:

$w(x,t)$- is the displacement of the beam at point *x* and time *t* [m],
EI - is the bending stiffness of the beam [kNm^2],
m_1 - is the mass per unit length of the beam [t],
$P_{v,i}\equiv P_i$ - is the loading force [kN],
$\delta(x)$ - is the Dirac function,
c - is a uniform speed of moving loads [m/s],
L_b - is the span length of the bridge [m],
d_v - is the identical interval between loading forces [m].

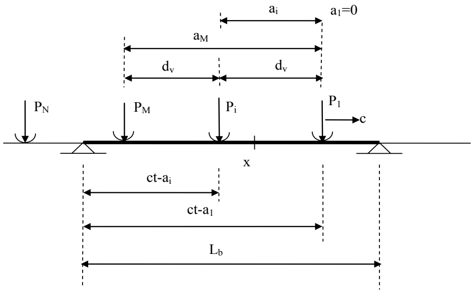

Fig. 2 The single-span bridge subjected to moving loads $\sum_n P_n$

For a simple beam the solution of the vertical deflection $w(x,t)$ in Equation (1) becomes the harmonic analysis [1, 2]. The particular solution $w(x,t)$ for a simply supported beam can be expressed in terms of the modal time coordinates $q_{(j)}(t)$ for the beam vibration and the modal shapes $\phi_j(x)$ as

$$w(x,t)=\sum_j q_{(j)}(t)\phi_j(x)=\sum_j q_{(j)}(t)\sin\left(\frac{j\pi x}{L_b}\right), \qquad (2)$$
$$j=1,2,3,\ldots,$$

where:

$q_{(j)}(t)$ - are the generalized coordinates that define the amplitude of vibration with time *t*,

$\phi_j(x)=\sin\left(\frac{j\pi x}{L_B}\right)$ - is a fundamental mode shape and for the simply beam is of the sinusoidal type (the first mode is an one-half cycle; the second mode is a full cycle).

Thus, the dynamic deflection may be represented by the summation of modal components. When the first and last moving load on the bridge span be P_1 and P_M at a time *t*, Equation (1) can be expressed in terms of the generalized coordinates as

$$\frac{d^2q_{(j)}(t)}{dt^2}+\omega_{(j)}^2q_{(j)}(t)=\frac{2P}{m_1L_b}\sum_{n=0}^{M-1}\sin\left(\frac{j\pi c}{L_b}\left(t-\frac{nd_v}{c}\right)\right)H_n, \qquad (3)$$
$$n=1,2,\ldots M$$

for *M* forces moving on the bridge,
where:

$H_n=\theta\left(t-\frac{nd_v}{c}\right)-\theta\left(t-\left(\frac{nd_v}{c}+\frac{L_b}{c}\right)\right)$ is the Heaviside function determining whether the load *P* is on the bridge or not.

The modal coordinate $q_{(j)}(t)$ for the *j*-th mode of vibration of the beam from Equation (3) can be expressed as:

$$q_{(j)}(t)=\frac{\hat{q}_{(\mathrm{j})\mathrm{st}}}{1-\alpha_{(j)}^2}\sum_{n=0}^{M-1}\left[\sin\left(\omega_{(\mathrm{j})\mathrm{dr}}\left(t-\frac{nd_v}{c}\right)\right)\right.$$
$$\left.-\alpha_{(j)}\sin\left(\omega_{(j)}\left(t-\frac{nd_v}{c}\right)\right)\right]H_n(t), \qquad (4)$$

where:

$\hat{q}_{(j)st}=\frac{2P}{m_1L_b\omega_{(j)}^2}=\frac{2PL_b^3}{j^4\pi^4EI}$ - is the modal amplitude - the static deflection caused by the force *P* with respect to the *j*-th mode,

$\omega_{(j)}=\frac{\pi j^2}{L_b^2}\sqrt{\frac{EI}{m_1}}$ - is the *j*-th circular frequency of the beam vibration,

$\alpha_{(j)}=\frac{\omega_{(j)dr}}{\omega_{(j)}}\equiv\frac{c}{c_{cr}}$ is the non-dimensional speed parameter,

$c_{cr}=2f_{(1)}L_b=\frac{\omega_{(1)}L_b}{\pi}$ is the critical speed,

$\omega_{(j)dr}=\frac{j\pi c}{L_b}$ - is the circular driving frequency of the moving force for the *j*-th mode of vibration.

2.1 The single-mode analytical solution

The vertical deflection $w(x,t)$ in Equation (1) for a simply supported beam for a moving load problem can be well simulated by considering the first mode of vibrations $\omega_{(1)}$ only. The corresponding modal coordinate from Equation (4), taking into account *M*-vehicles on the bridge, is given by superposition of a forced response (a quasi-static response) due to the moving load and a transient response (the dynamic part of the response), can be expressed as follows:

$${}^{(c)}q_{(1),(P_1,P_2\ldots P_M)}(t)=\frac{\hat{q}_{(1)st}}{1-\alpha_{(1)}^2}\sum_{n=0}^{M-1}\left[\sin\left(\omega_{(1)dr}\left(t-\frac{nd_v}{c}\right)\right)-\alpha_{(1)}\right.$$
$$\left.\sin\left(\omega_{(j)}\left(t-\frac{nd_v}{c}\right)\right)\right]H_n(t) \qquad (5)$$

where:

$\alpha_{(1)} = \frac{\omega_{dr(1)}}{\omega_{(1)}} = \frac{\pi c}{L_b \omega_{(1)}} = \frac{c}{c_{cr}}$ is the non-dimensional speed parameter corresponding to the first mode of vibrations $\omega_{(j)}$,

The vertical deflection ${}^{(c)}w_{(1),(P_1,P_2,\dots P_N)}(L_b/2,t)$ for the mid-span $x = L_b/2$ is equal to the modal coordinate ${}^{(c)}q_{(1),(P_1,P_2,\dots P_N)}(L_b/2,t)$, because $\sin\left(\frac{\pi x}{L_b}\right) = \sin(\pi/2) = 1$.

$$\begin{aligned}&{}^{(c)}w_{(1),(P_1,P_2,\dots P_N)}(L_b/2,t) = {}^{(c)}q_{(1),(P_1,P_2,\dots P_N)}(L_b/2,t) = \\ &= \frac{\hat{q}_{(1)st}}{1-\alpha_{(1)}^2}(1,0)\sum_{n=0}^{M-1}\left[\sin\left(\omega_{(1)dr}\left(t-\frac{nd_v}{c}\right)\right)-\right. \\ &\left.-\alpha_{(1)}\sin\left(\omega_{(j)}\left(t-\frac{nd_v}{c}\right)\right)\right]H_n(t)\end{aligned} \tag{6}$$

2.2 Displacement response at the mid-span of the beam

The important practical significance is just the dynamic deflection ${}^{(c)}w_{(1),(P_1,P_2,\dots P_N)}(L_b/2,t)$ at the mid-span $x = L_b/2$ for loads of a moving series (P_1, P_2,... P_N). If the number of the loads, moving out of the span, is K and the number of moving forces moving just on the span is M at the time t, the displacement response of the beam can be generalized considering the superposition of the next loading effects [2, 5-6]:

$$\begin{aligned}&{}^{(c)}w_{(1),(P_1,P_2,\dots P_N)}(L_b/2,t) = {}^{(c)}q_{(1),(P_1,P_2,\dots P_N)}(L_b/2,t)\phi_1(L_b/2) = \\ &= \frac{\hat{w}_{(1)st}(L_b/2)}{1-{}^{(c)}\alpha_{(1)}^2}(1,0)\sum_{n=K}^{M-1}\sin{}^{(c)}\omega_{(1)dr}\left(t-\frac{nd_v}{c}\right)- \\ &-\frac{\hat{w}_{(1)st}(L_b/2)}{1-{}^{(c)}\alpha_{(1)}^2}(1,0)\sum_{n=K}^{M-1}{}^{(c)}\alpha_{(1)}e^{-\omega_d\left(t-\frac{nd_v}{c}\right)}\sin\omega_{(1)}\left(t-\frac{nd_v}{c}\right)- \\ &-\frac{\hat{w}_{(1)st}(L_b/2)}{1-{}^{(c)}\alpha_{(1)}^2}\sum_{n=0}^{K-1}\left({}^{(c)}\alpha_{(1)}e^{-\omega_d\left(t-\frac{nd_v}{c}\right)}\sin\omega_{(1)}\left(t-\frac{nd_v}{c}-\frac{L_b}{c}\right)\right)- \\ &-\frac{\hat{w}_{(1)st}(L_b/2)}{1-{}^{(c)}\alpha_{(1)}^2}\sum_{n=0}^{N-1}\left({}^{(c)}\alpha_{(1)}e^{-\omega_d\left(t-\frac{nd_v}{c}-\frac{L_b}{c}\right)}\sin\omega_{(1)}\left(t-\frac{nd_v}{c}-\frac{L_b}{c}\right)\right)\end{aligned} \tag{7}$$

for n = 1,2,3,... $N = M+K$, and for $\sin(\pi/2) = 1$.

The first term in Equation (7) represents the component corresponding to each moving load P_n travelling over the beam – it produces *the force vibration response* (the quasi-static part of the response). The second and the third term in Equation (7) produce *the free vibration response* (the dynamic part of the response) considering forces moving just on the beam and forces moving away of the span, respectively. The fourth term in Equation (7) represents the free vibrations' term after all the moving loads left the span. Thus, the beam response ${}^{(c)}w_{(1),(P_1,P_2,\dots P_N)}(L_b/2,t)$ can be symbolically written as

$$\begin{aligned}&{}^{(c)}w_{(1),(P_1,P_2,\dots P_N)}(L_b/2,t) = {}^{(c)}w_{(1)st,(P_1,P_2,\dots P_M)}(L_b/2,t)+ \\ &+{}^{(c)}w^{(1)}_{(1)dyn,(P_1,P_2,\dots P_M)}(L_b/2,t)+{}^{(c)}w^{(2)}_{(1)dyn,(P_1,P_2,\dots P_K)}(L_b/2,t)\end{aligned} \tag{8}$$

2.3 Condition of the resonance

When all the moving loads have passed the beam, the force part of the vibration terminates immediately. However, the free vibration part continues to exit until it is eventually damped out. Our parametric studies for different train speeds show that both the phenomena of resonance and cancellation are related to the free vibration component of the beam vibrations only. Thus, the sum of the free vibration response components by each moving load can result in the resonance if the total number N of the moving loads is large enough.

If the forces act on the bridge at equal distances d_v then their repeated action can cause a resonant vibration. The resonant condition follows from the well know condition [5-7]:

$$kf_{(d_v)} = f_{(1)} \rightarrow k\frac{c}{d_v} = \frac{\omega_{(1)}}{2\pi},\ k = 1,2,3\dots, \tag{9}$$

The resonant condition (9) is calculated from the time necessary for crossing the distance d_v at the speed c which is equal to the k-multiple of the natural beam vibration $f_{(1)}$. From Equation (9) results the resonant speed under the condition $\cos(\omega_{(1)}L_b/c)$ [7]:

$$c_{(i,res)} = \frac{\omega_{(1)}d_v}{2\pi k},\ \ k = 1,2,3\dots \tag{10}$$

Critical speeds $c_{(i,res)}$ according to Equation (10) are given in Table 1.

Critical speeds for train with IC-cars (d_v = 24.5 m)
and for L_b = 38 m
Table 1

k	$c_{i,res} = \frac{\omega_{(1)}d_v}{k2\pi}$	for L_b=38 m, d_v=24.5 m
1	$c_{1,res}$=130.1m/s	$\cos(\omega_{(1)}L_b/c_1) = -0.9506$
2	$c_{2,res}$= 65.03m/s	$\cos(\omega_{(1)}L_b/c_2) = 0.8072$
3	$c_{3,res}$= 43.35 m/s	$\cos(\omega_{(1)}L_b/c_3) = -0.5843$
4	$c_{4,res}$= 32.52 m/s	$\cos(\omega_{(1)}L_b/c_4) = 0.3034$

From the above resonance considerations follow:

- The dynamic response is strongly influenced by the free-vibration components in Equation (7) if the total number of moving loads is large enough.
- The resonant-response amplitude decreases when the value of k increases.
- The ratio L_b/c of the span L_b to the velocity of the moving loads c expressively influences the response amplitude.
- The difference between the phase angles in the dynamic components in Equation (7) affects the phenomena of resonance and its cancellation.
- The increase of the damping is an effective measure to reduce resonant – amplitude.

3. Dynamic deflection due to a series of moving load (P_1+P_2+.....+P_{10}) crossing the beam

The steel truss bridge L_b = 38 m is subjected by the series of 10 IC-cars (P_1+P_2+...+P_{10}) in the sense of Fig. 3. The load of equal weights P = 524 kN is spaced at the car interval d_v = 24.5 m, the train speed is $c_{2,res}$= 65.03 m/s, see Table 1. Evaluation of all time dynamic response waveforms were applied from a programming system Wolfram Mathematica 8.0.1[8].

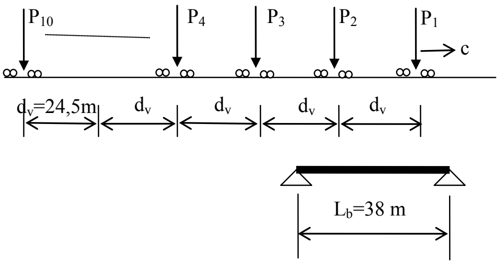

Fig. 3 The beam subjected to the series of loads (P1+P2+.....P10) moving across the beam

Input parameters: The bending stiffness of the bridge for the two rail loading model is:
EI = 7.58.10^7 kNm^2,
the beam mass per unit length $m_1 = m_{1(\mathrm{BStr})} + m_{1(\mathrm{Sup})}$= 3.18 t/m,

$$\omega_{(1)} = \frac{\pi^2}{L_b^2}\sqrt{\frac{EI}{\bar{m}_1}} = 33.34\left[\mathrm{s}^{-1}\right]$$

the first circular frequency of the bridge = 33.34 [s^{-1}],

$$^{((1)c_{2,res}=65)}\alpha_{(1)} = \frac{\omega_{(1)dr}}{\omega_{(1)}} = \frac{\pi^{(1)}c_{2,res}}{L_b\omega_1} = 0.1612,$$

$$^{((1)c_{2,res})}\alpha_{(1)} = \frac{c}{c_{cr}} = \frac{65.03}{403.27} = 0.1613,$$

$$c_{cr} = \frac{\pi}{L_b}\sqrt{\frac{EI}{m_1}} = 403.27\, m/s \text{ is the critical speed,}$$

$$\hat{w}_{(1)st}\left(L_b/2\right) = \frac{2PL_b^3}{\pi^4 EI} = 0.00791\,\mathrm{m} \text{ is the amplitude of the static}$$

deflection induced by vehicle, corresponding to the *1*-st mode of vibrations

$$^{((1)c_{2,res})}\omega_{(1)dr} = \frac{\pi^{(1)}c_{2,res}}{L_b} = 5.3735\left[\mathrm{s}^{-1}\right],$$

$$\frac{\hat{w}_{(1)st}\left(L_b/2\right)}{\left(1-{}^{((1)c_{2,res})}\alpha_1^2\right)} = \frac{0.0079}{1-0.1612^2} = 0.0081\,\mathrm{m},$$

$$\frac{L_b}{^{(1)}c_{2,res}} = \frac{38}{65.03} = 0.5843\,\mathrm{s},\quad \frac{d_v}{^{(1)}c_{2,res}} = \frac{24.5}{65.03} = 0.3767\,\mathrm{s},$$

the damping coefficient = 0.1327 s.

3.1 Components of the beam deflection due to the sequence of load IC-cars (P_1+P_2+...P_{10})

Components of the beam response due to the sequence of load IC-cars (P_1+P_2+...P_{10}) are defined by expressions (7).

- **The quasi-static component** $^{(c_{2,res}=65)}w_{(1)st,(P_1,P_2,\ldots P_{10})}\left(L_b/2,t\right)$

The quasi-static component of the response includes the effect of forces moving direct over the beam (without damping) and is defined by the first term in Equation (7). Because of drawing the displacement *w* in the downward direction in Equation (11), the minus sign is applied. The result is plotted in Fig. 4.

$$^{(c_{2,res}=65)}w_{(1)st,(P_1,P_2,\ldots P_{10})}\left(L_b/2,t\right) = \\ = -\left[\frac{\hat{w}_{(1)st}\left(L_b/2\right)}{1-{}^{(c)}\alpha_{(1)}^2}\sum_{n=0}^{M=9}\sin\left({}^{(c_{2,res})}\omega_{(1)dr}\left(t-\frac{nd_v}{c_{2,res}}\right)\right)H_{(n)}\right] \tag{11}$$

Result $^{(c_{2,res}=65)}w_{(1)st,(P_1,P_2,\ldots P_{10})}\left(L_b/2,t\right)$

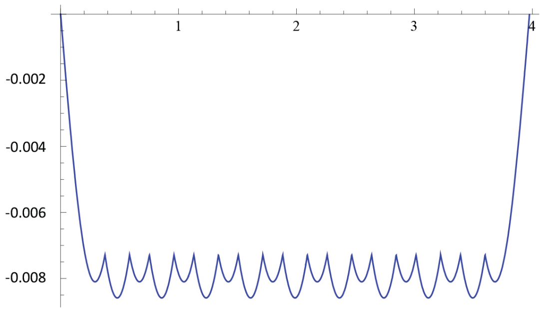

Axes x = t[s], y = w[m]
the load (P₁,P₂...P₁₀) = 10x528 kN that move direct over the beam
t = 0 to 3.97 s

Fig. 4 The quasi-static component of the deflection

- **The dynamic component** $^{(c_{2,res}=65)}w^{(1)}_{(1)dyn,(P_1,P_2,\ldots P_{10})}\left(L_b/2,t\right)$

The dynamic component of the beam deflection includes the response defined by the second term in Equation (7). This dynamic response is plotted in Fig. 5.

$$^{(c_{2,res}=65)}w^{(1)}_{(1)dyn,(P_1,P_2,\ldots P_{10})}\left(L_b/2,t\right) = \\ = -\left[\frac{\hat{w}_{(1)st}\left(L_b/2\right)}{1-{}^{(c)}\alpha_{(1)}^2}\sum_{n=0}^{M=9}\left(-{}^{(c_{2,res})}\alpha_{(1)}\sin\left(\omega_{(1)}\left(t-\frac{nd_v}{c_{2,res}}\right)\right)\right)H_{(n)}\right] \tag{12}$$

Result $^{(c_{2,res}=65)}w^{(1)}_{(1)dyn,(P_1,P_2,\ldots P_{10})}\left(L_b/2,t\right)$

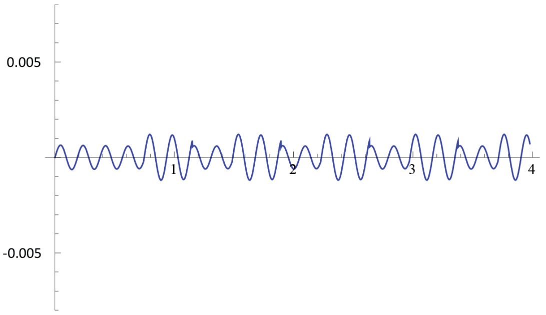

Axes x = t[s], y = w[m]
the loads (P1+P2,...+P10) move direct over the beam
t = 0 to 3.97 s

Fig. 5 The dynamic component

- **The total deflection beam response $^{(c_{2,res}=65)}w^{(a)}_{(1),(P_1,P_2,\ldots P_{10})}(L_b/2,t)$ corresponding to the load (P_1, $P_{2,}$ ....P_{10}) moving directly over the beam**

The total deflection response $^{(c_{2,res}=65)}w^{(a)}_{(1),(P_1,P_2,\ldots P_{10})}(L_b/2,t)$ is superposition of the quasi-static and the dynamic component. The result is plotted in Fig. 6.

$$^{(c_2=33)}w^{(a)}_{(1),(P_1,P_2,\ldots P_{10})}(L_b/2,t)={}^{(c_{2,res}=65)}w_{(1)st,(P_1,P_2,\ldots P_N)}(L_b/2,t)+ \\ +{}^{(c_{2,res}=65)}w^{(1)}_{(1)dyn,(P_1,P_2,\ldots P_N)}(L_b/2,t) \tag{13}$$

Result $^{(c_{2,res}=65)}w^{(a)}_{(1),(P_1,P_2,\ldots P_{10})}(L_b/2,t)$

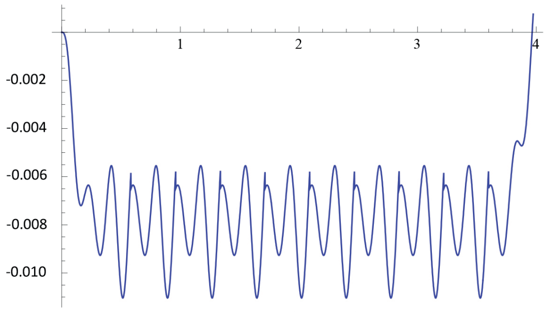

Axes x = t[s], y = w [m]
the loads (P1+P2,...+P10) = 10x528 kN move over the beam
t = 0 to 3.97 s

Fig. 6 The deflection response

The dynamic amplifier factor $^{(c_2=33)}\Delta^{(a)}_{dyn(P_1,P_2,\ldots P_{10})}=\dfrac{0.011}{0.0092}=1.1957.$

- **The dynamic component $^{(c_{2,res}=65)}w^{(2)}_{(1)dyn,(P_1,P_2,\ldots P_{10})}(L_b/2,t)$ for the load moving (P_1,P_2....P_{10}) out of the span**

This dynamic component belongs to loads that have passed the beam, but they still influence the response. The result is plotted in, Fig. 7.

$$^{(c_{2,res}=65)}w^{(2)}_{(1)dyn,(P_1,P_2,\ldots P_{10})}(L_b/2,t)=- \\ -\left[\begin{array}{l}\dfrac{\hat{w}_{(1)st}(L_b/2)}{1-{}^{(c_{2,res})}\alpha^2_{(1)}} \\ \displaystyle\sum_{n=0}^{K=9}\left(-{}^{(c_{2,res})}\alpha_{(1)}e^{-\omega_d\left(t-\frac{nd_v}{c_2}\right)}\sin\omega_{(1)}\left(t-\frac{nd_v}{c_{2,res}}-\frac{L_b}{c_{2,res}}\right)\right)H_{(n)}\end{array}\right] \tag{14}$$

Result $^{(c_{2,res}=65)}w^{(2)}_{(1)dyn,(P_1,P_2,\ldots P_{10})}(L_b/2,t)$

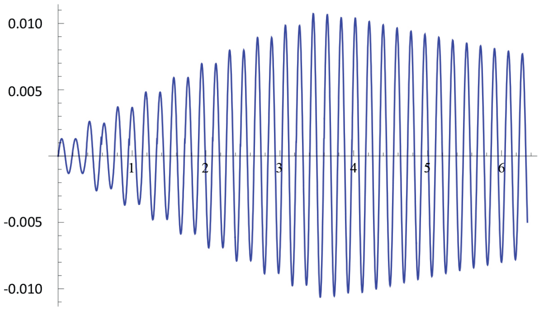

Axes x = t[s], y = w [m]
the loads (P_1, P_2.....P_{10}) = 10x528 kN that have passed the beam
t = 0 to 6.35 s

Fig. 7 The dynamic component

- **Components of the total response**

The components of the total deflection response $^{(c_{2,res}=65)}w_{(1),(P_1,P_2,\ldots P_{10})}(L_b/2,t)$, belong to the load ($P_1$, $P_{2,}$....P_{10}) that move directly over the beam and to the loads that have passed the beam are depicted in Fig. 8. The components are described by Equations (9), (10) and (12). The components of the total deflection are $^{(c_{2,res}=65)}w_{(1)st,(P_1,P_2,\ldots P_{10})}(L_b/2,t)$, $\left\{{}^{(c_{2,res}=65)}w^{(1)}_{(1)dyn,(P_1,P_2,\ldots P_{10})}(L_b/2,t)+{}^{(c_{2,res}=65)}w^{(2)}_{(1)dyn,(P_1,P_2,\ldots P_{10})}(L_b/2,t)\right\}$

Result

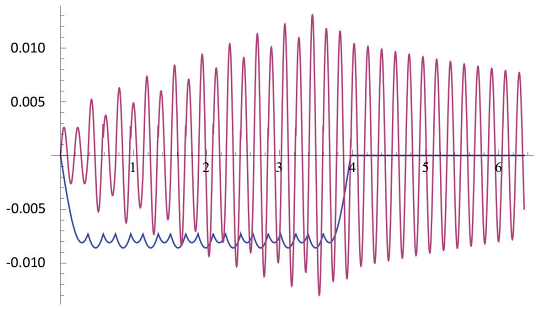

Axes x = t[s], y = w[m]

Fig. 8 Components of the total deflection:

3.2 The total response due to the series of loads IC-cars (P_1+P_2+...P_{10})

The total response $^{(c_{2,res}=65)}w^{(a+2)}_{(1),(P_1,P_2,\ldots P_{10})}(L_b/2,t)$ due to the series of load IC-cars (P_1+P_2+...P_{10}) is defined by superposition of the quasi-static and the dynamic components described by expressions (11), (12) and (14). The total beam response $^{(c)}w^{(a+2)}_{(1),(P_1,P_2,\ldots P_N)}(L_b/2,t)$ can be symbolically written as the superposition of effects:

$$^{(c_{2,res}=65)}w^{(a+2)}_{(1),(P_1,P_2,\ldots P_{10})}(L_b/2,t)={}^{(c_{2,res})}w_{(1)st,(P_1,P_2,\ldots P_{10})}(L_b/2,t)+ \\ +{}^{(c_{2,res})}w^{(1)}_{(1)dyn,(P_1,P_2,\ldots P_{10})}(L_b/2,t)+{}^{(c_{2,res})}w^{(2)}_{(1)dyn,(P_1,P_2,\ldots P_{10})}(L_b/2,t) \tag{15}$$

The result is plotted in Fig. 9.

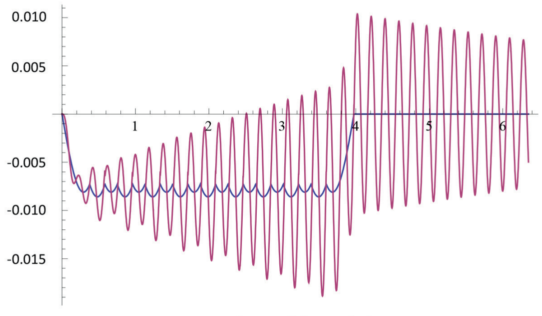

Axes x = t[s], y = w [m]
t= 0 to 6.35 s

DAF $^{(c_{2,res}=65)}\Delta^{(a+2)}_{dyn(P_1,P_2,\ldots P_{10})}=\dfrac{0.0185}{0.0085}=2.1765$

Fig. 9 The total beam displacement response

Comparison of the dynamic amplifier factor ${}^{(c_{2,res}=33)}\Delta^{(a)}_{dyn,(P_1,P_2,\dots P_{10})} = \dfrac{0.011}{0.0092} = 1.1957$ for the deflection corresponding only the load acting directly on the beam and the factor ${}^{(c_{2,res}=65)}\Delta^{(a+2)}_{dyn,(P_1,P_2,\dots P_{10})} = \dfrac{0.0185}{0.0085} = 2.1765$ involving also the effect of the residual free vibration of the beam caused by moving loads that have passed the beam, demonstrates the strong increase of the DAF at 54.93 %.

4. Conclusions

The dynamic response of bridges of small and medium spans, is markedly influenced just by composition of the periodic load of moving vehicles, due to the loading interval of vehicles, the rate of the moving loads, and the bridge length. The total dynamic deflections ${}^{(c_{2,res}=33)}w^{(a+2)}_{(1),(P_1,P_2,\dots P_{10})}(L_b/2,t)$ due to load by the series of IC-cars (P_1+P_2+...P_N) is defined by superposition of the quasi-static and the dynamic components described by expressions (11), (12) and (14). For small and medium spans and for low speeds c < 160 km/h, the response does not lead to a significant increase, but at speeds c ≥ 160 km /h the dynamic amplifier factor ${}^{(c_2=33)}\Delta^{(a+2)}_{dyn,(P_1,P_2,\dots P_N)}$ increases significantly in particular due to the dynamic components ${}^{(c)}w^{(2)}_{(1),(P_1,P_2,\dots P_N)}(L_b/2,t)$.

Comparison results for the train speed c_2 = 33 m/s and $c_{2,res}$ = 65 m/s depicted on the Fig. 10 confirms the above statement.

The occurrence of resonant speeds $c_{i,res}$ results from parameters of the bridge and the train (distance axles of the train and the train speed). The resonant speeds $c_{i,res}$ are reflected in a cumulative increase in dynamic response. With an increasing number of load forces n = 1,2, ... N, for M-forces moving along the bridge and K-forces that have passed the beam, the deflection amplitude ${}^{(c_{2,res}=33)}w^{(a+2)}_{(1),(P_1,P_2,\dots P_{10})}(L_b/2,t)$ increases.

Acknowledgment

This work was supported by the projects of Slovak Science Agency VEGA No.1/0336/15 and No. 2/0033/15 of the Slovak republic.

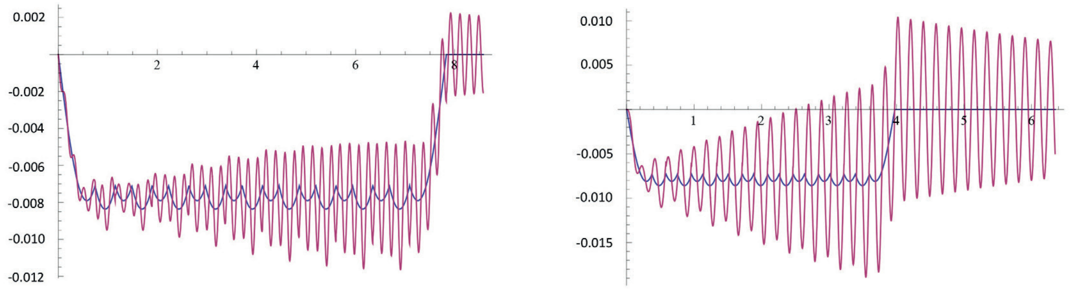

Axes: x = t [s], y = w [m]

Fig. 10 Comparison the total dynamic response for the train speed c_2 = 33 m/s and $c_{2,res}$ = 65 m/s

References

[1] KOLOUSEK, V.: *Structural dynamic - Part I.* (in Czech). SNTL, Praha, p. 263, 1954.

[2] BIGGS, J. M.: *Structural Mechanics*. McGraw-Hill, New York, 1964.

[3] FRYBA, L.: *Vibration of Solids and Structures under Moving Loads*. Telford, London, 1999.

[4] STN 1991-2: The European Standard EN 1991-2 (in Slovak), 2006.

[5] JANG, Y. B., LIN, C. W.: Vehicle-Bridge Interaction Dynamics and Potential Applications. *Journal of Sound and Vibration*, 284, 205-226, 2005.

[6] LI, J., SU, M.: The Resonant Vibration for a Simply Supported Girder Bridge under High-Speed Trains. *Journal of Sound and Vibration*, 224(5), 897-915, 1999.

[7] NAPRSTEK, J.: *Resonance Speeds of Axle Forces Row Moving Along a Beam.* Colloquium "Dynamics of Machines 2000", Czech Republic, 2000.

[8] https://www.amazon.com/Wolfram-Mathematica 8.0.1 [online].

https://doi.org/10.26552/com.C.2017.3.102-108

Radoslav Ponechal - Daniela Staffenova*

INSULATION THICKNESS VERSUS DYNAMIC THERMAL PARAMETERS OF EXTERNAL WALLS WITH REGARD TO THE THERMAL STABILITY

It appears that the walls, insulated according to the new requirements for thermal resistance, can contribute to thermal stability. This is advantageous not only for the thermal comfort during the summer but in the cases of the intermittent heating, or overheating, as well. This article evaluates some alternatives of insulated and uninsulated external walls. The phase time shift of the indoor surface temperature with respect to the outdoor surface, together with the periodic penetration depth of indoor surface temperature, are considered in this analysis. Analyzing subsurface temperature courses we evaluate the ability of construction to accumulate heat gains, which can arise during the day.

Keywords: *Penetration depth, thermal damping factor, phase time shift, thermal accumulation.*

1. Introduction

The criterion of thermal resistance is undoubtedly the important criterion in the process of the building material selection. However, if the values of thermal resistance are approximately at the same level, the builders would come to a number of other criteria, such as the construction technology or internal environment, created by these construction products.

The thermal comfort is one of the main components in forming the internal environment. For its fulfillment, some form of thermal stability of the internal environment is required. The wide temperature fluctuation that can be visible inside residential buildings is mainly due to the increase of heat sources. During the summer, overheating, specifically due to solar gains and ventilation with warm air, can occur. According to Durica et al. [1], the risk of overheating from the point of view of frequency (with a temperature over 25 °C) can occur in different kinds of passive house constructions. All of the exterior envelope structures evaluated in this study reach the same thermal transmittance. The lowest percentage of overheating occurrence (0.58 %) was reached by the version with walls made of the lime-sand block covered with expanded polystyrene and ceiling made of reinforced concrete. The highest incidence (2.6 %) was found in the version with walls and ceilings made of wooden frame construction filled with sheep wool insulation. Nemecek solved similar problems in the passive house [2]. In his contribution based on simulation calculations of summer overheating, he ranks an energy storage capacity of construction in the 4th place, according to the importance, behind heat gains from solar radiation, internal heat gains and ventilation regime. The difference between air temperatures by light-weight or heavy-weight construction is about 1-1.5 K.

During the winter, overheating may be caused by too much power used for heating in combination with not optimal thermal control of the heating system. Overheating problems associated with the use of wood stoves are documented in Ponechal [3]. Results from the temperature recorder installed in family house showed relatively large temperature fluctuations during the day from 22 up to 27 °C. High temperatures are reached at night, which are opposite to an ideal state when the night-time temperatures should fall in terms of healthy and good sleeping. The short-term overheating can also be used in a positive way, particularly by the intermittent heating, blackouts, etc. Stock of the heat accumulated in building construction during the period of overheating (ideally when the space is not being occupied) can be used to maintain the thermal stability during the cooler part of the day, as suggested by Wolisz [4]. It is a shame that it was realized on the building with relatively large heat losses, which reduced the general benefit of this idea.

By increasing of thermal inertia of the building, the influence of internal structures is usually evaluated. Figure 1 [5] documents the contribution of reinforced concrete ceiling on the thermal inertia. Houses with higher levels of thermal protection cool down slower.

---

* **Radoslav Ponechal, Daniela Staffenova**
Department of Building Engineering and Urban Planning, Faculty of Civil Engineering, University of Zilina, Slovakia
E-mail: daniela.staffenova@fstav.uniza.sk

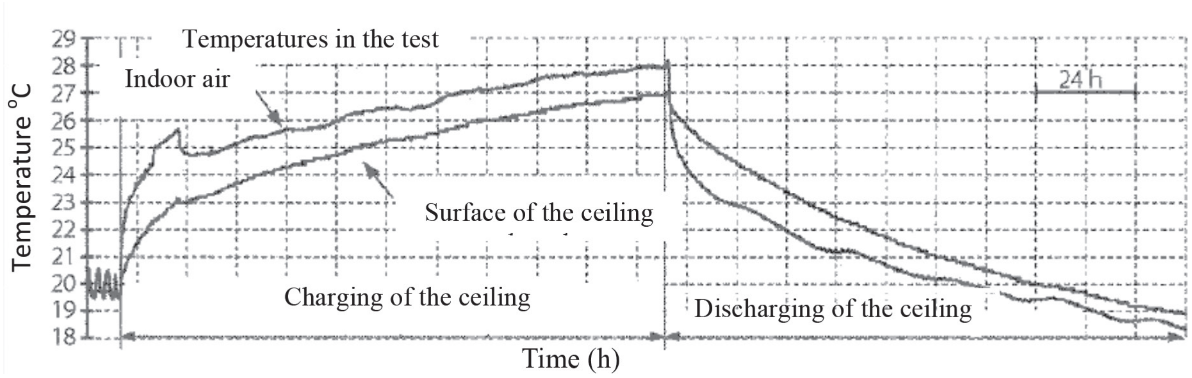

Fig. 1 Experiment of the thermal response. By the absence of residents and switched-off heating and ventilating system, an increase in temperature was reached. This was ensured by the defined heating source in the place of residence, and led to the heating of the reinforced concrete ceiling. After turning off the source, the noticeable thermal inertia is shown, when air in the room is heated by the heat released from the concrete ceiling [5]

Just a temperature discharging process in uninhabited low energy building could be seen in Fig. 2. The presented course of temperature damping is extracted without internal heat gains. With internal heat gains, the temperature damping will be running slower. The effect of internal heat gains is well known and described in details in the literature, e. g. [6].

2. Dynamic thermal properties

Because of the fact that the overheated room temperature is influenced by many factors, it is advisable to look at the comparison of basic dynamic characteristics of building materials separately. The International Standard ISO 13786 [7] describes dynamic thermal parameters of multi-homogeneous-layered walls/roofs based on sinusoidal variations of temperature or the heat flow rate on the one hand and the constant air temperature on the other hand. The parameters relate cyclic heat flow rate to cyclic temperature variations. These parameters are expressed as complex numbers.

Three groups of parameters for the thermal evaluation of building envelope variants in unconditioned buildings are analyzed in this work: thermal damping factor, the phase time shift and the penetration depth of indoor surface temperature. The thermal damping factor (DFs) and phase time shift (LTs) of the indoor surface temperature with respect to the outdoor

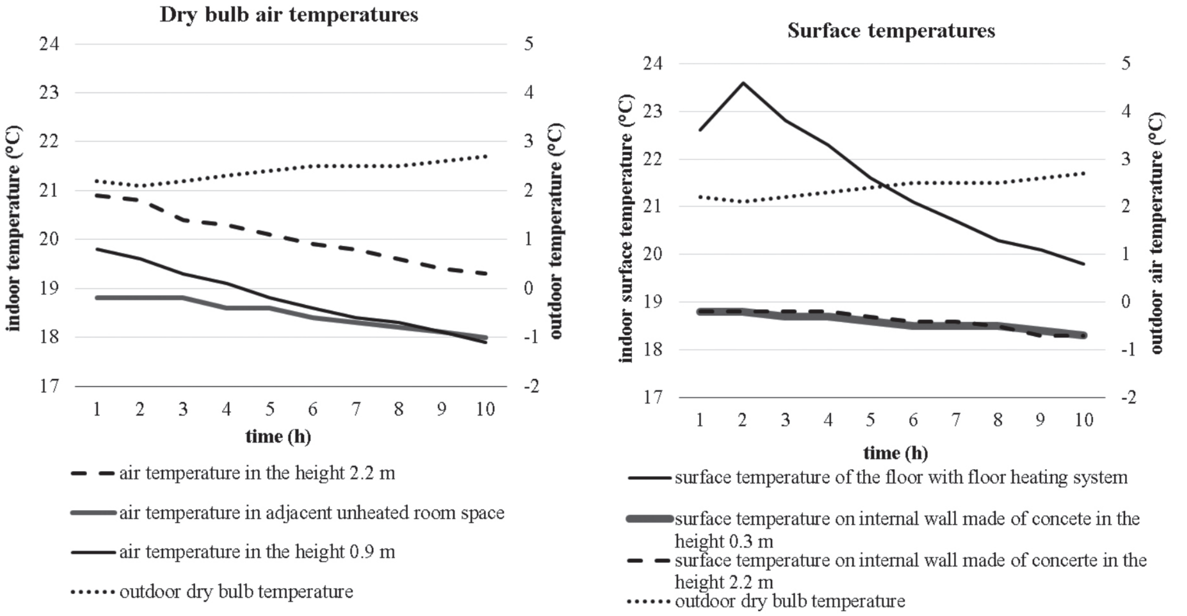

Fig. 2 Experiment of the temperature damping in a low energy family house. The measured building has two floors; the measurement was performed on the 1st floor. The external wall is made of perforated bricks insulated with 200 mm EPS, inner walls are made of 200 mm concrete and partition walls of 115 mm perforated brick. The roof includes 320 mm of mineral wool as the thermal insulation

surface, together with the daily average of the indoor surface temperature θ_{is}, are considered in the analysis. The thermal damping factor is calculated by this formula [8]

$$DFs = \frac{(\theta_{si,\max} - \theta_{si,\min})}{(\theta_{se,\max} - \theta_{se,min})} (\text{-}) \qquad (1)$$

where $\theta_{\mathrm{si,max}}$ and $\theta_{\mathrm{si,min}}$ are the maximum and minimum values of the indoor surface temperature during the day, and $\theta_{\mathrm{se,max}}$ and $\theta_{\mathrm{se,min}}$ are the maximum and minimum values of the outdoor surface temperature.

The phase time shift is defined as

$$LTs = t(\theta_{si,\max}) - t(\theta_{se,\max}) \text{ (h), [8]} \qquad (2)$$

where $t(\theta_{\mathrm{si,max}})$ and $t(\theta_{\mathrm{se,max}})$ are the times, when the indoor surface and outdoor surface temperatures reach their maxima, respectively.

3. Description of the demonstrational constructions

The three wall configurations with four different insulation thicknesses are studied and presented: perforated brick wall (BR), heavy weight concrete wall (HC), porous concrete wall (PC) with thermal insulation made of expanded polystyrene (EPS) or mineral wool (MW). These three wall variants have very similar U-values, but differ from each other in dimensions, material density and thermal conductivity. Each of the wall compositions (according to Fig. 3) has some selected different insulation thicknesses. The first variant fulfills the requirement for minimal thermal resistance $R_{\min}$, second variant fulfills desired value R_N, third variant fulfills recommended value R_{r1} (considered for the year 2016) and the last variant fulfills the final thermal resistance R_{r2} (considered for the year 2021) by the STN 73 0540 standard [9]. The wall layers compositions are described in Fig. 3.

4. Impact of thermal resistance variations on DFs and LTs

The experiment analyzes several of the above mentioned external wall compositions with the calculation of thermal damping factor and phase time shift of the temperature oscillation, which was conducted based on EN ISO 13786. The results from all calculations are shown in Table 1 and Fig. 4.

Constructions designed for new buildings (with the thermal resistances R_{r1} and R_{r2}) reach significantly higher values of the thermal damping factor than constructions with minimum requirements for thermal resistance. There are strongly significant differences between the porous concrete wall and the other two alternatives. While by the other insulated walls the thermal damping factor is as high as it is meaningless, this is not the case of the porous concrete wall. Comparing differences by phase time shift, it is necessary to take into account the values of temperature setback, too.

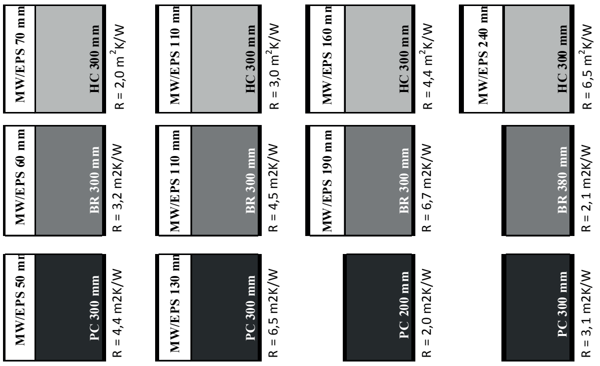

Fig. 3 Evaluated variants of external wall

Results of thermal performance variables reached for evaluated wall variants

Table 1

	Construction	R	DFs	LTs
1	HC 300 + MW 70	2.032	160.8	11.7
2	HC 300 + EPS 70	2.032	156.1	10.5
3	BR 380	2.111	261.4	18.4
4	PC 200	2.083	28.2	8.1
5	HC 300 + MW 110	3.085	294.8	13.4
6	HC 300 + EPS 110	3.085	255	11.5
7	BR 300 + MW 60	3.246	333.3	17.2
8	BR 300 + EPS 60	3.246	314.9	16.1
9	PC 300	3.125	87	12.2
10	HC 300 + MW 160	4.401	575.1	15.6
11	HC 300 + EPS 160	4.401	417.8	12.9
12	BR 300 + MW 110	4.562	726.3	19.3
13	BR 300 + EPS 110	4.562	597.3	17.5
14	PC 300 + MW 50	4.441	119.3	14.4
15	PC 300 + EPS 50	4.441	95	13.5
16	HC 300 + MW 240	6.506	1555	19.1
17	HC 300 + EPS 240	6.506	827.6	15.0
18	BR 300 + MW 190	6.667	2071.6	22.8
19	BR 300 + EPS 190	6.667	1277.4	19.6
20	PC 300 + MW 130	6.546	413.1	17.9
21	PC 300 + EPS 130	6.546	262.6	15.7

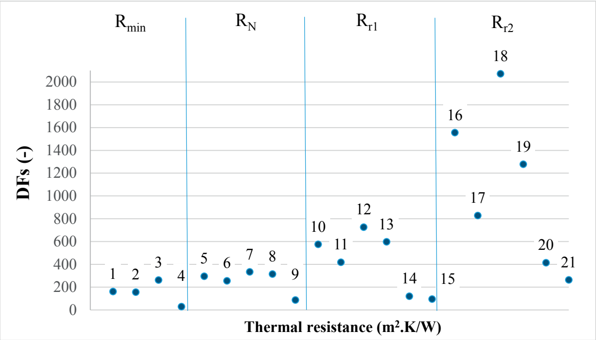

Fig. 4 Thermal damping factor (DFs) vs. thermal resistance of the wall variations. Characteristics: perforated brick (BR) λ = 0.18 W/(m.K), ρ = 930 kg/m^3, porous concrete (PC) λ = 0.096 W/(m.K), ρ = 300 kg/m^3, heavy-weight concrete (HC) λ = 1.58 W/(m.K), ρ = 2400 kg/m^3

If the value of temperature damping is high (e.g. 200 and more), the phase time shift does not play such a role and the inner surface temperature will increase up to 0.5 degree only. It is not so crucial according to the fact at what time this occurs.

Some uncertainty in the results may be caused by the moisture content. Weather and other boundary conditions and circumstances can produce humidity that can act on the building structure, e.g., by changing its heat capacity, heat transfer coefficient and other factors [10]. It is therefore necessary to measure the sorption behaviours of the construction materials [11].

Calculations of DF and LT are meaningful only in terms of heat transfer in fragments of building envelope constructions (walls, roofs, etc.). The complete image of the building or a room in the building, in terms of summer overheating, will be given

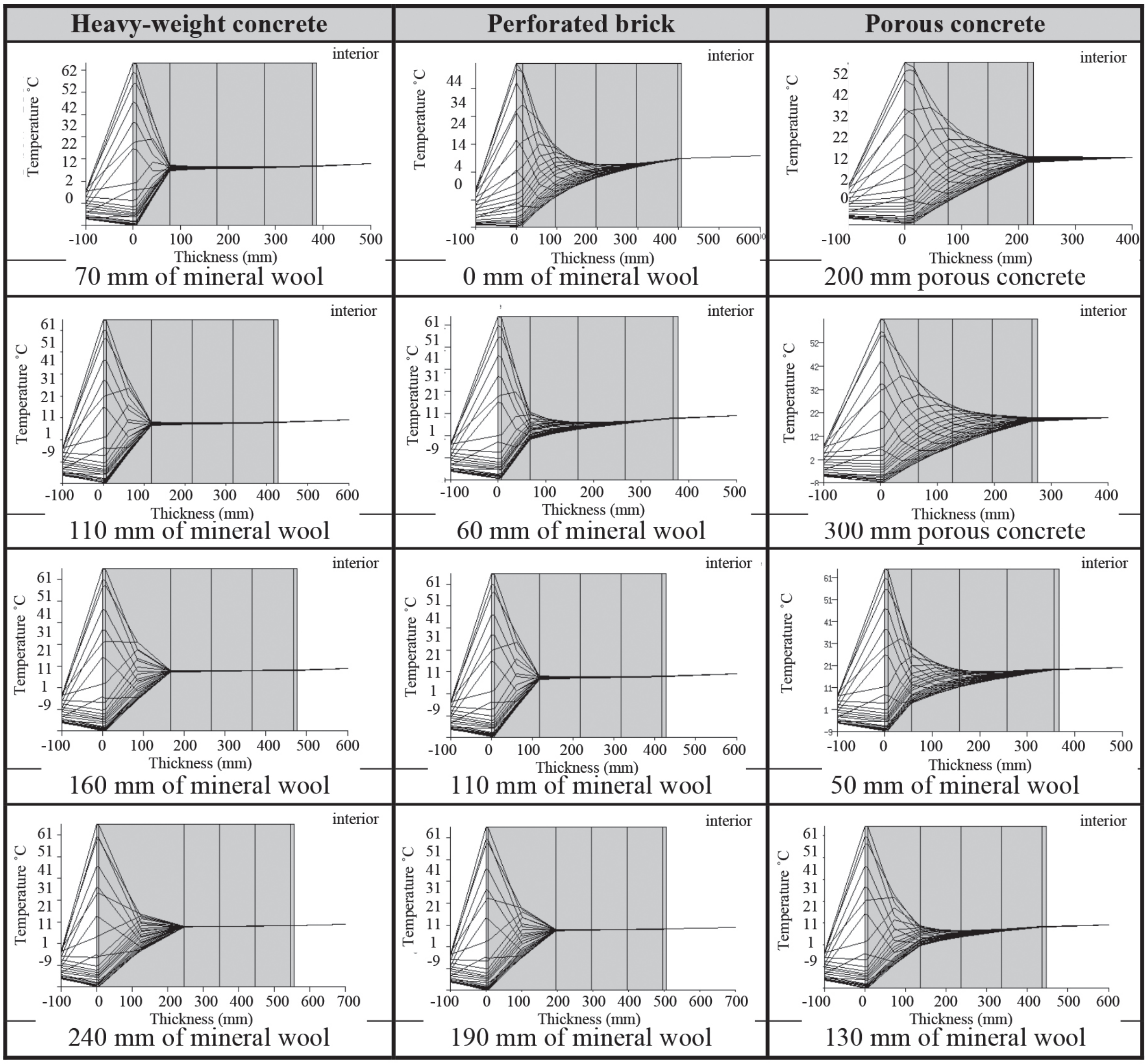

Fig. 5 External surface temperature penetration depth on a typical winter sunny day for the southward oriented facade

only by complex calculations of the thermal stability or computer simulations.

5. Impact of variation in wall construction on external surface temperature penetration depth

Insulated wall can resist temperatures from the inside and from the outside with a difference. Although the greater insulation thickness features very high DF values (200 and more and thus the amplitude of temperature on the inner surface is very small), we can see the difference between the external surface temperature penetration depths. An overview of the daily temperature operation on a sunny winter day in each type of wall can be seen in Fig. 5. The simulation model was calibrated by comparison to real measurements in a research laboratory [12]. The temperature measurements were made for the lightweight wall construction, which consists of three different material solutions and three different color solutions of external coating. The ESP-r software [13] was used to perform the thermal simulation. The facade is oriented southward with a rotation of 17 degrees from the west. Indoor air temperature was set as ideal to 20 °C for the whole duration of the experiment. For simulation the test reference year from IWEC database for Ostrava was used.

The amplitude of the external surface temperature is very large in all evaluated alternatives of simulation. In majority of cases, it expires at the position between the thermal insulation and bearing wall. This statement does not go for the wall without insulation or with a very small insulation thickness.

6. Impact of the wall material variation on internal surface temperature penetration depth

The periodic penetration depth δ is a depth at which the amplitude of the temperature variations is 2.71 times reduced in a homogeneous material of infinite thickness subjected to sinusoidal temperature variations on its surface. Another representation of the concept is:

$$\delta = \sqrt{\frac{\lambda T}{\pi . \rho . c}} \text{ (m)} \qquad (3)$$

When we look at the course in Fig. 6, we can see that the difference in the depth of penetration of thermal waves is negligible in the first hours. The significant difference between the concrete wall and the others occurs when the temperature wave operates longer than T = 12 hours. Penetration depth 100 mm (which is currently under consideration in the calculation of heat accumulation in structures) is achieved by use of new bricks in 24 hours or more. This has practically nothing to do with diurnal variations in temperature.

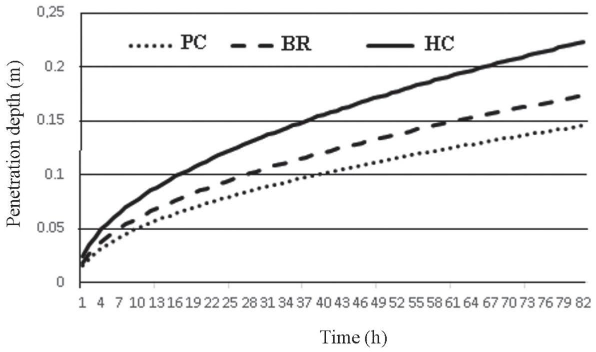

Fig. 6 Dependence of penetration depth vs time, perforated brick (BR), porous concrete (PC), heavy-weight concrete (HC)

7. Impact of variation in wall construction on subsurface temperature

Impact of the wall variation on temperature at the position of 50 mm under the inner wall surface was studied at the above described simulation model. The 50 mm is the penetration depth in case of the 4 - 10 hour time interval. The evaluation was made in an extreme summer week when several hot sunny days followed each other. To simplify, the internal air temperature was set as constant with the value of 22 °C. The resulting behavior of subsurface temperatures is shown in Fig. 7. Thermal insulation of the walls significantly reduces the rise of inside subsurface temperature, particularly by the brick wall. When comparing a brick wall to a porous concrete wall, the brick wall has the lower subsurface temperature by the identical thermal resistance. The 300 mm perforated brick wall with 110 mm of mineral wool reached the maximum temperature of 22.8 °C, while the porous concrete wall 300 mm thick with mineral wool of thickness 50 mm reached the temperature of 24.2 °C (Fig. 8). The brick wall has a surface thermal capacity of 79 680 kJ/K, while the porous concrete wall has only 30 000 kJ/K. If we consider that the internal air temperature at a given time is 26 °C, we get an accumulation potential of 254 976 kJ for the brick wall and 54 000 kJ for the porous concrete, which is five times less.

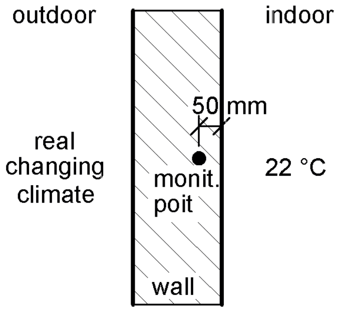

Fig. 7 Position of the subsurface temperature monitoring point

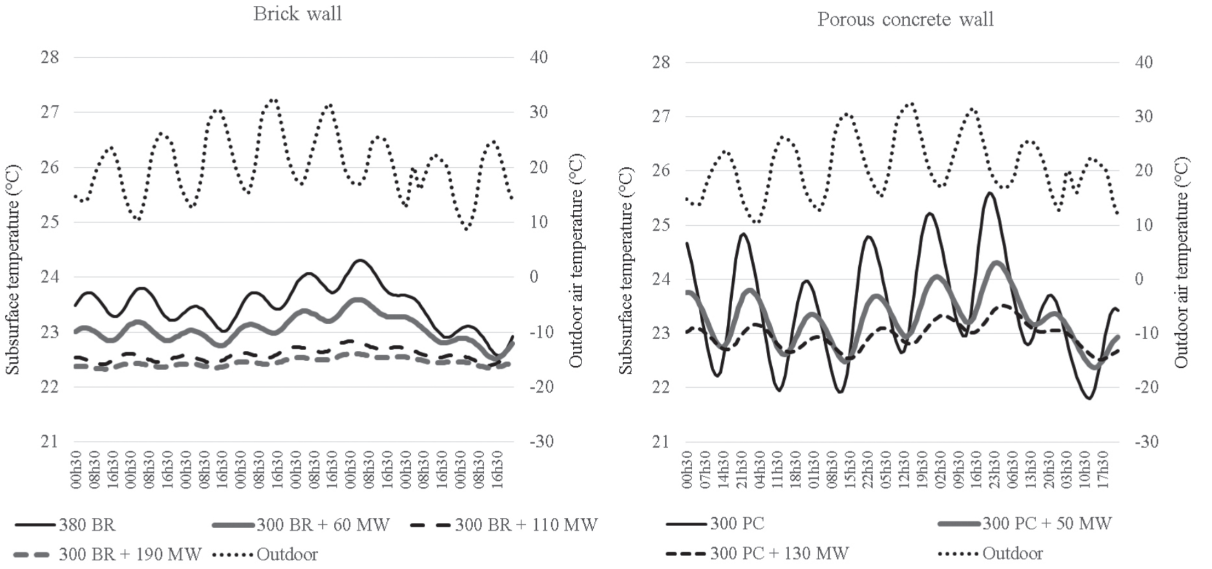

Fig. 8 Subsurface temperature in perforated brick wall and porous concrete wall (50 mm under the interior surface)

8. Conclusion

By use of the thermal stability calculation and possibility of overheating, the internal heat capacity of the floor, ceiling and dividing walls is taken into account, as well as the measure of heat gains from internal sources and solar radiation.

The impact of external wall on overheating could be defined in two ways: as the structure, through which the heat is transferred from the exterior and it warms the interior or (less usual) as the structure, which by its accumulative ability contributes to the thermal stability of interior.

In the first case, the thermal damping factor, which is very high for the walls in new buildings, is an important criteria. The thermal insulation protects the wall from rapid temperature changes. Assessment in terms of the daily cycle of temperature rise and fall is an insignificant phenomenon from this point of view. If we use a simplified assessment, based on the thermal damping factor and phase time shift, the use of any of the examined alternatives for external walls does not represent a significant risk in terms of overheating, except for porous concrete wall with small thickness.

The second method, when the external walls could affect the interior overheating is its accumulative ability. The simplified calculation does not account for external walls thermal capacity. Integrating of simulation approach could eliminate this imperfection. It appears that the walls insulated in compliance with the new requirements for the thermal resistance can contribute to thermal stability of the room. From the point of view of the daily temperature increase only the internal layer is important. Well shielded, insulated and ventilated buildings are able to resist overheating during the several hot days. We think, that in the future it might be interesting to track the ability of building to resist the long-term higher temperatures during the summer or failure of a heat source during the winter. The external wall, which holds more heat, has a higher potential to stabilize the interior temperature.

Acknowledgement

Presented results were obtained with the support of the grant project VEGA no. 1/0945/16. Thanks to Caroline Kyzek, M.A. for language proofreading.

References

[1] DURICA, P., BADUROVA, S., PONECHAL, R.: Life Cycle Greenhouse Gas Emissions and Energy Analysis of Passive House with Variable Construction Materials. *Selected Scientific Papers - Journal of Civil Engineering,* 8(2), 21-32, 2013.

[2] NEMECEK, M., KALOUSEK, M.: *Internal Heat Accumulation of Passive Houses and Summer Heat Stability* (in Czech) [online]. Available: www.tzb-info.cz.

[3] PONECHAL, R., KANDERKOVA, M.: *Thermal Environment in a Room with Dynamic Infrared Fireplace Heater.* Proc. of CESBP 2013, Austria, 373-380, 2013.

[4] WOLISZ, H., HARB, H., MATTHES, P., STREBLOW, R., MULLER, D.: *Dynamic Simulation of Thermal Capacity and Charging: Discharging Performance for Sensible Heat Storage in Building Wall Mass*. Proc. of 13th Intern. Conference of the Intern. Building Performance Simulation Association (IBPSA 2013), France, 2716-2723, 2013.

[5] TYWONIAK, J., et al.: *Monitoring of Energy Performance of Passive Houses* (in Czech). GRADA, Praha, 2012.

[6] STAZI, F., DI PERNA, C.: Influence of the Internal Inertia of the Building Envelope on Summertime Comfort in Buildings with High Internal Heat Loads. *Journal of Energy and Buildings*, 43, 200-206, 2011.

[7] STN EN ISO 13786: *Thermal Performance of Building Components. Dynamic thermal characteristics*. Calculation methods. Slovak office of standards, metrology and testing, Bratislava, 2007.

[8] BARRIOS, G., HUELSZ, G., RECHTMAN, R., ROJAS, J.: Wall/Roof Thermal Performance Diferences between Air-Contidionted an Non Air-Conditioned Rooms. *Energy and Buildings*, 43, 219-223, 2011.

[9] STN 73 0540:2012: *Thermal Performance of Buildings and Components. Thermal protection of buildings*. Slovak office of standards, metrology and testing, Bratislava, 2012.

[10] LAKATOS, A., KALMAR, F.: Analysis of Water Sorption and Thermal Conductivity of Expanded Polystyrene Insulation Materials. *Building Services Engineering Research and Technology*, 34, 407-416, 2013.

[11] DURICA, P., VERTAL, M.: Verification of the Water Transport Parameter - Moisture Storage Function of Autoclaved Aerated Concrete - Approximately Calculated from a Small Set of Measured Characteristic Values. *Communications - Scientific Letters of the University of Zilina*, 13(4), 92-97, 2011.

[12] SUSTIAKOVA, M., DURICA, P., PONECHAL, R., CANGAR, M.: *Comparison of Experimental and Computational Characteristics of Light Perimeter Walls of Wooden Buildings* [online]. *6th Intern. Conference on Contemporary Problems of Architecture and Construction, Czech Republic*, p. 6, 2014. Available: http://www.scientific.net/AMR.1020.25.

[13] CLARKE, J. A.: *Energy Simulation in Building Design.* Butterworth-Heinemann, Oxford, 2012.

https://doi.org/10.26552/com.C.2017.3.109-114

Vukic Lazic - Dusan Arsic - Ruzica R. Nikolic - Miodrag Arsic - Branislav Hadzima*

SELECTING THE LOW ALLOY-TEMPERED STEEL FOR MANUFACTURING THE HIGHLY LOADED RESPONSIBLE PARTS

The selecting procedure of the optimal material for manufacturing the highly loaded responsible parts for military applications is presented in this paper. The considered part is in exploitation subjected to complex compressive-impact loading and cyclically to high temperatures, as well. The proper selection of material can be done exclusively based on the theoretical and experimental analysis of properties of the steel in question. The theoretical and experimental selecting of adequate steel for manufacturing such parts is done based on requirements arising from their working conditions. Based on the available data for various steels, chemical composition, mechanical and technological properties, available CCT diagram, the optimal steel was selected for the given working conditions. After the selection of the material, experimental investigations on specially prepared material samples were conducted. The real chemical composition of material was established, its most important mechanical properties were determined, the hardness was measured and the microstructure was determined, as well. After the conducted theoretical and experimental investigations, the responsible machine part was manufactured from the selected material by forging. Then, the mechanical and heat processing was executed, after which the part was tested in the real working conditions. Based on investigations of part's behavior in the real working conditions, it was concluded that the selection of the material was adequate.

Keywords: *Low-alloyed steel, mechanical properties, microstructure, machine parts.*

1. Introduction

At the very beginning of the material selection, it is necessary to perform an analysis of all the influential parameters that could lead to that selection to be optimal. The poor material selection can be the cause of various failures and damages, which could bring about both financial losses and injuries [1]. During the selection of material for manufacturing this highly loaded and extremely responsible part, authors of this paper were guided by their own experience, as well as that of other researchers. Though today exist numerous quantitative methods for material selecting, which have been verified as quite reliable, the part made of the selected material must be, at the end, tested in the real exploitation conditions [2]. This is why one can say that the experimental investigations are those that provide for the most reliable results, as well as that this kind of experience can also be achieved during the material selecting for reparation of the damaged machine systems by welding or surfacing/hard facing. In paper [3] authors have shown how a material can be successfully selected and thus the undesired consequences, due to presence of non-metallic inclusions in material, can be avoided. In research reported in [4] it was shown how a reparation of the damaged pulley of a bucket wheel boom hoist system can be successfully executed when the adequate material for hard facing was selected.

Material that is to be selected in this work ought to satisfy all the criteria related to good wear resistance [5 - 9], increased operating temperature [10 - 11], as well as the high pressures, which could be greater than 1000 bar (100 MPa). In material testing, authors were guided by procedures applied by other researchers, as well [8], in order to obtain as relevant results as possible. This paper is, to a certain extent, a report on material investigation and estimate whether it could be successfully used for the given purpose.

2. The proposed material

For the machine part, analyzed in this paper, the characteristic loads are the following: impact-compressive, cyclic repetitive and high temperature. Taking into account that the part is a highly

---

* **[1]Vukic Lazic, [1]Dusan Arsic, [1,3]Ruzica R. Nikolic, [2]Miodrag Arsic, [3]Branislav Hadzima**
[1]Faculty of Engineering, University of Kragujevac, Serbia
[3]Institute for testing of materials - IMS, Belgrade, Serbia
[4]Research Center, University of Zilina, Slovakia
E-mail: dusan.arsic@fink.rs

Prescribed chemical composition and mechanical properties of steel 25CrMo4 Table 1

Content of elements, weight %				
C	Si	Mn	Cr	Mo
0.22-0.29	max 0.40	0.60-0.90	1.05	0.25
Mechanical properties Ø = 40-100 mm				
R_m, MPa	$R_{p0,2}$, MPa	*A*, %	*Z*, %	*KCV, J*
800-950	min. 600	min. 15	min. 55	min. 50

responsible one, the material selection was immediately reduced to alloyed steels. Considering the purpose and the function of the part, based on experience and recommendations from other authors, the selection was narrowed down to low-alloy tempered steel 25CrMo4 [12]. The prescribed chemical composition and mechanical properties of this material, as per manufacturer's declaration, are shown in Table 1.

Based on these chemical and mechanical properties, as well as on the performed analysis of the fatigue strength and toughness [5 - 7] and wear resistance [8 - 9], authors have assumed that this material can fulfill the requirements set for this construction.

3. Experimental testing

After the material was selected, the tests on adequate samples were performed. The following properties were tested: chemical composition, mechanical properties, hardness and microstructure. The first two categories were certified by the manufacturer, but they were tested anyway, for the authors had to be certain that declared properties were correct, since any deviation could lead to part's improper functioning or damages and injuries of the user. After all the properties were tested and verified, the tube was produced of the selected material and tested in the real operation conditions.

3.1 Chemical composition

The first test was checking of the material's chemical composition. It was done by the optical emission spectrometry, according to the corresponding standard [13]. Obtained results are shown in Table 2. These results have exhibited certain deviations from those specified by the manufacturer, primarily in the content of chromium and molybdenum. This is, however, explained by the aimed military application of the part, where certain other (internal and specific) standards are applicable. The laboratory tests results have established that the considered steel, according to mechanical properties, corresponds the most to steel 25CrMo4.

The increased chromium content could be explained by the fact that with Cr increase the steel's hardenability and fire resistance also increase. In addition, in some steels, with carbon content that is higher than needed for creation of perlite, special chromium carbides ($Cr_{23}C_6$, Cr_7C_3 and Cr_3C_2) are created, which, if stable, contribute to increased wear resistance. On the other hand, molybdenum in structural steels, with contents 0.20 – 0.60 %, causes grain size decreasing what contributes to increase of toughness and hardenability and decreases affinity of steels to overheating, since V with carbon forms the carbide (VC), which prevents increase of the grain size.

3.2 Tensile and impact testing

After the chemical composition checking, the tensile test on selected material samples was performed. The test was performed in the accredited laboratory on the universal testing machine WPM ZD 40, on the standard cylindrical sample (Fig. 1), according to the adequate standard [14]. In addition, samples for determination of the impact toughness at the room temperature were prepared. The test was done on the Charpy pendulum, according to standard SRPS EN ISO 148-1:2012 [15]. Results of both tests are shown in Table 3.

Analyzed chemical composition of steel 25CrMo4 Table 2

Content of elements, weight %											
C	Si	Mn	Cr	Mo	Ni	Cu	Al	V	Ti	P	S
0.273	0.387	0.526	3.387	0.578	0.108	0.184	0.006	0.011	0.002	0.020	0.017

Results of tensile properties test of 25CrMo4 steel Table 3

Material	Yield strength $R_{p0.2}$, MPa	Tensile strength R_m, MPa	Elongation A, %	Contraction Area reduction %	Impact energy, J	Hardness HV 10
25CrMo4	784	925	40	68	143	275
	775	923	40	68	142	273

Tensile testing

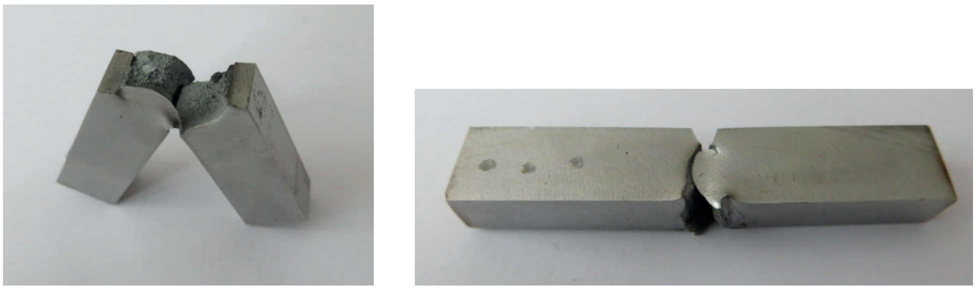

Impact toughness testing

Fig. 1 Broken specimens after testing

Analysis of obtained results confirmed that the data guaranteed by the steel manufacturer were correct and that the material can be used for the planned part manufacturing. In situations when the quick verification of the material properties is needed, one can also use the numerical simulations, which turned out to be quite reliable for checking the materials strength [11].

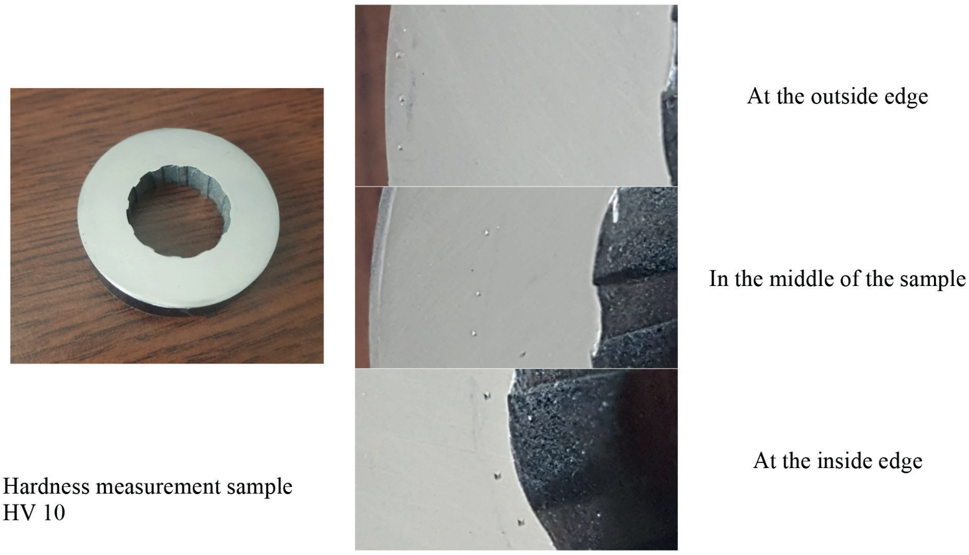

Fig. 2 Hardness measurements - sample and places

3.3 Hardness measurement and microstructure examination

The material hardness measurement and testing of microstructure were done on cylindrical ring samples, shown in Figs. 2 and 3. Tests were done at the inside edge of the tube, in the middle and at outside edge of the tube. The samples' hardness was within range 273 to 275 HV (Table 3), while the obtained microstructure appearances are shown in Fig. 3. Considering that the hardness is less than 350 HV, one can say that creation of martensite was avoided.

3.4 Estimate of microstructure based on the CCT diagram

Obtained microstructure can be also estimated based on the corresponding CCT diagram (Fig. 4). The red-off microstructure – bainite and tempered martensite – corresponds to quenching in water and high tempering, what constitutes the heat treatment prescribed by the steel manufacturer, as well. It is extremely important that there is no pure martensite in the final structure, since it could act as the stress concentrator due to the dynamic loading during the exploitation.

The considered tube was obtained by the following procedures and with the following regimes:

- forging – at the forging bat from the steel piece heated up to 1100 °C;
- normalization – at 870 °C;
- quenching – at 860 °C and cooling in oil;
- tempering – at 600 °C and cooling in the furnace.

It is possible to adopt the procedure of continuous bainite or isothermal bainite quenching from the temperature of 860 °C, for manufacturing of the considered part, in order to avoid appearance of martensite (Fig. 3). From the CCT diagram (Fig. 4), one can see that the incubation period, since the beginning of the martensite dissolution is approximately 15 s, what must be taken into account during the heat treatment procedure.

4. Conclusion

The procedure for selecting and testing of the material for manufacturing the responsible structural part is presented in this paper. The selection was performed primarily based on authors' own experiences, as well as on recommendations from other researchers. Since the part in question is a constituent of a very responsible structure, all the properties of the material were tested. It was confirmed that the material is adequate for the assumed application. It has fulfilled all the exploitation requirements of the structure and the tests on the real, manufactured part were also

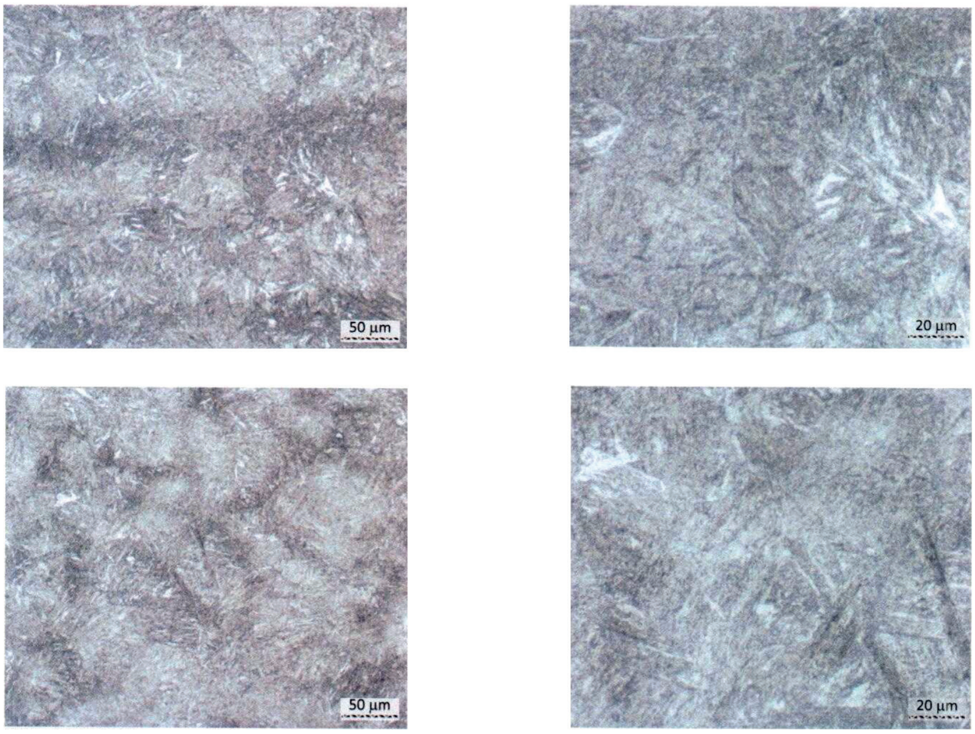

Fig. 3 Microstructure of steel 25CrMo4: tempering microstructure - bainite + tempered martensite

performed. The tube, made of the selected steel by forging, has passed all the tests and trials.

Authors consider that the procedure, presented in this paper, must be obeyed in selection of material for manufacturing the responsible structures and their parts, besides the other theoretical and analytical methods that could be of help.

Acknowledgement

This research was partially financially supported by the European regional development fund and Slovak state budget by the project "Research Centre of the University of Zilina" – ITMS 26220220183 and by the Ministry of Education, Science and Technological Development of Republic of Serbia through grants: ON174004 and TR35024.

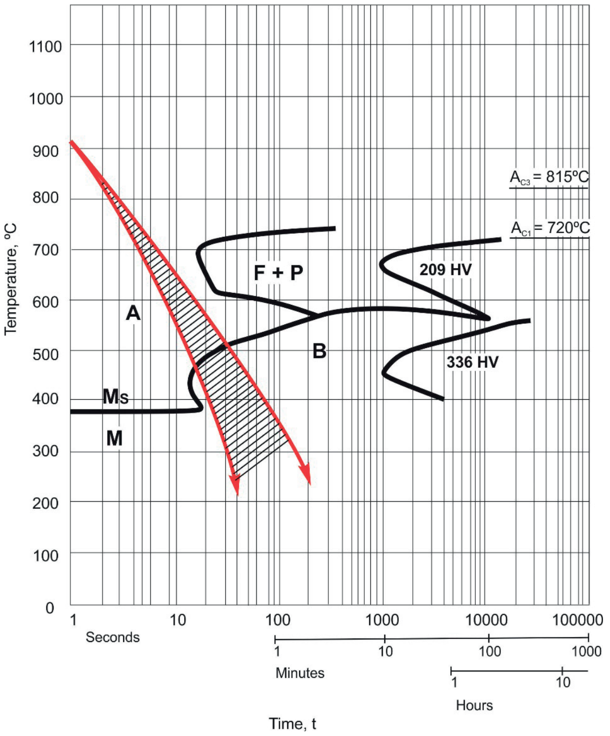

Fig. 4 The CCT diagram for 25CrMo4 steel with shown optimal regime of the continuous bainite quenching

***Note:** This research was partially reported at the 22^{nd} International Seminar of PhD Students "SEMDOK 2017" – reference [16].*

References

[1] LAZAREVIC, Z., ARANDJELOVIC, I., KIRIN, S.: An Analysis of Random Mechanical Failures of Bucket Wheel Excavator. *Structural Integrity and Life*, 15(3), 2015, 143-146.

[2] GOLUBIC, S., CIKIC, A., HRSAK B.: Applying Quantitative Methods in the Selection of Materials. *Tehnicki glasnik-Technical Journal*, 6(1), 1-6, 2012.

[3] ARSIC, D., LAZIC, V., ALEKSANDROVIC, S., NIKOLIC, R., MARINKOVIC, P., DJORDJEVIC, M., RATKOVIC, N.: Theoretical-Experimental Fracture Analysis of a Responsible Machine Part. *Structural Integrity and Life*, 14(2), 141-146, 2014.

[4] BOSNJAK, S., ARSIC, M., SAVICEVIC, S., MILOJEVIC, G., ARSIC, D.: Fracture Analysis of the Pulley of a Bucket Wheel Boom Hoist System. *Eksploatacja i Niezawodnosc-Maintenance and Reliability*, 18(2), 155-163, 2016.

[5] LUKE, M., VARFOLOMEEV, I., LUTKEPOHL, K., ESDERTS, A.: Fatigue Crack Growth in Railway Axles: Assessment Concept and Validation Tests. *Engineering Fracture Mechanics*, 78(5), 714-730, 2011.

[6] VARFOLOMEEV, I., LUKE, M., MOROZ, S.: Experimental and Numerical Investigations of Fatigue Crack Growth in Various Specimen Geometries. *Procedia Engineering*, 2(1), 1829-1837, 2010.

[7] CARBONI, M., REGAZZI, D.: Effect of the Experimental Technique onto R Dependence of ΔK_{th}. *Procedia Engineering*, 10, 2937-2942, 2011.

[8] KHANAFI-BENGHALEM, N., FELDER, E., LOUCIF, K., MONTMITONNET, P.: Plastic Deformation of 25CrMo4 Steel during Wear: Effect of the Temperature, the Normal Force, the Sliding Velocity and the Structural State. *Wear*, 268(1-2), 23-40, 2010.

[9] ARSIC, D., LAZIC, V., MITROVIC, S., DZUNIC, D., ALEKSANDROVIC, S., DJORDJEVIC, M., NEDELJKOVIC, B.: Tribological Behavior of Four Types of Filler Metals for Hard Facing under Dry Conditions. *Industrial Lubrication and Tribology*, 68(6), 729-736, 2016.

[10] JONSTA, P., VLCKOVA, I., JONSTA, Z., HEIDE, R.: Materials Analysis of Degraded Steam Turbine Rotor. *Communications - Scientific Letters of the University of Zilina*, 18(3), 78-826, 2016.

[11] ARSIC, D., DJORDJEVIC, M., ZIVKOVIC, J., SEDMAK, A., ALEKSANDROVIC, S., LAZIC, V., RAKIC, D.: Experimental-numerical Study of Tensile Strength of the High-Strength Steel S690QL at Elevated Temperatures. *Strength of Materials*, 48(5), 687-695, 2016.

[12] EN 10027-1: 2015, Designation systems for steels - Part 1: Steel names.

[13] SRPS C.A1.011: 2004, Methods of chemical analyses – Optical emission spectrometric method with spark excitation for quantitative chemical analyses of pig iron, cast iron, low alloyed steels, high alloyed steels, aluminum alloys and copper alloys (Serbian standard).

[14] EN ISO 6892-1: 2016, Metallic materials - Tensile testing - Part 1: Method of test at room temperature.

[15] SRPS EN ISO 148-1: 2012, Metallic materials - Charpy pendulum impact test - Part 1: Test method (ISO 148-1: 2009).

[16] LAZIC, V., ARSIC, D., NIKOLIC, R., ARSIC, M., HADZIMA, B.: *Procedure for Selecting the Low Alloy-Tempered Steel for Manufacturing the Responsible Highly Loaded Parts.* Proc. of 22nd Intern. Seminar of PhD Students (SEMDOK 2017), Slovakia, 72-76, 2017.

COMMUNICATIONS – Scientific Letters of the University of Zilina
Author guidelines

1. Submitted papers must be unpublished and must not be currently under review for any other publication.
2. Submitted manuscripts should not exceed 8 pages including figures and graphs (in Microsoft WORD – format A4, Times Roman size 12, page margins 2.5 cm).
3. Manuscripts written in good English must include abstract and keywords also written in English. The abstract should not exceed 10 lines.
4. Submission should be sent by e-mail – as an attachment – to the following address: komunikacie@uniza.sk.
5. Uncommon abbreviations must be defined the first time they are used in the text.
6. Figures, graphs and diagrams, if not processed in Microsoft WORD, must be sent in electronic form (as JPG, GIF, TIF, TTF or BMP files) or drawn in high contrast on white paper. Photographs for publication must be either contrastive or on a slide.
7. The numbered reference citation within text should be enclosed in square brackets - in numerical order. The reference list should appear at the end of the article (in compliance with ISO 690).
8. The numbered figures and tables must be also included in the text.
9. The author‘s exact mailing address, full names, E-mail address, telephone or fax number, the name and address of the organization and workplace (also written in English) must be enclosed.
10. The editorial board will assess the submitted paper in its following session. If the manuscript is accepted for publication, it will be sent to peer review and language correction. After reviewing and incorporating the editor‘s comments, the final draft (before printing) will be sent to authors for final review and minor adjustments.
11. Submission deadlines are: September 30, December 31, March 31 and June 30.

COMMUNICATIONS

SCIENTIFIC LETTERS OF THE UNIVERSITY OF ZILINA
VOLUME 19

Address of the editorial office:
University of Zilina
EDIS – Publishing House
Univerzitna 8215/1
010 26 Zilina
Slovakia

E-mail: komunikacie@uniza.sk

Individual issues of the journal can be found on:
http://www.uniza.sk/komunikacie

Each paper was reviewed by two reviewers.

Journal is excerpted in **COMPENDEX** and **SCOPUS**.

Published quarterly by University of Zilina in
EDIS – Publishing House of University of Zilina

Registered No: EV 3672/09

ISSN 1335-4205

ICO 00397 563

September 2017